Electronic transport in graphene nanoribbon junctions

Kristians CERNEVICS

To Elija. . .

Acknowledgements

First and foremost I would like to thank my thesis supervisor Prof. Oleg V. Yazyev. He has persistently encouraged me to undertake completely new projects and greatly expanded my horizons. I am grateful for the support and advises given throughout my Ph.D.

Next, I would like to express my gratitude to all of the other members of my thesis jury – Prof. Roman Fasel, Prof. Stephan Roche, Prof. Alfredo Pasquarello and Prof. Oleg Boyarkine – who gladly accepted the invitation and will devote their valuable time.

I would also like to thank the collaborators I met and worked with during my Ph.D. First of all it is Prof. Roman Fasel and his group at EMPA, where I had the pleasure to visit and discuss my research with many of the group members. This visit resulted in on-going collaboration and multiple successful projects together. Special thanks goes to Dr. Gabriela Borin Barin, who was always happy to give an insight from the experimental side of the research, as well as Dr. Pascal Ruffieux and Prof. Shiyong Wang.

Next, it is the group of Prof. Andras Kis with whom I worked together on explaining diverse phenomena in 2D materials. I especially want to thank the group members – Yanfei Zhao, Gabriele Pasquale and Dr. Zhe Sun for the patience and guidance showed to me when I first started tackling the world of 2D materials.

I am also grateful to the members of the group of Prof. Nicola Marzari for their invaluable help with setting up the web application and dealing with the Materials Cloud platform. Many meetings and emails were shared between me and Dr. Valeria Granata with help from Dr. Leopold Talirz, Dr. Du Dou and many others.

I would also like to thank Dr. Peter H. Jacobse from the group of Prof. Mike Crommie at University of California, Berkley, who gave me the opportunity to be involved in very exciting research and once again tackle previously unseen problems.

I'm also very grateful to Prof. Alfredo Pasquarello with whom I had the opportunity to work together on a project and also learn a lot from following his course.

Another thanks goes to Martin Fuechsle and Mohammad Choucair from Archer, who involved me in the world of quantum technology and will be supporting me as a Post-Doc to continue working together on our project.

I'm very much indebted to the past and present secretaries of our group, Tanya Castellino, Annick Evequoz and Patricia Byron for their help with both scientific support and also everyday issues. And of course, also the IT staff, Florence Hagen and Aubry Jaquier for quickly resolving all of the issues. I would also like to thank the administrative assistant of the doctoral school, Anne Lene Odegaard, for always having answers to arising questions and for the great help of

Abstract

Graphene nanoribbons (GNRs) – one-dimensional strips of graphene – share many of the
exciting properties of graphene, such as ballistic transport over micron dimensions, strength
and flexibility, but more importantly, they exhibit a tunable band gap that depends on the
atomic structure. Recent advances of fabricating atomically precise bottom-up GNRs with
unprecedented control over their atomic structure have attracted interest from the field of
nanoelectronics. However, a big part of the future success of GNRs depends on the ability
to produce and integrate GNR junctions into complex next-generation devices. Much more
effort is needed in both perfecting the production techniques and improving the theoretical
understanding of these exciting nanostructures.

This thesis is, therefore, devoted to exploring electronic transport properties in graphene
nanoribbon junctions and unraveling their underlying structure-property relationships. Using
tight-binding models, density functional theory and Green's function method, we determine
the electronic properties of both experimentally synthesized and theoretically proposed
junctions.

In the first part of the thesis, we examine width-modulated GNR nanostructures and discover
a subtle interplay between the localized states in the scattering region and the continuum of
states in the leads. We show that depending on the size of the scattering region, we observe
contrasting behavior on the electronic transport properties. Next, we expand the width-
modulated region and show that a width-dependent transport gap opens in the presence
of a quantum dot, thereby yielding built-in one-dimensional metal-semiconductor-metal
junction.

Part II of this thesis is dedicated to a joint experimental and theoretical effort in order to
reveal the detrimental effect of "bite" defects, resulting upon the cleavage of phenyl groups of
precursor molecules. We explore their effect on the electronic transport from first-principles
calculations and show how conduction is disrupted at the band edges. We then generalize our
theoretical findings to other nanoribbons in a systematic manner, thus establishing guidelines
to minimize the detrimental role of such defects. Later, we show that strategically placed
"bite" defects can selectively modify electronic transport properties and apply this concept to
construct two prototypical components for nanoelectronics.

Whereas, in Part III we employ high-throughput screening of over 400000 angled junctions
in order to find potential candidates for interconnects in logic circuits and determine design
rules based on structure-property relationships. We discover that the bipartite symmetry

Abstract

of graphene lattice and the presence of resonant states, localized at the junction, play an important role in determining the transport properties of angled junctions. Besides, we also provide a web application that allows easy design and calculation of electronic properties of GNR junctions. Finally, the last chapter of the thesis involves developing a more realistic model for transport calculations by including finite length and contact effects in order to reduce the gap between the experimental and theoretical results.

Keywords: Graphene, Graphene Nanoribbons, GNR, Junctions, One-dimensional Structures, Electronic Transport, Conductance, Tight-binding, Green's Function, High-throughput Screening.

iv

Résumé

Les Nanorubans de graphène (GNR) – des bandes uni-dimensionnelles de graphène – partagent beaucoup des propriétés du graphène, comme le transport balistique sur des distances micrométriques, la résistance et la flexibilité. Mais surtout, ils présentent une bande interdite réglable qui dépend de la structure atomique. Le succès récent dans la fabrication atomiquement précis GNRs avec un contrôle sans précédent sur la structure a attiré l'attention de la nanoélectronique. Cependant, le futur succès des GNRs dépend de la possibilité de produire et d'intégrer les jonctions des GNR dans des appareils complexes. Par conséquent, beaucoup d'efforts sont nécessaires tant dans le perfectionnement des techniques de production que dans l'amélioration de la compréhension théorique de ces nanostructures.

Cette thèse est donc dévouée à l'exploration du transport électronique dans les jonctions des GNRs et à la resolution des relations entre des propriétés et de la structure. En utilisant le méthode des liaisons fortes, la théorie de la densité fonctionnelle et la fonction de Green, nous avons déterminé les propriétés électriques des jonctions qui sont été synthétisées expérimentalement et aussi découvertes théoriquement.

Dans la première partie de cette thèse, nous avons examiné la largeur ajustable des GNR nanostructures et nous avons découvert l'interaction subtile entre les états localisés dans la région de diffusion et les états continus dans les électrodes. Nous avons montré que'en fonction de la taille de la région de diffusion un comportement contrasté sur les caractéristiques électriques est observé. Ensuite, nous avons étendu la région de la largeur ajustable et prouvé qu'un écart de conduction dépendant de la largeur se créé en présence d'un point quantique.

La deuxième partie de cette thèse est dédiée à un effort à la fois expérimental et théorique dans le but de révéler l'effet néfaste des imperfections de "morsures" créé à partir du clivage du cycle phényle. Nous avons exploré leur effet sur la conductance électrique et nous avons prouvé qu'ils ont considérablement perturbés les propriétés aux bords des bandes. Nous avons ensuite généralisé nos conclusions théoriques aux autres nanorubans et par conséquent nous avons défini des bonnes pratiques pour minimiser le rôle néfaste de ces imperfections. Ensuite, nous avons montré que ces imperfections stratégiquement placées peuvent modifier sélectivement le transport électronique et appliquer ce concept à la construction de composants prototypés pour la nanoélectronique.

Dans la troisième partie, nous avons utilisé une criblage à haut débit de plus de 400000 de jonctions avec le but de trouver des candidats potentiels pour des interconnections dans des circuits logiques et pour déterminer les règles de conception. Nous avons découvert que la symétrie bipartite des mailles de graphène et la présence d'états résonnants situés à la jonction

Résumé

joue un rôle important dans la détermination des propriétés de transport électronique. En plus, nous avons aussi fourni une application web qui permet de concevoir facilement et calculer les propriétés électroniques des jonctions des GNR. Pour conclure, le dernier chapitre de notre thèse implique le développement d'un modèle plus réaliste pour les calculs de conductance en incluant une longueur finie et des effets de contact pour réduire l'écart entre les résultats expérimentaux et théoriques.

Mots-clés : Graphène, Nanorubans de graphène, GNR, Jonctions, structures uni-dimensionnelles, Transport électronique , Conductance, Méthode des liaisons fortes, Fonction de Green, Criblage à haut débit.

List of Contributions

14. Jacobse, P.H.*, McCurdy, R.D.*, Čerņevičs, K.*, Daugherty, M., Wang, Z., Dorit, R., Liu K., Lu, J., Yazyev, O.V., Fischer, F.R. and Crommie, M.F. Exploring topological magnetism in graphene nanoribbons through five-membered rings. – In preparation

13. † Čerņevičs, K., Yazyev, O.V. Finite length and contact effects on electronic transport in graphene nanoribbon heterostructures. – In preparation

12. † Čerņevičs, K., Yazyev, O.V. From defect to effect: controlling electronic transport in chevron-type graphene nanoribbon nanostructures. – In preparation

11. Pasquale, G., Lopriore, E., Sun, Z., Čerņevičs, K., Tagarelli, F., Watanabe, K., Taniguchi, T., Yazyev, O.V. and Kis, A. Flat-band detection by out-of-plane tunneling photocurrent in a layered semiconductor. – In preparation

10. Pasquale, G., Sun, Z., Čerņevičs, K., Perea-Causin, R., Tagarelli, F., Watanabe, K., Taniguchi, T., Malic, E., Yazyev, O.V. and Kis, A. Exciton complexes in a charge-tunable metal monochalcogenide semiconductor. – Submitted

9. Zhao, Y., Tripathi, M., Čerņevičs, K., Avsar, A., Ji, H.G., Gonzalez Marin, H.F., Cheon, C.Y., Wang, Z., Yazyev, O.V., and Kis, A. Electrical spectroscopy of defect states and their hybridization in monolayer MoS_2. – Submitted

8. † Čerņevičs, K., Yazyev, O.V. Design rules for interconnects based on graphene nanoribbon junctions. – Submitted

7. † Pizzochero, M.*, Čerņevičs, K.*, Borin Barin, G., Wang, S., Ruffieux, P., Fasel, R. and Yazyev, O.V. (2021). Quantum electronic transport across "bite" defects in graphene nanoribbons *2D Materials*, 8:035025.

6. Pizzochero, M., Borin Barin, G., Čerņevičs, K., Wang, S., Ruffieux, P., Fasel, R. and Yazyev, O.V. (2021). Edge disorder in bottom-up zigzag graphene nanoribbons: implications for magnetism and quantum electronic transport *J. Phys. Chem. Lett.*, 12:4692.

---

†Publications related to the thesis
*These authors contributed equally to this work

List of Contributions

5. [†] Čerņevičs, K., Granata, V. and Yazyev, O.V. (2020). [‡]Tight-Binding Electronic Transport Application (TBETA) for graphene nanoribbon junctions, *Materials Cloud Archive* 2020.66, doi: 10.24435/materialscloud:av-24.

4. [†] Čerņevičs, K., Yazyev, O.V. and Pizzochero, M. (2020). Electronic transport across quantum dots in graphene nanoribbons: Toward built-in gap-tunable metal-semiconductor-metal heterojunctions. *Phys. Rev. B*, 102:201406(R).

3. Martino, E., Santos-Cottin, D., Le Mardelé, F., Semeniuk, K., Pizzochero, M., Čerņevičs, K., Baptiste, B., Delbes, L., Klotz, S., Capitani, F., Berger, H., Yazyev, O.V. and Akrap, A. (2020). Structural phase transition and bandgap control through mechanical deformation in layered semiconductors 1T–ZrX$_2$ (X = S, Se). *ACS Materials Lett.* 9:1115.

2. [†] Čerņevičs, K., Pizzochero, M. and Yazyev, O.V. (2020). Even–odd conductance effect in graphene nanoribbons induced by edge functionalization with aromatic molecules: basis for novel chemosensors. *Eur. Phys. J. Plus*, 135:681.

1. Hamdan, A. Čerņevičs, K., Cha, M.S. (2017). The effect of electrical conductivity on nanosecond discharges in distilled water and in methanol with argon bubbles. *J. Phys. D*, 50:185207.

[‡]Web application

viii

Contents

Contents

List of Figures

1 Introduction

The single-atom-thick graphene is the first truly two-dimensional material isolated in 2004 by Novoselov and Geim [Novoselov et al., 2004]. This groundbreaking Nobel-prize-winning work defied expectations that two-dimensional materials should not exist in nature [Peierls, 1935] and therefore, rightly propelled graphene to great acclaim. Owing to numerous novel physical properties such as unparalleled thermal conductivity [Balandin et al., 2008], high carrier mobility [Morozov et al., 2008], ballistic transport over micron dimensions [Bolotin et al., 2008], strength and flexibility [Lee et al., 2008], huge hopes have been placed on this carbon-based material from numerous science and industrial fields starting from biology, condensed matter physics and chemistry to energy storage, sensor and even aerospace industry [Barkan, 2019; Reiss et al., 2019]. Perhaps, one of the most exciting expectations for graphene is to replace silicon-based electronics in a new technological revolution to push and eventually exceed the limits of Moore's law [Moore, 1998], which states that the number of transistors per unit area doubles every two years. However, almost 20 years latter graphene has not impacted our everyday lives as much as we have hoped for.

Some of the reasons why graphene has not taken off so far stem from the fact that it simply takes "time and money" to bring a new material to market and although there have been great improvements, it is still quite expensive and challenging to produce defect-free graphene in large amounts [Reiss et al., 2019]. While other reasons are linked to the intrinsic properties of a graphene sheet. For example, while graphene has an extraordinary semi-metallic electronic structure and exhibits massless Dirac fermions [Novoselov et al., 2005], some potential applications in nanoelectronics dictate that the material requires a band gap opening. Interestingly, both of these problems can be tackled by utilizing different kinds of graphene-based nanostructures – with new production methods and tweaked electronic properties. These potential materials include the plethora of sp^2-hybridized carbon nanostructures that extend over all dimensionalities – 0D (fullerene, graphene flakes, carbon nano-onions), 1D (nanoribbons, nanotubes), 2D (haeckelites) and 3D (nanofoams, nanoribbon/nanotube hydrogels).
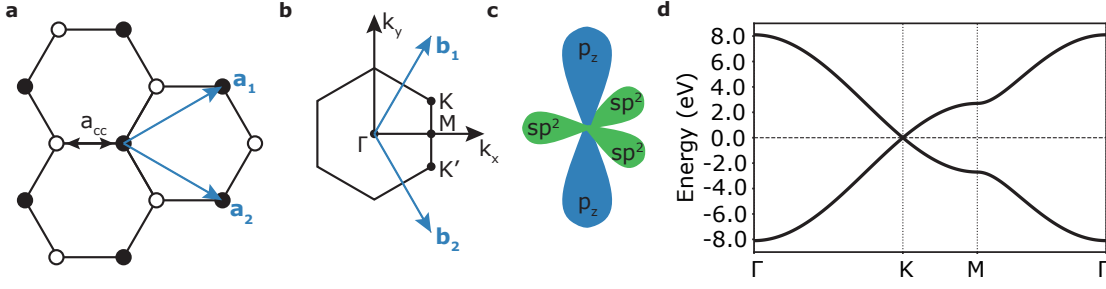
Figure 1.1: Overview of graphene's properties. (a) Honeycomb atomic structure of graphene with the basis vectors $\mathbf{a}_1$ and $\mathbf{a}_2$. (b) The reciprocal lattice of graphene with high-symmetry points K, K', M, Γ and the associated basis vectors $\mathbf{b}_1$ and $\mathbf{b}_2$. (c) Valence orbitals of sp^2-hybridized carbon in graphene – sp^2 orbitals combine to form in-plane σ bonds with neighboring carbon atoms, while out-of-plane p_z orbitals overlap laterally to form π bonds. (d) Band structure of graphene as obtained from the nearest-neighbor tight-binding model with $t_1 = 2.7$ eV.

Special interest has awakened in the case of graphene nanoribbons (GNRs) – few-atom-wide strips of graphene that exhibit a band gap [Son et al., 2006] and can be produced with atomic precision through a bottom-up approach [Cai et al., 2010]. Pairing the unique physical properties of graphene such as the aforementioned long mean free path of electrons, with a tunable band gap [Han et al., 2007] that depends on the atomic structure of GNR [Yazyev, 2013] has rocketed them to the forefront for potential applications in nanoelectronics [Areshkin and White, 2007; Wang et al., 2021a]. However, the probable future success of GNRs is still a pending question and much more effort is needed in both perfecting the production techniques and improving the theoretical understanding of these exciting nanostructures. This thesis will be devoted to examining GNR nanostructures as potential building blocks of novel nano-electronics and focus on establishing structure-property design rules for electronic transport. We will start this introductory chapter by taking a small step back and first introducing the physical properties of graphene, while latter moving on to GNRs and discussing the electronic properties, production and characterization techniques, and finally, current and potential applications in nanoelectronics.

1.1 Graphene

Graphene – the two-dimensional allotrope of carbon – consists of sp^2-bonded carbon atoms arranged in a honeycomb structure. It can be described by a triangular lattice with a basis of two atoms per unit cell and the corresponding lattice vectors:

$$\mathbf{a}_1 = \frac{a}{2}(\sqrt{3}, 1), \quad \mathbf{a}_2 = \frac{a}{2}(\sqrt{3}, -1), \tag{1.1}$$

where $a = \sqrt{3}a_{cc} = 2.46$ Å and $a_{cc} = 1.42$ Å, which is the carbon-carbon bond length in graphene as seen in Figure 1.1(a). Similarly the reciprocal-lattice vectors then are expressed as

$$\mathbf{b}_1 = \frac{2\pi}{\sqrt{3}a}(1, \sqrt{3}), \quad \mathbf{b}_2 = \frac{2\pi}{\sqrt{3}a}(1, -\sqrt{3}). \tag{1.2}$$

Particular attention should be paid to the existence of two nonequivalent K high-symmetry points in the reciprocal space shown in Figure 1.1(b), which give rise to many of the interesting physical properties in graphene. These points in the momentum space are given by

$$\mathbf{K} = \frac{4\pi}{3a}(\frac{\sqrt{3}}{2}, \frac{1}{2}), \quad \mathbf{K}' = \frac{4\pi}{3a}(\frac{\sqrt{3}}{2}, -\frac{1}{2}). \tag{1.3}$$

Although graphene was previously considered to be thermodynamically unstable [Peierls, 1935], key electronic properties were already theoretically investigated by Wallace in 1947 [Wallace, 1947]. This happened almost sixty years before graphene was experimentally isolated with the help of a scotch tape by Novoselov and Geim [Novoselov et al., 2004]. We can generally distinguish two types of bonds in graphene-based structures – three (s, p_x, p_y) valence orbitals are hybridized into sp^2 orbitals and combine to form the in-plane σ bonds, while the perpendicular p_z orbitals laterally interact with the neighboring p_z orbitals and form the π bonds [see Figure 1.1(c)]. Due to the lack of p orbitals in the core of carbon and hence the small atomic radius, the formed covalent σ bonds are short and strong that in turn enhance the mechanical flexibility and strength of the material [Meunier et al., 2016; Torres et al., 2020]. However, it has been noted that there is a considerable separation between bonding and antibonding σ bands (due to the filled shell) and the low-energy physics of graphene can be accurately described by just taking the half-filled π band into account [Wallace, 1947]. In practice this means that simple models such as one-orbital (p_z) tight-binding (TB) approximation (which will be covered in Section 2.3) is often sufficient to describe the electronic structure and the arising peculiar properties of graphene-based structures.

Within this simple approximation the conductance and valence electronic bands can be expressed as [Wallace, 1947]

$$E_{c,v}(\mathbf{k}) = \pm t_1 \sqrt{3 + f(\mathbf{k})} - t_2 f(\mathbf{k}), \tag{1.4}$$

$$f(\mathbf{k}) = 2\cos\left(\sqrt{3}k_y a_{cc}\right) + 4\cos\left(\frac{\sqrt{3}}{2}k_y a_{cc}\right)\cos\left(\frac{3}{2}k_x a_{cc}\right), \tag{1.5}$$

where $t_1 \approx 2.7$ eV and $t_2 \approx 0.2$ eV are the nearest-neighbor and next-nearest neighbor hopping energy [Reich et al., 2002] and the Fermi level is usually shifted to 0 eV. Often only first-nearest-neighbor (1NN) coupling is taken into account and electron-hole symmetry can be observed as seen in the band structure of graphene in Figure 1.1(d), this symmetry disappears if further-laying neighbor couplings are included. From the band structure one can also immediately notice the linear dispersion around the $K(K')$ point and the crossing at $E = 0$ eV, which is dubbed as a Dirac point. First, this shows that graphene lacks a band gap and is indeed a

semi-metal and second, the dispersion close to the K point can be approximated as [Wallace, 1947]

$$E_{c,v}(\mathbf{q}) \approx \pm \hbar v_F |\mathbf{q}|, \tag{1.6}$$

where we assume $\mathbf{k} = \mathbf{K} + \mathbf{q}$ with $|\mathbf{q}| << |\mathbf{K}|$ and $\mathbf{q}$ is the momentum measured relative to the K point, while $v_F = \frac{3ta_{cc}}{2\hbar}$ is the Fermi velocity. The electronic properties in these six corners of the Brillouin zone hence mimic those of massless Dirac fermions and display an effective "speed of light" around 10^6 m/s.

1.2 Graphene nanoribbons

One-dimensional graphene nanoribbons share many of the exciting properties of graphene, but more importantly, they also exhibit unprecedented degree of tunability of their electronic characteristics based on the atomic structure [Yazyev, 2013]. This degree of control makes GNRs extremely appealing for building atomic-scale logic devices, which require switching capability and an on-off ratio in the order of $10^4 - 10^7$. To achieve this band gaps of over 0.4 eV are required, which call for the GNRs to be scaled down to mere nanometers [Schwierz, 2010].

GNRs can be imagined as being cut out from a graphene sheet with two typical cutting directions that result in either armchair or zigzag edges as seen in Figure 1.2(a). Both of these directions are separated by 30° and cutting in-between the two typical orientations will result in GNRs with more complex edge structures. Although initially the top-down methods such as cutting a graphene sheet or carbon nanotubes were employed [Kosynkin et al., 2009; Tapasztó et al., 2008; Mohanty et al., 2012], they resulted in GNRs with rough edges that induced unwelcome scattering and suppressed ballistic transport. Excellent progress was made in last decade, when Cai *et al.* [Cai et al., 2010] introduced on-surface synthesis of atomically precise GNRs as an alternative bottom-up method utilizing rationally designed precursor molecules. We present the atomic structures of such pristine armchair (AGNR) and zigzag (ZGNR) ribbons in Figure 1.2(b) and Figure 1.4(a). We will follow the convention [Nakada et al., 1996; Wakabayashi et al., 1999] of marking the number of dimer or zigzag lines for AGNRs and ZGNRs, respectively, to classify them by width and denote it by N-AGNR (N-ZGNR), where N is the number of lines. Furthermore, as the hydrogen atoms contribute negligibly to the electronic properties near to the Fermi level, in most TB calculations they are neglected and the atomic structures are usually drawn without them. We note that in the following chapters the edges are always assumed to be singly passivated by hydrogen atom. The rest of this section is structured as follows: we will address the electronic structure of GNRs with a focus on the more commonly used AGNRs, then discuss both the production methods and characterization techniques, and finally review the current state of the research on GNR-based electronics.
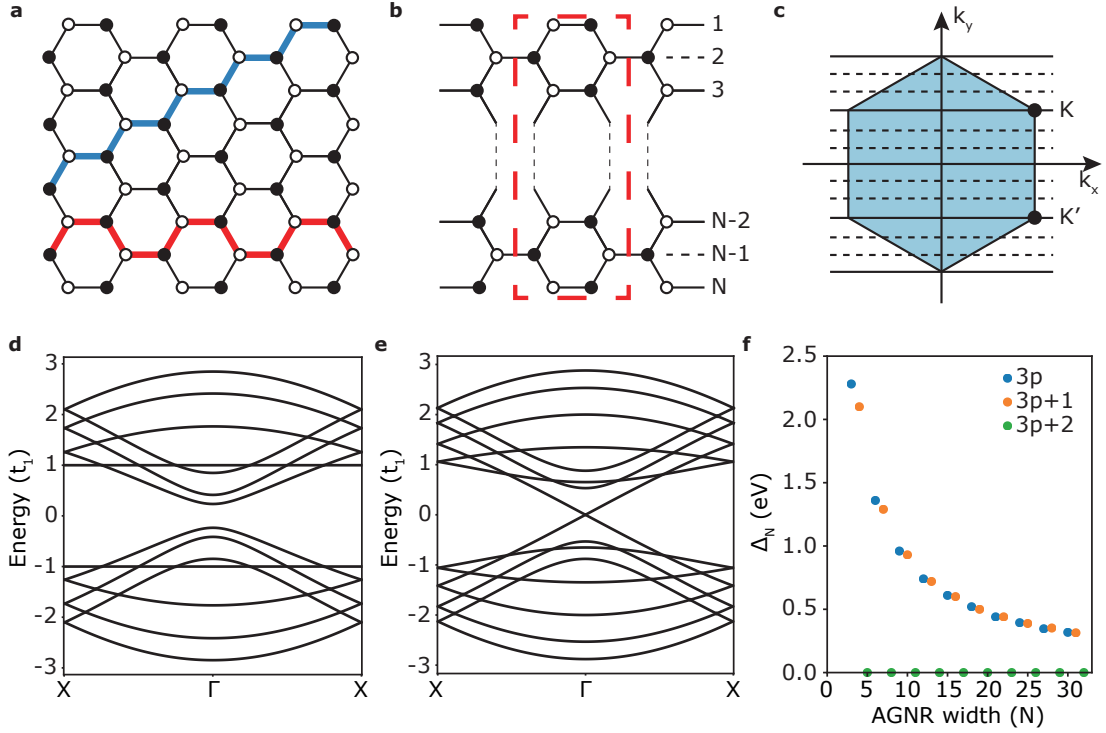
Figure 1.2: Overview of AGNRs. (a) Atomic structure of a graphene sheet and the two typical cutting directions – armchair (red) and zigzag (blue). (b) The atomic structure of N-AGNR, where the dashed red line marks the unit cell and numbers indicating the width of the AGNR in terms of dimer lines. (c) The Brillouin zone of graphene and $k_y = const$ cuts through the zone – full lines indicate crossing of Dirac point, while dashed lines cross Dirac cone. (d) 7-AGNR and (e) 8-AGNR band structure obtained with the 1NN-TB model. (f) Band gaps Δ_N of N-AGNRs calculated by the 1NN-TB model.

1.2.1 Electronic structure

An excellent starting point to obtain the electronic structure of graphene nanoribbons can be achieved by taking the graphene tight-binding model and introducing boundary conditions. By setting a condition for the electron wavefunction to be confined in the lateral direction of the GNR we will observe that the electron wave vector will be quantized. This quantization will show a strong dependence on the atomic structure of the ribbon and result in drastically different electronic properties based on the edge type and GNR width.

Armchair graphene nanoribbons

Considering a N-AGNR, we can follow the derivation provided in references [Brey and Fertig, 2006; Rozhkov et al., 2009] to express the quantization of the wavevector k_y as

$$k_y = \frac{2\pi n}{\sqrt{3}(N+1)a_{cc}},$$

(1.7)

where n is an integer between with possible values of $0 < n < N + 1$. The full AGNR spectrum thus can be built up from N equidistant k_y one-dimensional cuts $\epsilon_n(k_x)$ of the graphene band structure. In Figure 1.2(c) we show how the imposed quantization of k_y cuts through the Brillouin zone of graphene, with full lines representing cuts through the Dirac points, while dashed lines indicating cuts through the Dirac cone. Interestingly, the quantization condition enforces three families of N-AGNRs with $N = 3p, N = 3p + 1$ and $N = 3p + 2$ (where p is an integer) that determine whether the nanoribbon is metallic or semiconducting. For $N = 3p + 2$ family the possible k_y values dictate that one of the cuts ($k_y = \frac{4\pi}{3\sqrt{3}a_{cc}}$) will go right through the K point and hence the resulting nanoribbon will inherit the zero band gap of graphene.

The band structures of the semiconducting 7-AGNR ($3p + 1$) and metallic 8-AGNR ($3p + 2$) are displayed in Figure 1.2(d) and (e) where the Dirac point can be seen for the 8-AGNR, while 7-AGNR exhibits a direct band gap at Γ. In general, the band gap Δ_N of a N-AGNR is inversely proportional to its width when considering GNRs within the same family, while the hierarchy between the families is given by $\Delta_{3p} \geq \Delta_{3p+1} > \Delta_{3p+2}$. The band gaps of the $3 \leq N \leq 32$ N-AGNRs computed by the 1NN-TB model are displayed in Figure 1.2(f), with corresponding analytical solutions [Cresti et al., 2008]:

$$
\Delta_{3p} = t_1(4\cos\frac{\pi p}{3p + 1} - 2),
$$
$$
\Delta_{3p+1} = t_1(2 - 4\cos\frac{\pi(p + 1)}{3p + 2}), \tag{1.8}
$$
$$
\Delta_{3p+2} = 0.
$$

However, one needs to note that the zero band gap of $N = 3p + 2$ family is only observed in the 1NN tight-binding approximation and a finite band gap is opened with higher level theory calculations [Rozhkov et al., 2009]. For example, first-principles calculations of the "metallic" 8-AGNR predict a band gap opening of $\Delta_8 \approx 0.22$ eV that has been associated with electron-electron interactions [Zarea and Sandler, 2007] and edge relaxations [Son et al., 2006]. Interestingly, some of the effects can also be captured in improved TB models as was done by Son *et al.* [Son et al., 2006], who included modified edge atom coupling due to the shorter carbon-carbon bonds. It was noted that the edge carbon-carbon bond length shortens by about 3.5% compared to bulk bonds and the corresponding hopping term hence increases by about 12%. In practice, we can introduce another hopping term only applied to the edge atoms, where $t_{edge} = t_1 + \delta t$ and $\delta t \approx 0.1 t_1$. Similar effects can be achieved by introducing additional longer-range coupling terms [White et al., 2007] such as second- (2NN) or third-nearest-neighbor (3NN) coupling, which in turn introduce additional edge scattering and a destruction of hidden long-range symmetry [Tepliakov et al., 2022]. Finally, it has also been observed that depending on the theory level $3p$ and $3p + 1$ families can exchange their positions in the band gap size hierarchy [Son et al., 2006].

Alternative AGNR grouping in the same three families also follows by considering the number of Clar formulas for a particular width [Wassmann et al., 2010; Martín-Martínez et al., 2012].
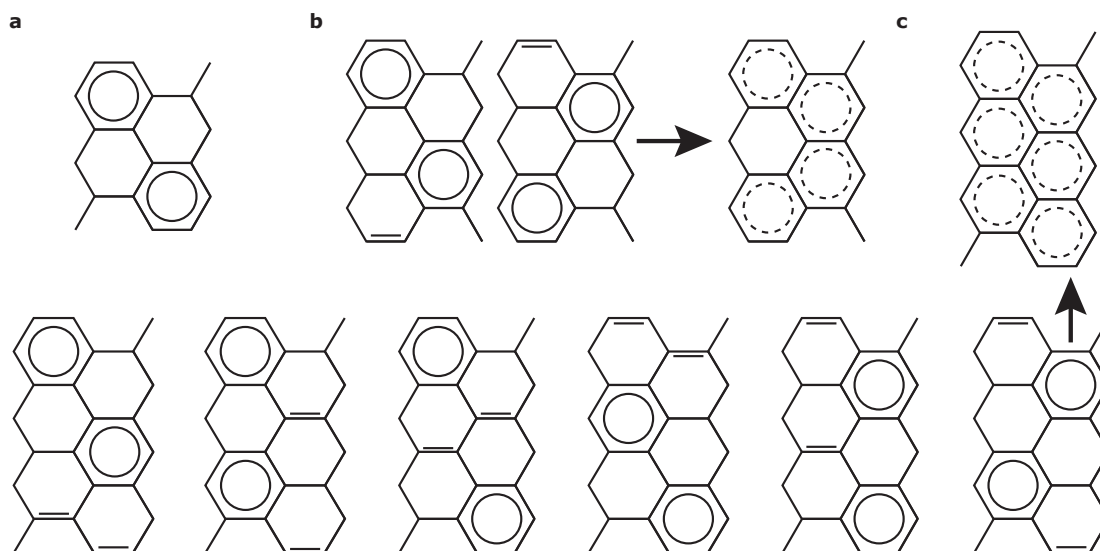
Figure 1.3: Clar's sextet distribution in N-AGNRs. (a) $N = 3p$ family only has one Clar formula, (b) $N = 3p + 1$ family displays two Clar formulas with localized double bonds and the resulting superposition. (c) $N = 3p + 2$ family displays $3p$ Clar formulas with localized double bonds and the resulting superposition with delocalized Clar sextets over all of the structure. Adapted from [Corso et al., 2018].

Clar's rule [Clar and Clar, 1972] states that the Kekulé resonance structure with the largest number of disjointed aromatic π-sextets (six π electrons localized in single benzene-like ring) is the most representative and stable structure. This is an important measurement of aromaticity and it gives an indication about bond length alternation in the structure that in turn has been identified of one of the main causes for opening band gaps in conjugated organic systems [Yang et al., 2004]. For $N = 3p$ and $N = 3p + 1$ families there are one and two Clar formulas, respectively, [Figure 1.3(a) and (b)] and the superposition of these structures does not result in all benzene rings having a π-sextet. This in turn leads to both single and localized double bonds, and a large bond length variation that induces the opening of a band gap. However, the $N = 3p + 2$ family has $3p$ different Clar formulas as seen in Figure 1.3(c) and a linear combination of these structures leads to highly aromatic system with negligible bond length alternation in the middle part of the AGNR and hence a very small band gap [Corso et al., 2018].

Zigzag graphene nanoribbons

As this thesis mainly deals with AGNRs, we will only briefly mention some of the peculiar ZGNR properties and will not provide an extensive derivation of the electronic structure from the boundary conditions and the resulting wavevector quantization. Although similar formalism of slicing graphene's band structure can be applied, added difficulty arises from introducing curved slices and emergence of additional edge states that cannot be associated with the
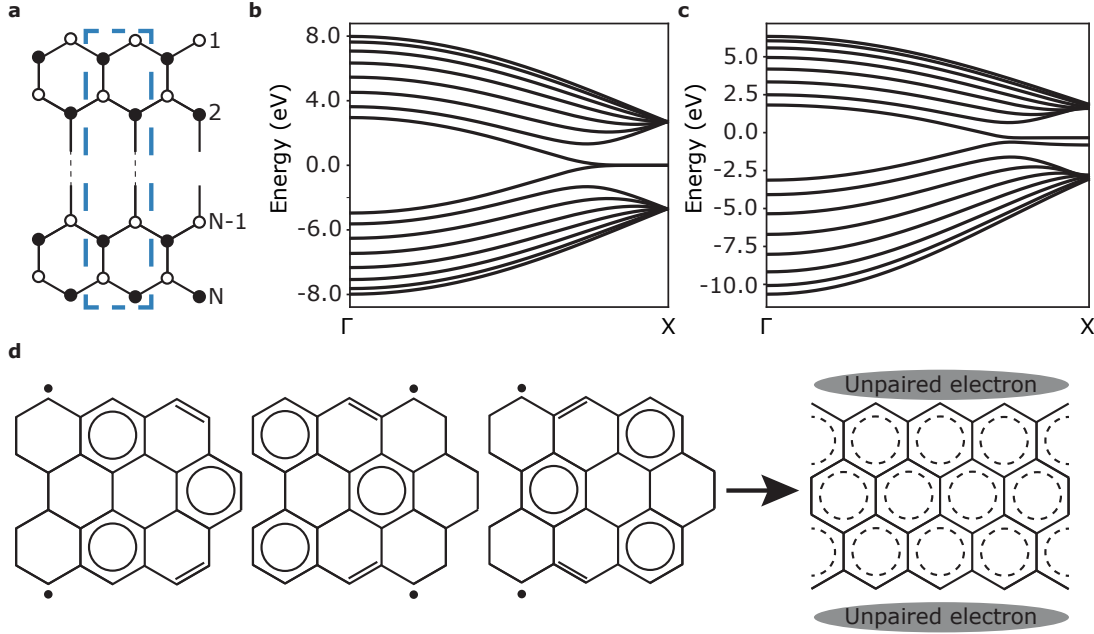
Figure 1.4: Overview of ZGNRs. (a) The atomic structure of N-ZGNR, the dashed blue line marks the unit cell and numbers indicate the width of the ZGNR. (b) Band structure of 8-ZGNR calculated by the 1NN-TB model, displaying a degenerate flat band at $E = 0$ eV. (c) Band structure of 8-ZGNR calculated by the mean field Hubbard model including 3NN couplings. The band structure experiences a band gap opening due to the magnetic ground state. (d) Clar formulas and the resulting superposition structure displaying Clar's sextets in every benzene ring and additional unpaired electrons at the edges that give raise to the edge states. Adapted from [Corso et al., 2018].

graphene's band structure. For more in-depth discussion one can consult references [Dubois et al., 2009] and [Wakabayashi et al., 2010].

We start by addressing the atomic structure of an N-ZGNR and the resulting band structure of 8-ZGNR calculated by nearest-neighbor TB model in Figure 1.4(a) and (b). Fascinatingly, both edges are comprised of opposite sublattice atoms that leads to the peculiar doubly-degenerate flat band with zero energy near the X point in the Brillouin zone ($\frac{2\pi}{3} < |k| < \pi$). The electron density associated with these flat bands is mainly localized on the opposite edges (sublattices) and rapidly decays towards the center of the ZGNR, while density of states (DOS) display a sharp peak at E_F [Wakabayashi et al., 1999]. Small dispersion in these bands is acquired if the nanoribbon is sufficiently narrow ($N \approx 3$) and therefore overlapping edge states can form bonding and antibonding levels [Nakada et al., 1996], however all wider ZGNRs are metallic at the simple tight-binding level.

Intriguingly, this is no longer the case, when spin-polarization is considered – ZGNRs are predicted to have a semiconducting magnetic ground state with ferromagnetic coupling along the edge and anti-ferromagnetic coupling across the edges [Wakabayashi et al., 1999; Son

et al., 2006]. Figure 1.4(c) displays the band structure of 8-ZGNR, but this time calculated with the mean field Hubbard model ($U = 2.0$ eV) including up to third-nearest-neighbor couplings ($t_2 = 0.2$ eV, $t_3 = 0.18$ eV). The band gap opens due to the staggered sublattice potentials that result from the magnetic ordering – opposite spin states on opposite edges occupy different sublattices [Kane and Mele, 2005]. Furthermore, with increasing ZGNR width the staggered potentials decrease in the middle of the ribbon and hence the band gaps are also inversely proportional to width of the ribbon.

Analyzing ZGNRs in the framework of Clar's rule displays a very interesting picture – by allowing the introduction of radicals into the structure, we can distribute Clar sextets over the whole ZGNR length. We show in Figure 1.4(d) some of the possible Clar formulas and the resulting superposition that exhibits Clar's sextets over the whole ZGNR as well as the unpaired electrons on the edges. This implies high aromaticity, low bond length modulation and hence small band gap. Furthermore it also confirms the emergence of the edge states at Fermi level due to the unpaired electrons and the spin polarized nature of such states [Corso et al., 2018].

1.2.2   Production methods

Among the first production methods of GNRs, the so-called "top-down" approach was the most prevalent with unzipping of nanotubes [Kosynkin et al., 2009; Jiao et al., 2009, 2010], etching and lithography of graphene [Chen et al., 2007; Ci et al., 2008; Campos et al., 2009; Bai et al., 2009; Wang and Dai, 2010; Yang et al., 2010; Abramova et al., 2013] leading the way. Recently Chen *et al.* [Chen et al., 2021] demonstrated that sub-10-nm wide GNRs can be produced by squashing carbon nanotubes and then selectively etching the edges, whereas atomically precise cutting using hydrogenation as pseudo-crack has been proposed by Qi [Qi et al., 2020]. However, these techniques are lacking reproducibility and/or atomic precision, which is essential to gain control over the electronic properties of GNRs. Alternative route was proposed by Cai and colleagues [Cai et al., 2010], when they showed that it was possible to grow atomically precise GNRs from precursor molecules, hence establishing a "bottom-up" method. The tremendous advantage of this technique is the possibility to chemically design a particular molecule, which will uniquely define the width, edge structure and doping pattern of the GNR and thus also their electronic properties [Yazyev, 2013]. Furthermore, due to the ultrahigh-vacuum conditions variety of issues, such as dangling bonds or oxidation products are excluded. This work sparked a renewed interest into GNR research and a wide plethora of different GNRs by on-surface [Abdurakhmanova et al., 2014; Kimouche et al., 2015; Basagni et al., 2015; Liu et al., 2015; Ruffieux et al., 2016; Moreno et al., 2018; Sun et al., 2019a; Pawlak et al., 2020; Keerthi et al., 2020; de la Torre et al., 2020] and in some cases in-solution or solid phase [Kim et al., 2013; Gemayel et al., 2014; El Gemayel et al., 2014; Jordan et al., 2016; Vo et al., 2014; Zhang et al., 2020; Yano et al., 2020; Dubey et al., 2021; Yao et al., 2021] synthesis have been made since. We display an overview of (some) experimentally synthesized GNRs in Figure 1.5 grouped by the three main edge types (armchair, zigzag or chiral) and the associated sub-types.
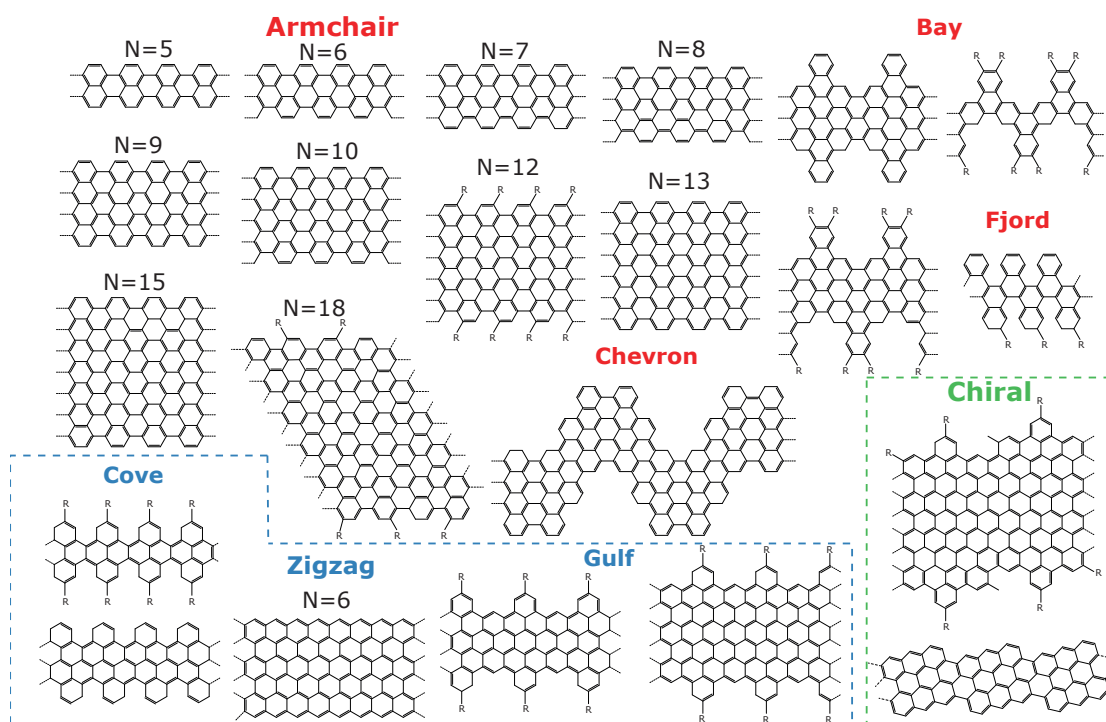
Figure 1.5: Representative examples of bottom-up synthesized GNRs.

Typical on-surface reactions follow two thermally activated main steps – first polymerization through Ullmann coupling and then cyclodehydrogenation to obtain flat GNRs as seen in Figure 1.6(a) [Cai et al., 2010]. These reactions are usually carried out under ultrahigh-vacuum and start with thermal sublimation of the precursor molecules onto a solid surface that yield surface-stabilized biradical species. Such surface-catalyzed dehalogenation allows lower reaction temperatures in order to escape unwanted side-reactions or molecular desorption [Björk et al., 2013; Dong et al., 2015]. After the first thermal activation step, biradical species diffuse across the surface and bind covalently to form linear polymer chains entirely defined by the precursor molecule. Depending on the substrate, metastable metal-organic intermediates have also been detected to form during this step [Dong et al., 2015]. Figure 1.6(c) shows the scanning tunneling microscopy (STM) image of a polymer chain after the first step. Finally, second thermal activation step involves transforming the polymer chains into planar, atomically precise GNRs through cyclodehydrogenation [Figure 1.6(d)]. Additional processes, such as the lateral fusion of GNRs, can be observed if higher annealing temperatures are used, which can decrease the selectivity of the reaction as GNRs of different widths are formed [Chen et al., 2017b].

Interestingly, the choice of substrate is not only facilitating the dehalogenation process, but can also determine the resulting product. For example, Han *et al.* [Han et al., 2014] showed that substituting the traditional Au(111) or Ag(111) surface with Cu(111), while utilizing the same precursor molecule (10,10′-dibromo-9,9′-bianthryl) used for synthesis of 7-AGNR, one
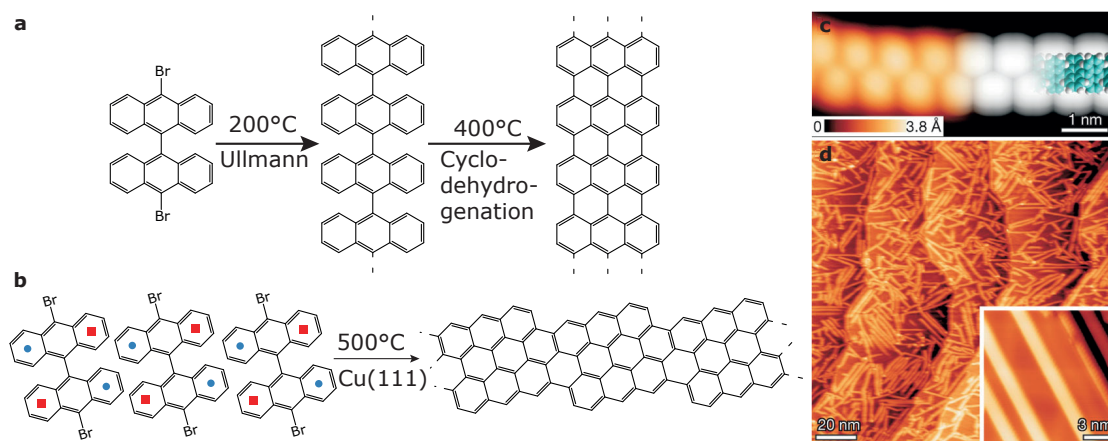
Figure 1.6: On-surface synthesis of GNRs. (a) Reaction scheme of 7-AGNR starting from a bianthryl monomer. (b) Reaction scheme for the polymerization of bianthryl monomer into (3,1)-AGNR. The blue dots(red squares) indicate regions that are close to (away from) the Cu(111) surface. (c) STM image (left) of the polymer before the final cyclodehydrogenation step and density-functional theory simulated STM image (right) overlaid with model of the polymer (carbon in blue, hydrogen in white). (d) Overview STM image after the final synthesis step showing 7-AGNRs, with the inset showing a higher-resolution STM. Panels (c) and (d) are adapted from [Cai et al., 2010].

can obtain a GNR with chiral-edge configuration. Figure 1.6(b) shows the reaction scheme of bianthryl monomer polymerization into (3,1)-GNR that passes over the traditional Ullmann coupling and undergoes intermolecular cyclodehydrogenation instead. Whereas, Schulz and co-workers [Schulz et al., 2017] confirmed the role of the substrate by modifying the precursor molecule and still observing the chiral GNR product. Furthermore, substrate can also have a major impact on the length of resulting GNRs – as Au(111) brings down the threshold temperatures of polymerization and cyclodehydrogenation closer to each other the radical quenching by liberated H atoms can terminate the polymer growth and result in shorter GNRs [de Oteyza et al., 2016]. Whereas it has been shown that the use of stepped surfaces, such as Au(788) [Linden et al., 2012], can lead to well-aligned and longer GNRs.

Besides the substrate, another possible method to control reaction conditions and/or resulting GNR properties has been achieved by modifying the type of halogen atom attached to the precursor molecule. For example, GNR length has been considered as the most critical parameter for device integration and hence careful optimization of the growth conditions is necessary. It has been shown that by substituting bromine atoms for iodine in the precursor molecules it is possible to triple (quintuple) the average length of 5-AGNRs (9−AGNRs) [Giovannantonio et al., 2017; Borin Barin et al., 2022]. On the other hand, Jacobse *et al.* [Jacobse et al., 2016] showed that the geometry of the final product can be drastically altered, when bromine was substituted with chlorine in the 7-AGNR's precursor molecule. Curiously, for the chlorine-functionalized precursor cyclodehydrogenation occurs before polymerization and therefore random branches of polybisanthenes are formed instead of straight GNRs. Whereas

Teeter [Teeter et al., 2021] showed that removing halogens from the precursor molecules result in synthesis of non-covalent 2D structures. However, perhaps the most important effect of halogen functionalization has been the ability to combine different halogens in order to control the sequence of individual Ullmann couplings and hence design complex GNR junctions. The seminal work of Cai and co-workers [Cai et al., 2010] showed controlled growth of a triple junction by depositing two different monomers with bromine and iodine groups as seen in Figure 1.7(a) and (b).

The ability to produce GNR junctions is of the highest importance to make them attractive options as components for nanoelectronics. Unlike doping or modifying pristine GNRs to tailor the band structure, one can introduce modifications locally to regulate electronic properties in specific segments and hence achieve promising junction interfaces for innovative GNR-based devices. Therefore, it is essential that individual GNRs exhibiting different properties can be coupled in a controlled and precise way without introducing unwelcome effects. For example, combining segments with different widths and hence electronic band gaps has been achieved by Chen *et al.* [Chen et al., 2015], where a type-I semiconductor heterojunction was produced by on-surface synthesis as seen in Figure 1.7(d) and (e). Whereas a type-II heterojunction was achieved by combining pristine chevron-GNRs with their nitrogen-substituted equivalents [Cai et al., 2014]. The resulting heterostructure behaved similarly to traditional $p-n$ junction and exhibited a band shift of 0.5 eV. Moreover, utilizing only straight GNRs is insufficient to effectively produce or connect two-dimensional components, so nanostructures that exhibit directional turns can be considered as the most basic building-blocks for circuit integration. In this regard, Han *et al.* [Han et al., 2015] produced a two-terminal junction that couples two $(3, 1)$-AGNRs together in an angle as seen in Figure 1.7(c). Whereas Sun and co-workers [Sun et al., 2019b] synthesized 3 different 7-AGNR $(180°, 120°, 60°)$ junctions by introducing an additional 1,3,6,8-tetrabromopyrene precursor molecule in the reaction. Such junctions could act as potential interconnects or "wires" to connect multiple components together. Finally, another exciting direction has involved synthesizing heterojunctions exhibiting topological interface states [Cao et al., 2017; Gröning et al., 2018; Rizzo et al., 2018]. These topological boundary states at GNR interfaces can serve as key elements to produce qubits, quantum spin chains or induce new 1D bands that would be useful for applications in quantum information devices [Wang et al., 2021a].

1.2.3   Characterization methods

Although numerous GNRs and GNR junctions have been successfully synthesized, precise exploration and characterization of the underlying properties remains a challenging task. Large variation in the reported values can be seen depending on the experimental technique or even the substrate employed for measurements. For example, Zhang *et al.* [Zhang et al., 2015] reported unexpectedly large band gap of 2.8 eV for 5-AGNR based on scanning tunneling spectroscopy (STS) measurements on Au(111) surface, whereas Chen and co-workers [Chen et al., 2017b] reported a much smaller optical band gap of 0.9 eV that they measured with
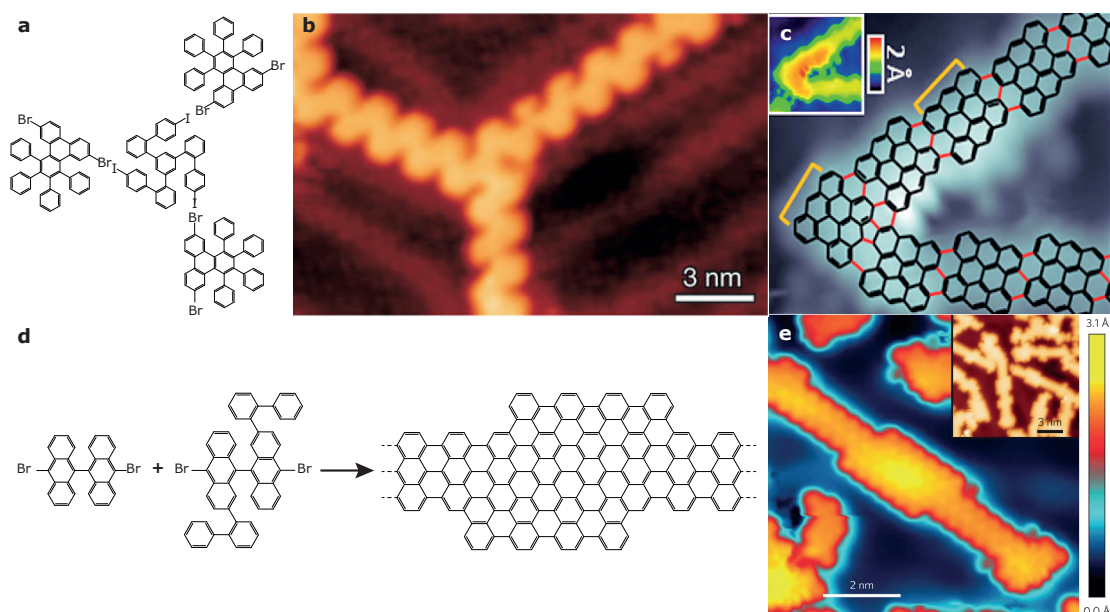
Figure 1.7: GNR-based junctions. (a) Schematic model of triple junction fabrication process. (b) STM image on gold of a triple GNR junction obtained from the two monomers displayed in panel (a). Adapted from [Cai et al., 2010]. (c) Proposed atomic structure of a $(3,1)$-AGNR junction, whereas the inset shows STM topographic image. Adapted from [Han et al., 2015]. (d) Synthesis of 7-13-AGNR heterojunctions from two molecular precursors. (e) STM topograph of 7-13-AGNR heterojunction, whereas the inset shows large scale image of multiple GNR heterojunctions. Adapted from [Chen et al., 2015].

ultraviolet-visible-near infrared spectroscopy on silica substrates. Due to situations like these, it is important to develop a consistent set of techniques and parameters that can be used in combination to compare and characterize GNRs more precisely.

There is a multitude of experimental methods that have been used to probe the electronic properties (angle-resolved and inverse photoemission, high-resolution electron energy loss and optical spectroscopy) [Bronner et al., 2012; Denk et al., 2014; Jordan et al., 2017], chemical structure (X-ray photoelectron spectroscopy) [Cai et al., 2010; Jordan et al., 2017] and vibrational modes (Raman spectroscopy) [Cai et al., 2010; Chen et al., 2017b] of GNRs. However, one of the most widespread and functional characterization tools used for determining the physical properties of GNRs is the scanning probe microscopy (SPM). Two main methods – scanning tunneling microscopy [Figure 1.8(a)] and atomic force microscopy (AFM) are well-known tools for investigating the surface topography, whereas scanning tunneling spectroscopy (an extension of STM) can be used to analyze electronic properties of the samples, such as density of states and band gap. Although, SPM techniques are known to be very sensitive to surface cleanness (tunneling measurement can be disturbed by adsorbants or chemical modifications) this issue is largely absent when characterizing GNRs due to the fact that typically the structures are synthesized under ultrahigh-vacuum conditions.
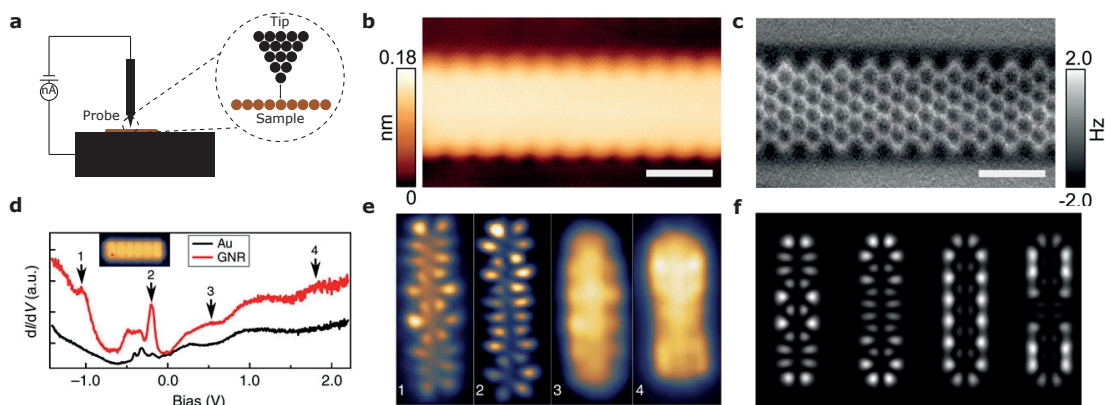
Figure 1.8: SPM characterization of GNRs. (a) Scanning tunneling microscope schematic diagram. (b) STM image of a 9-AGNR on gold. (c) nc-AFM image of a 9-AGNR on gold. Panels (b) and (c) are adapted from [Talirz et al., 2017]. (d) $\frac{dI}{dV}$ spectra on three-monomer long 9-AGNR with the location of the spectra marked with red dot in the inset, while the black curve is measured on Au(111). (e) Experimental constant-height $\frac{dI}{dV}$ maps and the corresponding (f) simulated LDOS maps at the bias voltages marked by arrows in (d). Panels (d), (e) and (f) are adapted from [Kimouche et al., 2015].

Scanning tunneling microscopy

STM has been one of the most common tools for characterizing bottom-up synthesized GNR and is often used for direct determination of chemical structure and surface topology [Cai et al., 2010; Dienel et al., 2015; Nguyen et al., 2017; McCurdy et al., 2021]. Other uses include imaging the reaction intermediates to provide better understanding of the reaction mechanism [Ammon et al., 2017]. We show an example topography of a 9-AGNR obtained by STM in Figure 1.8(b). In its core, the method is based on electron tunneling between a sharp conductive tip and surface. Structural information can be gained by scanning the tip across the surface in constant current or constant height modes. In constant current mode, the distance between the tip and the sample is adjusted by feedback electronics – if the current decreases below some set level the tip is brought closer to the sample and vice versa. Whereas in the constant height mode both the tip distance from the surface and the voltage is kept constant and hence the tunneling current, which is exponentially dependent on the distance is recorded. Both modes have its advantages and disadvantages, with constant height mode being faster, but may be more prone to damage the equipment if rough surfaces are investigated. Furthermore, electronic transport measurements on bottom-up GNRs have been carried out by lifting one end with the help of an STM tip and leaving the other one on a conductive surface. Then current between the surface and the tip can be measured as a function of applied bias and the tip-sample distance [Koch et al., 2012; Chong et al., 2018]. Interestingly, this method also allows measuring the impact of GNR length on transport as by lifting the STM tip higher up a larger part of GNR is suspended between the two electrodes. Alternatively, multiple-probe setups can be used to spatially resolve transport measurements [Aprojanz et al., 2018].

Atomic force microscopy

Higher-resolution images of more than 1000 times the optical diffraction limit, can by obtained by AFM. It is often used to identify the bonding structure of pristine and defective GNRs [van der Lit et al., 2013; Sánchez-Sánchez et al., 2016; Talirz et al., 2017; Pizzochero et al., 2021a], as well as their junctions [Dienel et al., 2015] as the method provides atomic resolution. AFM can also be operated in multiple modes, for example, in contact mode, a tip is attached to a cantilever that is swept across the surface to measure the force between tip and sample. Whereas in non-contact mode the cantilever is oscillated close to its resonant frequency and changes in the amplitude of the oscillations are measured when the tip approaches the surface. This data is then used to generate the resulting topographic image as seen, for example, in Figure 1.8(c). In both modes laser is reflected from the cantilever and captured by a set of photodiodes in order to measure the position of the cantilever.

Scanning tunneling spectroscopy

Lastly, STS is a measurement that uses STM to gain an insight about the local density of states (LDOS) at a particular position of the sample at which the tip is located by measuring the current-voltage $(I - V)$ characteristics and sweeping the sample bias. Practically it is done by recording the derivative of the tunneling current with respect to the bias voltage, which is proportional to LDOS in the Tersoff-Hamann approximation [Tersoff and Hamann, 1985]:

$$\frac{dI}{dV}(V, \mathbf{r}) \propto \rho(E, \mathbf{r}). \tag{1.9}$$

V is the sample bias, $\mathbf{r}$ is the position of the tip and ρ is the LDOS at energy $E = E_F + |e|V$, with Fermi energy denoted by E_F. This is a very versatile method – for instance, we show a sample $\frac{dI}{dV}$ curve of a 5-AGNR on a gold surface in Figure 1.8(d) that can be used to extract GNR's band gap value and gain an insight about electronic states. Whereas spatial mapping of a specific states as seen in Figure 1.8(e) can be obtained by sweeping the tip across the surface [Ruffieux et al., 2012; van der Lit et al., 2013; Chen et al., 2013; Nguyen et al., 2017]. For more precise effective masses, band alignment and electronic band dispersion Fourier-transformed STS can be employed. This method involves a transformation from the real space $\frac{dI}{dV}$ map to the reciprocal space $(\rho(E, x) \to \hat{\rho}(E, q))$ and allows determining energy versus momentum dispersion that can give very precise band gap values [Bergvall and Löfwander, 2013; Söde et al., 2015]. Finally, by sweeping the tip-sample distance and keeping the voltage constant it is also possible to obtain a local work function.

Theoretical calculations

Although we already saw that electronic structure of GNRs can be explained by simple theoretical models, such as Clar's theory and tight-binding method – computational simulations can often be used to alleviate some of the technically challenging, time-consuming and expensive

experimental techniques. For example, calculations can be carried out to predict the specific properties of a GNR and hence indicate which targets are worth pursuing experimentally. Moreover, simulations can often be of help in explaining complex measurements, such as microscopy or spectroscopy results. As an example, we show in Figure 1.8(e) and (f) the experimentally recorded and the simulated STS maps of 5-AGNR's electronic states. It can be seen that the simulated images resemble the experimentally recorded maps and provide a better insight into the underlying physical properties. The background of the theoretical calculations is covered in more detail in Chapter 2 of this thesis, while insight about current state of theoretical transport calculations will be given in the next subsection about technological applications.

1.2.4   Graphene nanoribbon electronics

Among the broad scope of potential applications, GNR-based nanoelectronics have probably attracted the largest attention. As the transistor size in integrated circuits has reached nanometres, it has become increasingly difficult to achieve further device miniaturization from bulk semiconductors. Requirements, such as the need for higher performance with smaller device footprint and lower power consumption, dictate that low-dimensional materials, like GNRs, have to be considered as potential candidates [Chau et al., 2007]. Although the GNR research field has developed in a rapid pace over the past decade it is still at the stage of laboratory exploration and extensive investigations have to be conducted to successfully integrate GNRs in electronic devices. In a perspective by Wang *et al.* [Wang et al., 2021a] the authors have proposed a GNR-based electronics technology roadmap for the next 10 years focusing on three directions – material synthesis, device design and circuit integration, each with its own challenges and possible solutions. We use this roadmap as a basis to show the relevant categories associated with the work done in this thesis and highlight the issues we try to solve in Figure 1.9.

Experimental studies of GNR integration in devices has mainly focused on utilizing them as components in field-effect transistors (FET) [Zschieschang et al., 2015; Candini et al., 2017; Martini et al., 2019; Tries et al., 2020], however, this field has been lagging behind both the production of GNRs and the theoretical studies. Main challenges in this field are related to the post-transfer process of on-surface synthesized GNRs or growing GNRs directly on insulating substrates. Initial attempts have shown GNRs being transferred to non-conducting surfaces, such as SiO_2, to fabricate field-effect transistors, for instance a 7-AGNR connecting Pd electrodes was shown to exhibit on-off ratio of 10^3 [Bennett et al., 2013]. Few years later Llinas *et al.* [Llinas et al., 2017] achieved even higher on-off ratio of 10^5 and high on-current of 1 μA with 9- and 13-AGNR based FETs [Figure 1.10(a)]. They also found that GNR-metal contact Schottky barrier severely limits the performance of these devices. In this regard, advances have been achieved by using electron beam lithography-defined graphene electrodes for contacting the 9-AGNRs [Braun et al., 2021] to avoid the high contact resistance and screening effects. Whereas recent success has been achieved with 5-AGNRs that have been considered
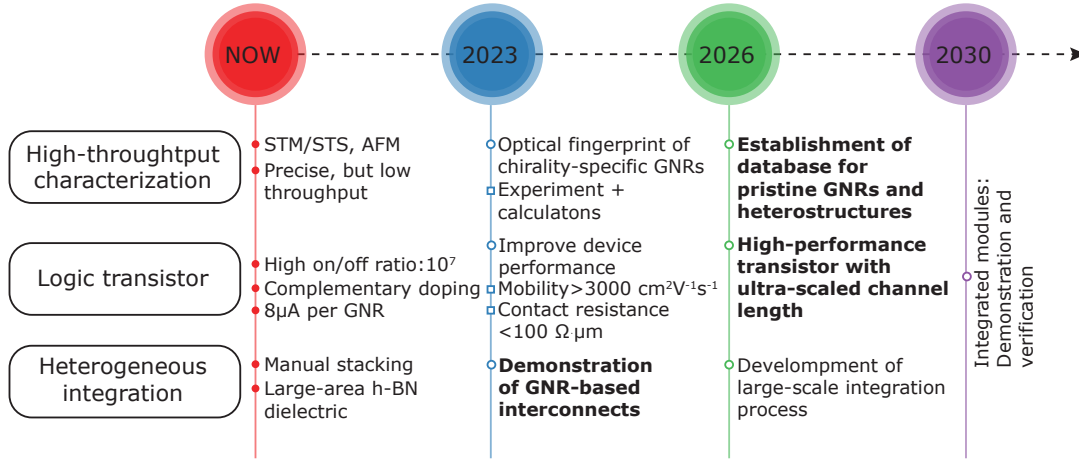
Figure 1.9: Technology roadmap [Wang et al., 2021a] for GNR-based electronics (full circles indicate achieved steps, empty circles show the challenges and aims, empty squares are possible solutions and bold text denotes challenges tackled in this thesis).
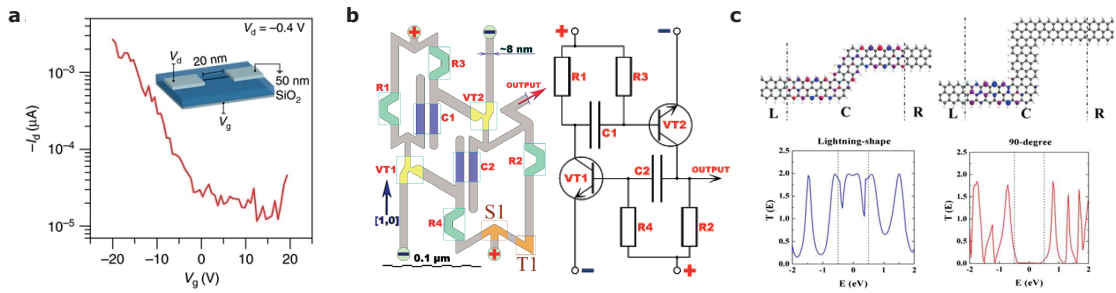
Figure 1.10: GNR-based nanoelectronics. (a) $I_d - V_g$ characteristics of the 9-AGNR device (in inset) gated by the thick 50 nm SiO_2 gate oxide. Adapted from [Llinas et al., 2017]. (b) GNR-based flip-flop circuit and the corresponding electronic scheme. Adapted from [Areshkin and White, 2007]. (c) Transmission eigenstates and transmission spectra of the lightning-shaped and 90° GNR heterojunctions (regions L,R indicate left and right lead, while C indicates device region). Adapted from [Chen et al., 2017a].

to have an optimal band gap for device integration. Borin Barin *et al.* [Borin Barin et al., 2022] realized the first FET based on 5-AGNRs that exhibited switching behavior at room temperature. Although ample improvements have been made in GNR-based FET production, further work in overcoming technical challenges in contacting the GNRs, understanding possible influence of defects and device geometry is still needed to push the performance limits of GNR-based electronics.

One of the possible solutions to make further progress is utilizing computer simulations of the potential devices in order to find best experimental targets. While the electronic properties of novel pristine GNRs [Liu et al., 2019; Li et al., 2021a; Silva and Girão, 2021; Wang et al., 2021c; Blackwell et al., 2021] can be investigated with relative ease, detailed comprehension is lacking for more complex junctions or defective GNRs and hence a unified picture concerning the

relationship between structure and electronic properties remains to be established. This is an important initial step to design GNR-based structures with intended characteristics that could be used to make-up the components in all-GNR electronic circuits as proposed in Figure 1.10(b). Furthermore, we would not just tackle two of the challenges outlined in the technology roadmap – manufacturing interconnects and transistors, but also already start building a basis for general GNR databases as vast amount of systems need to be studied in order to establish these design rules.

Initial attempts to theoretically quantify the transport in nanostructures has been focused on specific geometries. For example, Wakabayashi [Wakabayashi and Sigrist, 2000; Wakabayashi, 2001] explored different width ZGNR junctions and found a rich structure of many zero-conductance dips in the low-energy region. Whereas Chen and colleagues [Chen et al., 2017a] found that the transport properties of lightning-shaped ZGNR structures strongly depend on numerous factors, such as width and symmetry of the leads as well as size and edge structure of the scattering region. They showed that keeping the same edge structure throughout the heterojunction conserves the transmission better than introducing an AGNR segment as seen in Figure 1.10(c). Similar observations were made by Wurm [Wurm et al., 2009] and Liwei *et al.* [Liwei et al., 2016], where AGNR segment acts as a bottleneck for electronic transport in AGNR-ZGNR heterostructures. Interestingly, out of plane junctions that consist of pristine GNRs overlapping have also been investigated as an alternative route to bottom-up synthesized in-plane junctions. For instance, Richter and co-workers [Richter et al., 2020] modeled a network of overlapping 5- and 9-AGNRs between two electrodes and observed that transport is governed by inter-ribbon hopping, while Deng *et al.* [Deng et al., 2019a,b] examined the dependency of a twist angle and nanopores on thermoelectric transport performance between two overlapping GNRs. Others have investigated impact of width [Li et al., 2011], stacking [Habib et al., 2011; Chu et al., 2017; Mohammadi and Haji-Nasiri, 2018] and overlap length [Zheng et al., 2012; Yin et al., 2013] in similar structures.

Furthermore, ballistic transport has also been explored in GNR-quantum dot systems [Xiong and Xiong, 2011; Xu et al., 2013], crossed junctions [OuYang et al., 2009; Brandimarte et al., 2017] and nano-constrictions [Muñoz-Rojas et al., 2006; Kawai et al., 2011; Motta et al., 2012; Xu and Wu, 2020; Zhou et al., 2021], where the dependence on size and edge type was established. Whereas Saiz-Bretin and co-workers [Saiz-Bretín et al., 2019] showed that device geometry can be tuned to increase the thermoelectric transport in graphene nanoring structures through Fano resonances. Others have investigated the influence of defects, such as edge distortions [Cresti and Roche, 2009; Dubois et al., 2010; Tien et al., 2019; Niu et al., 2021], vacancies [Bahamon et al., 2010; Kihira and Aoki, 2017; Aydin et al., 2022], nanopores [Tran and Cresti, 2021; Cuong, 2021; Zhang and Liu, 2022; Zhang et al., 2022; Majhi et al., 2022] and doping [Biel et al., 2009; Cresti et al., 2011; Lopez-Bezanilla and Roche, 2012; Marconcini et al., 2012; Yang et al., 2019; Zaminpayma et al., 2021; Wang et al., 2021b] in GNRs. However, in spite of the growing number of theoretical works analyzing GNR junctions there is still a large disconnect between the theoretically examined systems and the experimentally achievable structures. For instance, single-atom vacancies are seldom seen in bottom-up synthesized GNRs. Even

more, as most works limit themselves to a particular system it is hard to establish overarching design rules that could be applied to wide range of junctions. Accordingly, this thesis will try to address these issues by investigating either experimentally synthesized systems or by surveying the geometry space in a way that more general conclusions can be drawn.

1.3   Outline of the thesis

This thesis focuses on computational investigations of electronic transport properties in graphene nanoribbon junctions. Mainly, we employ a combination of density functional theorem or tight-binding model with Green's function methodology to establish structure-property relationships. The rest of this thesis is organized as follows:

- Chapter 2 is dedicated to review the methodology employed throughout this thesis, including Kohn-Sham density functional theory, semi-empirical tight-binding model and non-equilibrium Green's function used to calculate ballistic transport properties.

- Part I (Chapters 3 and 4) covers the electronic transport in two-terminal width-modulated graphene nanoribbon junctions. Starting with the shortest possible junction that can also be reimagined as a perfect GNR hosting an edge-functionalized molecule, we discuss the effect on the electronic transport that stems from interplay between the localized states in the wider region and the continuum of states in the lead. Next, we examine experimentally synthesized GNRs hosting a quantum-dot and systematically analyze the transport gap dependency on length and width of metal-semiconductor-metal junctions.

- Part II (Chapters 5 and 6) considers the effects of experimentally observable "bite" defects on the electronic transport properties in armchair-edge GNRs and chevron-type GNRs. First, we characterize the impact and prevalence of such defects in 9-AGNRs and then extend our investigation to wider ribbons in order to establish underlying principles of the adverse response on transport properties. Next, we employ the identified design rules to create potential components for nanoelectronics based on chevron-type GNR nanostructures with selectively engineered defects.

- Part III (Chapters 7 and 8) is devoted to exploring GNR-based nanostructure incorporation in next-generation nanoelectronic circuits. We employ high-throughput screening to characterize more than 400000 junctions with 60° and 120° turns in order to find promising candidates for electronic interconnects and examine structure-property relationships. In addition we build a web-based application with a simple graphical interface to streamline the calculations of similar junctions. Lastly, Chapter 8 focuses of including the finite-size effects and metallic leads in order to simulate experimentally relevant transport measurements.

- Chapter 9 summarizes the key results of this thesis and gives an outlook for future research directions in this field.

- Appendix A gives an overview of the web-based tight-binding application TBETA, where simple graphical interface allows to design and calculate electronic properties of GNR junctions. Appendix B briefly describes the structure and contents of our GNR angled junctions library. Whereas Appendix C provides an analytical derivation of the binary conductance phenomenon across metallic 120° junctions.

2 Methodology

The ever-growing list of novel graphene-based nanostructures calls for a fast, efficient and reliable computational methods of obtaining the electronic and transport properties. Hence, in this section we will recall the theory behind two of the most common electronic structure methods routinely used in our calculations - density functional theory (DFT) and the tight-binding model. Starting from the well-known Schrödinger equation, we will show that DFT can be used for computational quantum mechanical modeling of the ground state of many-body configurations, such as atoms, molecules and periodic systems. Afterward, we will introduce the semi-empirical tight-binding model, often parameterized from the aforementioned DFT calculations, which has emerged as a computationally low-cost alternative especially for the graphene-based systems. In addition, as most of the thesis is related to the examination of the ballistic transport properties within various graphene-based nanostructures, we will establish the Landauer-Büttiker formalism and the non-equilibrium Green's function (NEGF) approach, which can be combined with either DFT or TB methods as one of the prime options for treating the electronic transport characteristics.

2.1 Schrödinger equation

Schrödinger equation can be used to precisely describe the world around us within the quantum mechanics (QM) framework. We can use the time-independent version to express the energy of any system as

$$\mathbf{H}\psi(\mathbf{r}) = E\psi(\mathbf{r}), \tag{2.1}$$

where we assert that the electronic state of a system can be fully characterized by a wavefunction $\psi(\mathbf{r})$, total energy E and the Hamiltonian $\mathbf{H}$. The total energy operator $\mathbf{H}$ can be divided into potential and kinetic operators - $\mathbf{V}$ and $\mathbf{T}$:

$$\mathbf{H} = \mathbf{T} + \mathbf{V}, \tag{2.2}$$

that are then expand to obtain expressions involving electrons and nuclei as

$$\mathbf{H} = \mathbf{T}_e + \mathbf{T}_n + \mathbf{V}_{ee} + \mathbf{V}_{nn} + \mathbf{V}_{en}. \tag{2.3}$$

Here, we note that for a system of N electrons and K nuclei, the Hamiltonian depends on the nuclear masses M_J, charges eZ_J and positions $\mathbf{R}_J$ in addition to the electron masses m_i, charges $-e$, and positions $\mathbf{r}_j$. Subscripts j, i and J, I denote the i-th and j-th electron and the I-th and J-th nucleus, respectively. Our Hamiltonian is hence

$$\mathbf{H} = -\sum_i^N \frac{\hbar^2}{2m_i} \nabla_i^2 - \sum_I^K \frac{\hbar^2}{2M_I} \nabla_I^2 + \frac{e^2}{2} \sum_i^N \sum_j^N \frac{1}{\mathbf{r}_{ij}} + \frac{e^2}{2} \sum_I^K \sum_J^K \frac{Z_I Z_J}{\mathbf{R}_{IJ}} - \frac{e^2}{2} \sum_i^N \sum_I^K \frac{Z_I}{\mathbf{r}_{iI}}, \tag{2.4}$$

where the factor $\frac{1}{2}$ handles the double counting.

Due to the hugely different masses of nuclei and electron that differ by four orders of magnitude, the electrons will always see the atoms in a static configuration. Therefore, applying the Born-Oppenheimer approximation [Born and Oppenheimer, 1927], we can treat the nuclei as classical point-like particles separately from electrons. This allows us to introduce the electron-only Hamiltonian:

$$\mathbf{H}^{el} = -\sum_i^N \frac{\hbar^2}{2m_i} \nabla_i^2 + \frac{e^2}{2} \sum_i^N \sum_j^N \frac{1}{\mathbf{r}_{ij}} - \frac{e^2}{2} \sum_i^N \sum_I^K \frac{Z_I}{\mathbf{r}_{iI}}. \tag{2.5}$$

Now, the electron wavefunction will only depend parametrically on the nuclear coordinates

$$\mathbf{H}^{el} \psi_n(\mathbf{r}_1, ..., \mathbf{r}_N \vee \mathbf{R}_1, ..., \mathbf{R}_K) = E^{el} \psi_n(\mathbf{r}_1, ..., \mathbf{r}_N \vee \mathbf{R}_1, ..., \mathbf{R}_K), \tag{2.6}$$

and the total energy E^t of the system can simply be recovered by re-introducing the contribution of classical point-like nuclei terms back into our equations:

$$E^t = E^e + E^n. \tag{2.7}$$

Although any system can be described with Eq. 2.5, exact solutions only exist for hydrogen molecular ion and hydrogen atom. Hence, approximations, such as variation principle, can be used to find the energy closest to the exact solution

$$E[\Phi] = \frac{\langle \Phi | \mathbf{H} | \Phi \rangle}{\langle \Phi | \Phi \rangle} \geq E_0, \tag{2.8}$$

where Φ is some trial function, which depends on some parameters $\Phi(c_1, ...c + i)$. We then try to minimize the energy with respect of varying the parameters and if $E[\Phi] = E_0$, then we have found the exact ground-state wavefunction. However, as the many-electron wavefunction features 4 degrees of freedom per electron (3 spatial and 1 spin), it raises an exponentially growing computational problem with increasing number of electrons. In order to treat large scale systems, alternative methods that can find approximate solutions to the Schrödinger

equation with reasonable computational effort are hence needed.

2.2 Density functional theory

In the search for another variable to replace the wavefunction, electron density emerges as an appealing parameter. It can be easily obtained from the square of the wavefunction, measured experimentally and more importantly, it is remarkably simpler than the many-body wavefunction. Moreover, electron density can be considered as a "basic variable" since any property of a system can be considered as a unique functional of the ground-state density. For example, positions and the charges of nuclei can be determined from the cusps in the density, whereas the number of electrons in the system can be expressed as

$$\int \rho(\mathbf{r}) d\mathbf{r} = N. \tag{2.9}$$

In 1964 Hohenberg and Kohn [Hohenberg and Kohn, 1964] proved that electron density uniquely determines the Hamiltonian operator and established a variational principle linking electron density with energy. For some trial electron density ρ_t we get

$$E[\rho_t] \geq E_0. \tag{2.10}$$

Once again, if the trial density gives energy equal to the true ground-state energy, we have found the exact electron density. Hence, the best approximation to ρ can be found by minimizing energy with respect to changes in the density. Although Hohenberg and Kohn proved that $E[\rho]$ exists, their theorems do not tell anything about how to find or construct it. If we start by expanding the electronic energy functional

$$E[\rho] = T[\rho] + E_{ee}[\rho] + E_{ne}[\rho], \tag{2.11}$$

we know how to calculate the exact electron-nuclear attraction $E_{ne}[\rho]$ and Coulomb repulsion of a charge distribution $J[\rho]$, while we don't know how to obtain the non-classical electron-electron interaction $E_{ee}[\rho] - J[\rho]$. Moreover, we have difficulties in calculating the kinetic energy of the interacting electrons from the electron density, $T[\rho]$.

To overcome some of the problems, Kohn and Sham [Kohn and Sham, 1965] formulated a non-interacting model by imagining a reference "Slater" system where the electrons do not interact with each other. It is proposed that the ground-state density of the real interacting system is equivalent to the density of a chosen noninteracting system. This leads to exactly soluble independent particle equations for the noninteracting system, while the complex many-body terms are incorporated into exchange-correlation functional of the density. To begin with, orbital description is re-introduced with Kohn-Sham orbitals ϕ^{KS}, which can form the exact wavefunction of the non-interacting system and sum up to the true density of the

fully interacting system:

$$\psi_s = \frac{1}{\sqrt{N!}} \det |\phi_1^{ks}...\phi_N^{KS}|, \tag{2.12}$$

$$\rho_s = \sum_i^N |\phi_i^{KS}|^2. \tag{2.13}$$

Now the kinetic energy term, which is exact for the non-interacting system can be expressed as

$$T_s = -\frac{1}{2} \sum_i^N \langle \phi_i^{KS} | \nabla_i^2 | \phi_i^{KS} \rangle. \tag{2.14}$$

Then, the Kohn-Sham energy functional can be defined as

$$E^{KS}[\rho] = T_s[\phi_i^{KS}] + E_{ne}[\rho] + J[\rho] + E_{xc}[\rho], \tag{2.15}$$

where we are left with one unknown term – the exchange-correlation functional $E^{xc}[\rho]$. This term includes the non-classical contribution to electron kinetic energy and electron-electron interactions:

$$E_{xc}[\rho] = T[\rho] - T_s[\phi_i^{KS}] + V_{ee}[\rho] - J[\rho]. \tag{2.16}$$

If $E_{xc}[\rho]$ was known, the Kohn-Sham scheme would be exact. However, we do not know the exact form of $E_{xc}[\rho]$ and therefore it needs to be approximated. The attempts to find the best approximations are still ongoing and each form has its pros and cons, and while one true (best) functional does not exist, one needs to choose in accordance to the task in hand. The approximations begin with simple and inexpensive options, such as local density approximation (LDA) [Ceperley and Alder, 1980] that assumes that the electron density of a system corresponds to the density of a uniform electron gas. Improvements in precision can be seen, when LDA is expanded by introducing the gradient of the density in a new class of functionals called generalized gradient approximation (GGA). This class includes different versions of parametrization, like PW91 [Perdew and Wang, 1992] or PBE [Perdew et al., 1996a]. Even higher complexity class called Meta-GGA incorporate also the Laplacian of the density and once again offer multiple parametrizations including the TPSS [Sun et al., 2011] and SCAN [Sun et al., 2015] functionals. Finally, very precise, but computationally expensive hybrid functionals, like PBE0 [Perdew et al., 1996b] and HSE06 [Krukau et al., 2006] are based on retaining a fraction of orbital-dependent exchange in the exchange and correlation functional.

After a sufficient level of approximation is selected, we can calculate the energy of the system by minimizing $E^{KS}[\rho]$ with respect to variations in ρ. The minimum is reached when

$$\frac{\delta E^{KS}[\rho]}{\delta \rho} = 0 \tag{2.17}$$

Energy is minimum if Kohn-Sham orbitals satisfy the Schrödinger-like Kohn-Sham equation:

$$\mathbf{h}^{KS} \phi_i^{KS}(\mathbf{r}) = \epsilon_i^{KS} \phi_i^{KS}(\mathbf{r}), \tag{2.18}$$

where ϵ_i^{KS} is the energy of the i-th Kohn-Sham orbital with the one-electron Hamiltonian:

$$\mathbf{h}^{KS} = -\frac{1}{2}\nabla^2 - \sum_I^N \frac{Z_I}{\mathbf{r} - \mathbf{R}_I} + \int \frac{\rho(\mathbf{r}')}{\mathbf{r} - \mathbf{r}'} d\mathbf{r}' + v_{xc}(\mathbf{r}), \tag{2.19}$$

$$v_{xc}(\mathbf{r}) = \frac{\delta E^{KS}[\rho]}{\delta \rho}. \tag{2.20}$$

The Kohn-Sham equations behave as independent-particle equations that do not depend on any of the approximations to the exchange-correlation functional and would lead to the exact ground-state solution if the exact functional would be known. In practice the Kohn-Sham equations are solved in self-consistent manner following these steps:

1. Guess the initial electron density $\rho(\mathbf{r})_i$.

2. Construct the Kohn-Sham Hamiltionian $\mathbf{h}^{KS}$.

3. Diagonalize $\mathbf{h}^{KS}$ to find the corresponding eigenvalues and eigenvectors.

4. Obtain the new electron density $\rho(\mathbf{r})_{i+1}$.

5. If the new electron density is significantly different from last guess return to step 2. If the difference is smaller than the utilized tolerance, the result has converged and calculation is complete.

The exponential increases in computer power and the emergence of multitude of complex computer codes in the past years have made DFT a common tool for many scientists to understand complex systems. The large appeal of DFT is due to it being a parameter free method that does not rely on fitting other results, while having a good predictive power (strongly dependant on the employed exchange-correlation functional). However, in situations, where computational resources are scarce or system sizes increase even further, empirical methods have to be considered.

2.3 Tight-binding approximation

The tight-binding model is a semi-empirical approximation, which is used to predict the electronic properties of a solid by expanding the crystal wavefuctions in the basis of functions centered at each atomic site. At the groundwork of this approximation we consider that an electron at a particular lattice site has little interaction with electrons and atoms positioned elsewhere. We start by considering that the single particle states must obey Bloch's theorem

$$\psi_{n\mathbf{k}}(\mathbf{r} + \mathbf{R}) = e^{i\mathbf{k}\cdot\mathbf{R}}\psi_{n\mathbf{k}}(\mathbf{r}), \tag{2.21}$$

where the band index is labeled by n, $\mathbf{k}$ is the wavevector in the first Brillouin zone and $\mathbf{R}$ is the translation vector of a crystal. The single atomic orbitals ϕ_n clearly do not obey the Bloch's

theorem, but we can use them as a basis to expand the crystal wavefunction

$$\psi_{nk}(\mathbf{r}) = \frac{1}{\sqrt{N}} \sum_{\mathbf{R}} e^{i\mathbf{k}\cdot\mathbf{R}} \big|\phi_{nk}(\mathbf{r}-\mathbf{R})\big\rangle, \tag{2.22}$$

where N designates the number of lattice sites in the crystal and the $\dfrac{1}{\sqrt{N}}$ factor ensures normalization.

Let's now consider the simplest case with one atom in unit cell and, where only atomic s-orbital $\phi_s(\mathbf{r})$ contributes to the crystal state, then Eq. 2.22 becomes

$$\psi_k(\mathbf{r}) = \frac{1}{\sqrt{N}} \sum_{\mathbf{R}} e^{i\mathbf{k}\cdot\mathbf{R}} \big|\phi_s(\mathbf{r}-\mathbf{R})\big\rangle. \tag{2.23}$$

We now can insert this expression into the dispersion relation obtained from the time-independent Schrödinger equation [Eq. 2.1] and obtain the following expressions:

$$E(\mathbf{k}) = \big\langle \psi_{\mathbf{k}}(\mathbf{r}) \big| \mathbf{H} \big| \psi_{\mathbf{k}}(\mathbf{r}) \big\rangle, \tag{2.24}$$

$$E(\mathbf{k}) = \frac{1}{N} \sum_{\mathbf{R}} \sum_{\mathbf{R}'} e^{i\mathbf{k}\cdot(\mathbf{R}'-\mathbf{R})} \big\langle \psi_s(\mathbf{r}-\mathbf{R}) \big| \mathbf{H} \big| \psi_s(\mathbf{r}-\mathbf{R}') \big\rangle$$
$$= \frac{1}{N} \sum_{\mathbf{R}} \sum_{\mathbf{R}'} e^{i\mathbf{k}\cdot(\mathbf{R}'-\mathbf{R})} \big\langle \psi_s(\mathbf{x}) \big| \mathbf{H} \big| \psi_s(\mathbf{x}-(\mathbf{R}'-\mathbf{R})) \big\rangle, \tag{2.25}$$

where we have introduced $\mathbf{x} = \mathbf{r} - \mathbf{R}$. Now for each $\mathbf{R}$ in Eq. 2.25 we have $\mathbf{R}' - \mathbf{R} = \mathbf{R}''$, which is another translation vector and can be used instead of $\mathbf{R}'$ as the summation over $\mathbf{R}'$ covers all translation vectors. Hence substituting $\mathbf{R}''$ we obtain

$$E(\mathbf{k}) = \frac{1}{N} \sum_{\mathbf{R}} \sum_{\mathbf{R}''} e^{i\mathbf{k}\cdot\mathbf{R}''} \big\langle \psi_s(\mathbf{x}) \big| \mathbf{H} \big| \psi_s(\mathbf{x}-\mathbf{R}'') \big\rangle, \tag{2.26}$$

which now leads to a further simplification – as each of the terms in the sum over $\mathbf{R}$ is now identical it simply results in factor N, thus obtaining

$$E(\mathbf{k}) = \sum_{\mathbf{R}''} e^{i\mathbf{k}\cdot\mathbf{R}''} \big\langle \psi_s(\mathbf{x}) \big| \mathbf{H} \big| \psi_s(\mathbf{x}-\mathbf{R}'') \big\rangle. \tag{2.27}$$

We now will separate different terms in the sum over $\mathbf{R}''$ by considering that our atomic orbitals $\psi_s(\mathbf{r})$ are tightly localized – away from $\mathbf{r} = 0$ these orbitals decay rapidly, while for small $\mathbf{r}$ they are large. If $\mathbf{R}'' = 0$ then the expression becomes

$$\big\langle \psi_s(\mathbf{x}) \big| \mathbf{H} \big| \psi_s(\mathbf{x}-\mathbf{R}'') \big\rangle = \big\langle \psi_s(\mathbf{x}) \big| \epsilon_s \big| \psi_s(\mathbf{x}-\mathbf{R}'') \big\rangle = \epsilon_s, \tag{2.28}$$

due to the fact that $H\psi_s(\mathbf{x}) = \epsilon_s \psi_s(\mathbf{x})$ and the atomic states $\psi_s(\mathbf{x})$ are normalized. Essentially,

we can see that $\mathbf{R}'' = \mathbf{0}$ gives us the energy ϵ_s of the atomic s-orbital in an isolated atom. However, if we consider large $\mathbf{R}''$ then we can expect the expression $\langle \psi_s(\mathbf{x}) | \mathbf{H} | \psi_s(\mathbf{x} - (\mathbf{R}'')) \rangle \approx 0$, because of the small overlap between wavefunctions separated by large distances. Hence, typically only terms where $\mathbf{R}''$ is small are included in the tight-binding calculations. If one only considers the nearest-neighbor atoms, where $\mathbf{R}'' = \boldsymbol{\tau}$, with $\boldsymbol{\tau}$ being the translation vector between an atom and its nearest-neighbor, we can write

$$E(\mathbf{k}) = \epsilon_s + \sum_{\boldsymbol{\tau}} e^{i\mathbf{k}\cdot\boldsymbol{\tau}} \langle \psi_s(\mathbf{x}) | \mathbf{H} | \psi_s(\mathbf{x} - \boldsymbol{\tau}) \rangle. \tag{2.29}$$

Then, instead of trying to evaluate the overlap $\langle \psi_s(\mathbf{x}) | \mathbf{H} | \psi_s(\mathbf{x} - \boldsymbol{\tau}) \rangle$ explicitly, we replace it with an empirical parameter t, called the hopping integral, whose value we adjust to match the experimental or theoretical data and set

$$t(\boldsymbol{\tau}) = \langle \psi_s(\mathbf{x}) | \mathbf{H} | \psi_s(\mathbf{x} - \boldsymbol{\tau}) \rangle. \tag{2.30}$$

Finally, we can express the energy $E(\mathbf{k})$ as

$$E(\mathbf{k}) = \epsilon_s + \sum_{\boldsymbol{\tau}} e^{i\mathbf{k}\cdot\boldsymbol{\tau}} t(\boldsymbol{\tau}). \tag{2.31}$$

For example, the general shape of graphene's band structure around the Fermi level can already be obtained with this very simple expression including only one p_z orbital per atom and only considering the 1NN interactions (see Figure 2.1(a)). Small deviations from the DFT only become apparent at energies further away from the Fermi level. Moreover, if 2NN and 3NN couplings are considered, the tight-binding model is comparable to first-principles calculations over wide range of energies and over the entire Brillouin zone [Reich et al., 2002]. In Figure 2.1(b) we compare the conductance profiles obtained by different 3NN models [Kundu, 2011; Hancock et al., 2010; Gunlycke and White, 2008] and DFT calculations for a defective 9-AGNR. It can be seen that the transport properties near band edges are reproduced quite well and noticeable differences only arise at higher energies due to different bandwidths. However, the key features, such as the conductance dips ($E = 1.0t - 1.3t$), are reproduced regardless of the model. All TB calculations carried out in this thesis are utilizing the TB parameters by Hancock [Hancock et al., 2010] ($t_1 = 2.7, t_2 = 0.2, t_3 = 0.18$), unless stated otherwise. Overall, we note that TB approximation exhibits excellent scalability and can easily treat graphene-based systems containing thousands of atoms as seen, for example, in twisted bilayer structures [Haddadi et al., 2020], but some limitations arise when studying systems in different chemical environments. For instance graphene nanostructures deposited on metal surfaces or systems containing hetero-atoms are often too complex to describe with simple TB approximation and DFT calculations need to be considered.
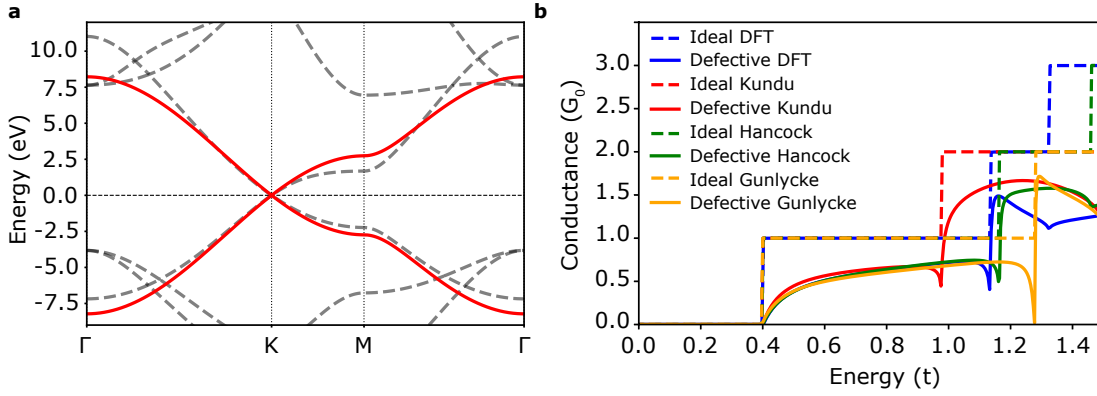
Figure 2.1: (a) Graphene band structure calculated using DFT calculation (dashed grey lines) versus the one-orbital nearest-neighbor tight-binding calculation (red line). (b) Conductance plots of pristine (dashed line) and defective (solid line) 9-AGNRs calculated with DFT and different parametrizations of 3NN TB.

2.4 Ballistic transport

The electron transport in a system is dependent on the relationship between the system size L and electron mean-free path λ that can be defined as the average distance that the charge carrier will travel before being scattered. The scattering events can be both elastic and inelastic and the overall contribution can be approximated by summing individual contributors:

$$\frac{1}{\lambda} = \frac{1}{\lambda_{el-el}} + \frac{1}{\lambda_{impurity}} + \frac{1}{\lambda_{defect}} + \frac{1}{\lambda_{boundary}} + \frac{1}{\lambda_{lattice}} + ..., \qquad (2.32)$$

where the scattering lengths due to separate events, such as electron-electron interactions, impurities, defects, boundaries, phonons, etc. are considered.

When the device size is comparably larger than the mean-free path, the carrier flow enters the diffusive transport regime and is described by the conventional mobility theory. On the other hand, when the mean-free path of a charge carrier is longer than the system dimensions (e.g. due to the minimization of the system) the electron experiences negligible scattering (or negligible electrical resistivity) and enters ballistic transport regime. We note that in this case the only observable scattering and hence the change of the electron's path is due to the collisions with the boundaries of the system, while other scattering events due to the impurities, defects or thermal fluctuations are absent. Ballistic transport is usually observed in reduced dimensionality systems, such as 2D sheets (graphene) or even quasi-1D structures, like nanoribbons or nanotubes, due to the quantization effects. Comparison between the two regimes is displayed in Figure 2.2(a).

In the case of ballistic transport, mobility is no longer applicable to describe the electron behaviour and conductance is used instead. We adopt the Landauer formalism to match the scattering properties with the electrical conductance of the conductor. Current I_{LR} through a
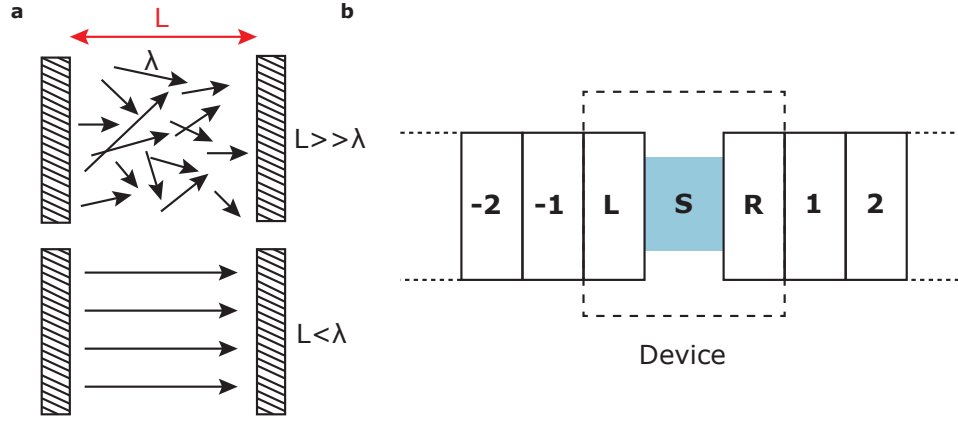
Figure 2.2: (a) Scheme of diffusive transport (upper panel) and ballistic transport (lower panel) between the source and drain (shaded regions). (b) Typical partition of the infinite system for transport calculations within the non-equilibrium Green function method.

conductor attached to left (L) and right (R) electrodes can be expressed by:

$$I_{LR} = \frac{2e}{h} \int_{E_R}^{E_L} M(E) f'(E) T(E) dE, \tag{2.33}$$

where $f'(E) = f(E, \mu_1) - f(E, \mu_2)$ is the difference between the two Fermi functions of the contacts with chemical potentials μ_1 and μ_2, e is the electron charge, V is the voltage and $T(E)$ is the transmission probability. Due to the confinement of electronic states in reduced dimensionality structures, such as nanoribbons, there are multiple energy subbands at a given energy and hence the total current is given by the sum of the currents of all the subbands (also called channels). The number of channels, denoted by $M(E)$, varies with energy depending on the band structure of the system. Finally, Fermi function $f(E, \mu)$ that describes the average (over time) number of electrons in any energy level is expressed as

$$f(E, \mu) = \frac{1}{1 + e^{(E-\mu)/k_B T}}, \tag{2.34}$$

depends on the chemical potential μ and temperature T of the reservoir connected to the electrodes.

Assuming a ballistic transistor with no scattering and having perfect contacts we can re-write the Eq. 2.33 by introducing conductance quantum G_0:

$$I = \frac{2e}{h}(eV) = \frac{2e^2}{h} V = G_0 V, \tag{2.35}$$

$$G_0 = \frac{2e^2}{h} = 7.75c \times 10^{-5} S, \tag{2.36}$$

$$R_0 = \frac{1}{G_0} = 12.95 k\Omega. \tag{2.37}$$

Hence, the quantum of conductance is the smallest possible non-zero conductance and on the flip side, the quantum of resistance R_0 is the highest possible resistance for an ideal ballistic conductor without scattering. Otherwise, scattering events within the ballistic transport regime are usually treated by the introduction of the transmission probability, which tells us the rate at which electrons transmit from source to drain contacts through the device. Transmission can take values $0 \leq T(E) \leq 1$, with $T(E) = 1$ describing ideal ballistic conductance and $T(E) = 0$ describing complete back-scattering. Transmission is commonly obtained either from the scattering-matrix or Green's function methods that we will discuss in the next section. Consequently we can express the conductance G of a ballistic conductor as a multiple of quantum conductance that depends on the number of accessible channels and the transmission probability:

$$G = G_0 M(E) T(E). \tag{2.38}$$

Often the transmission is already given in the range of $0 \leq T(E) \leq M(E)$ to include the number of available channels. Finally, we note that the conductance of any system cannot exceed the maximum conductance defined by the ideal leads with $T = 1$.

2.5   Non-equilibrium Green's function

Green's function is a mathematical tool, which is used to solve difficult ordinary and partial differential equations. It can also be applied to solve quantum mechanical problems in physics, such as calculating ballistic transport in complex nanostructures with or without applied bias. For instance, if the electrodes are not in equilibrium with each other, the central part of the system will acquire a non-equilibrium electron density that can't be solved with DFT and therefore needs to be paired with Green's function technique to obtain the steady-state solution. This method can provide an alternative descriptor of the system just like the wavefunction or electron density. Albeit Green's function is not as intuitive to work with as the electron density, it can often lead to simpler calculation of a necessary property of the system as compared to working with electron density. For example, kinetic energy calculation form electron density can be a tedious and expensive task as it is necessary to compute a density matrix, whereas Green's function is a generalization of the density matrix and often can provides simple expressions for expectation values of 1-body operators.

First, we can re-write the Schrödinger equation [Eq. 2.1] to divide the Hamiltonian and wavefunction of the system into contact $H_{L,R}, |\psi_{L,R}\rangle$ and device subspace $H_D, |\psi_D\rangle$ as shown Figure 2.2(b). Typically, the device region contains the scattering center and one unit cell of each lead, while the left and right leads are considered semi-infinite, thus the Hamiltonian is expressed as

$$\begin{pmatrix} \mathbf{H}_L & \boldsymbol{\tau}_L & 0 \\ \boldsymbol{\tau}_L^\dagger & \mathbf{H}_D & \boldsymbol{\tau}_R^\dagger \\ 0 & \boldsymbol{\tau}_L & \mathbf{H}_R \end{pmatrix} \begin{pmatrix} |\psi_L\rangle \\ |\psi_D\rangle \\ |\psi_R\rangle \end{pmatrix} = E \begin{pmatrix} |\psi_L\rangle \\ |\psi_D\rangle \\ |\psi_R\rangle \end{pmatrix}, \tag{2.39}$$

where $\boldsymbol{\tau}_{L(R)}$ is the interaction between the device region and left (right) lead. Here we have

assumed two leads that do not couple to each other, but in practice we can have N contacts connecting to the device. Now, we define the unperturbed Green's function as

$$(E - \mathbf{H})\mathbf{G}(E) = \mathbf{I}, \tag{2.40}$$

where $\mathbf{I}$ is the identity matrix used for orthogonal basis set. Here, we will use the orthogonal representation without loss of generality, while it is also possible to use non-orthogonal basis with the overlap matrix $\mathbf{S}$ instead. We now will introduce a constant perturbation $|v\rangle$ in the Schrödinger equation [Eq. 2.1]

$$\mathbf{H}|\psi\rangle = E|\psi\rangle + |v\rangle, \tag{2.41}$$

and express the response to this perturbation as

$$(E - \mathbf{H})|\psi\rangle = -|v\rangle, \tag{2.42}$$

$$|\psi\rangle = -\mathbf{G}(E)|v\rangle. \tag{2.43}$$

If we know the response to the perturbation, it is easier to calculate other properties instead of solving the whole eigenvalue problem. For example, the wavefunction of right contact $|\psi_R\rangle$ can be easily expressed form the wavefunction of the device $|\psi_D\rangle$. Using Eq. 2.39

$$\mathbf{H}_R|\psi_R\rangle + \boldsymbol{\tau}_R|\psi_D\rangle = E|\psi_R\rangle, \tag{2.44}$$

$$(E - \mathbf{H}_R)|\psi_R\rangle = \boldsymbol{\tau}_R|\psi_D\rangle, \tag{2.45}$$

$$|\psi_R\rangle = \mathbf{g}_2(E)\boldsymbol{\tau}_R|\psi_D\rangle, \tag{2.46}$$

where $\mathbf{g}_R$ is the Green's function of the right contact. One needs to note that we obtain two solutions for an infinite system – advanced and retarded solutions corresponding to incoming and outgoing waves in the contacts. We will denote the retarded solutions with a dagger ($G^\dagger$).

As stated before, Green's function is often easier to calculate than solving the whole Schrödinger equation and to make it even more manageable, we can calculate part of the Green's function corresponding only to the device $\mathbf{G}_D$ separately. Starting from the Eq. 2.40:

$$\begin{pmatrix} E - \mathbf{H}_L & -\boldsymbol{\tau}_L & 0 \\ -\boldsymbol{\tau}_L^\dagger & E - \mathbf{H}_D & -\boldsymbol{\tau}_R^\dagger \\ 0 & -\boldsymbol{\tau}_L & E - \mathbf{H}_R \end{pmatrix} \begin{pmatrix} \mathbf{G}_L & \mathbf{G}_{LD} & \mathbf{G}_{LR} \\ \mathbf{G}_{DL} & \mathbf{G}_D & \mathbf{G}_{RD} \\ \mathbf{G}_{RL} & \mathbf{G}_{RD} & \mathbf{G}_R \end{pmatrix} = E \begin{pmatrix} \mathbf{I} & 0 & 0 \\ 0 & \mathbf{I} & 0 \\ 0 & 0 & \mathbf{I} \end{pmatrix}, \tag{2.47}$$

we select the second column and write the 3 equations:

$$(E - \mathbf{H}_L)\mathbf{G}_{LD} - \boldsymbol{\tau}_L\mathbf{G}_D = 0, \tag{2.48}$$

$$-\boldsymbol{\tau}_L^\dagger\mathbf{G}_{LD} + (E - \mathbf{H}_D)\mathbf{G}_D - \boldsymbol{\tau}_R^\dagger\mathbf{G}_{RD} = 0, \tag{2.49}$$

$$(E - \mathbf{H}_R)\mathbf{G}_{RD} - \boldsymbol{\tau}_R\mathbf{G}_D = 0. \tag{2.50}$$

We can solve equations 2.48 and 2.49 for $\mathbf{G}_{LD}$ and $\mathbf{G}_{RD}$

$$\mathbf{G}_{LD} = \mathbf{g}_L \boldsymbol{\tau}_L \mathbf{G}_D = 0, \tag{2.51}$$

$$\mathbf{G}_{RD} = \mathbf{g}_R \boldsymbol{\tau}_R \mathbf{G}_D = 0, \tag{2.52}$$

and substituting them into Eq. 2.49 we obtain

$$-\boldsymbol{\tau}_L^\dagger \mathbf{g}_L \boldsymbol{\tau}_L \mathbf{G}_D - (E - \mathbf{H}_D)\mathbf{G}_D \boldsymbol{\tau}_R^\dagger \mathbf{g}_R \boldsymbol{\tau}_R \mathbf{G}_D = \mathbf{I}. \tag{2.53}$$

Here, we can finally express our device Green's function $\mathbf{G}_D$ as

$$\mathbf{G}_D = (E - \mathbf{H}_D - \boldsymbol{\Sigma}_L - \boldsymbol{\Sigma}_R)^{-1}, \tag{2.54}$$

where $\boldsymbol{\Sigma}_{L(R)}$ is the self-energy containing information about the left (right) semi-infinite lead. The self-energies are obtained self-consistently using Dyson's equation:

$$\boldsymbol{\Sigma}_{L(R)}(E) = \boldsymbol{\tau}_{L(R)}^\dagger (E\mathbf{I} - \mathbf{H}_{L(R)} - \boldsymbol{\Sigma}_{L(R)}(E))^{-1} \boldsymbol{\tau}_{L(R)}. \tag{2.55}$$

One can notice that the effect of the leads is to add the self-energies to the device Hamiltonian $\mathbf{H}_D$ in order to obtain an effective Hamiltonian $\mathbf{H}_{eff}$ of the system

$$\mathbf{H}_{eff} = \mathbf{H}_D + \boldsymbol{\Sigma}_L + \boldsymbol{\Sigma}_R. \tag{2.56}$$

It is important to mention that usually, for numerical calculations, one adds a small ($\eta \to 0^+$) imaginary character to the Green's function in order to facilitate the matrix inversions:

$$\mathbf{G}_D(E) = ((E + i\eta)\mathbf{I} - \mathbf{H}_D - \boldsymbol{\Sigma}_L - \boldsymbol{\Sigma}_R)^{-1}, \tag{2.57}$$

Consequently we can calculate the transmission coefficient by taking the trace of the following product

$$T(E) = Tr[\boldsymbol{\Gamma}_L \mathbf{G}_D \boldsymbol{\Gamma}_R \mathbf{G}_D^\dagger], \tag{2.58}$$

where the broadening function $\boldsymbol{\Gamma}_{L(R)}$ due to the leads is calculated from the self-energies

$$\boldsymbol{\Gamma}_{L(R)}(E) = i[\boldsymbol{\Sigma}_{L(R)}(E) - \boldsymbol{\Sigma}_{L(R)}(E)^\dagger]. \tag{2.59}$$

Next, we use the transmission coefficient $T(E)$ obtained above to express conductance G in terms of conductance quantum G_0 using the Landauer formula [Landauer, 1957]:

$$G(E) = G_0 T(E) = \frac{2e^2}{h} T(E). \tag{2.60}$$

In addition to transmission and conductivity, other important properties that one can calculate from Green's function are, for example, spectral density $A_{L(R)}(E)$ originating from left (right)

lead and the density of states (DOS),

$$A_{L(R)}(E) = \mathbf{G}_D \mathbf{\Gamma}_{L(R)} \mathbf{G}_D^\dagger(E), \tag{2.61}$$

$$DOS = \frac{1}{\pi} Tr[Im(\mathbf{G}_D)]. \tag{2.62}$$

Furthermore, as the probability to find an electron on the device is conserved in the steady-state, we can also define an expression for finding the incoming probability current $i_{L(R)}$ from the left (right) electrode as

$$i_{L(R)} = -\frac{ie}{\hbar}(\langle \psi_{L(R)} | \mathbf{g}_{L(R)} | \psi_D \rangle - \langle \psi_{L(R)} | \mathbf{g}_{L(R)}^\dagger | \psi_D \rangle). \tag{2.63}$$

Moreover, for non-equilibrium setups, we can also express current between two leads at different chemical potentials μ_i:

$$I = \frac{q}{h} \int_{-\infty}^{\infty} (f_1(E,\mu_1) - f_2(E,\mu_2)) Tr[\mathbf{\Gamma}_L \mathbf{G}_D \mathbf{\Gamma}_R \mathbf{G}_D^\dagger]. \tag{2.64}$$

Some of the drawbacks of NEGF techniques are connected to the inefficiency of the implemented algorithms and memory restraints, which is why the calculations rarely exceed 1,000 atoms. Main complexity arises from two computationally heavy steps – the self-energy calculations require multiple iterations of matrix inversions and additionally non-equilibrium calculations require a triple matrix product [Papior, 2016]. It is possible to mitigate some of the problems by choosing the smallest possible unit cell and employing the Bloch's theorem to treat periodic directions and, more importantly, choosing an appropriate algorithm to effectively invert matrices.

Width-Modulated Graphene Nanoribbon Junctions

3 Edge-Functionalized Graphene Nanoribbons

We theoretically investigate the electron transport in armchair and zigzag graphene nanorib-bons (GNRs) chemically functionalized with p-polyphenyl and polyacene groups of increasing length. Our nearest-neighbor tight-binding calculations indicate that, depending on whether the number of aromatic rings in the functional group is even or odd, the resulting conductance at energies matching the energy levels of the corresponding isolated molecule are either unaffected or reduced by exactly one conductance quantum as compared to the pristine GNR, respectively. Such an even-odd effect is shown to originate from a subtle interplay between the electronic states of the guest molecule that are spatially localized on the binding sites and those of the host nanoribbon. We next generalize our findings by employing more accurate tight-binding Hamiltonians along with density-functional theory calculations, and critically discuss the robustness of the observed physical effects against the level of theory adopted. Our work offers a comprehensive understanding of the influence of aromatic molecules bound to the edge of graphene nanoribbons on their electronic transport properties, an issue which is instrumental to the prospective realization of graphene-based chemosensors.

This chapter is adapted from:

Čerņevičs, K., Pizzochero, M. and Yazyev, O.V. (2020). Even–odd conductance effect in graphene nanoribbons induced by edge functionalization with aromatic molecules: basis for novel chemosensors. *Eur. Phys. J. Plus*, 135:681. [pre-print: arXiv: 2005.05834]

My contribution to this work was conceiving the original idea, performing the tight-binding calculations, analysis of the data and writing the paper.

3.1   Motivation

Edge functionalization with p-polyphenyl and polyacene groups of increasing length, for AGNRs and ZGNRs respectively, can be either seen as the shortest possible heterojunction consisting of one unit cell of different width GNR connecting two equal-width leads or a pristine GNR with side-attached defect. Regardless, it is an excellent fundamental system to establish the effects of width-modulated junctions on electronic transport in GNRs. Furthermore, chemical functionalization with molecules on the edge [Rosales et al., 2008b,a] and on the surface [López-Bezanilla et al., 2009] of GNRs has been theoretically investigated and the influence on the electronic structure of both armchair- and zigzag-edge graphene nanoribbons has been identified. It has been shown that upon binding, each functional group leaves a unique "fingerprint" reflecting its energy levels. This finding has made GNRs also an appealing platform for the realization of novel chemosensors.

On the basis of 1NN-TB Hamiltonians described by the hopping integral t_1 between the p_z orbitals, customarily taken to be $t_1 = 2.70$ eV, it has been predicted that the formation of a chemical bond between GNRs and either p-polyphenyl or polyacene groups may affect the conductance spectra at all values of energy matching those of the isolated molecule. Surprisingly, a phenomenon emerges in both AGNR and ZGNR, where the conductance at energy $E = \pm 2.70$ eV is unaltered when the guest molecule features an even number of rings, whereas for an odd number of rings a Fano anti-resonance (stemming from the interference between the continuum of states of the hosting GNRs and the states localized on the guest molecule [Miroshnichenko et al., 2010]) occurs and removes one conductance quantum [Rosales et al., 2008b]. Despite its potential in designing GNR-based sensors for aromatic molecules, such an intriguing effect remains very poorly understood to date.

A previous work [Rosales et al., 2008b] justified this even-odd effect by suggesting that an isolated molecule featuring an odd (even) number of rings would (not) exhibit such an electronic state located at $E = \pm 2.70$ eV, in close analogy with chains hosting even or odd number of quantum dots [Orellana et al., 2003]. Yet, we remark that polyacenes or p-polyphenyls, irrespective of the number of rings, *do present* an energy level at $E = \pm t_1 = \pm 2.70$ eV in their spectra at the 1NN-TB level of theory, thus proving the previous argument false. Hence, this consideration highlights that the conductance profile of such edge-functionalized GNRs depends only *partially* on the energy levels of the isolated functional group, signaling that more complex effects ensuing from the interaction of the electronic structure of the hosting nanoribbon with that of the guest molecule are operative and have to be clarified. In addition, it remains to be ascertained whether such even-odd phenomenon is actually physical or simply emerges as an artifact of the (possibly oversimplified) 1NN-TB model.

In this chapter, we investigate in detail, at different TB and also first principles levels of theory, the effect of p-polyphenylene and polyacene molecules of varying length covalently bound to the edge of AGNRs and ZGNRs on the electron transport by means of non-equilibrium Green's function calculations. We first unravel the origin of the even-odd conductance effect

upon binding of guest molecules and rationalize the otherwise unclear loss of exactly one conductance quantum in terms of the spatial distribution of the incoming wavefunction. Next, we extend our findings to higher levels of theory in order to critically examine the robustness of the observed effects with respect to the adopted theoretical models. Overall, we establish a comprehensive picture of the impact of the aromatic functional groups on the electron transport properties of graphene nanoribbons, hence contributing to lay the conceptual foundations underlying the practical realization of GNR-based chemosensors.

3.2 Methodology

We obtain Hamiltonians at both tight-binding and density-functional theory levels. Our TB Hamiltonians include one p_z orbital per atom and take the general form

$$H = \sum_i \epsilon_i c_i^\dagger c_i - \sum_{i,j} t_{i,j}(c_i^\dagger c_j + H.c), \tag{3.1}$$

where ϵ_i is the on-site energy at lattice position i, $t_{i,j}$ is the hopping integral between the atoms (i, j), and $c_i^\dagger(c_i)$ creates (annihilates) an electron at lattice site i. We adopt two TB models, both setting on-site energies $\epsilon = 0$ eV and including either first-nearest-neighbor hopping solely ($t_1 = 2.70$ eV) or up to the third-nearest-neighbor hopping ($t_1 = 2.70$ eV, $t_2 = 0.20$ eV, and $t_3 = 0.18$ eV) for carbon atoms both in nanoribbon and the edge-bound molecule. This latter corresponds to the model proposed and benchmarked by Hancock and coworkers [Hancock et al., 2010]. All our TB calculations are performed using the `Kwant` package [Groth et al., 2014]. For deeper insight to the TB model, please refer to Section 2.3.

Kohn-Sham DFT calculations are performed under the generalized gradient approximation to the exchange and correlation functional devised by Perdew, Burke, and Ernzerhof [Perdew et al., 1996a] as implemented in `Siesta`[Soler et al., 2002]. Core electrons are described by separable norm-conserving pseudopotentials [Troullier and Martins, 1991] whereas single-particle wavefuctions of valence electrons are expanded in a linear combination of atomic orbitals of double-ζ polarization (DZP) quality. Real space integrations are performed with a 400 Ry mesh cutoff while the Brillouin zone is sampled with the equivalent of $21\times1\times1$ k-mesh per unit cell in all cases but transport calculations, for which it is increased to $400\times1\times1$. We optimize the atomic coordinates until the residual force acting on each atom converges to 0.02 eV/Å. We introduce guest molecules of increasing number of rings in in a $7\times1\times1$ and $14\times1\times1$ supercells of AGNRs and ZGNRs (yielding similar supercell lengths of 30.19 Å and 34.58 Å) containing 126 and 140 atoms, respectively. Replicas along non-periodic directions are separated by a vacuum region larger than 10 Å.

With the tight-binding and Kohn-Sham Hamiltonians H at hand, transport properties are next calculated using the non-equilibrium Green's function (NEGF) formalism as presented in Section 2.5 and conductance is expressed in terms of the conductance quantum G_0 within the Landauer formula [see Eq. 2.60]. Our quantum electronic transport calculations are
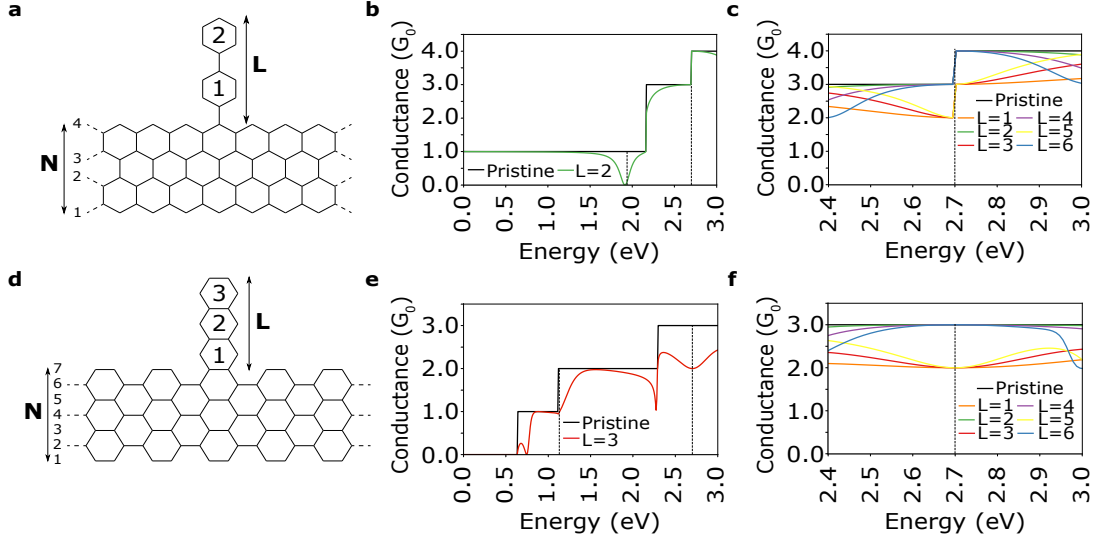
Figure 3.1: (a) Atomic structure of 4-ZGNR edge-functionalized with a p-polyphenylene group with $L = 2$ (biphenyl). (b) Conductance spectra of 4-ZGNR hosting biphenyl group ($L = 2$) with dashed lines indicating the electronic states of the molecule. (c) Conductance spectra of 4-ZGNR hosting p-polyphenylene groups with $1 \leq L \leq 6$ in the region of 2.70 eV. (d) Atomic structure of 7-AGNR edge-functionalized with a polyacene group with $L = 3$ (anthracene). (e) Conductance spectra of 7-AGNR hosting anthracene molecule ($L = 3$) with dashed lines indicating the electronic states of the molecule. (f) Conductance spectra of 7-AGNR hosting polyacene groups with $1 \leq L \leq 6$ in the region of 2.70 eV.

performed with the help of `Kwant` [Groth et al., 2014] and `Transiesta` [Papior et al., 2017].

3.3 Results and discussion

3.3.1 Origin of even-odd effect in edge-functionalized graphene nanoribbons

As compared to their wider counterparts, narrow GNRs are more suitable systems to explore the conductance spectra upon functionalization, as less energy bands are present around $E = \pm 2.70$ eV. Hence, in the following we restrict our investigation to 4-ZGNR and 7-AGNR without loss of generality, as the Fano anti-resonances due to the binding molecule occurs irrespective of the number of carbon atoms N across the GNR [Rosales et al., 2008b].

We start our investigation by relying on the 1NN-TB model Hamiltonians. In Figure 3.1(a), (b) and (c), we show 4-ZGNR hosting a p-polyphenyl functional group of increasing lengths, ranging from phenyl (possessing a number of rings $L = 1$) to p-hexaphenyl ($L = 6$), along with its effect on the resulting conductance spectra. Only the conduction states are given, as the electron-hole symmetry is preserved in the 1NN-TB model in the entire energy spectrum. In Figure 3.1(b) one clearly notices the presence of drop in the conductance at $E = 1.94$ eV corresponding to the electronic state of the molecule, as well as a superimposition at $E = 2.70$

eV to the conductance profile of that of the pristine system. Hence, the electronic state of the molecule at $E = 2.70$ eV has no effect on the conductance profile in this particular case. We observe that depending on the number of rings in the guest molecule, distinct effects in the conductance spectra of the hosting nanoribbon emerges [see Figure 3.1(c)]. We stress again that all p-polyphenyls host an electronic state at $E = 2.70$ eV, but 4-ZGNR functionalized with p-polyphenyl groups possessing an even number of aromatic rings clearly shows conductance spectra approaching that of the the pristine nanoribbon at $E = 2.70$ eV. On the other hand, the spectra upon the introduction of a p-polyphenyls with an odd number of rings display a Fano anti-resonance at $E = 2.70$ eV. We unambiguously observe the even-odd effect in the vicinity ($\pm \delta E$) of the conductance step, and in the following we will present our results at $E = 2.70 \pm \delta E$ (with $\delta E = 0.001$ eV) to ensure avoidance of the irregularity. A parallel conclusion can be drawn for 7-AGNR edge-functionalized with polyacenes displayed in Figure 3.1(d)−(f). In this case, however, the lack of a conductance step at $E = 2.70$ eV makes Fano anti-resonances even more visible, as we show in Figure 3.1(f). Again, resonant transport is observed when the edge-attached molecule possesses an even L, while an anti-resonance is seen for an odd L, which becomes narrower as the length of the chain increases, suggesting a weaker coupling to the nanoribbon [Miroshnichenko et al., 2010]. Interestingly, the Fano anti-resonance occurs at the position of the flat band in AGNRs as calculated by 1NN-TB model, whereas $E = 2.70$ eV is the energy, where multiple sub-bands cross at X point of the Brillouin zone in ZGNRs.

We complement our analysis of this fascinating even-odd phenomenon by presenting in Figure 3.2 the local densities of states (LDOS), local probability current maps, and the wavefunctions of 4-ZGNR and 7-AGNR upon binding of p–polyphenyls ($L = 1, 2$) and polyacenes ($L = 2, 3$), respectively, at the relevant energy $E = 2.70$ eV. The LDOS of 4-ZGNR functionalized with a phenyl group at the edge ($L = 1$) shown in Figure 3.2(a) indicates a pronounced localization at both the inner region of 4-ZGNR as well as at the phenyl group, whereas no density is observed on the edge site of ZGNR which binds to the phenyl group. At this latter site, we also note the flow of the current is suppressed, see Figure 3.2(b). Moving from phenyl to biphenyl ($L = 2$), on the other hand, the LDOS is delocalized over the whole 4-ZGNR [Figure 3.2(d)] and no density resides at the site which bridges the functional group to 4-ZGNR. Furthermore, the probability current remains unperturbed and features a symmetric flow through both edges of the nanoribbon, see Figure 3.2(e). These results lend further support to the observations discussed in the previous paragraph, *i.e.* that changes in the transport properties of edge-functionalized GNRs depend on the number of rings in functional group, with odd number of rings causing the disruption of the electronic structure at $E = 2.70$ eV. Similar observations translate to 7-AGNR. In the case of naphtalene ($L = 2$) [Figure 3.2(g)], the LDOS is fully delocalized and no density can be found on the two atoms which bind the polyacene with the nanoribbon, hence displaying local currents resembling those of pristine 7-AGNR [Figure 3.2(h)]. In contrast, functionalization with anthracene ($L = 3$) gives rise to strong localization which in turn hinders the current to flow between the two edge atoms in the nanoribbon at which the guest molecule binds, as seen in Figure 3.2(j) and (k).

In the case of guest aromatic molecules with $L = 2$, we observe that the state that is localized
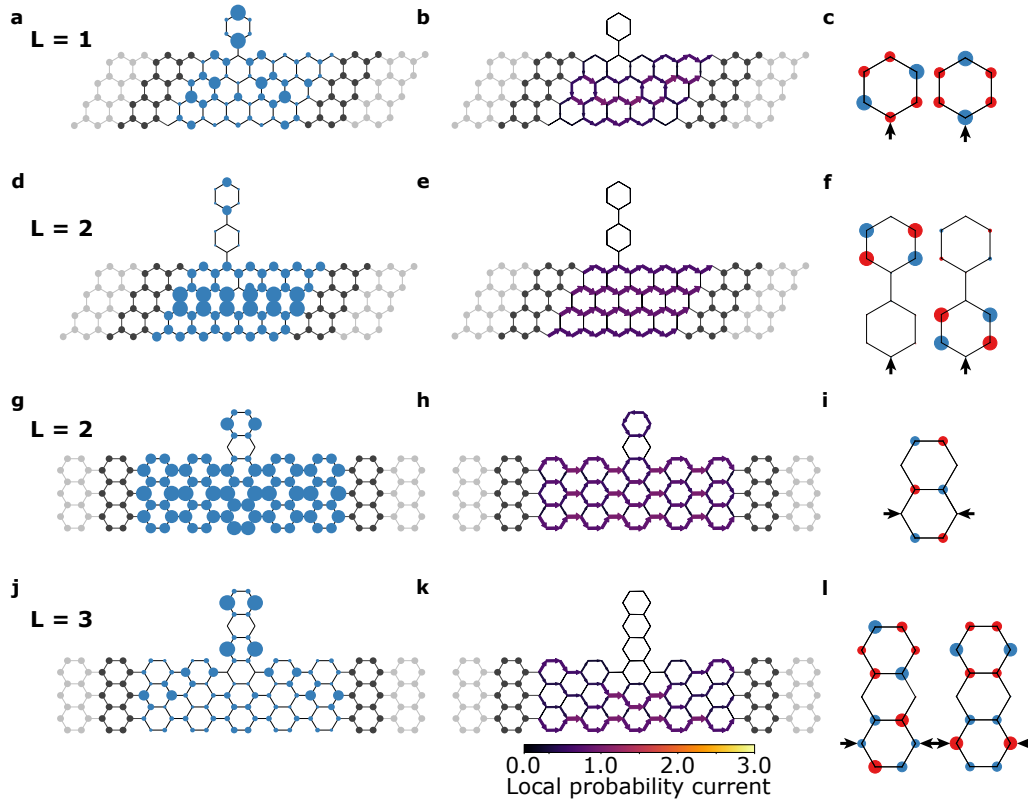
Figure 3.2: (a) LDOS and (b) probability current at $E = 2.70 - \delta E$ eV (with $\delta E = 0.001$ eV) in 4-ZGNR edge-functionalized with a phenyl ($L = 1$) group. (c) Wavefunctions of the isolated benzene ($L = 1$) molecule at $E = 2.70$ eV, with colors indicating a phase difference of π and black arrows indicating the binding sites. (d) LDOS and (e) probability current at $E = 2.70 - \delta E$ eV in 4-ZGNR edge-functionalized with biphenyl ($L = 2$) group. (f) Wavefunctions of the isolated biphenyl molecule at $E = 2.70$ eV. (g) LDOS and (h) probability current at $E = 2.70$ eV in 7-AGNR edge-functionalized with naphtalene ($L = 2$). (i) Wavefunctions of the isolated naphtalene molecule at $E = 2.70$ eV. (j) LDOS and (k) probability current at $E = 2.70$ eV in 7-AGNR edge-functionalized with anthracene ($L = 3$). (l) Wavefunctions of the isolated anthracene molecule $E = 2.70$ eV.

on the molecule is not interacting with the continuum of states of the nanoribbon, and the conductance at $E = 2.70$ eV is the same as that of the ideal lead [Figure 3.2(d) and (g)]. The reason for this traces back to the spatial distribution of the electronic states in the corresponding isolated molecules at $E = \pm 2.70$ eV, as given in Figure 3.2(c), (f), (i), and (l). At variance with benzene [Figure 3.2(c)]], in the biphenyl group the wavefunction [Figure 3.2(f)] does not localize on the atoms that are directly bound to GNRs, thereby preventing any interactions with the continuum of states of GNR to occur. In general, the spatial distribution of the wavefunction is similar in all p-polyphenyl molecules possessing an even number of rings, showing zero-weight at the binding sites and strong localization along the molecular armchair edges. On the other hand, aromatic molecules featuring an odd number of rings feature a wavefunction that does localize on the sites binding to the nanoribbon, thus leading to interaction with the
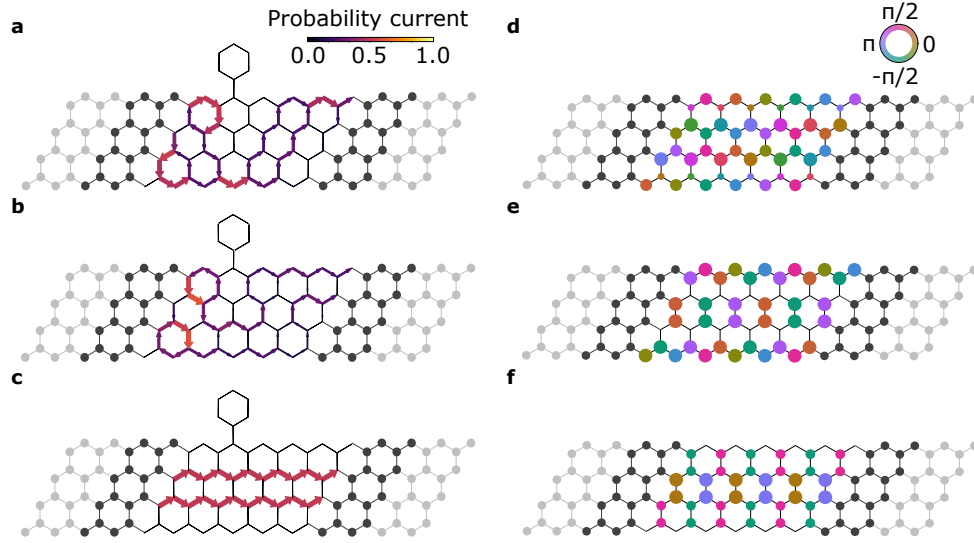
Figure 3.3: Map of probability current of 4-ZGNR edge-functionalized with a phenyl group at $E = 2.70$ eV for incoming (a) mode I, (b) mode II, and (c) mode III from the left lead. Wavefunction of 4-ZGNR at $E = 2.70$ eV for incoming (d) mode I, (e) mode II, and (f) mode III from the left lead.

ZGNR states and resulting in Fano anti-resonances located at $E = \pm 2.70$ eV. Differently from p-polyphenyls, in the case of polyacenes groups shown in Figure 3.2(i) and (l), there exist two sites which bind to 7-AGNR. Similarly to p-polyphenyls, however, depending on whether the wavefunction does reside or not on the binding sites, either an intact or disrupted transport emerges in the current maps. Hence, we conclude that the localization of the wavefunction at the sites of the guest functional groups which bind to the GNRs is the key ingredient in governing the destructive interference of the electron transport in the hosting nanoribbon.

As shown in Figure 3.1((c) and (f), edge-functionalization of the nanoribbon with a molecule containing an odd number of aromatic rings removes exactly one quantum from the conductance at $E = \pm 2.70$ eV. Furthermore, we see that the local currents in Figure 3.2(b) and (k) break the symmetry along the edges and hence indicate a different response from the incoming modes. For the representative case of 4-ZGNR edge-functionalized with a phenyl group ($L = 1$), we present in Figure 3.3 (a)−(c) the current maps due to the three incoming modes from the left lead at $E = 2.70 - \delta E$. Our results demonstrate that, while the current is disrupted in panels (a) and (b), it is fully preserved in panel (c). The origin of this effect can be rationalized by inspecting the behavior of the incoming wavefunction, as shown in Figure 3.3(d)−(f). Of the three wavefunctions displayed, only the one presented in Figure 3.3(f) does not exhibit finite weight on the atoms at the edge of the nanoribbon, thereby indicating that the local current in the inner region of the nanoribbon is not affected by the guest molecule. On the other hand, the wavefunctions shown in 3.3(d) and (e) are localized to some degree on the edge atoms as well. This is further reflected in the current maps of Figure 3.3(a) and (b), in which one can observe how the local current is not flowing through the site that is

bound to the phenyl group. A similar behavior has been previously reported in carbon-based sp^2-hybridized structures whereby one atom experiences a large on-site potential [Chen et al., 2018]. We stress that the same effect is displayed by 7-AGNR edge-functionalized with a group containing an odd number of rings (not shown here), with the difference that in this latter case the guest molecule is covalently bound through two distinct carbon sites as compared to 4-ZGNR. Remarkably, we demonstrate that the even-odd phenomenon boils down to the interaction between two (four) sites, *i.e.* one (two) on the ZGNR (AGNR) and one (two) on the edge-attached aromatic molecule.

3.3.2   Even-odd effect arising from higher-level theoretical models

Next, we expand our investigation by employing more realistic models, namely third-nearest-neighbor TB model and DFT calculations in order to verify that the observed even-odd effect is not an artifact of the possibly oversimplified 1NN-TB model. In Figure 3.4, we present the conductance spectra of 4-ZGNR and 7-AGNR hosting p-polyphenyl and polyacene groups of length $1 \leq L \leq 6$ bound to the edge. As expected, 3NN-TB model and DFT calculations break the electron-hole symmetry observed in the 1NN-TB model. Hence, both valence and conduction states are presented. In Figure 3.4(a) and (c), we observe that the even-odd effect is retained when the 3NN-TB model is adopted for 4-ZGNR system both in the valence and conduction states, even though the energy at which it takes place is shifted by ~0.6 eV with respect to the 1NN-TB model for the latter. Additionally, we remark that there are no distinct resonances and anti-resonances occurring at a particular energy, rather such effect appears within the energy window in which the conductance takes approximately the value of 4.0 or 3.0 G_0. Furthermore, DFT results shown in Figure 3.4(b) and (d) also allow one to discriminate between odd and even values of L, both in valence and conduction states, and, similar to the 3NN-TB model, the phenomenon is again slightly shifted in energy w.r.t. the 1NN-TB model, yet to a different extent as compared the 3NN-TB results. The conductance spectra of edge-functionalized 7-AGNR obtained at the 3NN-TB and DFT levels are given in Figure 3.4(e) and (f), respectively. While the even-odd effect is observed in the 3NN-TB model calculations, we found that, upon increasing L, the conductance deviates from the the resonance and anti-resonance behaviors observed in the 1NN-TB model. Hence, the even-odd effect becomes difficult to be resolved in longer aromatic functional groups. Furthermore, DFT calculations of the valence states yield only a weak separation between odd and even L at $E \approx -2.80$ eV, though for even values of L resonant transport is preserved. The 3NN-TB results for the conduction states shown in Figure 3.4(g) reveal that the effect can still be clearly observed, but, similar to 4-ZGNR, it appears shifted to $E = 2.30$ eV and spread over a wider energy window. Finally, we did not single out any even-odd effect characteristics for 7-AGNR with side-attached aromatic molecules in the conduction states calculated by means of DFT. Overall, we establish that the even-odd phenomenon is not an artifact of the 1NN-TB model, though it appears largely exaggerated by this simplified approach.

We then determine the band structure of pristine 7-AGNR to rationalize the discrepancy in the
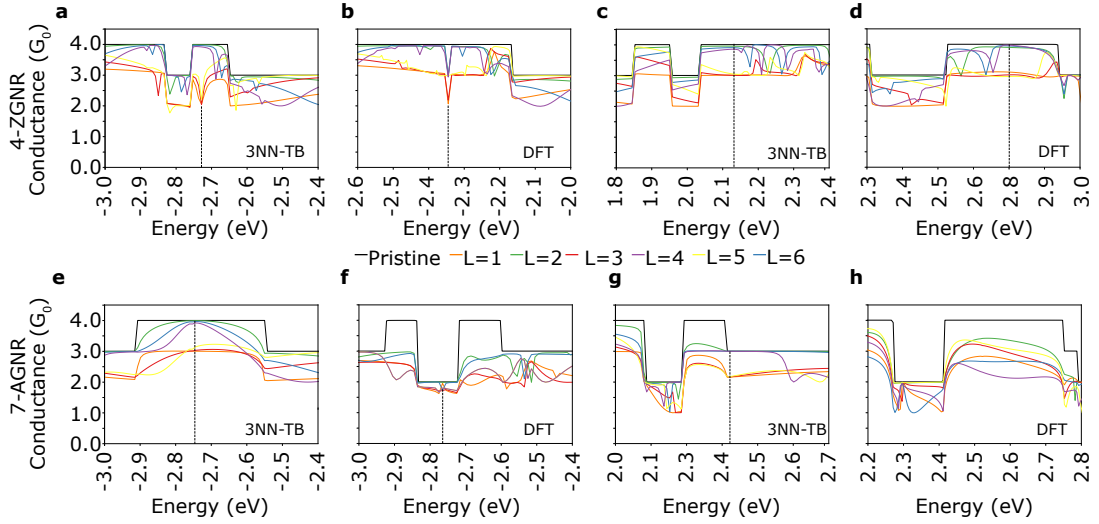
Figure 3.4: Conductance spectra of 4-ZGNR edge-functionalized with p-polyphenylene groups of $1 \leq L \leq 6$ below the Fermi level at the (a) 3NN-TB, and (b) DFT levels, as well as above the Fermi level at the (c) 3NN-TB and (d) DFT levels. Conductance spectra of 7-AGNR edge-functionalized with polyacene groups of $1 \leq L \leq 6$ below the Fermi level at the (e) 3NN-TB, and (f) DFT levels, as well as above the Fermi level at the (g) 3NN-TB and (h) DFT levels.

even-odd effect emerging in the different adopted levels of theory. Our results are presented in Figure 3.5. The band structure obtained at the 1NN-TB level exhibits a flat band at $E = \pm 2.70$ eV [see Figure 3.5(a)], $i.e.$ where the even-odd effect occurs. On the other hand, both the 3NN-TB model and DFT calculations reveal that such band acquires some dispersion character and slightly shifts in energy as compared to the 1NN-TB result. Such a poor description of the band structure of 7-AGNR at the 1NN-TB level explains why the even-odd effect is shifted away from $E = 2.70$ eV in higher levels of theory, and also accounts for the fact that this phenomenon is observed at wider energy windows which correspond to the bandwidth. Furthermore, at variance with the 1NN-TB model, the DFT band structure [Figure 3.5(c)] clearly shows strongly dispersed character of the conduction states, hence substantially quenching the even-odd effect in this energy range.

Finally, we discuss the observed deviation from the conductance values of 4.0 and 3.0 G_0 shown in Figure 3.4(e), for even and odd values of L, respectively, on the basis of the 3NN-TB model LDOS of 7-AGNR systems at $E = 2.70$ eV. We compare the LDOS of the pristine system [Figure 3.5(d)] with that of the nanoribbon hosting a tetracene ($L = 4$) [Figure 3.5(e)] or an octacene ($L = 8$) [Figure 3.5(f)]. Our findings indicate that the LDOS in the inner region of the 7-AGNR edge-functionalized with tetracene closely resembles that of the pristine system, with the LDOS on the functional group being well separated from the 7-AGNR and resulting in resonant transport. The increase in the number of the rings, $e.g$ moving from tetracene to octacene, is accompanied by a disruption in the LDOS in the lead, as shown in Figure 3.5(f). In addition, the LDOS starts to develop on the two binding sites, hence detrimentally perturbing the transport properties and suppressing its resonant character. We conclude that a further
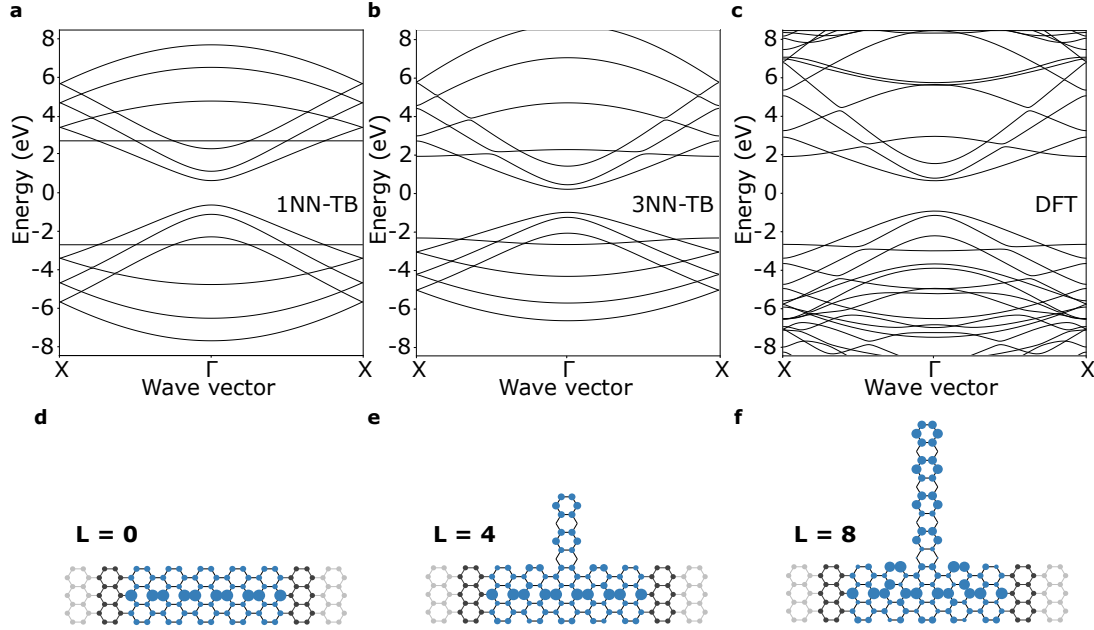
Figure 3.5: Electronic band structure of pristine 7-AGNR obtained at the (a) 1NN-TB, (b) 3NN-TB, and (c) DFT levels. (d) 3NN-TB model LDOS at $E = -2.70$ eV for (d) pristine, (e) edge-functionalized with tetracene ($L = 4$), and (f) edge-functionalized with octacene ($L = 8$) 7-AGNR.

increase in the length of acenes containing an even number of rings promotes a significant hybridization of the localized state on the guest molecule with the continuum of states in the hosting AGNR, yielding a decrease in the conductance.

3.4   Summary and conclusions

In summary, we have carried out a theoretical investigation of the transport properties of GNRs with edges chemically functionalized with p-polyphenyl and polyacene groups. Our 1NN-TB results indicate that, depending on whether the number of aromatic rings in the guest molecule is even or odd, either constructive or destructive interference takes place at $E = \pm t_1 = \pm 2.70$ eV in the conductance spectrum. In the case of functional groups with an even number of rings, this effect stems from the fact that the local density of states does not reside on the sites of the guest molecule which covalently bind to the nanoribbon, resulting in negligible interactions between the continuum of states in GNR and the localized state on the edge-attached molecule. On the other hand, upon binding of functional groups containing an odd number of rings to the nanoribbon, the electron transport is decreased by one quantum of conductance at $E = t_1$. Further analysis indicates that such functionalization affects local current and hence conductance to an extent which is governed by the behavior of the wavefunction in the lead.

We then established that the even-odd phenomenon is largely preserved when adopting higher levels of theory, *i.e.* 3NN-TB model and DFT. As compared to the simplified 1NN-TB model, however, this phenomenon is shifted in energy and spread over a larger energy window. This is a consequence of the approximate nature of the band structure obtained at the 1NN-TB level, especially at energies further away from the Fermi level. Also, we have suggested that such even-odd effect becomes less pronounced as the number of aromatic rings in the guest molecule increases.

In conclusion, we have revisited and clarified the origin of the even-odd conductance effect observed in graphene nanoribbons with armchair or zigzag edges chemically functionalized with aromatic functional groups. We have provided a detailed understanding of the interplay between the localized states on the guest molecules and the continuum of states of the hosting graphene nanoribbon, and on its role in governing the resulting electron transport. Overall, our results promote the validity of graphene nanoribbons as promising candidates for chemosensing devices, and offer a theoretical insight into the formulation of guidelines towards their realization.

4 Electronic Transport Across Quantum Dots in Graphene Nanoribbons

Success of all-graphene electronics is severely hindered by the challenging realization and subsequent integration of semiconducting channels and metallic contacts. Here, we comprehensively investigate the electronic transport across width-modulated heterojunctions consisting of a graphene quantum dot of varying lengths and widths embedded in a pair of armchair-edged metallic nanoribbons, of the kind recently fabricated *via* on-surface synthesis. We show that the presence of the quantum dot opens a width-dependent transport gap, thereby yielding built-in one-dimensional metal-semiconductor-metal junctions. Furthermore, we find that, in the vicinity of the band edges, the conductance is subject to a smooth transition from an antiresonant to a resonant transport regime upon increasing the channel length. These results are rationalized in terms of a competition between quantum-confinement effects and the coupling between the states in quantum dot and the states in the lead. Overall, our work establishes graphene quantum dot nanoarchitectures as appealing platforms to seamlessly integrate gap-tunable semiconducting channels and metallic contacts into an individual nanoribbon, hence realizing self-contained carbon-based electronic devices.

This chapter is adapted from:

Čerņevičs, K., Yazyev, O.V. and Pizzochero, M. (2020). Electronic transport across quantum dots in graphene nanoribbons: Toward built-in gap-tunable metal-semiconductor-metal heterojunctions. *Phys. Rev. B*, 102:201406(R) [pre-print: arXiv: 2006.15075]

My contribution to this work was writing the code for TB calculations, performing part of the calculations (LDOS, eigenvalues, coupling strength), analysis of the data and co-writing the paper.

4.1   Motivation

We have already mentioned in introductory Section 1.2.2 that the atomically precise bottom-up GNRs are fully defined by the selection of the precursor monomers [Cai et al., 2010] and that there has been a broad assortment of experimentally synthesized GNRs featuring diverse widths [Dong et al., 2018; Beyer et al., 2019; Yamaguchi et al., 2020], edge geometries [Abbas et al., 2014; Wang et al., 2021d] and chemical compositions [Chen et al., 2016; Liu et al., 2017; Carbonell-Sanromà et al., 2017; Hayashi et al., 2017], hosting novel physical phenomena, such as magnetism [Ribeiro et al., 2011; Li et al., 2019a; Sun et al., 2020; Pizzochero and Kaxiras, 2021, 2022], engineered topological states [Cao et al., 2017; Gröning et al., 2018; Rizzo et al., 2018; Li et al., 2021b] and induced metallicity [Rizzo et al., 2020]. More importantly, the large degree of control that has been experimentally achieved over the atomic-level features of GNRs has also sparked the opportunity to realize complex heterostructures, including two-terminal [Blankenburg et al., 2012; Cai et al., 2016; Ma et al., 2019], triple- [Sánchez-Sánchez et al., 2017; Zuzak et al., 2020], as well as hetero-junctions [Marangoni et al., 2016; Nguyen et al., 2017; Bronner et al., 2018].

Of particular interest among this rich variety of carbon-based architectures is the assembly of width-modulated armchair graphene nanoribbons. These heterojunctions have been recently fabricated either through lateral fusion of two distinct AGNR segments of different length *via* cross-dehydrogenative coupling [see Figure 4.1(a)] or following a co-deposition of two distinct precursors on metal surface, yielding armchair nanoribbons that are smoothly edge-functionalized with guest graphene quantum-dots of varying length and width [Chen et al., 2015; Wang et al., 2017; Jacobse et al., 2017; Chen et al., 2017b; Rizzo et al., 2018, 2021]. Figure 4.1(b) shows the STM image of several experimentally synthesized 7-14-7-AGNR quantum dot structures with varying lengths, while a high resolution nc-AFM image of one such structure is presented in Figure 4.1(c).

Strikingly, these heterojunctions can be seen as an extension of the AGNR nanostructures investigated in Chapter 3, where the wider central region is now extended laterally. Such nanoarchitectures may hold promise towards graphene electronics by virtue of the tunable band-gap of the constituent AGNR building-blocks [Jacobse et al., 2017] due to the width dependent electronic properties (discussed in more depth in Section 1.2.1). For example, combining N-AGNRs from the quasi-metallic $N = 3p + 2$ family with the semiconducting $N = 3p$, $N = 3p + 1$ families can result in novel integrated metal-semiconductor one-dimensional heterojunctions.

Although graphene-based quantum dots and constrictions have been previously theoretically studied [Darancet et al., 2009; González et al., 2011; Xiong and Xiong, 2011], a comprehensive picture of the electronic structure of the aforementioned width-modulated armchair graphene nanoribbons is still missing. In this chapter, we fill this gap in knowledge by systematically investigating the charge transport across graphene quantum-dots of different geometries embedded in armchair-edged graphene nanoribbons. With the help of atomistic simula-

tions, we achieve a detailed understanding of the interplay between their atomic structure and electronic transport. Importantly, we establish guidelines to assemble all-graphene electronic devices composed of a semiconducting quantum-dot channel seamlessly connected to metallic leads. Overall, our findings expedite the potential of as-synthesized graphene quantum-dots to develop complete built-in carbon-based electronic devices in one dimension.

4.2   Methodology

Our calculations are conducted at the tight-binding level, in which the Hamiltonian describing the p_z electrons takes the form of Eq. 3.1. We set the on-site potential ϵ_i to 0 eV and fix the nearest-neighbor hopping integral t_1 to 2.75 eV. The choice of resorting to the tight-binding framework instead of *e.g.* first-principles calculations is dictated by the large number of atoms considered in our realistic models (up to several thousands) and supported by the well-known satisfying description that the TB Hamiltonian provides as far as the experimentally relevant low-energy physics of graphene nanostructures is concerned.

Transport properties are calculated using the non-equilibrium Green's function formalism as presented in Section 2.5 and implemented in `Kwant` [Groth et al., 2014]. We express conductance in terms of the conductance quantum G_0 following Eq. 2.60.

4.3   Results and discussion

We consider the nanoarchitectures experimentally reported in *e.g.* [Wang et al., 2017; Jacobse et al., 2017]. Figure 4.1(d) shows a model of our width-modulated AGNRs in which a channel containing a graphene quantum-dot of width M and length L is contacted to a pair of equivalent semi-infinite leads of width N, hence giving rise to a N-$(N+M)$-N in-plane heterojunction. As is customary [Wakabayashi et al., 1999], both N and M are quantified as the number of dimer lines across the transport direction. We set $N = 5, 8, 11$ (that is, $N \in 3p + 2$) to ensure the metallic character of the leads at the adopted level of theory, whereas we extensively cover the width space of the quantum dot by choosing $5 \leq M \leq 13$. In analogy with experiments [Wang et al., 2017], we span a length interval of the quantum dot $L = n \times a_0$ ranging from 0.9 to 21.3 nm, *i.e.* corresponding to $2 \leq n \leq 50$ unit cells of lattice constant $a_0 = 4.26$ Å. The combination of the geometrical parameters N, M, and L leads to over 1300 distinct atomic structures. For each of them, we have obtained both the conductance spectrum and the electronic density of states. These results are given in the Supplemental Material[‡], which serves as an "atlas" to understand the electronic properties and further guide the design of such width-modulated AGNRs.

In the following, we identify the general trends and uncover the physical effects that govern the

---

[‡]See Supplemental Material at https://journals.aps.org/prb/supplemental/10.1103/PhysRevB.102.201406 for additional results.
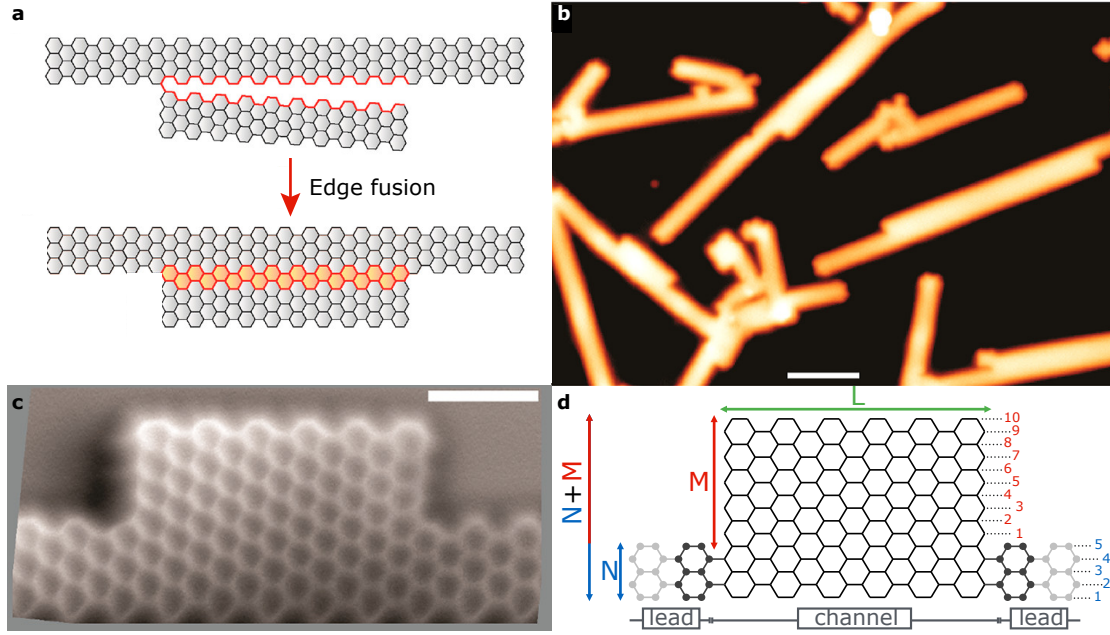
Figure 4.1: AGNR quantum dots. (a) Schematic illustration of the formation of a 14-AGNR quantum dot by edge fusion of two 7-AGNRs. (b) STM image showing several 7-14-7 quantum dot heterostructures on Au(111). Scale bar: 5 nm. (c) nc-AFM frequency shift image of a 7-14-7-AGNR heterojunction. Scale bar: 2 nm. Panels (a),(b) and (c) are adapted from [Wang et al., 2017]. (d) Atomic model of the nanostructure considered in our electron transport calculations, in which a quantum dot of varying width M (with $5 \leq M \leq 13$) and length L (with 0.9 nm $\leq L \leq$ 21.3 nm) acts as a channel region embedded in a pair of metallic N-AGNRs leads (with $N = 5, 8, 11$), giving rise to a N-$(M + N)$-N-AGNRs heterojunction.

electronic transport across these heterojunctions. Without loss of generality, we mainly focus on structures with $N = 5$ and $M = 5, 6, 7$ and increasing L. In Figure 4.2, we show the atomic structures of 5-10-5, 5-11-5, and 5-12-5-AGNR heterojunctions along with the evolution of their conductance spectra with the length of the quantum dot. Due to the electron-hole symmetry encoded in the employed tight-binding Hamiltonian, only positive energies are given. Irrespectively of the width of the quantum dot, comparable changes are observed in the conductance spectra upon lengthening the channel region. Specifically, conductance peaks sharpen, become denser, and step in energy towards the Fermi level. From a qualitative point of view, this situation is analogous to that of a particle encountering a double (symmetric) rectangular potential barrier, when the separation between the barriers is widened.

On a more rigorous ground, in the vicinity of the band edge, we can identify a *smooth* transition between two distinct transport regimes that emerge upon increasing the length of the graphene quantum dot. In Figure 4.3, we show the conductance spectrum and the density of states of the three selected heterojunctions mentioned above containing a short [Figure 4.3(a)], intermediate [Figure 4.3(b)], and long [Figure 4.3(c)] quantum dot. Also shown are the energy levels of the corresponding finite-size *isolated* $(M + N)$-AGNR of length L. On the one hand,
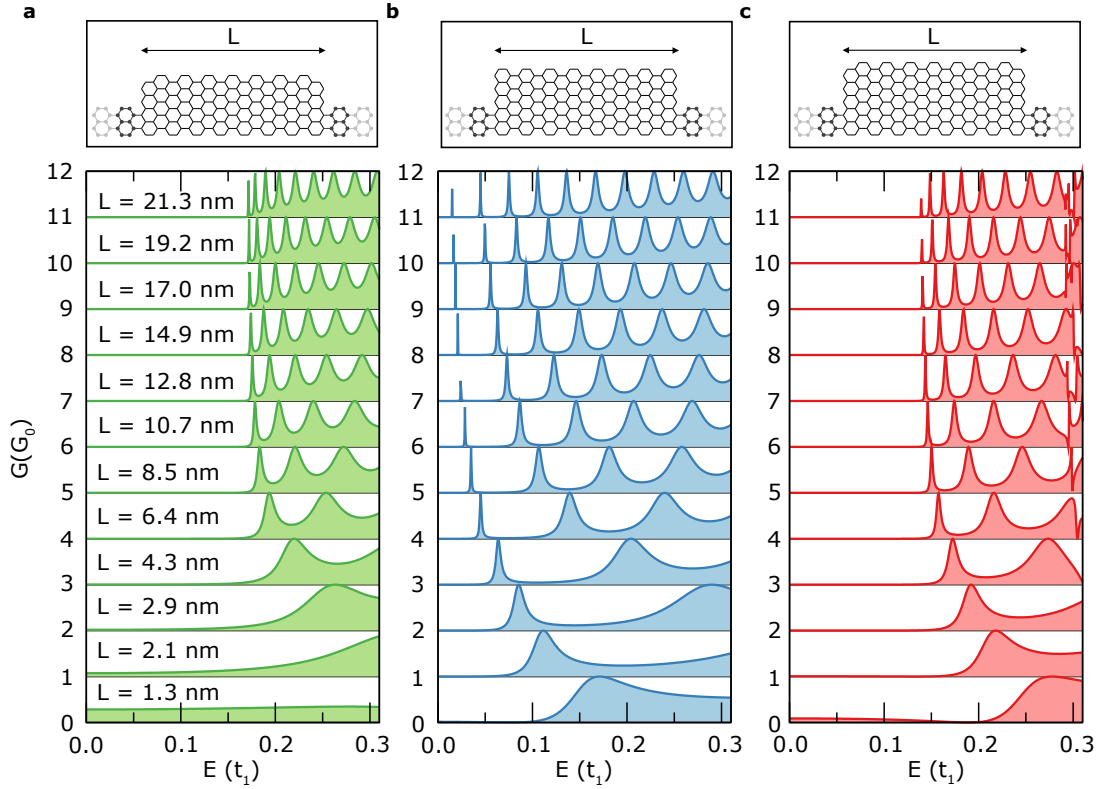
Figure 4.2: Atomic structure (upper panels) and conductance spectrum (lower panels) of (a) 5-10-5, (b) 5-11-5, and (c) 5-12-5-AGNR heterojunctions for increasing lengths of the quantum dot L, as indicated. Fermi level level is set to zero.

the introduction of a short (*e.g.* approximately $L < 5$ nm for 5-10-5-AGNR) quantum dot preserves the metallic character, substantially diminishes the conductance at the band edge, and gives rise to asymmetric Fano lineshape whose minimum is located in energy quite far from the level associated with the corresponding isolated dot [Mendoza et al., 2008; Deng et al., 2014]. Such antiresonances closely resemble those previously observed in the case of graphene nanoribbons upon functionalization with a *p*-polyphenyl or polyacene functional groups to the edge [Čerņevičs et al., 2020b]. On the other hand, the introduction of a long (*e.g.* approximately $L > 10$ nm for 5-10-5-AGNR) quantum dot turns the electronic transport into a resonant tunneling regime, where a finite transport gap opens and conductance peaks discretize, assume a unitary value, and eventually match in energy the spectrum of the isolated dot. These two transport regimes are bridged by an intermediate situation, where both resonant and antiresonant features coexist, though at different energy scales [Xiong and Xiong, 2011].

We suggest that the origin of the transition crossing the two transport regimes traces back to the different coupling strength between the states of the channel and those of the lead that occurs when moving from short to long quantum dots. This is further supported by the evolution of the local density of states (LDOS) at the band edge with the length of the quantum
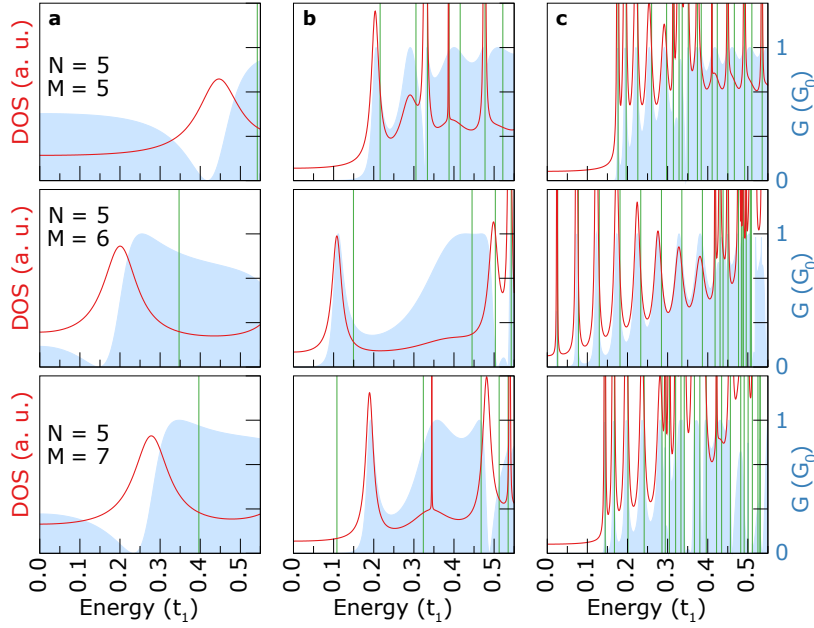
Figure 4.3: Selected representative density of states of the central channel (red lines), transmission spectrum (blue area), and energy levels of the isolated graphene quantum dot of width $(M + N)$ (green lines) corresponding to the (a) antiresonant ($L = 0.85$ nm), (b) intermediate ($L = 5.1, 3.0, 2.1$ nm for top, middle, and bottom panel, respectively), and (c) resonant tunneling ($L = 12.8$ nm) electronic transport regimes discussed in the text for $N = 5$ and $M = 5$ (top panels), $M = 6$ (middle panels), and $M = 7$ (bottom panels). Fermi level is set to zero.

dot, as displayed in Figure 4.4(a). For short quantum dots, the LDOS localizes at the ends, thereby offering electronic states that are available to interact with those of the leads, hence promoting a strong coupling between the states in channel and the leads. Oppositely, long quantum dots host a LDOS that resides in the inner region solely, hence behaving rather independently from the contacts. In addition, we remark that, due to the different behavior in the antiresonant and resonant regimes, the difference in energy between conductance peaks and corresponding levels of the isolated quantum dot [δ(E)] can be utilized as a suitable descriptor to monitor the transport crossover. This is indeed shown in the inset of Figure 4.6(f), where it can be noticed that the increase of L rapidly decreases δ(E), as we further detail below.

This argument holds for all topologically trivial heterojunctions, but at first glance seems to fail for junctions that display topologically protected interface states. In Figure 4.4(b) and (c), we compare the electronic properties of two structurally similar heterojunctions but, contrary to the 5-9-5-AGNR heterostructure, the 5-11-5-AGNR heterostructure is built from a pair of AGNRs belonging to different topological classes, i.e., that feature topological invariant $Z_2 = 1$ (5-AGNR) and $Z_2 = 0$ (11-AGNR), hence exhibiting a topologically protected interface state.
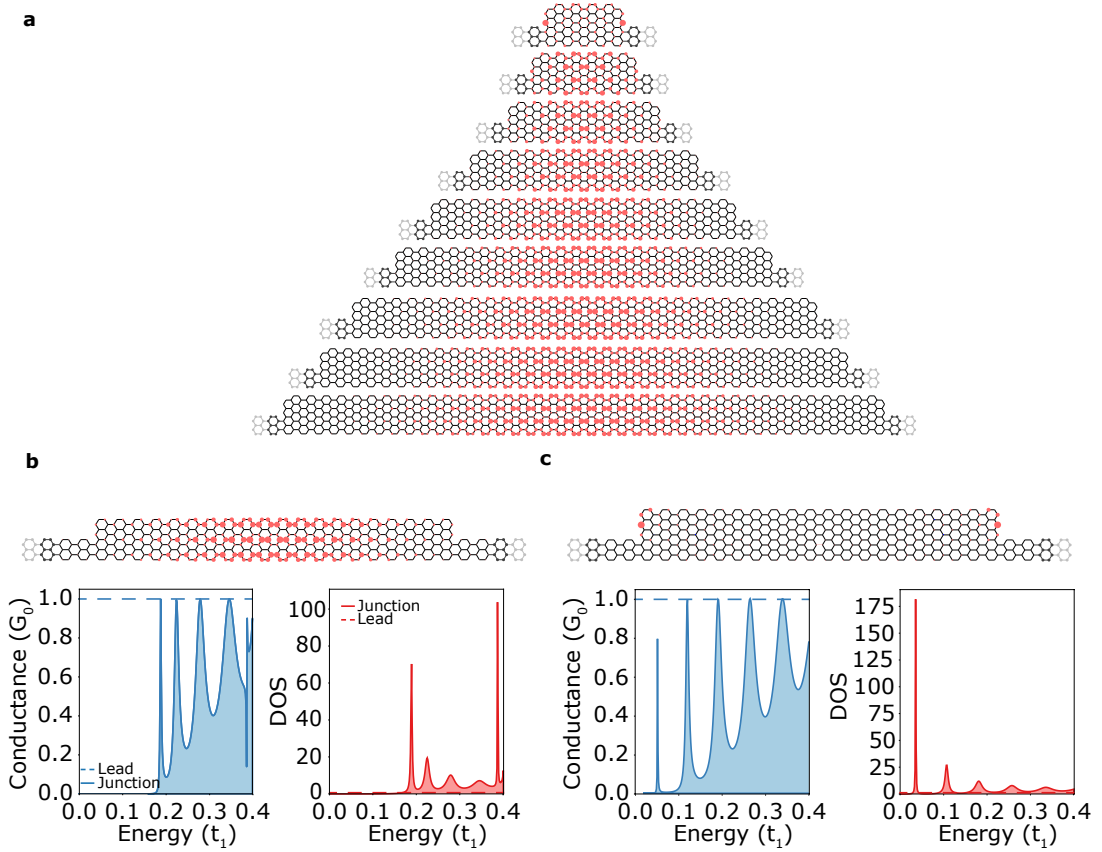
Figure 4.4: (a) Evolution of the local density of states at the band edge with L in the 5-10-5-AGNR heterojunction. Local density of states, conductance spectrum and density of states of the (a) 5-9-5-AGNR and (b) 5-11-5-AGNR heterostructures. The LDOS corresponds to the energy at which the first peak in the conductance spectrum occurs.

The Z_2 invariant for an N = odd armchair ribbon can be expressed as [Cao et al., 2017]

$$Z_2 = \frac{1 + (-1)^{[\frac{N}{3}] + [\frac{N+1}{2}]}}{2}, \tag{4.1}$$

while for N = even we have

$$Z_2 = \frac{1 - (-1)^{[\frac{N}{3}] + [\frac{N+1}{2}]}}{2}. \tag{4.2}$$

Although the topologically protected state in the 5-11-5-AGNR heterojunction exhibits a strong localization at the interface between the channel and the lead in contrast to topologically trivial junctions, our results indicate that no additional DOS or conductance peaks associated with the interface state arise. Furthermore, if we disregard the high LDOS concentrated at the interface of topological junctions, the central part of the GNR will recover the LDOS pattern observed in topologically trivial junctions, similar to Figure 4.4(a) and (b). Therefore, following the same principles for transition from antiresonant to resonant transport with increasing L. In addition, as no new conductance peaks are observed, the transport gaps, on which we
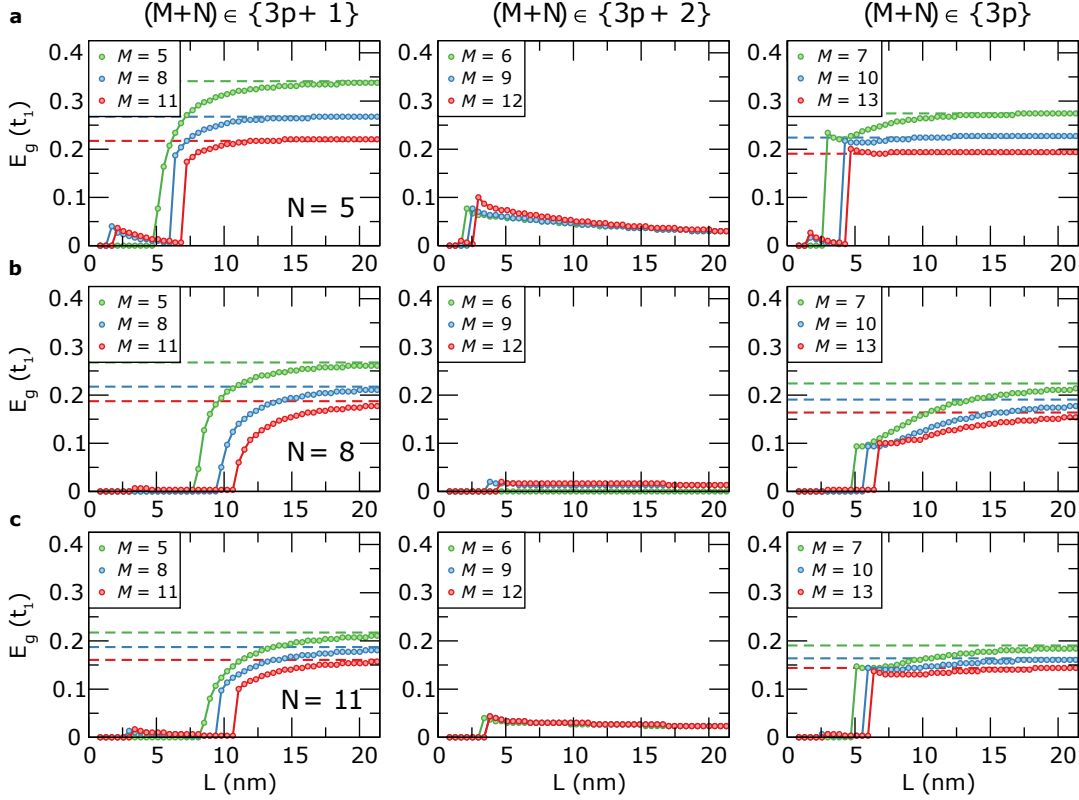
Figure 4.5: Evolution of the transport gap E_g in N-$(M + N)$-N-AGNR heterojunctions as a function of the length of the quantum dot L embedded in a lead of (a) $N = 5$, (b) $N = 8$, and (c) $N = 11$ and $5 \leq M \leq 13$. Dashed horizontal lines correspond to the band-gap of the corresponding periodic $(M + N)$-AGNR.

focus in this chapter, are also not sensitive to the topological interface states.

The weakening of the channel-to-lead states coupling induced by the increase of L and the accompanying transition between the two transport regimes discussed above have dramatic consequences on the transport gap. In Figure 4.5, we give such gap – as extracted from the conductance spectra – for all the heterojunctions considered in this work, featuring $N = 5$ [Figure 4.5(a)], $N = 8$ [Figure 4.5(b)], and $N = 11$ [Figure 4.5(c)]. Irrespective of the width $(M + N)$ of the channel, the introduction of short quantum dots and the ensuing antiresonant transport regime either retain the metallic character or open only a tiny transport gap. However, as the length of the quantum dot is increased and the resonant tunneling regime is reached, a substantial transport gap opens and eventually converges to that of the periodic $(M + N)$-AGNR. This implies that the channel in the considered structures featuring either $(M + N)$ $\in 3p$ or $(M + N) \in 3p + 1$ acquires semiconducting character [Jacobse et al., 2017], with a finite transport gap that can be engineered through the modulation of the quantum-dot width. This finding indicates that these heterojunctions feature a semiconducting channel based on a graphene quantum-dot that is is seamlessly contacted to a pair metallic leads, thereby
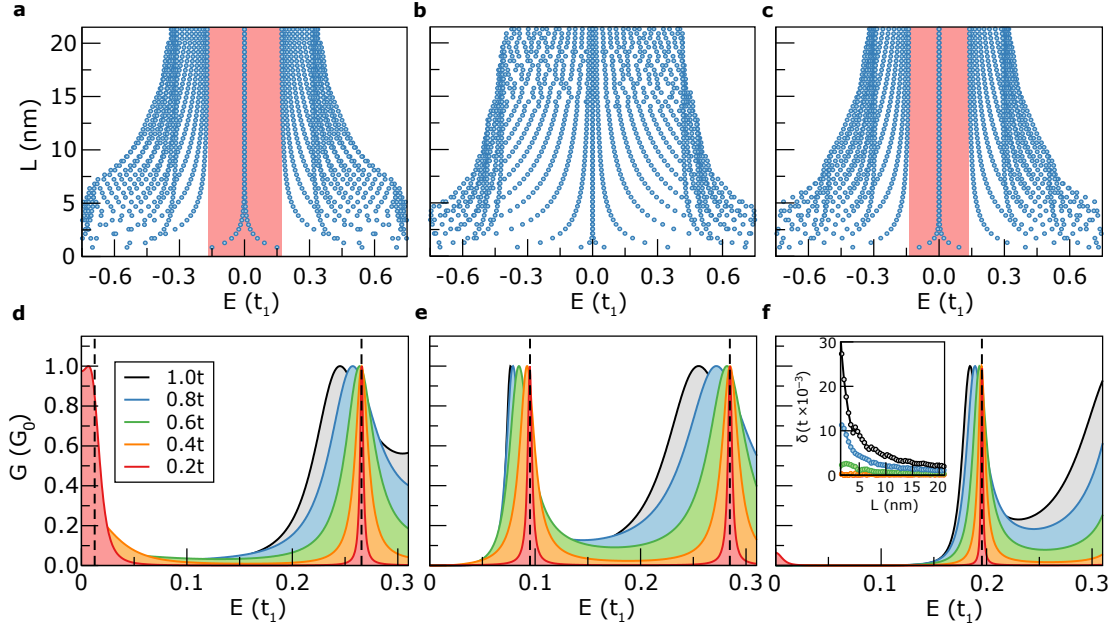
Figure 4.6: Energy spectra of finite-size (a) 10-, (b), 11-, and (c) 12-AGNR of a increasing length L. Red shaded area indicate the energy band-gap of the corresponding periodic AGNR. Evolution of the transmission spectrum with the hopping integral between the lead and the channel in (d) 5-10-5, (e) 5-11-5, and (f) 5-12-5-AGNR heterojunctions. The inset in panel (f) shows the energy shift between the energy levels of the isolated 12-AGNR and the resonant peaks in the transmission spectrum of the 5-12-7-AGNR junction as a function of L.

giving rise to complete all-carbon devices built into a single armchair graphene nanoribbon. Contrarily, the transport gap of heterojunctions featuring a quantum dot of width $(M + N) \in 3p + 2$ vanishes with L.

The results reported in Figure 4.5, in which we show that the energy gap *increases* with the length of the quantum dot, may appear counterintuitive on the basis of quantum-confinement effects solely, according to which one should expect the gap to *decrease* with the length of the nanostructure [Talirz et al., 2019]. In Figure 4.6(a)−(c), we present the energy spectra of finite-size AGNR of increasing length (notice that the zero-energy modes originate from the zigzag terminations and do not contribute to the electronic transport as they are selectively localized on one sublattice, hence effectively decoupled from the other lead). As expected, we observe that the energy gap decreases as the length of the AGNR increases, apparently at odds with the findings of Figure 4.5. However, we remark that another physical effect is operative and plays a central role in modulating the transport-gap width when the AGNR acts as a quantum dot. This corresponds to the coupling between the quantum dot states(channel) and the continuum of states in the semi-infinite AGNRs (lead) [Vergés et al., 2018], which in turn is very pronounced for small values of L, as we discussed above. In order to single out the impact of such coupling on the conductance spectrum, for the sake of illustration we gradually decrease the hopping integral t_1 between the atoms connecting the channel to

the leads and obtain the resulting transmission spectrum in Figure 4.6(d)−(f). Two distinct, though closely related, effects can be observed upon weakening the channel-to-lead coupling. Firstly, the conductance peaks step away from the Fermi level and approach the energy values of the isolated quantum dot AGNR, as shown in the inset of Figure 4.6(f). As the hopping integral decreases, this energy shift $\delta(E)$ vanishes, irrespective of the value of L considered within the antiresonant transport regime as well. Second, the broadening of the peaks in the conductance spectra is strongly reduced, such that the tails that were extending towards the Fermi level shrink, with a metal-to-semiconductor transition taking place even for short L. Hence, the emergence of the two transport regimes (antiresonant *vs.* resonant) and the consequent transport gaps (metallic *vs.* semiconducting) are found to be dominated by a subtle competition between the energy gap of the isolated quantum dot and the broadening of the conductance peaks that occurs upon contacting the channel to the leads.

4.4   Summary and conclusions

We have investigated the electronic transport in width-modulated heterojunctions consisting of graphene quantum-dots embedded in metallic armchair nanoribbon leads, similar to those recently synthesized *via* bottom-up approaches. We have considered over a thousand different configurations of varying geometries and determined their charge transport properties through a combination of atomistic tight-binding and non-equilibrium Green's functions calculations. The emerging picture indicates that the conductance is found to be dominated by the length scale of the quantum dot, which induces a smooth transition from a metallic antiresonant transport regime (similar to the one observed in Chapter 3) to a semiconducting resonant regime. Upon exceeding a critical length of the quantum dot – the value of which is governed by the interplay between the intrinsic band-gap and the strength of the coupling between the states in quantum dot and the lead – a width-dependent transport gap opens, thereby giving rise to built-in one-dimensional metal-semiconductor-metal junctions.

To conclude, our work demonstrates that the experimentally realized functionalization of metallic AGNRs with graphene quantum-dots offer an effective route to *directly* integrate a semiconducting channel into metallic electrical contacts while preserving the advantageous fine tunability of the AGNR band gap. Overall, our findings envisage graphene quantum-dot nanoarchitectures as self-contained electronic devices encoded in a sole graphene nanoribbon.

Defects in Graphene Nanoribbons Part II

5 Electronic Transport Across "Bite" Defects in Graphene Nanoribbons

On-surface synthesis has recently emerged as an effective route towards the atomically precise fabrication of graphene nanoribbons of controlled topologies and widths. However, whether and to which degree structural disorder occurs in the resulting samples is a crucial issue for prospective applications that remains to be explored. In this chapter, we show experimentally visualized ubiquitous missing benzene rings at the edges of 9-atom wide armchair nanoribbons that form upon cleavage of phenyl groups of precursor molecules. These defects are referred to as "bite" defects. First, we address their density and spatial distribution on the basis of scanning tunnelling microscopy and find that they exhibit a strong tendency to aggregate. Next, we explore their effect on the quantum charge transport from first-principles calculations, revealing that such imperfections substantially disrupt the conduction properties at the band edges. Finally, we generalize our theoretical findings to wider nanoribbons in a systematic manner, hence establishing practical guidelines to minimize the detrimental role of such defects on the charge transport. Overall, our work portrays a detailed picture of "bite" defects in bottom-up armchair graphene nanoribbons and assesses their effect on the performance of carbon-based nanoelectronic devices.

This chapter is adapted from:

My contribution to this work was conceiving the original idea, performing TB calculations, analysis of the data and co-writing the paper.

---

*These authors contributed equally to this work

5.1   Motivation

On-surface synthesis [Cai et al., 2010] has recently emerged as an effective route towards the atomically precise fabrication of graphene nanoribbons of defined topologies and widths. However, even this bottom-up approach does not produce entirely perfect GNRs as random cross-couplings [Dienel et al., 2015; Han et al., 2020] and even edge defects [Costa et al., 2018; Talirz et al., 2017; Teeter et al., 2019] have been observed experimentally. Furthermore, defects are considered to be a pivotal issue for potential applications in nanoelectronics, yet both the prevalence and the role on the electronic properties of GNRs remain to be explored.

Owing to their mechanical robustness, long-term stability under ambient conditions, easy transferability onto target substrates [Borin Barin et al., 2019], fabrication scalability [Di Giovannantonio et al., 2018], and suitable band-gap width [Talirz et al., 2017], 9-atom wide armchair graphene nanoribbons (9-AGNRs) have emerged among the most promising candidates to be integrated as active channels in field-effect transistors. In particular, among the graphene-based electronic devices realized so far, 9-AGNR-FETs are those displaying the highest performance, with 1 μA on-current and 10^5 on-off current ratio at $V_{\mathrm{D}} = -1$ V [Llinas et al., 2017]. Although the detrimental effect of defects on electronic devices is well known, current GNR-FETs are limited by significant Schottky barriers at the contacts. Which in turn has prevented an experimental characterization of the impact of GNR edge defects on device performance. In fact, to which extent structural disorder is present in atomically precise GNRs is an issue that has not been settled to date, despite its crucial consequence on the resulting devices.

Here, we combine experimental and theoretical efforts to investigate defects in bottom-up armchair graphene nanoribbons, with a special focus on 9-AGNRs. By means of scanning-tunneling and atomic-force microscopies, we identify missing benzene rings at the edges as abundant defects, and additionally underly their effect on the charge transport on the basis of extensive first-principles calculations. Overall, this chapter offers an unprecedented view on the nature of the structural disorder in bottom-up fabricated armchair graphene nanoribbons, which is instrumental to the realization of novel carbon-based electronic devices.

5.2   Methodology

First-principles calculations have been performed within the density-functional theory framework, as implemented in SIESTA [Soler et al., 2002]. We treated the exchange and correlation effects under the generalized gradient approximation of Perdew, Burke, and Ernzerhof [Perdew et al., 1996a]. Core electrons were described by separable norm-conserving pseudopotentials [Troullier and Martins, 1991], while the Kohn-Sham wavefuctions of valence electrons were expanded in a linear combination of atomic orbitals of double-ζ polarization (DZP) quality. Real space integrations have been performed with a 450 Ry mesh cutoff. The Brillouin zone was sampled with the equivalent of $21 \times 1 \times 1$ k-mesh per unit cell in all cases but transport

calculations, for which it was increased to $400 \times 1 \times 1$. We optimized the atomic coordinates until the residual force acting on each atom converges to 0.01 eV/Å. We introduced single "bite" defects in otherwise pristine $7 \times 1 \times 1$ supercells of N-AGNR of increasing widths ($6 \leq N \leq 26$), containing from 112 (6-AGNR) to 392 atoms (26-AGNR). Pairs of "bite" defects in 9-AGNR are modelled in a $14 \times 1 \times 1$ supercell containing 308 atoms. Replicas along non-periodic directions are separated by a vacuum region larger than 10 Å.

We also relied on a tight-binding model Hamiltonian with one p_z orbital per carbon atom with the help of KWANT package [Groth et al., 2014]. The Hamiltonian is expressed in Eq. 3.1. As proposed by Hancock *et al.* [Hancock et al., 2010], we included first-, second-, and third-nearest-neighbor hopping integrals with corresponding values of −2.70 eV, −0.20 eV, and −0.18 eV, respectively, while on-site terms are set to 0 eV. This tight-binding Hamiltonian yields results in excellent accord with density-functional theory calculations, as we have shown in Figure 2.1(b).

In order to investigate the quantum transport properties of armchair graphene nanoribbons, Hamiltonians obtained from density-functional theory and tight-binding calculations were next combined with the non-equilibrium Green's function formalism [Section 2.5], as implemented in `Transiesta` [Papior et al., 2017] and `Kwant` [Groth et al., 2014], respectively. $G(E)$ is expressed in terms of the conductance quantum G_0 following Eq. 2.60.

5.3 Results and discussion

5.3.1 Experimental characterization of "bite" defects in 9-AGNRs

We synthesize 9-AGNRs by relying on the coupling and subsequent cyclodehydrogenation of 3',6'-di-iodine-1,1':2',1"-terphenyl (DITP) precursor molecule on the Au (111) surface [Di Giovannantonio et al., 2018]. A representative STM image overviewing the resulting products is shown in Figure 5.1(a). It can be clearly observed that 9-AGNRs invariably exhibit missing atoms at the edges as a predominant type of disorder. We inspect the atomic structure of such defects through non-contact atomic-force microscopy imaging, as displayed in Figure 5.1(b). Our result reveals that these defects – that we dub "bite" defects – consist of a missing benzene ring, and we estimate their density to 0.19 ± 0.10 nm^{-1}. Such "bite" defects originate from the C-C bond scission that occurs during the cyclodehydrogenation step of the reaction [Talirz et al., 2017], as we show in Figure 5.1(e). Similar defects have also been observed in chevron-edged GNRs synthesized from 6,11-dibromo-1,2,3,4-tetraphenyltriphenylene precursors, and their formation was correlated with the cyclization of multiple flexible phenyl rings against each other [Cai et al., 2010].

Furthermore, we study the spatial distribution of "bite" defects. In Figure 5.1(c) and (d), we give the pair distribution function (*i.e.,* the normalized frequency of occurrence over a wide interval of relative distances) of "bite" defects forming either at the same edge [Figure 5.1(c)] or at opposite edges [Figure 5.1(d)]. A representative STM image of each of the two
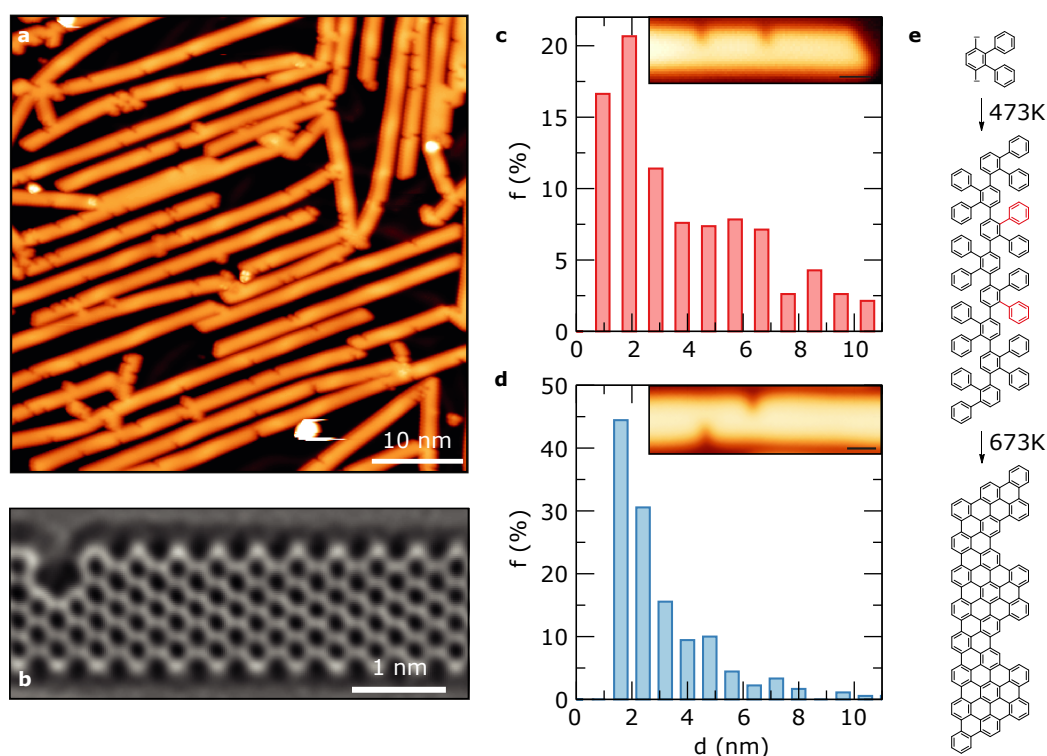
Figure 5.1: STM and NC-AFM characterization of 9-AGNRs on Au(111). (a) STM topography image of 9-AGNRs (LHe, −1.5 V, 0.01 nA). Notice the ubiquitous presence of missing atoms at the edges. (b) Laplace-filtered NC-AFM image acquired with a CO-functionalized tip (0.01 V, 0.002 nA) of a "bite" defect in 9-AGNR. Scale bar is 1 nm. (c,d) Positional correlation analysis of "bite" defects in 9-AGNRs, *i.e.* normalized frequency of occurrence (f) of relative distance between "bite" defects (d) forming at the same edge (c) or opposite edges (d). Insets show STM images of representative configuration of defects pair. (e) Reaction scheme for the on-surface synthesis of 9-AGNR via surface-assisted dehalogenation and polymerization, followed by cyclohydrogenation. Highlighted in red are the phenyl rings that undergo C-C scission during the dehydrogenation step, resulting in the formation of "bite" defects.
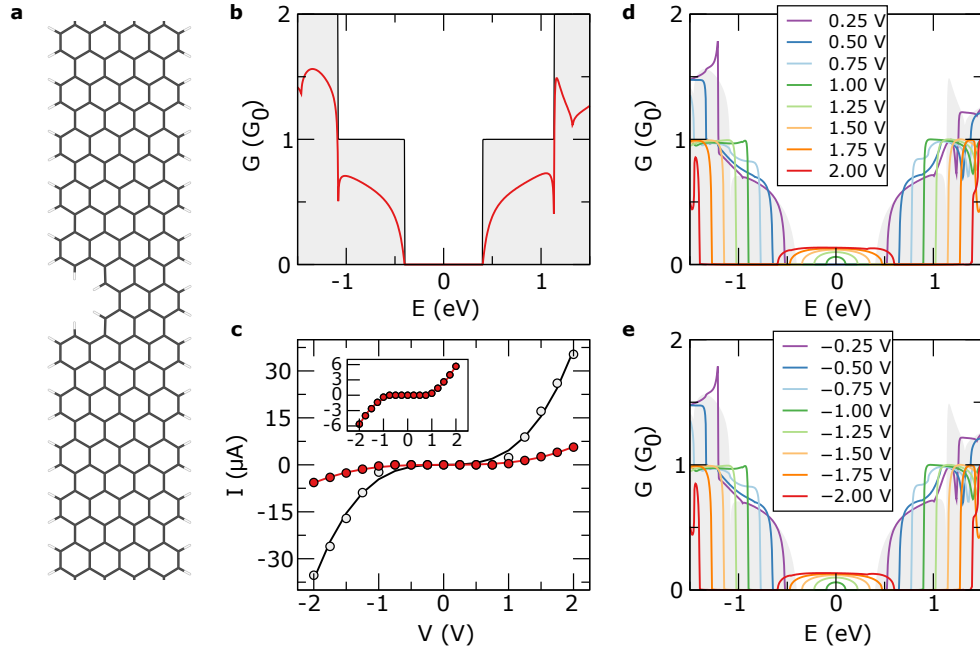
Figure 5.2: (a) Atomic structure of a "bite" defect in 9-AGNR. (b) Zero-bias conductance spectra of pristine (grey) and defective (red) 9-AGNR, the latter hosting a "bite" defect. (c) I-V characteristics of pristine (grey) and defective (red) 9-AGNR. Circles indicate results of first-principles calculations while solid lines are the fit to the Simmon's formula in to the intermediate-voltage regime, $I \propto (V + V^3)$. Evolution of the conductance in defective 9-AGNR under (d) positive and (e) negative bias voltages with respect to the zero-bias conductance (grey), with $0.25 \text{ eV} \leq |V| \leq 2.00 \text{ eV}$.

configurations is also shown in the corresponding insets. Our analysis demonstrates that "bite" defects strongly tend to agglomerate within approximately 2 nm, irrespective of whether the same or opposite edges are considered. Additionally, we found that the number of defects forming at the same edge is double than that forming at opposite edges, indicating that an edge selectivity is operative. Overall, we observe that "bite" defects preferentially form close to each other at the same edge of 9-AGNRs.

5.3.2 Theoretical investigation of "bite" defects in 9-AGNRs

With this systematic experimental exploration of "bite" defects in armchair graphene nanoribbons at hand, we next address their effect on the quantum charge transport by combining density-functional theory calculations with non-equilibrium Green's function technique. We start considering a single defect in 9-AGNR, the atomic structure of which is displayed in Figure 5.2(a). In Figure 5.2(b), we show the zero-bias conductance spectrum of a defective 9-AGNR, and additionally compare our result with that of the pristine nanoribbon that shows ideal conductance quantization. It is found that the introduction of a "bite" defect leads to a pronounced decrease of the transmission at the band edges. The transmission profiles are
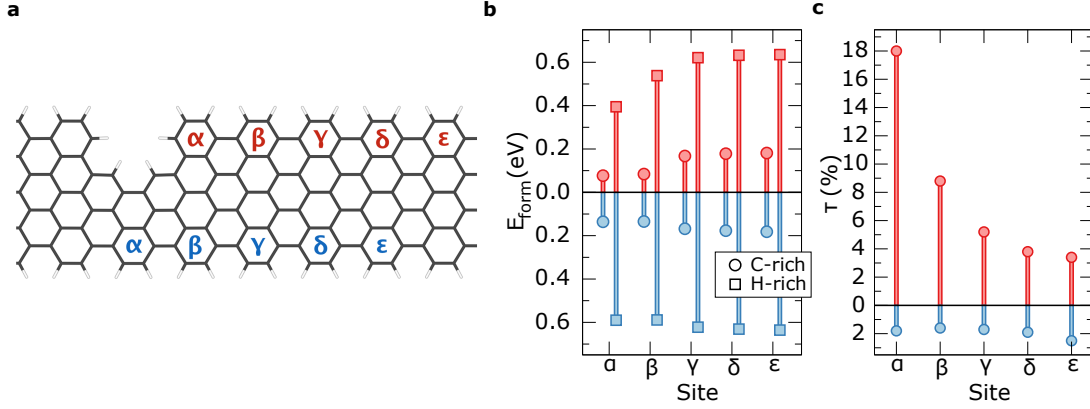
Figure 5.3: (a) Atomic structure of a single "bite" defect in 9-AGNR, along with the lattice sites at which the introduction of a second "bite" defect is introduced. (b) Formation energies of a pair of "bite" defects forming at the sites given in panel (a) under C-rich and H-rich conditions, with defects forming at the same (opposite) edge(s) given in red (blue). (c) Evolution of the τ descriptor [given in Eq. (5.1)] for pair of "bite" defects forming at the lattice sites given in panel (a), either at the same edge (red) or opposite edges (blue).

very similar at the edges of both the valence and conduction bands, but the electron-hole asymmetry becomes more pronounced at higher energies. In order to quantify the conductance suppression effect, we introduce a descriptor, τ, which estimates the fraction of the conductance which is preserved in the vicinity (δE) of the valence band maximum (VBM) and conduction band minimum (CBM) upon the defect formation as

$$\tau = \frac{\int_{\text{VBM}-\delta E}^{\text{CBM}+\delta E} G_{\text{d}}(E)}{\int_{\text{VBM}-\delta E}^{\text{CBM}+\delta E} G_{\text{p}}(E)} dE, \tag{5.1}$$

with $G_{\text{p}}(E)$ and $G_{\text{d}}(E)$ being the conductance of the defective and pristine armchair graphene nanoribbons, respectively. Here and below, we assume $\delta E = 0.10$ eV and find $\tau = 26\%$, thus indicating a considerable reduction of the conductance due to the presence of a "bite" defect at the edge of 9-AGNRs. We have explicitly verified that the values of τ obtained are rather insensitive to the choice of δE.

We extend our investigation through the determination of the charge transport properties under finite bias voltages. Figure 5.2(c) compares the I-V characteristics of a 9-AGNR with and without a "bite" defect. In both cases, currents arise when the applied bias voltage exceeds in magnitude the width of the band-gap (~1 eV at the adopted level of theory). Within this regime, zero-energy contributions emerge in the conductance spectra shown in Figs. 5.2(d) and (e), hence signalling the enhancement of the tunnelling probability induced by the increase of the bias voltage. The current grows with the applied bias voltage following a nearly cubic scaling, as supported by the excellent agreement between the results of our calculations and the fit to the Simmon's formula appropriate to the intermediate-voltage range $I \propto (V + V^3)$ [Simmons, 1963a,b], as displayed in Figure 5.2(c). The sign of the applied bias
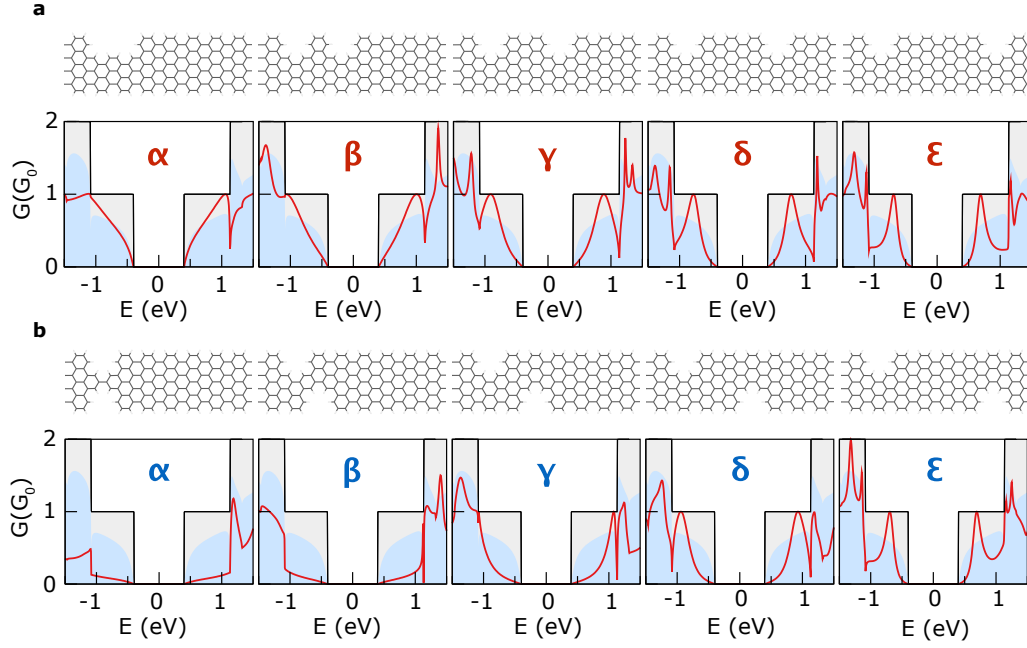
Figure 5.4: Conductance spectra of pairs of "bite" defects (red) forming at (a) the same edge and (b) opposite edges, labeled according to Figure 5.3(a). Upper panels show the atomic structure of the defects configuration considered in each case. Also given for comparative purposes are the conductance spectra of 9-AGNR either in the pristine case (grey) and hosting a single "bite" defect (light blue).

voltage is found to be irrelevant for shaping the evolution of both the current [Figure 5.2(c)] and conductance [Figs. 5.2(d) and (e)], as a consequence of the electron-hole symmetry which is largely retained in a wide energy interval in the defective lattice. The main difference in the I-V characteristics of pristine and defective 9-AGNR traces back to the current intensities, which are found to be lowered by one order of magnitude upon the formation of a "bite" defect. Overall, our findings clearly pinpoint the detrimental role that "bite" defects play on the electronic transport properties of 9-AGNRs.

We then address the formation of pairs of "bite" defects, either at the same edge or at the opposite edges of the nanoribbon, of the kind shown in the insets of Figure 5.1(c) and (d). The configurations considered are presented in Figure 5.3(a), and consist in introducing a second defect at increasing distances (up to 1 nm) from the first defective site. We assess the relative stability of "bite" defects through the determination of their formation energy E_{form}, which is the primary quantity of interest when thermodynamic equilibrium prevails. As graphene nanoribbons are binary compounds, the introduction of defects changes the nominal stoichiometry, thus rendering E_{form} a linear function of the chemical potential μ of the constituent elements. The formation energy reads

$$E_{\text{form}}(\mu) = E_{\text{d}} - E_{\text{p}} - n_{\text{H}}\mu_{\text{H}} + n_{\text{C}}\mu_{\text{C}}, \tag{5.2}$$
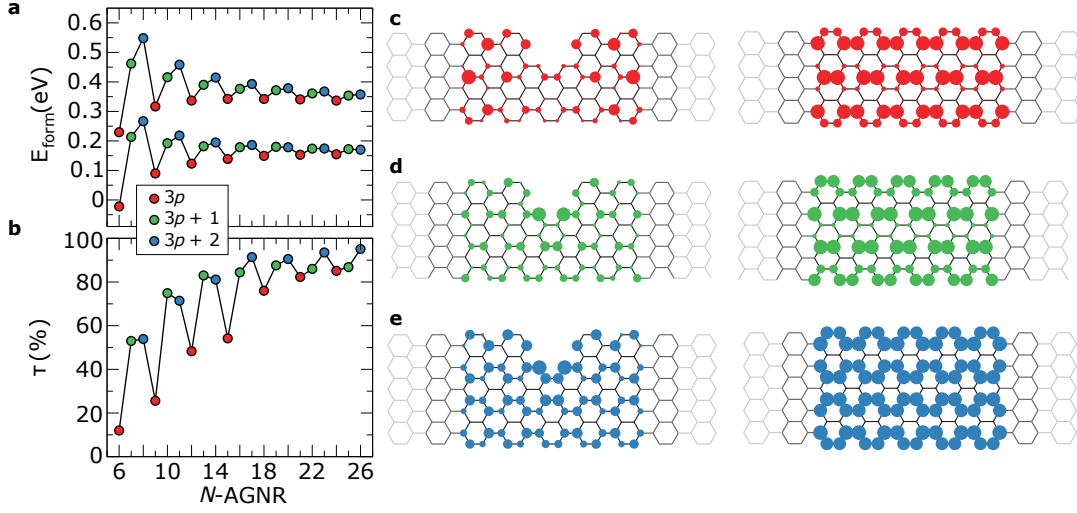
Figure 5.5: (a) Formation energy and (b) τ of a single "bite" defect in armchair graphene nanoribbons as a function of the increasing width N. Local density of states 0.05 eV below the valence band edge of defective (left panels) and pristine (right panels) armchair nanoribbons in (c) 9-, (d) 10-, and (e) 11-AGNR, as obtained at the tight-binding level of theory.

with E_d and E_p being the total energies of the defective and pristine models, respectively, n_H (n_C) the number of added (removed) H (C) atoms required to create the defect, while μ_C and μ_H are the corresponding chemical potentials. As usual, we assume that C and H are in thermal equilibrium with armchair graphene nanoribbons of general formula C_xH_y through the equality $\mu_{C_xH_y} = x\mu_C + y\mu_H$, where graphene and molecular hydrogen are assumed to be the reference systems for the determination of the chemical potential reservoirs. In Figure 5.3(b), we present the formation energy of pairs of "bite" defects. Our calculations indicate that their stability is enhanced when two defects are in proximity to each other (that is, sites α and β), with the formation energy attaining the lowest value when the second defect forms at nearest-neighboring site (α) at the same edge. In contrast, when the distance between the two defects is larger than ~9 Å (i.e., sites γ, δ, ϵ), E_{form} reaches its maximum and remains practically constant. Comparison of the results in Figure 5.3(b) with twice the formation energy of a single "bite" defect (0.64 eV and 0.16 eV in H-rich and C-rich conditions, respectively), suggests that, under thermodynamic equilibrium, "bite" defects exhibit a tendency to aggregate at shortest distances (positions α and β), but the interaction is negligible at larger distances. From a qualitative point of view, this theoretical result parallels the experimental analysis of Figure 5.1, although formation energies reflect the stability of defects under equilibrium, whereas the synthesis of 9-AGNRs (and of the defects emerging therein) is largely governed by the kinetic control.

In Figure 5.4, we overview the conductance spectra of pairs of "bite" defects in each of the ten configurations considered. In all cases, the conductance in the vicinity of the band edges is further reduced as compared to that of the nanoribbon containing either a single or no "bite" defect. However, the degree to which this reduction occurs is largely controlled by the relative
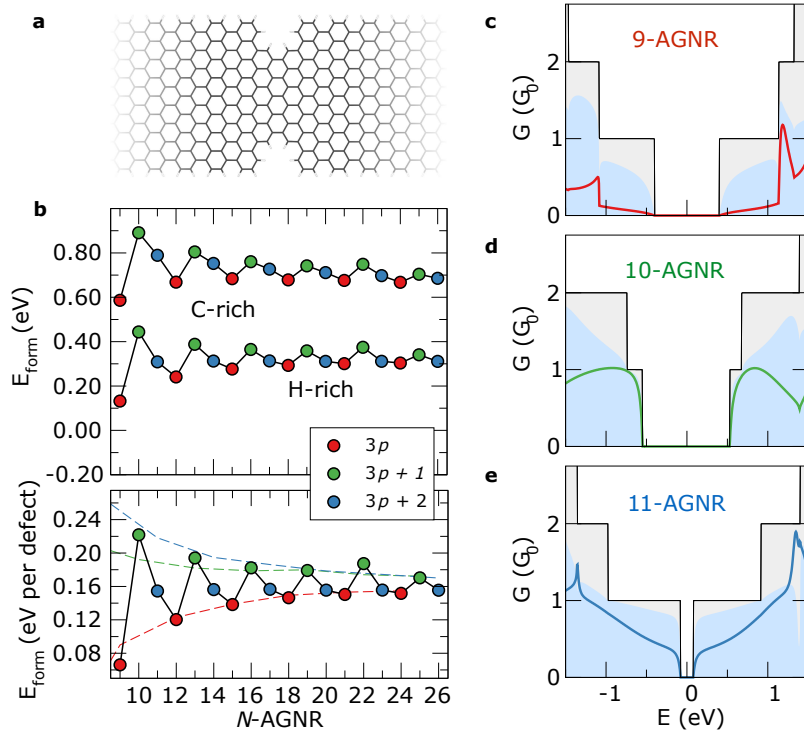
Figure 5.6: (a) Atomic structure of a coaxial "bite" defect in an armchair graphene nanoribbon (AGNR). (b) Upper panel: formation energy (E_{form}) in both C-rich and H-rich conditions of the chemical potential of coaxial double "bite" defects as a function of increasing width (N) of the hosting AGNR. Lower panel: Evolution of the formation energy per number of defects with N for coaxial double "bite" defects in the 3p (red), 3p+1 (green), and 3p+2 (blue) AGNR families. Conductance spectra of (c) 9-AGNR, (d) 11-AGNR, and (e) 12-AGNR, as representative members of the 3p, 3p+1, and 3p+2 families, respectively, containing a coaxial double "bit" defect (colored lines). Also superimposed for comparative purposes are the conductance spectra of the corresponding nanoribbon hosting single (blue area) or no (grey area) "bite" defects.

position of the defects. This can be clearly observed in Figure 5.3(c), in which we report the values of the descriptor τ given in Eq. (5.1) for pairs of "bite" defects. Depending on whether the defects are introduced at the same edge or at opposite edges, two distinct situations are identified. On the one hand, for defects forming at the same edges, τ decreases as the distance between defects increases. Specifically, the formation of a second defect at the α site preserves the largest amount of conductance (τ = 18%, only slightly lower than the value obtained in the single "bite" defect case discussed above, τ = 26%). It is worth noticing in this context that this configuration is the thermodynamically stable one, see Figure 5.3(b). On the other hand, the formation of a pair of defects at opposite edges yields an almost complete suppression of the conductance in the vicinity of the band edges ($\tau \approx 2\%$), with τ being insensitive to the specific defects configuration.
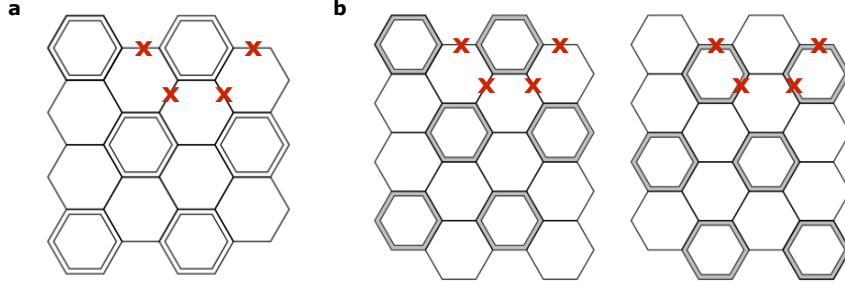
Figure 5.7: Representative Clar's formula of armchair graphene nanoribbons featuring (a) $N = 3p$ and (b) $N \neq 3p$. The red crosses indicates the bonds that have to break in order to create the "bite" defect, which exhibit lower bond orders in (a) and on average higher in (b).

5.3.3   Width-dependent response to "bite" defects in N-AGNRs

We next generalize our findings by comprehensively investigating the dependence of the stability and charge transport of "bite" defects on the width of the armchair graphene nanoribbon. We consider a range of widths (N) spanning an interval from 6 up to 26 atoms. The calculated properties show clear multiple-of-3 oscillations [Figure 5.5(a) and (b)], therefore we group the nanoribbons into the $N = 3p$, $3p+1$ and $3p+2$ families according to their width, where p is a positive integer ($2 \leq p \leq 8$ in the considered range of N). The stability of "bite" defects as a function of the increasing width of the hosting armchair graphene nanoribbon is given in Figure 5.5(a). The formation energy is highly sensitive to N. Specifically, this value increases with N in the $3p$ family, whereas it decreases when $N = 3p+1$ or $3p+2$. In all families, however, it remains approximately constant when the width is larger than 17 atoms. This finding suggest that, under thermodynamic equilibrium, narrow armchair nanoribbons belonging to the $3p$ family are the most susceptible systems to "bite" defects.

Additionally, results concerning the stability and conductance of pairs of "bite" defects at opposite edges of AGNR are given in Figure 5.6. Similarly to single "bite" defects discussed above, the formation energy increases (decreases) with N in the $3p$ ($3p+1$ or $3p+2$) family, and remains approximately constant when N exceeds 17 atoms [see Figure 5.6(b)]. Furthermore, in Figure 5.6 we show the formation energy per defect in order to estimate the aggregation tendency that is quantified by the difference in formation energy per number of defects between the pair of "bite" defects (circles) and a single "bite" defect (dashed line). We can see that the $3p + 1$ family displays largest difference in the formation energies and hence favours aggregation of defects, while the $3p + 2$ family displays the smallest difference and hence isolated defects are thermodynamically favoured. Overall, both tendencies weaken as the width of the graphene nanoribbon increases, while the $3p$ family does not show a clear preference for the aggregation regardless of the width.

The enhanced stability of "bite" defects in the $3p$ family can be interpreted in terms of Clar's rule as seem in Figure 5.7. For $N = 3p$, there exists a unique Clar's formula, whereas multiple,
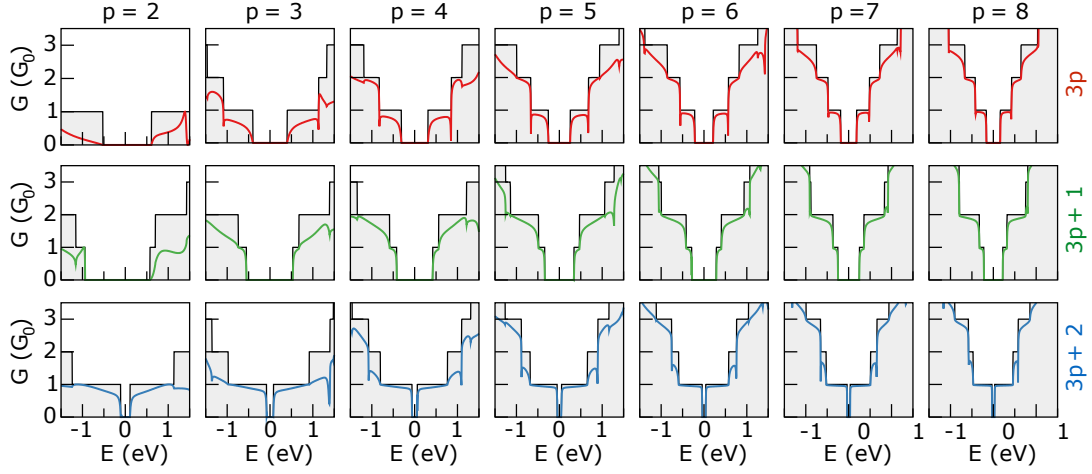
Figure 5.8: Conductance spectra of pristine (grey area) and defective (colored lines) armchair graphene nanoribbons for different widths, grouped according to their width into the $3p$ (red lines), $3p+1$ (green lines), and $3p+2$ (blue lines) families.

energy-degenerate Clar's formulas can be conceived for $N \neq 3p$. The formation of the defect requires four C-C bonds to break. In the case of $N = 3p$, these bonds have lower bond order, whereas for $N \neq 3p$ their bond order is (on average) higher. Therefore, a larger energy cost is needed to create the "bite" defect in armchair graphene nanoribbons of width $N \neq 3p$. For additional insight on how GNR electronic properties can be derived in terms of Clar's formalism, please refer to Subsection 1.2.1.

Finally, we broaden our study by addressing the charge transport in defective AGNRs of varying width. The conductance spectra upon "bite" defect formation in the $3p$, $3p+1$ and $3p+2$ families are shown in Figure 5.8. From a qualitative point of view, the disruption of the conductance is seen to be milder in wider nanoribbons as compared to the narrower ones. However, for a given value of p, the conductance in the vicinity of the band edges of $3p$ armchair nanoribbons undergoes the most drastic reduction. These effects can be translated on a quantitative basis through the determination of τ as a function of N, as given in Figure 5.5(b). As far as the transport properties are concerned, the conductance increases with increasing the nanoribbon width, with τ exceeding 85% in the case of armchair graphene nanoribbons of N larger than 22 atoms. This naturally reflects the decrease of edge-to-bulk ratio, end hence the effect of edge defects, upon increasing the width. Of the three families, however, we found that the conductance is the most strongly reduced in the $3p$ one. Indeed, τ is approximately halved in the $3p$ family as compared to both $3p+1$ and $3p+2$, when the same value of p is considered.

We rationalize the largest "bite" defect-induced disruption of the conductance observed in the $3p$ family in terms of the local density patterns. In Figure 5.5(c)−(e) we present the local density of states calculated at the tight-binding level (see Section 2.3 for the 3NN TB model comparison with DFT) slightly below the valence band edge for both pristine and defective 9-, 10-, and
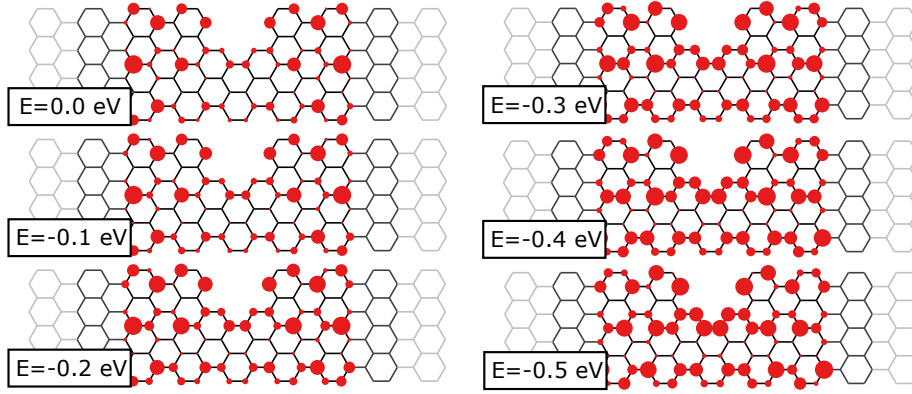
Figure 5.9: LDOS of 9-AGNR hosting a single "bite" defect for different values of energy E, from the 3NN TB model calculations. Energies are referenced to the valence band maximum (VBM).
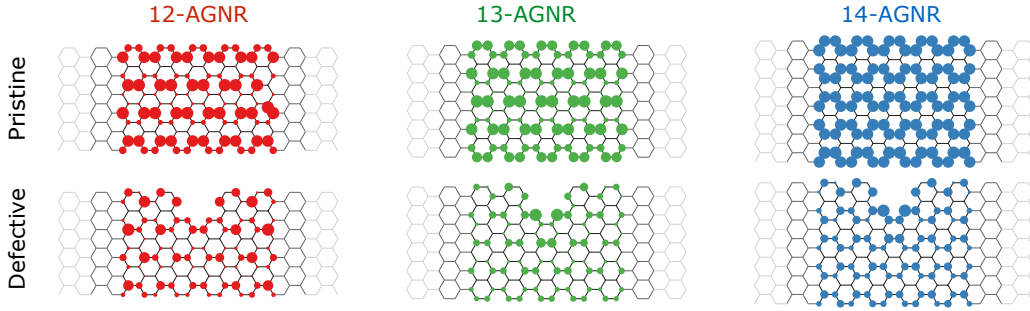
Figure 5.10: LDOS of armchair graphene nanoribbons with and without "bite" defect 0.05 eV below the valence band edge from the 3NN-TB model calculations.

11-AGNR, as representative members of the $3p$, $3p+1$, $3p+2$ families, respectively. Already in the pristine armchair nanoribbons, the local density of states behave differently in the three families, being mostly present on the two inner (outer) edge atoms in the $3p$ ($3p+1$) family, and rather uniformly distributed on the edges of the $3p+2$ family. Upon the introduction of the "bite" defect, in $3p$-AGNR we observe the emergence of a pronounced density on the sublattice that is the closest to the defect, strongly affecting the local density of states across the entire width, and eventually leading to a significant decrease of the conductance. We also note in the energy-resolved LDOS plots in Figure 5.9 that the disruption to the conductance is the most prominent at the band edges, while at larger energies this effect is less pronounced and the electron density is more homogenous even next to the defect site. Unfortunately, both of these observations indicate that the "bite" defects have a major impact on the electronic transport properties near the band edges and hence, defective 9-AGNRs could be ill-suited for FET fabrication.

In contrast, albeit a weaker perturbation around the "bite" defect is observed in the $3p+1$ and

$3p + 2$ families, the local density of states far from from the defective site is substantially less altered in these systems, closely resembling that of the corresponding pristine nanoribbons. Furthermore, we notice that such local effects become less relevant when the width of the nanoribbon is increased. Indeed, at larger values of N, the local density of states [see Figure 5.10] in the regions far from the defective site remains nearly unperturbed, thereby explaining the sizable recovery of conductance at the band edges in wide AGNRs containing a "bite" defects, as presented in Figure 5.5(b). Finally, similar conclusions can be extended to the pair of "bite" defects, where we show in Figure 5.6(c)−(e) that once again the largest disruption of the conductance upon defect formation occurs in the 9-AGNR ($3p$ family). Interestingly, while the introduction of another "bite" defect further suppresses the conductance near the band edge for both 9-AGNR and 11-AGNR, the conductance for 10-AGNR stays almost the same and larger changes are only visible at higher energies, hence establishing 10-AGNRs as a more robust alternative for the use in FETs.

5.4   Summary and conclusions

In summary, we have experimentally identified the "bite" defects, *i.e.*, missing benzene rings at the edges, as the predominant source of atomic-scale disorder in atomically precise 9-atom-wide armchair graphene nanoribbons. These defects form upon phenyl-ring cleavage occurring during the cyclo-dehydrogenation step of their synthesis, and exhibit a substantial tendency to aggregate within ~2 nm. Our first-principles calculations reveal that "bite" defects dramatically disrupt the charge transport of 9-AGNRs by reducing the transmission in the vicinity of the band edges from 74 % up to 98 %, depending on the number and configuration of defects considered. Additionally, we have expanded our theoretical investigation to N-AGNR (with $6 \leq n \leq 26$), and found that conduction properties become less sensitive to "bite" defects in wider nanoribbons and specifically in those belonging to the $3p+1$ and $3p+2$ families. Altogether, we suggest that the precursor molecule or the conditions employed in the 9-AGNRs synthesis need to be re-examined in order to fabricate "bite" defect-free nanoribbons for high-performance applications in electronic devices. Alternatively, N-AGNRs with $N \neq 3p$ qualify as better candidates to minimize the impact of such structural disorder on the electronic properties. To conclude, our work uncovers the role of "bite" defects on the charge transport of armchair graphene nanoribbons and establishes useful guidelines to mitigate their detrimental impact on the resulting electronic devices.

6 From Defect to Effect: Controlling Electronic Transport in Chevron-Type Graphene Nanoribbon Nanostructures

Although bottom-up synthesis allows for careful control over the properties of graphene nanoribbons, this method is not entirely defect free. Depending on the choice of the precursor molecule, edge defects, such as missing benzene rings resembling a "bite", have been observed in both armchair-edge and chevron-edge GNRs. Therefore we investigate the adverse effect of the "bite" defects on the transport properties in three chevron-type GNRs and discover that the extent of scattering is governed by the different defect positions. Moreover, due to the distinct electron density localization patterns for particular energy bands, the conductance at a specific energy can be altered selectively. Applying the concepts learned in single GNRs, we engineer defects in two nanostructures to construct prototypical components for nanoelectronics. First, we design a switch, consisting of three laterally fused fluorene-chevron GNRs, and place a pair of "bite" defects to effectively allow the switching between 4 binary states corresponding to distinct current pathways. Second, we show that conscientious placement of a "bite" defect pair can increase conductance between two leads in a triple chevron GNR junction. Overall, we outline how the incorporation "bite" defects affects transport properties in chevron-type nanostructures and provide a guide on how to design nanoelectronic components.

This chapter is adapted from:

Čerņevičs, K., Yazyev, O.V (2022). From Defect to Effect: Controlling Electronic Transport in Chevron-Type Graphene Nanoribbon Nanostructures – In preparation.

My contribution to this work was conceiving the original idea, performing the calculations, analysis of the data and writing the paper.

6.1 Motivation

In the previous chapter we characterized experimentally observed "bite" defect arising from a benzene ring cleaving during the polymerization process of 9-AGNR. We saw that the defects negatively affect the transport properties of the AGNRs and hence hinder the production of efficient electronic devices. However, a strong dependence on AGNR width was observed and potential candidates from the $N = 3p + 1$ and $N = 3p + 2$ families preserved the electronic transport properties even in the presence of multiple "bite" defects. This has raised a further questions about the overall impact of such defects and whether it is possible to design GNRs that could effectively be used in devices regardless of the structural faults.

Here, we continue our investigation of "bite" defects by considering a new class of GNRs with a chevron-edge type [see Figure 1.5 for sample of experimentally synthesized edge-types] that have also displayed missing benzene rings in the resulting synthesized structure [Cai et al., 2010]. Similar to 9-AGNRs [Pizzochero et al., 2021b], the defect also emerges due to the employed precursor molecule (6,11-dibromo-1,2,3,4-tetraphenyl-triphenylene) that hosts multiple flexible phenyl rings. These rings are presumed to cleave due to the steric-hindrance effects during the cyclization step and hence result in the same exact defect as observed in 9-AGNR. However, as the chevron-edge graphene nanoribbon (cGNR) can not be categorized in any of the three AGNR families and as no previous investigations have been made, the impact of these defects on electronic properties is unclear.

Interestingly, recent progress has been made in modifying the precursor molecule in order to obtain derivatives of the cGNRs – either laterally extended chevron GNRs (ecGNRs) [Mehdi Pour et al., 2017; Costa et al., 2018; Teeter et al., 2019] or fluorene-chevron GNRs (fcGNRs) [Jacobse et al., 2020] that can be coupled into a two-dimensional superlattice geometry and exhibit emergent interface-localized electronic states. Furthermore, Mutlu and co-workers [Mutlu et al., 2021] have used such laterally coupled fcGNRs to fabricate short-channel FETs with on-off ratios exceeding 10^4 and noted that structural perfection plays a remarkably important role in the charge transport. Nonetheless, due to the atomic structure of the base precursor molecule, "bite" defects are still expected in the newly synthesized nanostructures and thus cause a concern over the practicality of employing chevron-based GNRs in electronic devices.

In this chapter, to expedite the process of attaining optimal devices, we first explore experimentally observed defects in multiple chevron-type GNRs and investigate the effects on the electronic transport. Next, we use this knowledge to strategically place defects in complex nanostructures in order to gain control over the electronic transport characteristics and thus devise simple components for electronic circuits. Overall, we both reveal the adverse effects of defects and also show how they can be used to selectively control the electronic transport properties for realization of novel carbon-based electronic devices.

6.2 Methodology

Electronic properties were obtained using the 3NN TB model Hamiltonian. The Hamiltonian is expressed in Eq. 3.1 and as before, we utilize TB parameters from [Hancock et al., 2010] with corresponding values of -2.70 eV, -0.20 eV, and -0.18 eV for first-, second- and third-nearest-neighbor hopping integrals, while on-site terms are set to 0 eV.

Whereas electronic transport properties were calculated by using non-equilibrium Green's function formalism [see Section 2.5], where the transmission coefficient $T(E)$ can be expressed from Eq. 2.58 and the conductance is expressed in terms of the conductance quantum G_0 from Eq. 2.60. All our calculations were done with the help of `Kwant` package [Groth et al., 2014].

6.3 Results and discussion

6.3.1 Chevron-type graphene nanoribbons

In Figure 6.1 we show three experimentally obtainable GNRs, which all share a similar precursor molecule and thus also a common shape. Chevron-edge GNR [Figure 6.1(a)] was first synthesized by Cai *et al* [Cai et al., 2010] from tetraphenyl-triphenylene monomers and displays a pure armchair edge structure. Slightly modifying the tetraphenyl-triphenylene precursor molecule by an extra atom, yields a fluorene-chevron GNR [Figure6.1(b)] that has been shown to host an in-gap edge state and thus makes the ribbon truly metallic. Interestingly, Jacobse and colleagues showed that the metallic fcGNR can cross-link laterally to create nonporous semiconducting graphene with emergent interface electronic states [Jacobse et al., 2020]. Finally, more significant lateral extension of the cGNR can be obtained by attaching another benzene ring to the precursor molecule and thus the resulting extended-chevron GNR [Figure 6.1(c)] has been shown to exhibit a lower band gap [Teeter et al., 2019] in accordance with width-dependent band gaps in AGNRs.

Unusually, all these GNRs retain glide symmetry that display the peculiar band structure with doubly degenerate bands at X (brillouin zone boundary) point. We also notice that the low energy bands show only minor dispersion and do not cross each other, hence leading to discrete bands that in turn offer exciting opportunities for selective electronic transport engineering. Furthermore, multiple different phenyl-group attachments in chevron-based GNR precursor molecules further extend the tunability over the positioning of the "bite" defects and as we saw in Chapter 5 the transport properties can be greatly affected by varying the position and distances between these defects. In Figure 6.1, we present in red some of the possible cleavage points in the precursor molecules and the resulting final structure that arises from selective introduction of a defect.
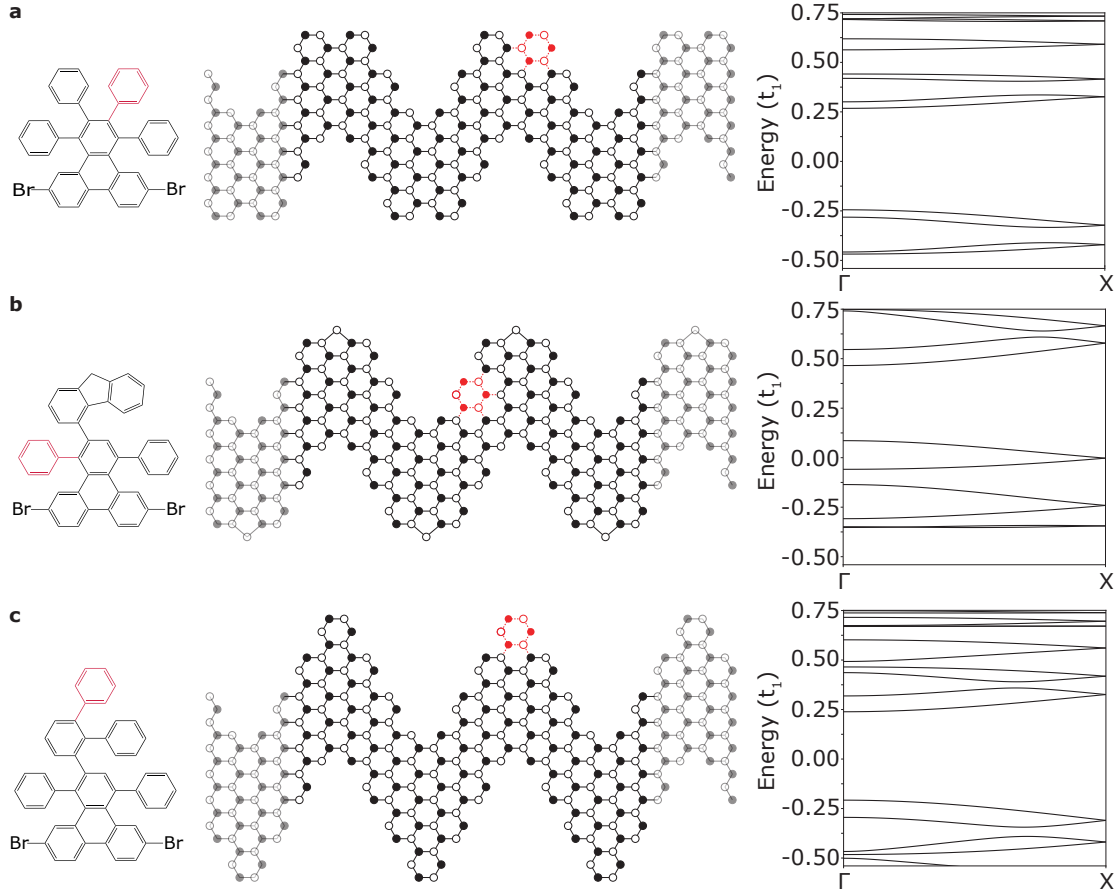
Figure 6.1: Overview of the precursor molecule, atomic structure and band structure of (a) chevron GNR, (b) fluorene-chevron GNR and (c) extended chevron GNR. Marked in red are the possible defect origin positions in the precursor molecule and the resulting GNR.

6.3.2 "Bite" defects in chevron-type graphene nanoribbons

As a starting point into engineering defects to control the transport properties, we have to establish the effects of a single point-like defect in an otherwise pristine system. In Figure 6.2(a) we show the unit cell of the cGNR and mark 8 possible defect positions, however only 2 of these are not symmetrically equivalent. We designate these positions as "Side" (1,4,5,8) and "Center" (2,3,6,7) defects and plot the corresponding conductance plots in Figure 6.2(b). We focus on the transport properties in valence and conduction bands, and, similar to Chapter 5, compare the conductance curves with the pristine cGNR with a descriptor τ [Eq. 5.1], which estimates the preserved conductance in an energy interval spanning from VBM$-\delta E$ to CBM$+\delta E$. In this case δE is set to extend over the bandwidth. For example, if a defect completely suppresses the conductance in both the valence and conduction bands then $\tau = 0$, while if a defect does not have any influence on the conductance in both bands, then $\tau = 1$. We can notice in Figure 6.2(b) that the center defect causes a larger disruption, with only $\tau = 0.39$ conductance preserved, while side defect induces significantly smaller scattering

Figure 6.2: (a) Atomic structure of the cGNR unit cell with red numbers marking the eight possible "bite" defect positions. (b) Conductance profiles of the valence and conduction bands with and without "bite" defects. (c) Local density of states and (d) probability current maps of pristine and defective cGNRs at $E = 0.28t_1$. (e) Conductance plots of "bite" defect pairs in cGNR. (f) Local density of states and probability current of 3-7 "bite" defect pair in cGNR at $E = 0.28t_1$.

with $\tau = 0.66$ conductance preserved in the two bands. We can explain these results by looking at the local density of states [Figure 6.2(c)] at the valence band ($E = -0.28t_1$), where the largest electron density is concentrated on the central atoms. Hence, center defects interact more heavily with the wavefunction associated with the band as opposed to the side defects, where only minuscule electron density is located. Similar observations can be also made for the conductance band due to the qualitative electron-hole symmetry. Furthermore, we also plot the spatial probability current maps in Figure 6.2(d) and show how the current pathways are affected by the introduced defects and confirm our observations based on the LDOS data.

Next, we check the conductance plots for a pair of defects in Figure 6.2(e) and observe that a pair of two center defects has the largest suppression of conductance only retaining $\tau = 0.18$ of the original conductance. Moreover, in the one-band region, e.g. $-0.3t_1 < E < 0.26t_1$, this
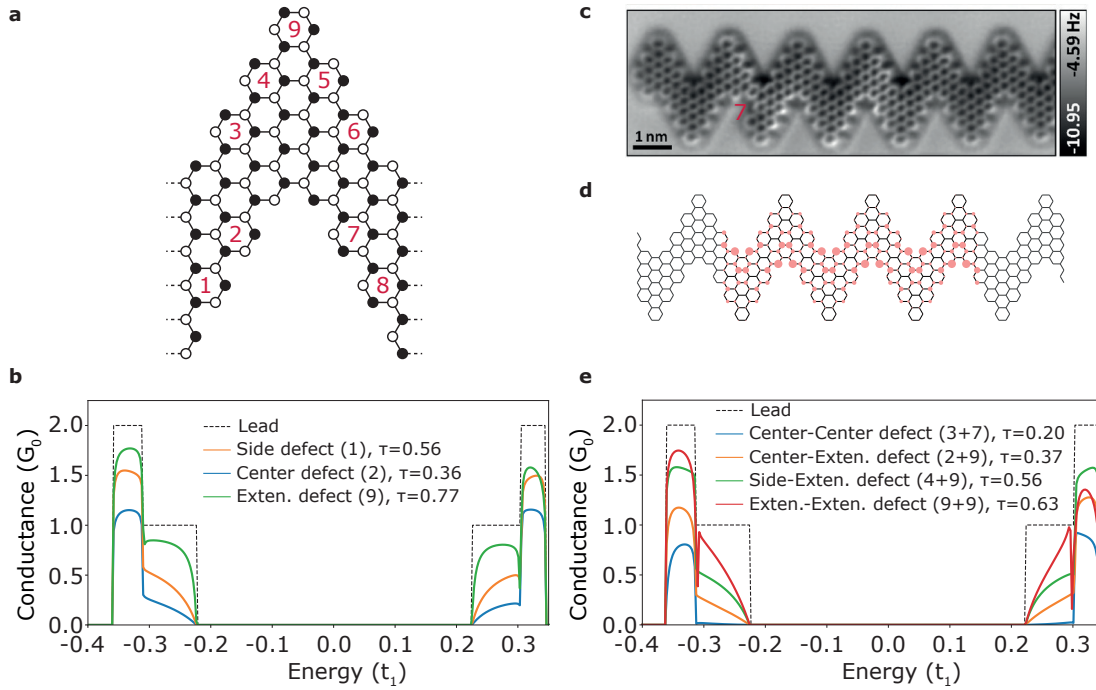
Figure 6.3: (a) Atomic structure of the ecGNR unit cell with red numbers marking the nine possible "bite"' defect positions. (b) Conductance profiles of the valence and conduction bands with and without "bite" defects. (c) nc-AFM image of ecGNR on Au(111) with the red number marking the defect position, adapted from [Teeter et al., 2019]. (d) Local density of states in ecGNR at $E = 0.28 t_1$. (e) Conductance plots of "bite' defect pairs in ecGNR.

defect pair can completely suppress the conductance. It can be noticed that the pair defects follow the same trends observed with an individual defect as the lowest scattering originating from two side defects ($\tau = 0.43$), while a middle ground is reached when a pair of side and center defects is considered ($\tau = 0.33$). Overall, we show that "bite" defects have a detrimental effect on conductance close to band edges and caution in the design of the precursor should be exercised, yet we also find that strategic placement of defects can allow a degree of control over the magnitude of conductance.

Similar principles of defect impact also extend to ecGNR shown in Figure 6.3(a), where another defect position is accessible due to the additional benzene ring in the precursor molecule. However, we observe that the extended defect has the smallest impact on the conductance ($\tau = 0.77$), followed by the side defect ($\tau = 0.55$), while the center defect is still the most adverse ($\tau = 0.36$) [Figure 6.3(b)], which agrees very well with our conclusions about bulk LDOS being concentrated in the middle of the cGNR. This can be also seen in Figure 6.3(d), where LDOS is being more localized on the central atoms akin to the cGNRs. In Figure 6.3(c) we show such center "bite" defect as characterized with the help of nc-AFM by Teeter and co-workers [Teeter et al., 2019]. Although the missing benzene ring in position 9 leads to the smallest transport disruption, the combination of two such defects represent a width-modulated ecGNR-cGNR-
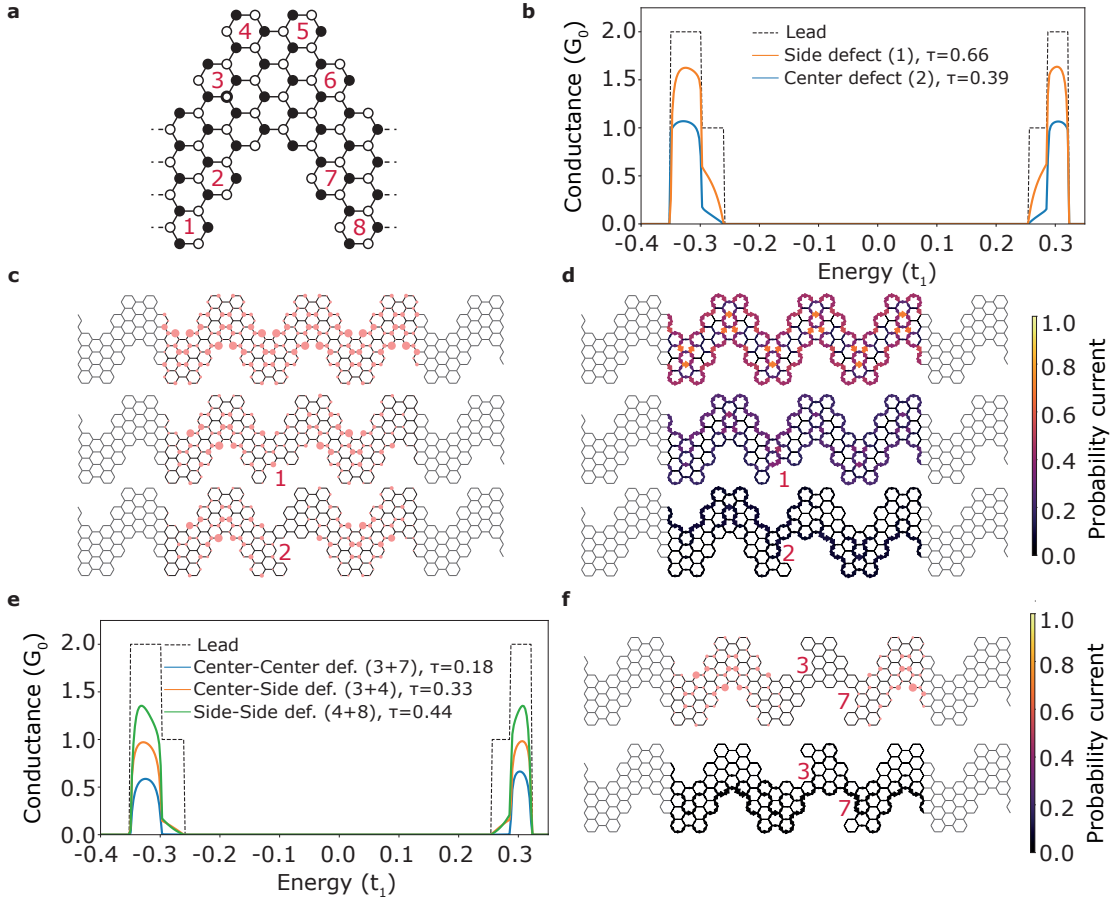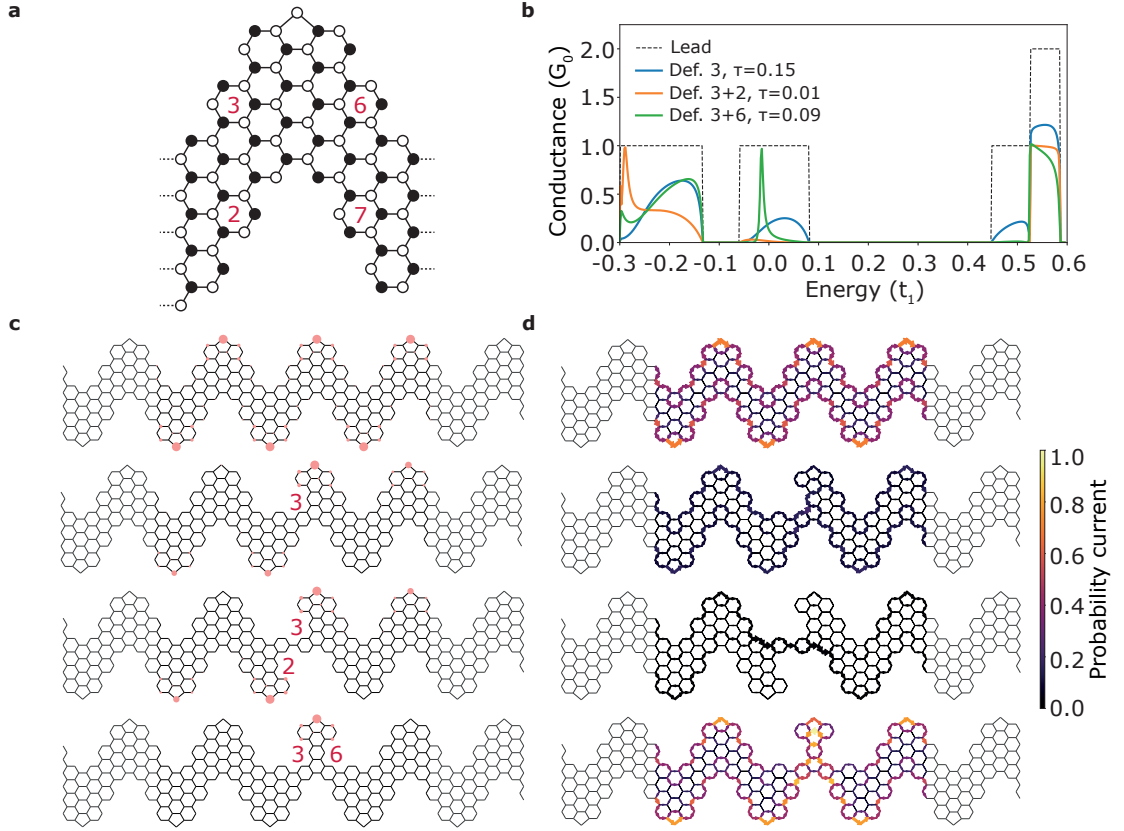
Figure 6.4: (a) Atomic structure of the fcGNR unit cell with red numbers marking the four possible "bite"' defect positions. (b) Conductance profiles of the three lowest energy bands with and without "bite" defects. (c) Local density of states and (d) probability current maps of pristine and defective fcGNRs at $E = 0$.

ecGNR heterostructure that not only decreases the transport in the two bands by about a third, but also induces an anti-resonance around $E = \pm 0.3\,t_1$ as seen in Figure 6.3(e). Interestingly, no such anti-resonances were observed in the valence or conduction bands of defective cGNRs.

On the other hand, electronic structure and hence also the electronic transport characteristics of fcGNRs differ widely from both cGNRs and ecGNRs. The out-most atom in the five-membered ring gives rise to a in-gap metallic band and opens additional possibilities for engineering the transport properties. We show the possible defect positions in Figure 6.4(a) and the conductance profiles in Figure 6.4(b). Note that τ is defined only for the metallic band now. One can notice that only center defects are possible due to the nature of the precursor molecule [see Figure 6.1(b)] and also see the detrimental effect on the metallic band, where only $\tau = 0.15$ conductance is preserved. The LDOS and current plots at $E = 0$ seen in Figure 6.4(c) and (d) show that the metallic band arises due to the five-membered ring and the current pathways are strongly confined to the band edges. Interestingly, we can observe that adding just a single defect at position 3 leads to both upper- and lower-edge current pathways disrupted, not just the top one. Whereas the LDOS plot displays a peculiar localization pathway –
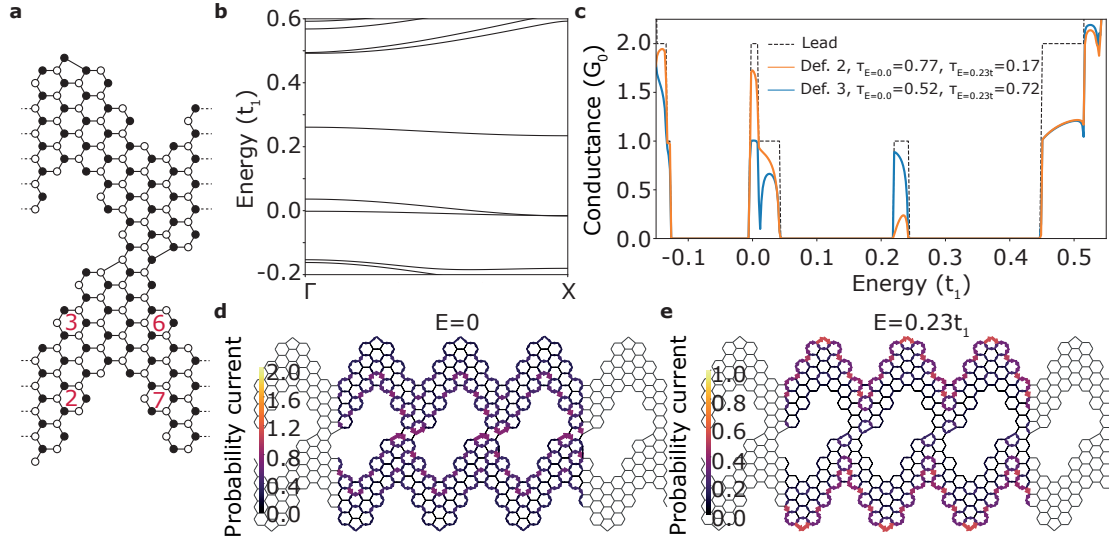
Figure 6.5: (a) Atomic structure of the laterally fused double fcGNR unit cell with red numbers marking the four possible "bite" defect positions in one fcGNR. (b) Band structure of double fcGNR. (c) Conductance profiles of double fcGNR with and without "bite" defects. Probability current of pristine double fcGNR at (d) $E = 0$ and (e) $E = 0.23t_1$.

the electron density is localized either on the top or the bottom side and hence prompts to negligible overlap between the sides, thus minimizing conductance. Adding a second defect can result in two drastically different outcomes – either further suppressed conductance or resonant tunneling at $E = 0$. First, adding a second defect at position 2 displays only negligible changes in both LDOS and current maps as compared to the single defect, but exhibiting a very low $\tau = 0.01$ value. Second, we can recover perfect conductance $G = G_0$ in our metallic band if we place the other defect in position 6. The resulting resonance peak corresponds to the localized state observed in Figure 6.4(c) that acts as a quantum dot and facilitates resonant transport. Additionally, we can observe that the band at $E \approx 0.5t_1$ qualitatively responds to the defects in the same way as cGNR and ecGNR, hence giving us an opportunity to selectively affect the electronic transport in different bands. With the knowledge gained from placing "bite" defects in the three chevron-type GNRs, we now turn our attention to more complex structures.

6.3.3 Engineering "bite" defects in graphene nanoribbon nanostructures

As a first step, we take two fcGNRs and fuse them laterally [Figure 6.5(a)] to obtain a nonporous graphene nanoribbon. Interestingly, we see in Figure 6.5(b) the emergence of another in-gap state at $E = 0.23t_1$ that arises due to the hybridization between the five-membered rings [Jacobse et al., 2020]. By exploring the probability current maps in Figure 6.5(d) and (e) we can assign these states to either inner ($E = 0$) or outer ($E = 0.23t_1$) five-membered rings. Whereas the previously equivalent defect positions can be split in two groups – defects 2 and 7 can be
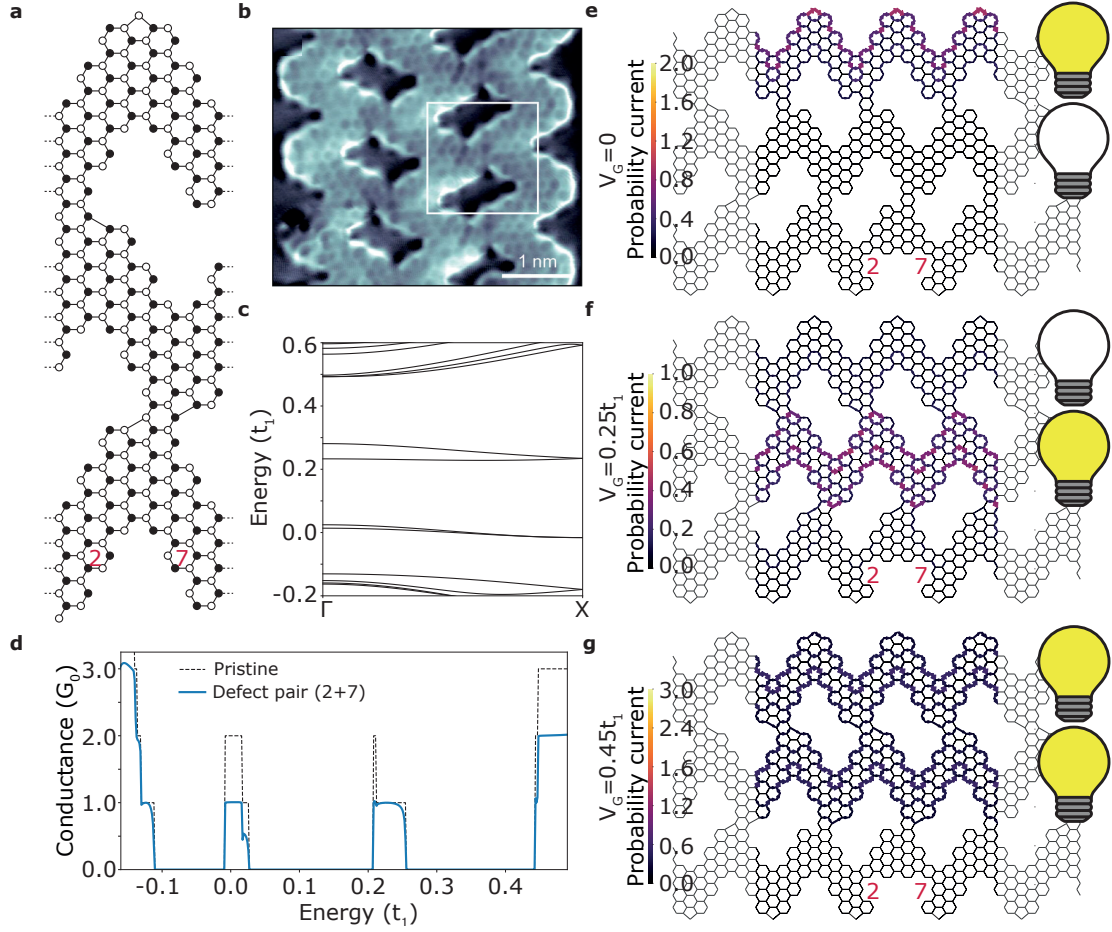
Figure 6.6: (a) Atomic structure and (b) bond-resolved STM image of laterally fused triple fcGNR. Panel (b) is adapted from [Jacobse et al., 2020]. (c) Band structure and (d) conductance profile of laterally fused triple fcGNR. Probability current plots in laterally fused triple fcGNR with 2-7 "bite" defect pair at (e) $V_G = 0$, (f) $V_G = 0.25t_1$ and (g) $V_G = 0.45t_1$ displaying the switching notion of the channels.

classified as the "outer", while defects 3 and 6 can be considered as "inner" positions. We show in Figure 6.5(b) the effect on conductance, when both of these defects are introduced. It is clear that now the defect positions will play a different role on both in-gap bands and, for example, the "outer" defect (2 or 7) has a small influence on the metallic band ($\tau = 0.77$), whereas conductance is drastically affected ($\tau = 0.17$) at $E = 0.23t_1$. This is a direct consequence of the different LDOS localization patterns and current pathways. Therefore, careful introduction of defects can lead to a selective closure of particular transport channels, while not affecting others.

We continue our investigation by fusing an additional fcGNR to our previous nonporous GNR and extend it laterally as seen in Figure 6.6(a) and (b). The resulting band structure and conductance plots in Figure 6.6(c) and (d) tell us that there are still two in-gap bands at $E = 0$
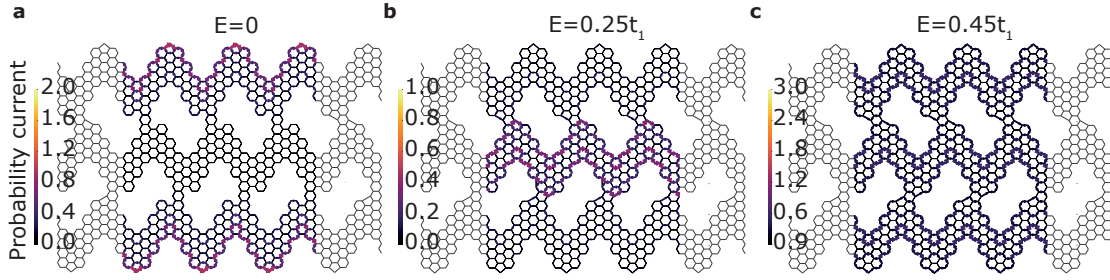
Figure 6.7: Probability current in laterally fused pristine fcGNRs at (a) $E = 0$, (b) $E = 0.25\,t_1$ and (c) $E = 0.45\,t_1$

and $E \approx 0.25\,t_1$ with maximum conductance of $G = 2G_0$ and $G = G_0$ (except for a very narrow energy range), respectively. Whereas the band at $E \approx 0.45\,t_1$ has the maximum conductance of $G = 3G_0$. Although we already observed the spatially resolved current pathways in double fcGNR corresponding to different bands, the effect is more prevalent in triple fcGNR. We show in Figure 6.7 that the metallic band is once again localized only on the very outer atoms similar to fcGNR and double fcGNR, while the $E \approx 0.25\,t_1$ band arising from the fusion of the inner five-membered rings is localized only on the middle ribbon. Finally, at $E \approx 0.45\,t_1$ we have three current pathways equally distributed over the 3 fused ribbons.

Resolving the spatial current map already gives us a degree of control over the transport properties. For example, in a device consisting of the triple fcGNR, we can vary the gate voltage (V_G) to target a specific band and hence control in which part of the fcGNR the current flows. Furthermore, using the previous results of defect impact on transport properties, we propose a more complex switch that can access four different binary states – (0,0),(1,0),(0,1) and (1,1), where 0 and 1 correspond to the magnitude of conductance G_0 delivered to two regions of the triple fcGNR. We show in Figure 6.6(e)−(g) the three different states associated with a specific gate voltage V_G and indicate the state with "light bulbs", where the yellow color demonstrates if the pathway is on (1) or off (0). It is straightforward to see that the fourth state (0,0) can be accessed at any energy that is not coinciding with a band, for example, at $E = 0.1\,t_1$.

Strikingly, we see that after the introduction of the $2 + 7$ defect pair in the bottom ribbon, we can completely close down one current pathway and decrease the conductance by exactly one conductance quantum G_0 [Figure 6.6(d)]. Although, we already observed some degree of selectivity over different bands by introducing a defect in particular positions in narrower chevron-based GNRs, the laterally fused triple fcGNR shows an unprecedented possibility to carefully control the transport properties. We attribute this characteristic to the distinct separation of different bands and the band's localized nature, where the wavefunction is confined to a particular fcGNR that makes up the extended structure. Interestingly, the strong confinement then allows us to selectively alter only a particular band, without affecting the spatial transport in other parts of the ribbon.

After showing that chevron-based GNRs can be used as building blocks for potential all-
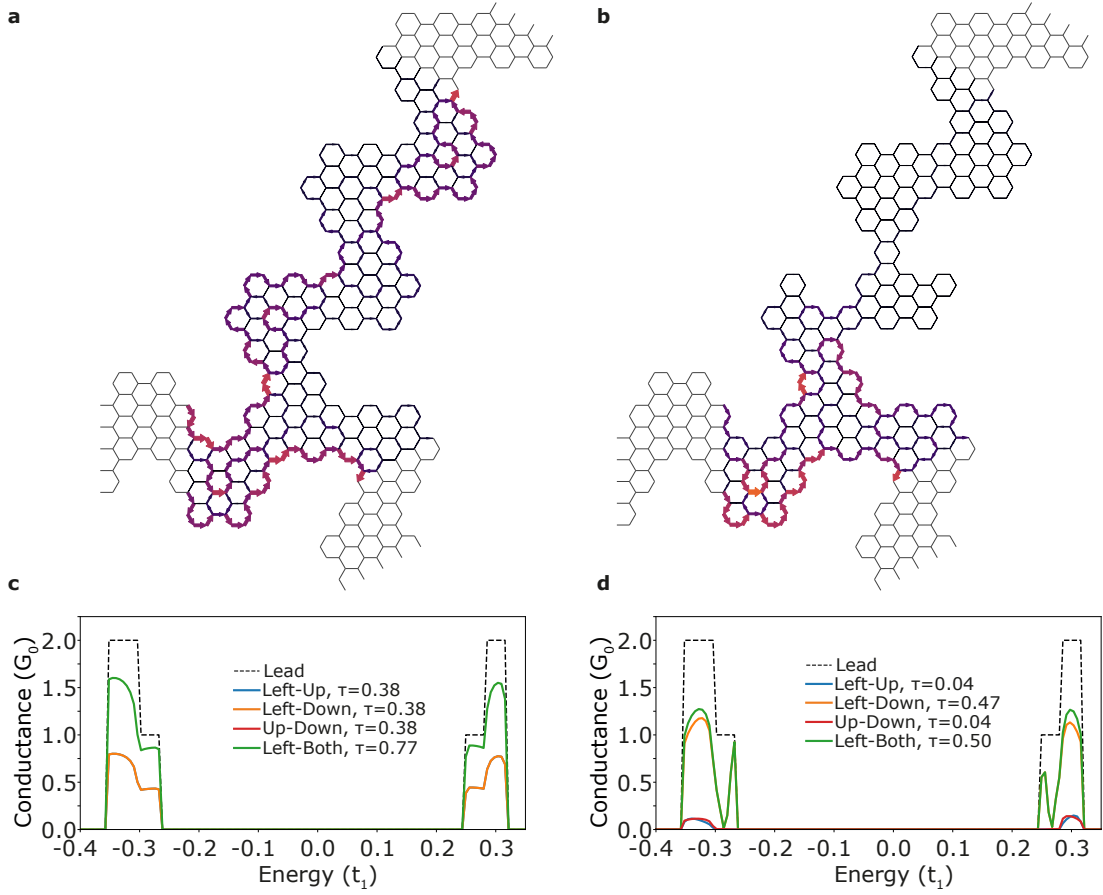
Figure 6.8: (a) Probability current arising from the left lead in triple cGNR and (b) the same junction, but with deliberately placed "bite" defects. (c) Conductance profile of the pristine junction in panel (a). (d) Conductance profile of triple cGNR junction with placed "bite" defects.

carbon devices and defect engineering gives a selective control over the electronic transport properties, we move on with investigating junctions composed from multiple GNRs. One of the first experimentally synthesized junctions by Cai *et al* [Cai et al., 2010] was a symmetric chevron-based triple junction [Figure 6.8(a)]. First, we show that such junction can be used as an electron beam splitter – the conductance of valence and conduction bands measured from the left lead to the upper(lower) lead exhibits low scattering with $\tau = 0.38$ and hence overall transmission of $\tau = 0.77$ to both leads [Figure 6.8(c)]. The low scattering stems from the fact that design of the central scattering region retains the symmetry and shape of the individual leads as shown by Chen *et al* [Chen et al., 2017b]. Next, we notice that careful engineering of the "bite" defects astonishingly can increase the conductance in a selected direction. Figure 6.8(b) shows a pair of two "bite" defects placed in the upper lead and the resulting current map at $E = 0.36t_1$ that shows an increased transmission to the right lead. We

calculate that the ratio of the retained conductance is increased from $\tau = 0.38$ to $\tau = 0.47$, while also minimizing the conductance to the upper lead down to $\tau = 0.04$. We propose that adding together multiple such triple-junctions with or without engineered "bite" defects can be used to selectively control and split the incoming current and effectively act as interconnects between components of an electric circuit.

6.4   Summary and conclusions

In summary, we investigated the electronic transport properties of three chevron-type graphene nanorribons in presence of "bite" defects. Our calculations show the detrimental effect of the defects on the conductance, however, we also notice that different defect positions lead to diverse response in particular energy bands, thus giving a degree of control over the transport properties. Furthermore, it can be seen that the spatial electron density localization and current pathways play a major role in predicting the effects of the defect and therefore this information can be used to selectively affect a distinct conductance channel.

Next, we applied the lessons learned about individual GNRs to construct more complex nanostructures and selectively engineer the electronic transport properties with the help of strategically placed "bite" defects. For example, we design a switch consisting of three laterally fused fluorene-cGNRs and place a pair of defects to effectively allow the switching between 4 binary states corresponding to current pathways. With varying gate voltage we can achieve current flow in one, two or none of the connections, while not introducing any additional electron scattering and maintaining electronic transport of exactly one conductance quantum per connection. Interestingly, experimental realization of such structure could be achieved in near future, as innovative designs of precursor molecules have already been utilized to synthesize GNRs with "bite"-like edges [Fu et al., 2020].

Finally, we show how an experimentally synthesized triple cGNR junction can act as an electron beam splitter and preserve 77% of the pristine cGNR's conductance in valence and conduction bands. In addition, deliberate placement of a defect pair can increase conductance between two of the leads from 38% to 47% of the maximum, hence turning the defect into a positive effect. We propose that using a triple junction as a building-block and placing defects strategically offers an excellent control over the current flow and thus can potentially be applied as interconnects in all-graphene nanocircuits. Further tunability of such system could be improved by applying a gate potential [Araújo et al., 2021] to create a switch or transistor-like system. Overall, we establish design rules of defect incorporation in cGNR structures to control electron transport.

Integrating Graphene Nanoribbons in Nanoelectronics

7 Design Rules for Interconnects Based on Graphene Nanoribbon Junctions

Graphene nanoribbons (GNRs) produced by means of bottom-up chemical self-assembly are considered promising candidates for the next-generation nanoelectronic devices. We address the electronic transport properties of angled two-terminal GNR junctions, which are inevitable in the interconnects in such graphene-based integrated circuits. We construct a library of over 400000 distinct configurations of 60° and 120° junctions connecting armchair GNRs of different widths. Numerical calculations combining the tight-binding approximation and the Green's function formalism allow identifying numerous junctions with conductance close to the limit defined by the GNR leads. Further analysis reveals underlying structure-property relationships with crucial roles played by the bipartite symmetry of graphene lattice and the presence of resonant states localized at the junction. In particular, we discover and explain the phenomenon of binary conductance in 120° junctions connecting metallic GNR leads that guarantees maximum possible conductance. Overall, our study defines the guidelines for engineering GNR junctions with desired electrical properties.

This chapter is adapted from:

My contribution to this work was performing the calculations, development of the web application, analysis of the data and writing the paper.

7.1   Introduction

In the two previous parts of this thesis we have investigated the electronic properties of various experimentally-obtainable GNR structures and also shown the degree of control one has over electronic properties by either introducing different width elements or engineering defect placement. As a consequence of this analysis, we have also proposed potential GNR-based components for next generation nanoelectronics, such as metal-semiconductor-metal junctions [Chapter 4], switches and splitters [Chapter 6]. However, these components were not designed with a conscious objective in mind, but were rather the byproduct of a fundamental study of transport properties in bottom-up synthesized systems. In this chapter we change our approach and conduct our investigation by computational high-throughput screening of hundreds of thousands of possible GNR junctions in order to find potential targets with specific electronic transport properties.

We start by searching for interconnects joining individual electrical components as they are the most basic and fundamental building blocks of any integrated circuit. Linear interconnects based on one-dimensional GNRs allow for little freedom in designing such circuits, while to effectively accommodate a large number of components on a plane one would desire graphene interconnects that follow paths with "turns" akin to the conductive traces of common printed circuit boards. Each "turn" can be viewed as a two-terminal GNR junction, and the electronic transport properties of such junction are expected to depend strongly on the details of its atomic structure. This is in contrast to macroscopic interconnects, such as printed circuit board traces or ordinary wires, since bending a wire does not generally affect its resistance. While the electronic and transport properties of one-dimensional GNRs are largely understood by now, relations between the structure and electronic transport properties of GNR junctions remain to be explored.

In this chapter, we address the structure-property relations of two-terminal GNR junctions and formulate design rules for engineering interconnects with minimal scattering for graphene-based nanoelectronic circuits. To achieve this goal, we systematically characterize over 400000 unique structures of GNR junctions connecting two identical armchair GNRs of different width at angles of 120 and 60 degrees. Extensive library of calculations performed using the combination of tight-binding model and Green's function technique allows to uncover several universal physical mechanisms underlying the electronic transport across GNR junctions and establish design rules necessary for engineering nanometer-width interconnects for graphene-based nanoelectronic circuits.

7.2   Methodology

We employ a tight-binding model with one p_z orbital per atom and only nearest-neighbor hopping integral that has been shown to provide reasonably accurate description of the electronic structure of graphene [Kundu, 2011] and GNRs [Hancock et al., 2010] near the

Fermi level. Importantly, this simple model is computationally inexpensive to conduct high-throughput screening. The Hamiltonian is expressed in Eq. 3.1. We set on-site energies $\epsilon_i = 0$ eV and a hopping integral $t_1 = 2.75$ eV between the nearest-neighbor atoms in our calculations. Electronic properties are calculated by using non-equilibrium Green's function formalism [see Section 2.5], where the transmission coefficient $T(E)$ can be obtained from Eq. 2.58 and the conductance $G(E)$ is expressed in terms of the conductance quantum G_0 from Eq. 2.60.

We invite the readers to use our web-based open-access application `TBETA` [Čerņevičs et al., 2020a] on the `Materials Cloud` portal [Talirz et al., 2020] that implements the described methodology and allows reproducing all our results. It is designed for easy-to-use construction of angled junction configurations and calculation of their electronic transport properties. Access to wider range of junctions can be achieved by manually selecting the scattering region, including leads of different width and shifting the position of leads in relation to each other. No coding knowledge is required to design a junction and run the calculations. Conductance and density of states can be computed over selected energy windows, while local density of states, local current and lead wavefunctions are computed at a selected energy. For more information see Appendix A. All results reported in our work and the web-based application use `Kwant` [Groth et al., 2014] as the engine for performing calculations.

7.3 Results and discussion

Although we are using the one-orbital nearest-neighbor tight-binding model, this minimalist methodology allows for sufficiently accurate description of the discussed properties, yet it is simple enough for performing massive high-throughput screening of a large number of junction structures and rationalizing the numerical results in terms of analytical models.

7.3.1 Construction of junction structures

Using this methodology we perform an exhaustive investigation of the electronic transport properties of 120° and 60° two-terminal GNR junctions connecting two armchair graphene nanoribbon (AGNR) leads of the same width. These junction angles, in addition to the trivial case of 180°, can be constructed without introducing any topological defects changing the crystallographic orientation of graphene lattice. We explored leads of different width defined by $3 \leq N \leq 9$ carbon atoms, hence covering the semiconducting ($N = 3p$, $N = 3p + 1$) and metallic ($N = 3p + 2$) AGNR families [Nakada et al., 1996]. Figure 7.1(a) shows an example $N = 7$ AGNR.

We then generate junction structures within the limits defined by a circular area as shown in Figure 7.1(b) for the 120° junctions of 7-AGNRs. The circle is defined by the intersection point of the lead axes such that there is no overlap between the leads. Note, the position of the circle center leads to 3 distinct classes of 120° junctions, which are denoted by lead intersection
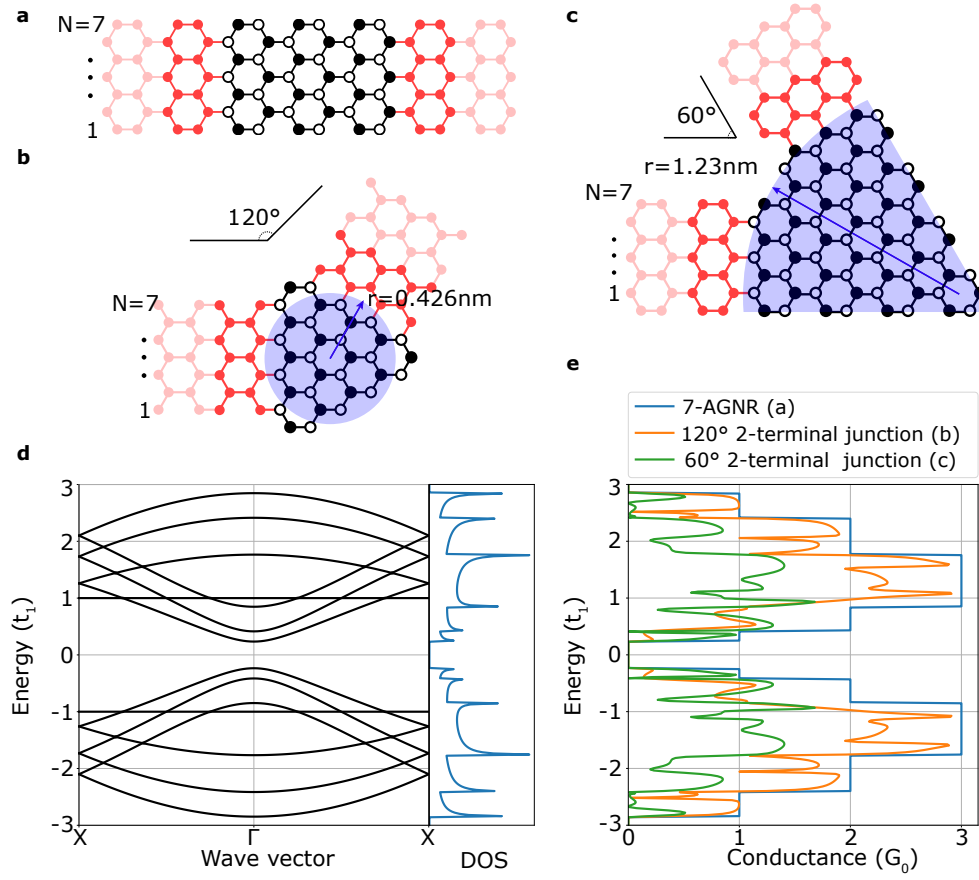
Figure 7.1: GNR junctions and their electronic properties. (a) Atomic structure of 7-AGNR, with black and white atoms representing the two sublattices and red atoms showing the semi-infinite leads. (b) An example of 120° two-terminal junction with 7-AGNR leads (IP_C). Area limiting the scattering region used in constructing various junction configurations is shown in blue. (c) An example of 60° junction with 7-AGNR leads. (d) Band structure and DOS of 7-AGNR. (e) Conductance profiles of 7-AGNR lead (panel (a)), 120° (panel (b)) and 60° (panel (c)) junctions.
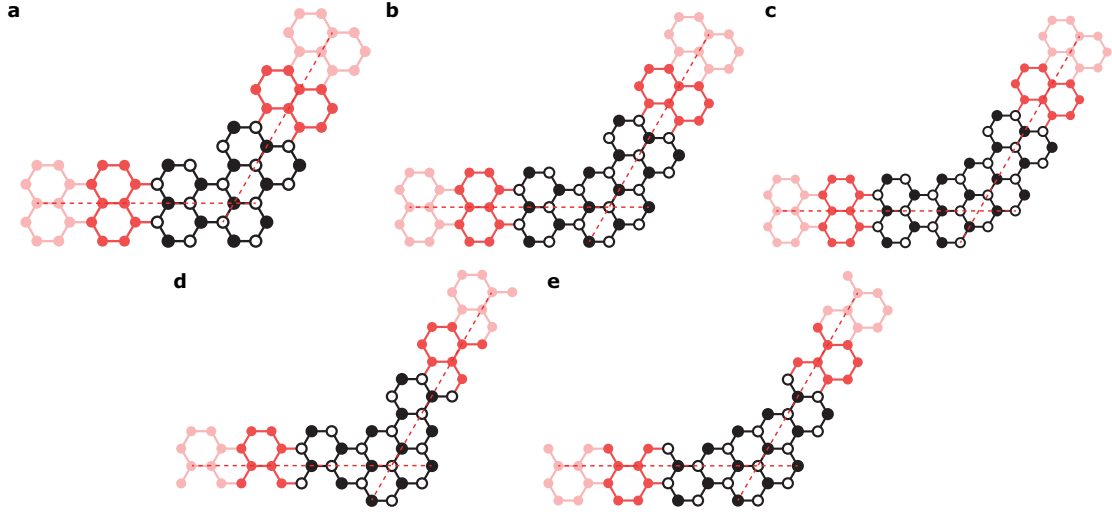
Figure 7.2: Definition of 3 classes of angled junctions. The axes of AGNR leads ($N = 5$ in this illustration) intersect (a) the atomic position in one of the sublattices marked with black (intersection point IP_A), (b) in the complementary sublattice marked with white (IP_B) or (c) in the empty (center of a hexagon) position (IP_C). The AGNR ($N = 4$) leads attached in the (d) *up* configuration and (e) *down* configuration.

point IP_I, with $I = A, B$ or C corresponding to sublattice A, sublattice B or the center of the hexagon [see Figure 7.2]. The intersection point IP can be controlled by adjusting the distance between the leads. Furthermore, for leads with even number of atoms across the width there are two possibilities for attaching the leads for each of the classes, hence doubling the number of structures. The distinctions *up* and *down* correspond to the aligned edge with respect of the (N+1)-AGNR. We also assume the edge carbon atoms to be hydrogen terminated, but due to the absence of π-bonding hydrogen they are not included in the one-orbital tight-binding model [Hancock et al., 2010]. Once the circular area is defined, we generate *all* possible junction configurations by removing atoms from it and imposing the following restrictions: mirror symmetry of the junction and the presence of only three- and two-fold coordinated carbon atoms. For 60° junctions, the circular area is defined in a similar way, except that the circle center is defined as the intersection of lines drawn along the GNR edges [Figure 7.1(c)].

The properties of the generated junctions are then compared to those of pristine AGNR leads. Figure 7.1(d) shows the band structure and density of states (DOS), while Figure 7.1(e) compares the conductance profiles of the three structures presented in Figure 7.1(a)−(c). The results are presented in terms of the nearest-neighbor hopping integral t_1 = 2.75 eV. Quantized conduction can be observed for the pristine 7-AGNR, reflecting the number of sub-bands (transmission channels) at a particular energy E, with a maximum value $G = 3G_0$ ($G_0 = 2e^2/h = 7.75 \times 10^{-5}$ S) when three channels are present and a minimum of $G = 0$ in the band gap. The conductance of junctions is bound from above by the lead conductance and is no longer quantized due to scattering. In general, GNR junctions show complex conductance profiles with pronounced differences between each other. For example, the 60° junction
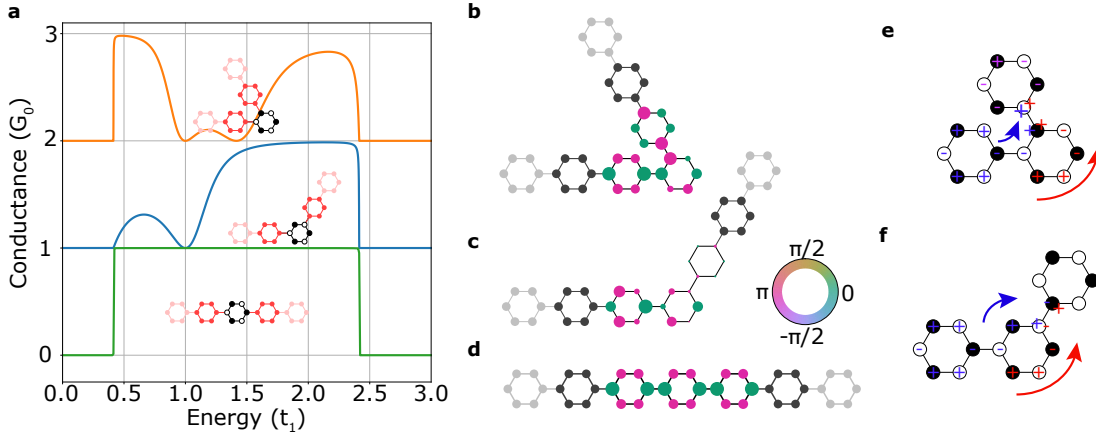
Figure 7.3: Quantum interference in 3-AGNR junctions. (a) Conductance plots of *ortho-*, *meta-* and *para-*attached 3-AGNR leads with the atomic structures displayed. The conductance profiles are offset with respect to each other by G_0 for clarity. The wavefunction inside the scattering region of (b)*ortho-*, (c)*meta-* and (d)*para-*attached 3-AGNR junctions at $E = 0.4t_1$. Schematic drawing of the two pathways (blue and red) and the phase (+ or − corresponding to phase difference of π) in (e)*ortho-* and (f)*meta-*attached 3-AGNR junctions.

exhibits conductance close to the quantized conductance of the lead near the band edge ($E = 0.3t_1$), but the conductance of 120° junction is suppressed at the same energy.

The objective of designing optimal graphene-based interconnects consists in minimizing the amount of scattering at each "turn", *i.e.* achieving conductance close to the limit defined by the conductance of the GNR leads. To quantify the junction conductance with respect to the ideal lead, we utilize slightly modified descriptor τ [Eq. 5.1] used in Chapters 5 and 6,

$$\tau = \frac{\int_{E_0}^{E_0+\delta E} G_j(E)\,dE}{\int_{E_0}^{E_0+\delta E} G_l(E)\,dE},\tag{7.1}$$

which estimates the preserved conductance in a narrow energy window $\delta E = 0.037t_1 = 0.1$ eV with E_0 being the conduction band minimum or the Fermi level for the semiconducting and metallic GNR leads, respectively. The chosen energy range roughly represents the expected operating conditions of graphene devices. $G_j(E)$ and $G_l(E)$ are the conductances of the junction and the ideal lead, respectively. From here on, we will be referring to well-conducting junctions if $\tau > 0.9$.

7.3.2 3-AGNR two-terminal junctions

We start our discussion of structure-property relationships by considering the simplest case of 3-AGNR junctions. Three possible configurations of the scattering region correspond to a single benzene ring connected to the leads in *ortho-*, *meta-* or *para-*positions, using chemistry notations, to obtain 60°, 120° and 180° junctions, respectively. The latter case is the ideal

3-AGNR, and hence no scattering is possible. Figure 7.3(a) shows the atomic structures of the junctions and displays the corresponding conductance spectra. We show only positive energies $0 \leq E \leq 3t_1$ since at negative energies the results are identical due to the electron-hole symmetry inherent to our tight-binding model.

In Figure 7.3(a), the 60° junction demonstrates conductance very close to that of the perfect 3-AGNR lead ($\tau = 0.99$) at the band edge ($E = 0.4t_1$), whereas for the 120° junction the conductance is essentially zero at this energy. One needs to note that seemingly small difference in the attachment points gives rise to distinct transport properties. Further differences between the three configurations can be observed in the scattering center wavefunctions at $E = 0.4t_1$ plotted in Figure 7.3(b)−(d). When the leads are attached in the *ortho-* position, the wavefunction is delocalized over all atoms in the scattering center but the phase is reversed upon transmission [Figure 7.3(b)]. In contrast, the wavefunction is localized only on one of the sublattices in the central region of the 120° junction and vanishes completely as it approaches the other lead [Figure 7.3(c)], hence manifesting in nearly zero conductance.

The aforementioned observations can be rationalized in terms of the quantum interference (QI) phenomenon. In Figure 7.3(e), we show a schematic representation of the 60° junction and graphically represent the phase of the incoming wavefunction as + or − as a continuation of the wavefunctions of the perfect 3-AGNR lead (Figure 7.3(d)). We note the two inequivalent pathways colored in blue and red result in constructive QI (violet) and explain the phase reversal as observed in Figure 7.3(b). Similarly, for the 120° junction [Figure 7.3(f)] the two pathways result in destructive interference. This simple model correctly predicts the wavefunctions in the scattering region [Figure 7.3(b) and (c)] and reaches an excellent agreement with a graphical model designed for visual inspection of the connectivity in π-conjugated systems [Zhao et al., 2017].

Although QI has been observed to influence electronic transport properties in organic molecules [Sautet and Joachim, 1988; Li et al., 2019b; Greenwald et al., 2021], only recently its effect has been investigated for more complex graphene nanostructures. Calogero and co-workers [Calogero et al., 2019a,b; Alcón et al., 2021] showed that the electronic transport in nanoporous graphene can be controlled through *para-* and *meta-*bridges. However, we observe that in GNR junctions QI effects are pronounced only in cases where the scattering center is attached to the lead through a single bond. For wider AGNR junctions involving multiple covalent bonds to leads it becomes difficult to interpret the results in terms of QI, and thus systematic numerical characterization of the electronic transport properties needs to be performed.

7.3.3 Systematic screening of electronic transport across junctions

The structures of N-AGNR junctions with lead widths $4 \leq N \leq 9$ were systematically constructed resulting in total of 438187 unique configurations. Regardless of the lead width and junction angle, it was always possible to identify configurations with $\tau \geq 0.9$. The entire database of investigated junctions ordered in terms of τ is provided in Supplementary
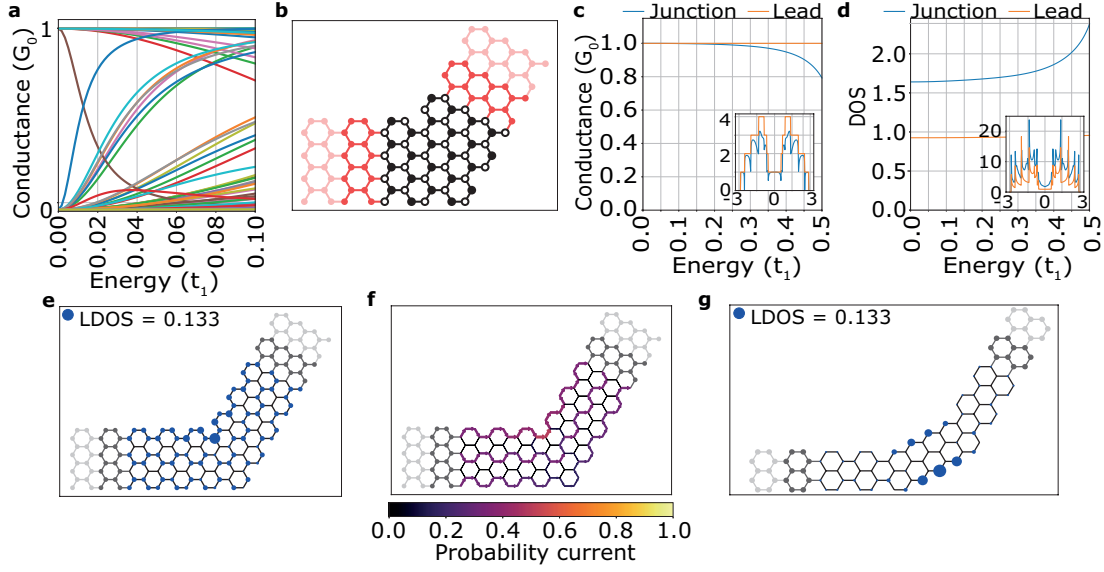
Figure 7.4: Electronic transport across metallic 120° junctions. (a) Conductance profiles of 150 representative 120° 8-AGNR junctions in $0 \leq E \leq 0.1t_1$ energy range. (b) Atomic structure of a selected 120° 8-AGNR junction with $\tau = 1$ and (c) its conductance profile in the $0 \leq E \leq 0.5t_1$ energy range. The full conductance profile is shown in the inset. (d) DOS of the junction in $0 \leq E \leq 0.5t_1$ energy range and the its full profile (inset). (e) LDOS and (f) local current across the junction at $E = 0$. (g) LDOS of a metallic 120° 5-AGNR junction with zigzag edges at $E = 0$.

Tables 1–36 [Čerņevičs and Yazyev, 2021] and described in Appendix B. Below, we focus on representative junctions that demonstrate conductances close to those of ideal leads and help establishing the underlying structure-property relationships.

120° junctions

We first discuss the 120° junctions by pointing at striking transport phenomenon observed for the metallic AGNR leads ($N = 5, 8$). Figure 7.4(a) shows conductance profiles of 150 randomly selected 8-AGNR junctions in the $0 \leq E \leq 0.10t_1$ energy range. The conductance at $E = 0$ is binary taking only values of $G = G_0$ or $G = 0$, and this effect is not observed for the 60° junctions. We also note that both the 60° and 120° junctions with semiconducting leads do not show this effect at the band edge. In Figure 7.4(b), we show a 120° 8-AGNR junction that features $G = G_0$ at $E = 0$ with practically no backscattering up to the energies as high as $E = 0.3t_1$ (~ 1 eV) [Figure 7.4(c)]. For this particular junction, there is no large variation in the DOS of the junction compared to the 8-AGNR lead [Figure 7.4(d)], and the local density of states is rather delocalized in the scattering region at $E = 0$ [Figure 7.4(e)]. Our observation is in agreement with the finding that a delocalized transmission eigenstate leads to conductance enhancement [Xia et al., 2020]. Besides, we show that such delocalization leads to homogeneous local current paths through the junction [Figure 7.4(f)] closely resembling local current in the lead.
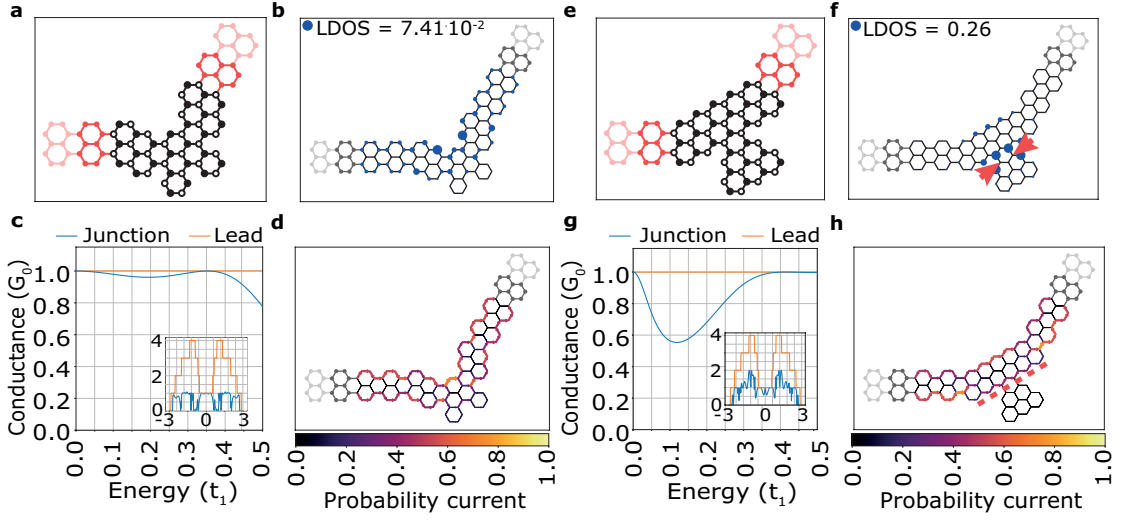
Figure 7.5: (a) Atomic structure of a selected 5-AGNR 120° junction with mixed-edge scattering centre. (b) LDOS of the junction at $E = 0$. (c) Conductance profile of the junction in the $0 \leq E \leq 0.5t_1$ energy range and the full conductance profile shown in the inset. (d) Local current across the junction at $E = 0$. (e) Atomic structure of a selected 5-AGNR 120° junction with sublattice imbalance $\delta N = -2$. (f) LDOS of the junction at $E = 0$ with red arrows pinpointing the attachment points. (g) Conductance profile of the selected junction in the $0 \leq E \leq 0.5t_1$ energy range and the full conductance profile shown in the inset. (h) Local current of the junction at $E = 0$ with dashed red line indicating the split between two regions.

Remarkably, we also discover that such perfectly transmitting 120° junctions can demonstrate a DOS peak at $E = 0$ and localized states associated with the zigzag edge segments [Figure 7.4(g)]. We note that the electronic characteristics of this junction indicate a weakly coupled localized state leading to the Fano resonance [Miroshnichenko et al., 2010], as previously observed for T-shaped junctions [Kong and Xiong, 2010] and quantum dots [Chapter 4 of this thesis and Xiong and Xiong [2011]]. Additionally, we reveal metallic 120° junctions [see Figure 7.5(a)−(d)] with perfect transmission that combine different types of edges–armchair, zigzag and mixed–thus concluding that the edge geometry in the scattering center does not play a central role in determining the transport properties. However, we note that all metallic 120° junctions with $\tau > 0.9$ are characterized by non-zero sublattice imbalance $\delta N = N_A - N_B$, with N_A and N_B being the number of atoms in the scattering area belonging to sublattices A and B, respectively.

Figure 7.6(a) shows a histogram of sublattice imbalance δN for 75 highest and 75 lowest transmitting metallic (5-AGNR, IP_A) junctions. All junctions with high transmission have the same sublattice imbalance $\delta N = -1$ with an exception of two structures characterized by $\delta N = -2$. This deviation can be rationalized in terms of LDOS that is only localized in a sub-region with $\delta N = -1$ as seen in Figure 7.5(e)−(h). We note that the lower triangular fragment is decoupled from the rest of the junction as the atoms marked with the red arrows in Figure 7.5(f) show no electron density a $E = 0$. Hence, the local current in Figure 7.5(h)
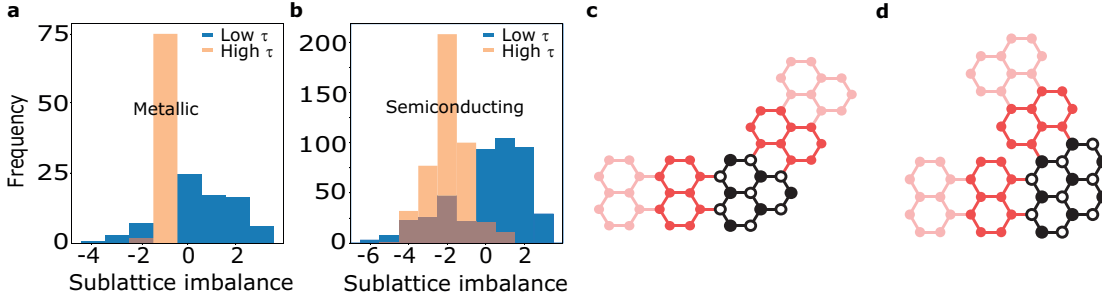
Figure 7.6: Effect of sublattice imbalance on the transmission. (a) Distribution of sublattice imbalance δN for 75 highest and 75 lowest (out of 712) values of τ among the considered 120° 5-AGNR (IP_C) junctions. (b) Distribution of sublattice imbalance δN for 450 highest and 450 lowest (out of 6817) τ values among the 120° 7-AGNR (IP_B) junctions. Examples of (c) 120° and (d) 60° junctions with sublattices A and B shown in black and white, respectively.

can only be observed in the region above the red dashed line, where sublattice imbalance of $\delta N = -1$ is preserved. Similar behavior with decoupled localized states is observed in GNRs with edge functionalized molecules as we saw in Chapter 3. We have also observed that for metallic 8-AGNR junctions the sublattice imbalance $\delta N = -3$ is associated with high τ value, whereas other sublattice differences δN produce $G = 0$ at $E = 0$. The increase in δN arises due to the two extra missing atoms at the interface between the scattering region and the lead for AGNRs with even number of carbon atoms across the width.

Therefore, we conclude that high conductance of 120° junctions with metallic AGNR leads is associated with negative ($\delta N < 0$) and odd ($\delta N \mod 2 \neq 0$) sublattice imbalance. In order to rationalize the observed binary conductance at $E = 0$, we first note that in 120° junctions the semi-infinite leads are connected to the same sublattice of the scattering region [Figure 7.6(c)], while the opposite is true for the 60° [Figure 7.6(d)] and 180° two-terminal junctions. Second, in the nearest-neighbor TB model the number of zero-energy states is equal or larger the absolute value of δN. The wavefunction of a such zero-energy states is localized on the majority sublattice [Wang et al., 2009]. It has been further shown that zero-energy states due to the sublattice imbalance facilitate the transmission of charge carriers [Kihira and Aoki, 2017]. Thus, we conclude that the resonant zero-energy states are involved in the electronic transport resulting in maximum conductance at $E = 0$ for metallic 120° junctions. Depending on the coupling strength between the leads and the scattering centre, the DOS peak width of the zero-energy states can be significantly broadened and hence facilitate the conductance over a wide energy range around $E = 0$. We show the conductance through a zero-energy state depending on the coupling strength with the leads in Figure 7.7, where low coupling leads to narrow, resonant-like conduction peaks. In contrast, metallic 120° junctions with no sublattice imbalance ($\delta N = 0$) or with a zero-energy state localized on the sublattice not connected to the leads ($\delta N > 0$) exhibit $G = 0$ at $E = 0$. In these cases we observe that the trace of the matrix product in Eq. (2.58) is zero due to diagonal elements having a pair with an opposite sign that stems from the symmetry of the device Hamiltonian and the fact that the self-energies $\Sigma_{L(R)}$ in
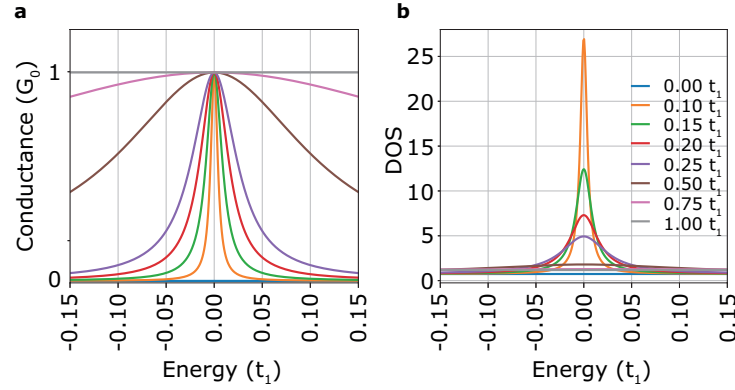
Figure 7.7: Transport through a zero-energy state. Evolution of (a) conductance and (b) DOS peak near $E = 0$ upon changing the strength t_1 of the coupling to the leads.

Eq. (2.57) affect only one sublattice. To support this finding, we present analytical derivation of the binary conductance phenomenon for metallic 120° junctions in the Appendix C.

Figure 7.6(b) presents the histogram of sublattice imbalance δN for 900 semiconducting 120° junctions (7-AGNR, IP_B) with highest and lowest conductance. Interestingly, the junctions with highest τ have predominantly sublattice imbalance of $\delta N = -2$, while $\delta N \geq 0$ is associated with low τ values. The results seem to indicate that the zero-energy states due to the sublattice imbalance still have a strong effect on electronic transport at the band edge. We note, however, that this behavior is difficult to quantify and further investigation is required. Finally, another common feature observed for $\tau > 0.9$ semiconducting 120° junctions is a narrow DOS peak at the band edge, resembling the DOS of the lead. The broadening of the DOS peak, on the other hand, leads to increased "smoothening" of the conductance profile and hence lower τ values. For example, we show in Figure 7.8(a)−(c) a junction displaying almost no backscattering and a very sharp DOS peak at the band edge, while in Figure 7.8(d)−(f) both of these features are less pronounced for a junction exhibiting $\tau = 0.78$. In extreme cases, we observe very small values of DOS near the band edge thus leading to $\tau = 0$ as seen in Figure 7.8(g)−(i).

60° junctions

As far as 60° junctions are concerned, the leads are connected to the complementary sublattices of the scattering region and hence no binary conductance at $E = 0$ is observed. Furthermore, all considered 60° junctions have no sublattice imbalance since only symmetric configurations are investigated in our work.

Nevertheless, several common properties are observed for the 60° and 120° junctions with high τ values. In Figure 7.9(a) we show a representative 5-AGNR 60° junction with $\tau = 1$. The conductance profile of the junction practically matches the one of the lead in the $0 \leq E \leq 0.5 t_1$ energy range [Figure 7.9(b)]. Moreover, DOS in Figure 7.9(c) is nearly constant, similar to the selected metallic 120° junction in Figure 7.4(d), and the LDOS at $E = 0$ reveals that the electron
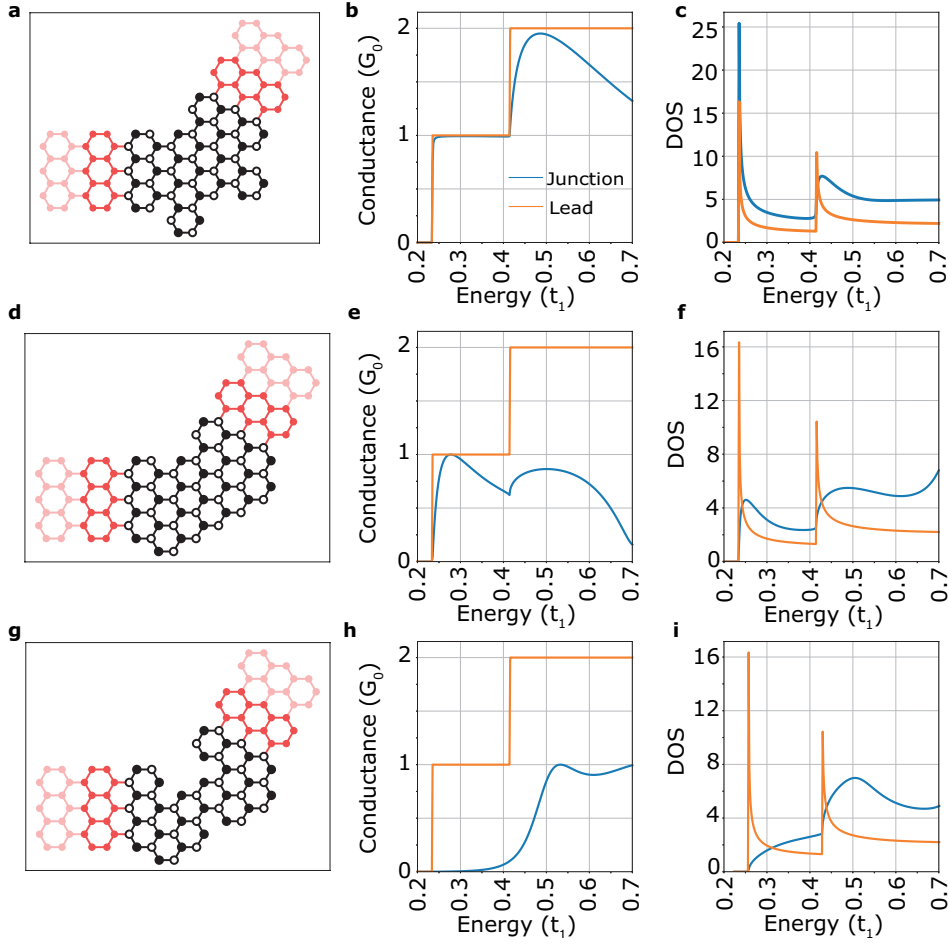
Figure 7.8: (a) Atomic structure of a 7-AGNR 120° junction with $\tau = 1$. (b) Conductance profile and (c) DOS of the junction in the $0 \leq E \leq 0.5t_1$ energy range. (d) Atomic structure of a 7-AGNR 120° junction with $\tau = 0.78$. (e) Conductance profile and (f) DOS of the junction in the $0 \leq E \leq 0.5t_1$ energy range. (g) Atomic structure of a 7-AGNR 120° junction with $\tau = 0$. (h) Conductance profile and (i) DOS of the junction in the $0 \leq E \leq 0.5t_1$ energy range.

density is delocalised over the scattering region [Figure 7.9(d)]. The effect of the localized states on conductance of 60° junctions is however different. While localized states due to sublattice imbalance facilitate transmission across 120° junctions, increased localization due to the presence of zigzag edges often leads to low τ values in metallic 60° junctions.

In extreme cases of $\tau = 0$ we notice that the electron density is localized only on one of the sublattices [Figure 7.9(e)]. However, rare exceptions are found among semiconducting 60° junctions where Fano resonances are observed near the band edge leading to high values of τ [Figure 7.9(f)]. These Fano resonances occur when localized states in the scattering center hybridize with the continuum of states in the lead [Miroshnichenko et al., 2010]. Overall, we observe that in 60° junctions with $\tau > 0.9$ local density of states resembles that in the leads and localization leads to lower transmission.
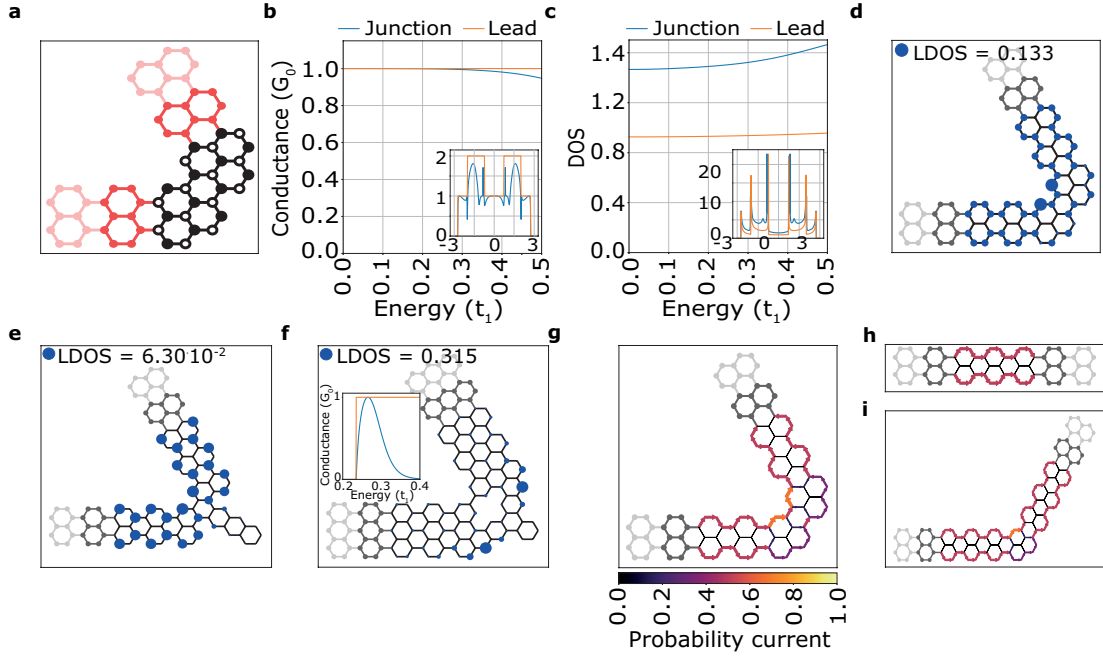
Figure 7.9: Electronic transport in 60° GNR junctions. (a) Atomic structure of a metallic 60° 5-AGNR junction with $\tau = 1$. (b) Conductance profile and (c) DOS of the junction in the $0 \leq E \leq 0.5 t_1$ energy range and the full profiles (insets). (d) LDOS of the junction at $E = 0$. (e) LDOS at $E = 0$ of a selected metallic 60° 5-AGNR junction characterized by $\tau = 0$ at $E = 0$. (f) LDOS at $E = 0$ of a selected semiconducting 60° 7-AGNR junction with $\tau = 0.83$. (g) Probability current at $E = 0$ in the scattering region of the junction shown in panel (a). (h) Probability current at $E = 0$ in the pristine 5-AGNR lead. (i) Probability current in a 120° 5-AGNR junction at $E = 0$ that represents half the 60° 5-AGNR junction in panel (a).

Analyzing local current distributions further helps establishing the design rules of GNR junctions. It can be seen that the current is mainly carried by well defined channels, in the case of 5-AGNR leads localized at the edges, and is preserved in the scattering region [Figure 7.9(g)]. Hence, comparing the probability current in the scattering center to the one of the pristine leads [Figure 7.9(h)] gives an indication about the junction conductance. Strikingly, deviations, such as the one observed in Figure 7.9(g), where the local current on the inside edge is around 2.5 times larger than the current on the outside edge (matching the deviation of LDOS in Figure 7.9(d)) can still lead to equal local current on both edges in the other lead. In general, we observe that junctions with preserved AGNR edges or even parts of scattering center resembling pristine AGNR geometry, usually display high τ values. This further supports the argument against inclusion of zigzag edges in the junctions as concluded from the LDOS analysis. Our observations agree with the work of Chen *et al.* [Chen et al., 2017b], where asymmetry and deviation from the lead geometry were found to decrease the conductance of the junctions.

Finally, we show that 60° junction with $\tau = 1$ [Figure 7.9(a)] can be viewed as two 120° junctions

with $\tau = 1$ connected in series. As the local current leaving the junction in Figure 7.9(i) matches the incoming current, the addition of a second junction with the same structure leads to a 60° "turn" characterized by a high conductance. We also note that combining two equivalent 120° junctions removes the sublattice imbalance and result in having both sublattices attached to the leads, thus eliminating the observed binary conductance phenomenon at $E = 0$.

7.4 Summary and conclusions

In summary, we performed a systematic and exhaustive exploration of 120° and 60° two-terminal junctions in armchair graphene nanoribbons by means of numerical calculations combining tight-binding approximation and Green's function formalism. Our calculations show that irrespective of the lead width and junction angle it is always possible to construct junctions with minimal electron scattering, which could be used as optimal interconnects in all-graphene nanocircuits. Furthermore, having analyzed 438187 unique configurations we propose clear design rules to control the electronic transport properties of such junctions. In particular, we discovered digital, either full on or full off, conductance of metallic 120° junctions, that is governed by sublattice imbalance. In contrast, for 60°-angled junctions highest conductance is achieved when armchair-type edge structure was preserved in the scattering center.

Finally, we present a complete library of results in Supplementary tables 1–36 [Čerņevičs and Yazyev, 2021], which are described in Appendix B. We also provide an easy-to-use online tool TBETA [Čerņevičs et al., 2020a] that allows reproducing all results presented in our work. TBETA is publicly available on the Materials Cloud portal [Talirz et al., 2020] and allows to construct arbitrary GNR junctions and calculate their electronic and transport properties. For more information see Appendix A and B. Overall, our results establish design rules necessary for engineering GNR junction with desired electrical characteristics.

8 Finite Length and Contact Effects on Electronic Transport in Graphene Nanoribbon Heterostructures

Further advances in both experimental and theoretical research are needed to effectively integrate GNRs as components in nanoelectronics. Besides, it is also extremely important to bring both of the approaches together in a complementary manner so that complex experimental phenomena can be explained within theoretical models. Although electronic transport calculations of infinite GNRs, carried out by tight-binding model and Green's function methods, give helpful insights into the characteristics of heterojunctions or defects, they are often difficult to compare with experimental observations. One of the reasons is the assumption that semi-infinite leads of the same geometry are attached to the localized scattering center, hence neglecting the effects of both finite size and realistic contacts. Here, we show that even a basic tight-binding description of metallic leads causes the emergence of interesting transport phenomena, like the edge-state facilitated transport or tunability of the transport gap. On one hand, our results agree with the experimental observation that the 7-AGNR exhibits the bulk band gap only if the length of the ribbon exceeds 8 nm, while on the other hand we show that very short ribbons display conductance peak at $E = 0$ and hence are metallic. Moreover, we also notice that these effects are robust against different lead configurations and attachment points, thus suggesting that it is often enough to include a simple description of metallic leads in order to improve the simulations. Lastly, we show a calculation using a more realistic model that resembles experimental measurements of transport properties with the help of an STM tip.

This chapter is adapted from:

Čerņevičs, K., Yazyev, O.V (2022). Finite Length and Contact Effects on Electronic Transport in Graphene Nanoribbon Heterostructures – In preparation

My contribution to this work was performing the calculations, analysis of the data and writing the paper.

8.1   Motivation

As we saw in the previous chapters, the electronic transport properties of GNRs are often
investigated assuming semi-infinite GNR leads and, therefore, the calculations usually exclude
important finite length effects. For example, Talirz [Talirz et al., 2019] showed a clear band-gap
dependence on the length and termination of 7-AGNRs, where the bulk gap value is only
achieved for 8 nm or longer ribbons. Zang [Zang et al., 2020] and Valdiviezo [Valdiviezo et al.,
2021] observed diverse length dependence on conductance in one-dimensional carbon wires.
Whereas the impact of GNR length on electronic, transport and aromatic properties was
recently explored by Zdetsis [Zdetsis and Economou, 2021]. However, the typical transport
calculations based on Green's function and Landauer formalism show no dependence on the
size of scattering center as semi-infinite leads of the same geometry are assumed to connect the
system. Although, such calculations allowed us to investigate the effects of local perturbations,
such as junctions [Chapters 3, 4 and 7] or defects [Chapters 5 and 6] on the electronic transport
properties, it is generally not sufficient to make comparisons with experimental results. More
importantly, the experimental transport measurements are mainly carried out by contacting
the finite length ribbons with metallic leads (e.g. lifting the GNR with an STM tip as reported
in Section 1.2.3), which are completely neglected in most theoretical models.

The inclusion of metallic leads in the calculations often means departing away from the simple
and efficient tight-binding models as the complexity of the Hamiltonian due to the description
of heteroatoms increases noticeably. Such systems can be then tackled by utilizing DFT
calculations as was done by Chong *et al.* [Chong et al., 2018], who included the gold STM tip in
the calculations to observe the effect on DOS in 7-AGNRs. Nonetheless, another problem arises
when considering the appropriate contact configuration, which is generally not known in the
experiments and can have a major impact on electronic transport properties. For example, it
has been shown that both the extent of hybridization and the contact length between metal
and carbon atoms in carbon nanotubes determine optimum transport conditions [Nemec
et al., 2006; Deretzis and Magna, 2006].

In this chapter, we show that even a very simple tight-binding model can give an invaluable
insight into phenomena that arises from the introduction of finite length systems and attach-
ment of metallic leads. First, we discuss the length-dependent properties, like the transport
gap and emergence of edge state conductance, while afterwards we focus on different con-
figurations of the attached leads. Finally, we apply the acquired knowledge to simulate an
experimentally relevant electronic transport measurement, where a GNR is lifted up from a
metallic surface by an STM tip.

8.2   Methodology

To describe the graphene nanoribbons we utilize a 3NN tight-binding model [see Section 3.2
and Eq. 3.1] with $t_C = t_1 = -2.78$ eV, $t_2 = -0.15$ eV and $t_3 = -0.095$ eV for the first-, second- and

third-nearest-neighbor hopping integrals [Kundu, 2011], whereas the square lattice metallic leads are described only by a single nearest-neighbor hopping integral $t_M = t_1 = -2.78$ eV. In all cases we use the same on-site potential $\epsilon = -0.4$ eV. Our results are expressed in the terms of the nearest-neighbor hopping integral $t_C = t_1 = -2.78$ eV.

Whereas the transport properties are calculated using the Green's function method [Section 2.5] and within the Landauer formalism [Section 2.4]. G is expressed in the terms of conductance quantum G_0 [Eq. 2.60]. The numerical calculations are performed with the help of `kwant` [Groth et al., 2014].

8.3   Results and discussion

We start by comparing the results of a semi-infinite GNR lead based calculation with one that includes the finite size effects and attaches simple metallic leads. We select 7-AGNRs as a representative example as they are one of the most commonly synthesized nanoribbons [Cai et al., 2010; Ma et al., 2017b; Deniz et al., 2017], whereas recently heterojunctions consisting of laterally fused 7-AGNRs have also been gaining attention [Ma et al., 2017a; Wang et al., 2017; Senkovskiy et al., 2021]. For example STM image of bottom-up synthesized 7-AGNRs and the corresponding heterojunctions see Figure 8.1(a). To better illustrate the difference between the calculation methods, the 7-14-AGNR heterojunction is chosen as an otherwise pristine structure except for the interface between the two widths. The main interest of investigating said system is understanding how the junction between the 7- and 14-atom wide segments scatters the electrons and hence affects electronic properties. Consequently, it is enough to prolong the pristine segments of 7- and 14-AGNR, and consider them as semi-infinite leads in order to determine the transport characteristics of the heterojunction [Figure 8.1(b)]. Yet, in this way we completely dismiss the finite size of the experimentally synthesized AGNR and make it difficult to compare our results with experimental measurements, where metal leads are often employed.

We show in Figure 8.1(d) that adding even a simple square lattice metallic leads [Figure 8.1(c)] to our model system provides a striking difference in conductance curves, when compared to the conventional infinite GNR calculations. The red curve corresponding to the semi-infinite GNR leads shows that conductance is affected negligibly near the band edges, with only minor scattering occurring due to the junction. However, the more realistic finite GNR calculations reveal a completely different story. First, we recognize that the conductance obtains a fine structure corresponding to the available localized states in the GNR and thus showing the effect of the contact resistance. Second, we notice the difference between the transport gap in the bulk system and our finite GNR – the closest conductance peaks are about $0.05\,t_C$ away from the band edge of 7-AGNR. Furthermore, we also identify non-negligible conductance from the in-gap states due to the quasi-metallic nature of the 14-AGNR ($3p + 2$ family), which was not observed with semi-infinite GNR leads.
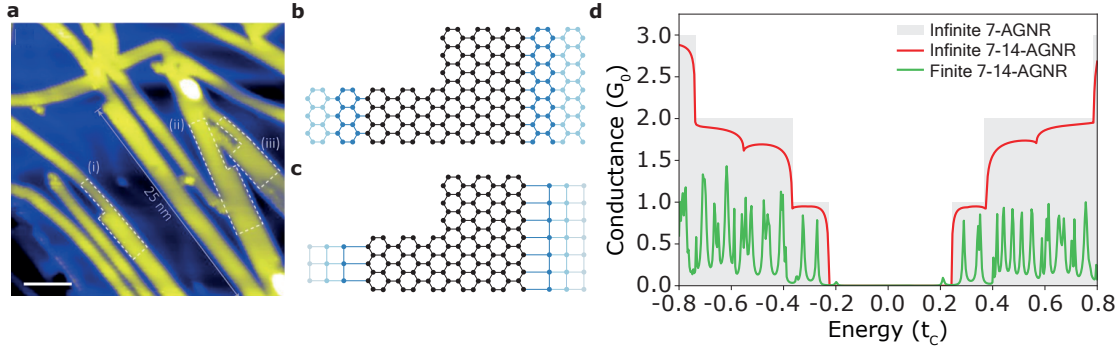
Figure 8.1: (a) STM image of experimentally synthesized 7-,14- and 21-AGNRs and (i) 7-14-AGNR, (ii)14-21- and (iii) 7-21-AGNR nanostructures marked in white. Adapted from [Ma et al., 2017a]. (b) Atomic structure of infinite 7-14-AGNR heterojunction. (c) Atomic structure of finite length 7-14-AGNR heterojunction with semi-infinite square lattice metallic leads. (d) Conductance plots of infinite 7-AGNR, infinite 7-14-AGNR heterojunction [panel (a)] and finite length 7-14-AGNR heterojunction with semi-infinite metallic leads [panel(b)].

8.3.1 Finite length and coupling strength effects

We continue by exploring the finite length effects of pristine 7-AGNR segments in Figure 8.2, where we vary the length L in terms of unit cells and then attach simple semi-infinite metallic nanowire leads to calculate transport properties. For simplicity, we set the metal nearest-neighbor hopping terms to the ones corresponding to graphene ($t_M = t_C = -2.78$ eV), while only varying the metal-carbon (t_{CM}) hopping term. Similar strategy of picking isotropic hopping parameters has been employed in carbon nanotube studies [Krompiewski, 2004]. To explore the importance of coupling between the leads and GNR, we vary the metal-carbon hopping term t_{CM}. We show in Figure 8.2(b) the conductance profile of $L = 10$ 7-AGNR system with varying coupling strength, which is expressed in terms of the nearest-neighbor carbon hopping parameter $t_{CM} = n t_C$, where $0.1 \leq n \leq 1$.

First, we establish that the fine structure of the conductance profile is independent of the metal-carbon hopping strength close to the Fermi energy and second, we observe that the transport is resonant, i.e. conductance peaks of $G = G_0$ appear at discrete energies and become more broadened with increasing t_{CM}. Furthermore, we notice a good correspondence of these conductance peaks with the eigenvalues of the finite 7-AGNR segment that are plotted as vertical black dashed lines. Interestingly, at $E = 0$ there is a conductance peak corresponding to the zigzag end states only at very weak coupling $t_{CM} = 0.1 t_C$, whereas it cannot be observed for larger couplings.

Due to the recognized negligible effect of the metal-carbon coupling on conductance profile, we choose $t_{CM} = 0.4 t_C$ corresponding to a resistive interface [Blanter and Martin, 2007] for further investigation of our finite systems. Finite length effects can be clearly seen in Figure 8.2(c), where longer 7-AGNR segments display conductance peaks closer to the band edge defined by the bulk system. These conductance peaks become more narrow and are shifted
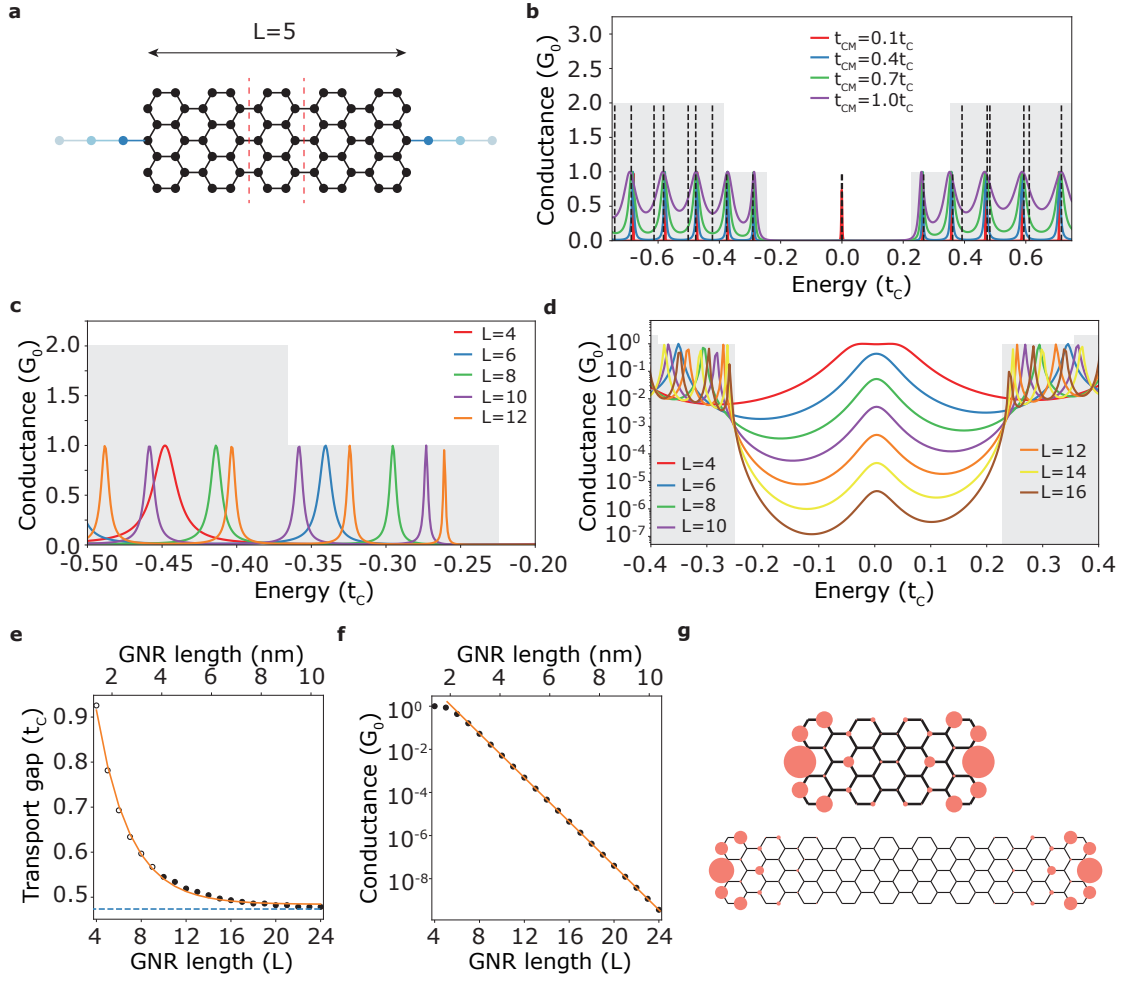
Figure 8.2: (a) Atomic structure of finite length $L = 5$ 7-AGNR with one-atom-wide metallic leads. (b) Conductance plots of $L = 10$ 7-AGNR system with metallic leads and various carbon-metal hopping integral values. (c) Conductance plot near the band edge ($-0.5t_C \leq E \leq 0.22t_C$) and (d) inside band gap ($-0.4t_C \leq E \leq 0.4t_C$) of the system in panel (a) with varying length L. (e) Plot of the transport gap versus the GNR length L, where the black circles indicate the band gap values, empty circles marking the band gap in the presence of a non-negligible zero energy peak, exponential decay ($\Delta_L = 1.65 \times e^{-0.33L} + 0.49$) is marked with red line and the bulk 7-AGNR band gap is illustrated with dashed blue line. (f) Conductance of the peak at $E = 0$ versus the GNR length L, where the numerical values are shown by black dots and the exponential ($G(0)_L = 563 \times e^{-1.16L} - 5.8 \times 10^{-6}$) decay by red line. (g) LDOS plot at $E = 0$ for $L = 4$ (upper) and $L = 10$ (lower) 7-AGNR.

towards the band edge with increasing length. In Figure 8.2(e) we show that the transport gap approaches the bulk value, when $L = 20$ or around 8.5 nm, which is in excellent agreement with Talriz [Talirz et al., 2019]. Here, we established our transport gap as a measure of separation between the two closest peaks inside the bulk bands with a minimum conductance of $G = 0.01G_0$. However, in Figure 8.2(d) we can notice a prominent zero energy peak for short segments of 7-AGNR. Indeed, if we employ the same search for conductance peaks of $G > 0.01G_0$ also inside the bulk gap, we will find that for $L < 10$ there is no transport gap and the short 7-AGNR segments are actually metallic. Depending on how one defines the threshold of minimum conductance, small variations can be observed in the cut-off length of metallic or semiconducting segments. For example, we can still distinguish a clear zero energy peak even for $L = 16$ 7-AGNR segments in Figure 8.2(d), although the amplitude of this peak is a couple orders of magnitude smaller than the conductance peaks in the bulk bands. The magnitudes of the zero conductance peak are plotted in Figure 8.2(f) and show an exponential dependence on the length of the 7-AGNR segment. We attribute this to the exponential decay of zigzag edge state's LDOS with each successive zigzag chain as observed by Nakada and co-workers [Nakada et al., 1996] in finite graphite systems with zigzag edges. We discover in Figure 8.2(g) that the majority of the density is located on zigzag edges of both sides of the 7-AGNR segments ($L = 4$ and $L = 10$) and that it quickly decays towards the center of the segment hence providing little overlap between the two edge states. Thus, we can observe that the magnitude of the conductance peak decreases exponentially with the longitudinal separation of the two zigzag ends. To recap, we show that already an extremely simplified lead model can give rise to exciting finite length effects on the electronic transport properties and the qualitative results are largely independent on the choice of parameters, such as metal-carbon coupling strength.

8.3.2 Lead configuration effects

Although we established that the fine structure of the conductance profile is largely independent of metal-carbon coupling t_{CM} magnitude, we can not fully dismiss the importance of the lead configuration. Therefore, we turn our attention to the geometric shape and position of our leads. For a greater variability of the lead geometry we now consider a 7-14-AGNR heterostructure defined by two segment lengths – $L_7 = 8$ and $L_{14} = 8$. Figure 8.3(a) displays three lead configurations corresponding to nanowire (red), half (blue) and full (green) square lattice leads.

We can vary the position of the attachment of the nanowire by moving it up or down in any of the seven sites on the right side marked by the numbers. We then calculate the conductance profiles of different attachment positions and display three characteristic profiles in Figure 8.3(c). It can be seen that the overall fine structure of the conductance displays peaks at the positions of the finite system's eigenstates and due to the extended 14-AGNR segment we also notice multiple in-gap states. Interestingly, these in-gap states are not fully resonant ($G \neq G_0$) and rather have a decaying intensity towards the zero energy state. Furthermore, it can be noted that different positioning of the leads can decrease the conductance by more than an
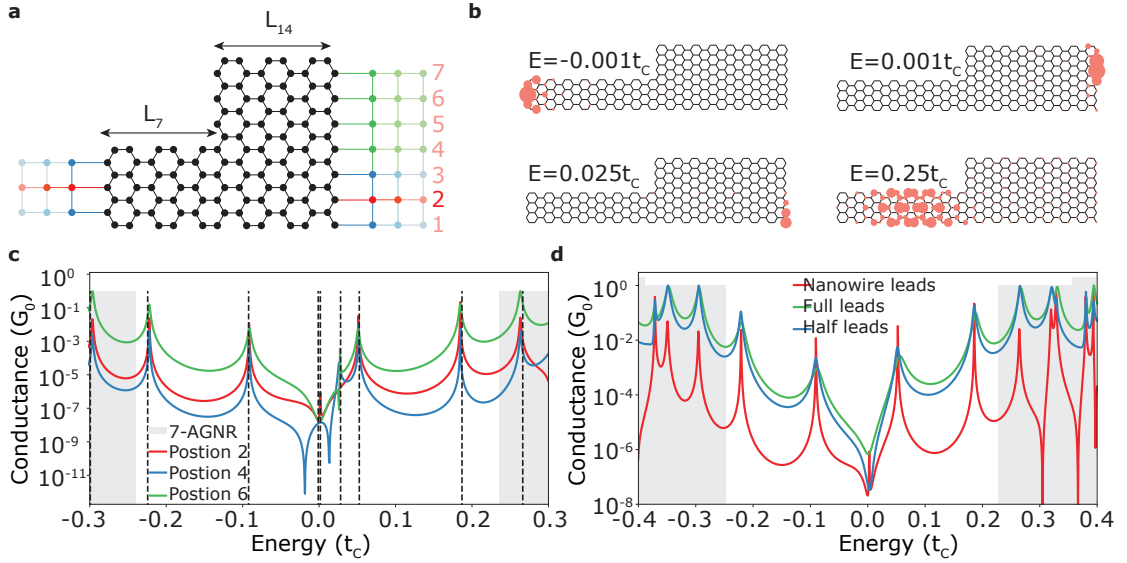
Figure 8.3: Lead attachment point dependence. (a) Atomic structure of 7-14-AGNR finite length structure with multiple lead attachment points. (b) LDOS of ($L_7 = 8$ and $L_{14} = 8$) 7-14-GNR nanostructure at different E values. (c) Conductance plot of 7-14-AGNR with one-atom-wide metallic leads attached at different positions. (d) Conductance plot of 7-14-AGNR with different metallic lead configurations.

order of magnitude. More apparent changes can be observed around the Fermi energy, where there are two almost degenerate zero energy states and one state at $E = 0.025 t_C$. When the right lead is attached in position 4, we discover two distinct anti-resonances around Fermi level, which are not observed in other configurations. The origin of these anti-resonances can be traced back to the LDOS of the low-energy states displayed in Figure 8.3(b). We show that the first three states are associated with the zigzag terminations and that the attachment position 4 gives the largest overlap between states 2 and 3 thus leading to an interference and prominent anti-resonances around Fermi level.

Noticing how the conductance characteristics can be influenced by varying the position of the nanowire attachment, we now expand our leads to a square lattice as seen in Figure 8.3(a) marked by the blue and green lattice points. First, we consider 3-atom wide leads fully connecting the left side of our heterostructure and the same exact lead on the right side attached on positions 1-3 and dub this configuration "half leads". Second, we consider "full leads", which have the same lead on the left side, but now expand our right lead over all seven attachment points hence fully covering both sides. Lastly, we also consider the nanowire attachment in position 2.

In Figure 8.3(d) we notice only marginal differences in the overall shape of the conductance profile, while main differences are observed in the magnitude of the peaks. We observe that square lattice leads display resonant peaks inside the bulk bands, where $G = G_0$. Whereas one-atom-wide nanowire has an order of magnitude lower conductance. For example, looking

at the LDOS of the $E = 0.25 t_C$ state, we notice that although the majority of density is concentrated on the 7-AGNR segment, the density is also more delocalized over the whole structure and thus attachment in multiple locations on the right side give rise to higher conductance. Intriguingly, the density associated with position 2 is comparatively lower than the density on other sites thus further decreasing the conductance of this particular state, when nanowire leads are attached. Overall, we discover that the positioning of the leads and the type of leads has an effect on the magnitude of the conductance, but the general shape of the conductance profile remains largely invariant. We attribute these changes in magnitude to the nature of LDOS, where either accurately placed or just a larger number of attachment points coinciding with the spatial distribution of the electron density can facilitate larger conductance through the localized states. Our observations agree with the work done by Nemec and colleagues [Nemec et al., 2006], where contact length of metals played a major influence on electronic transport properties in carbon nanotubes.

8.3.3 Simulating STM transport measurement

After establishing the importance of finite size effects and lead configurations, we aim to use our simplified model to simulate an experimental setup of measuring the conductance of a GNR heterostructure by an STM tip [see Section 1.2.3]. In a typical experiment one side of the GNR would be lifted by the STM tip, while the rest of the GNR would be in contact with the gold surface [Figure 8.4(b)]. The conductance then is measured in the free standing GNR segment between the STM tip and gold surface. Continuously lifting up the STM tip reveals an increasing length of free standing GNR segment. We model this setup by attaching a nanowire to one side of the GNR, while a full square lattice leads are attached to the other side of the GNR, thus representing STM tip and gold surface respectively. The lifting motion is modeled by increasing the length of our GNR as with increasing STM height we would make a larger part of the GNR free-standing [Fig 8.4(a)]. For our calculation we consider a QD-like system [Čerņevičs et al., 2020c] of 7-14-7-AGNR with the following length – $L_{AGNR} = L_7 + L_{14} + L_7 = 3.4 + 5.1 + 3.4 = 11.9$ nm.

Figure 8.4(c) reveals a conductance map with respect to the free-standing GNR length. As established earlier, the short 7-AGNR segments display metallic behaviour due to the zero energy conductance peaks, while the states corresponding to the bulk GNR can be seen to quickly converge towards the bulk value. Interestingly, when a segment of 14-AGNR becomes (lower red dashed line) free-standing, we can observe the emergence of in-gap states due to the quasi-metallic character of 14-AGNR. These states rapidly converge towards zero energy with increasing length of the 14-AGNR segment. However, we can notice that the magnitude of these peaks ($G \approx G_0 \times 10^{-6}$) is much lower than the states corresponding to the bulk 7-AGNR ($G \approx G_0$). Finally, once the 14-AGNR segment ends and another 7-AGNR segment emerges as free-standing (upper red dashed line), we notice slowing down of the convergence towards zero energy and the low-energy states remain almost constant with further increasing 7-AGNR segment length. This is a further confirmation of the metallic character of these emerging
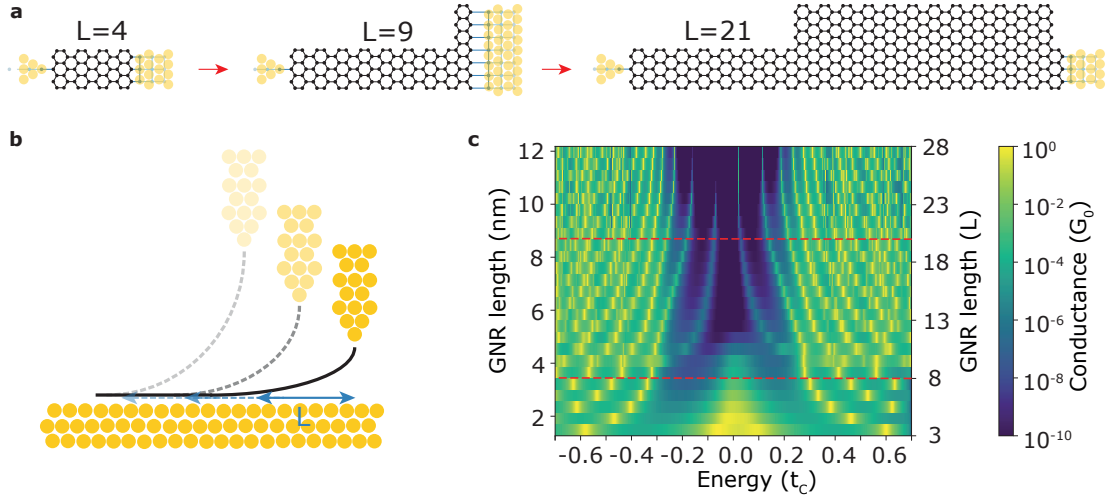
Figure 8.4: Modeling STM transport measurements. (a) Atomic structure of the GNR fragment of increasing length between metallic leads. (b) Scheme of STM tip lifting a GNR from gold surface. (c) Conductance map of increasing GNR fragment length. The lowest dashed red line indicates the transition from 7-AGNR to 7-14-AGNR segment, while the second one indicates transition from 7-14-AGNR to 7-14-7-AGNR segment as presented in panel (a).

states associated with the 14-AGNR segment. Although these metallic states are orders of magnitude lower than the states associated with bulk 7-AGNR, we have to consider the effect of our lead configurations seen in Section 8.3.2 and thus not discard the possibility of larger peak magnitudes with different lead setups.

8.4 Conclusions

In summary, we have investigated the impact of attaching simple metallic leads to finite GNR fragments. We show that in contrast to the standard calculations involving semi-infinite GNR leads, utilizing fixed-length GNR fragments yield drastically different conductance profiles and capture many finite length effects. For example, we reveal that transport gap of 7-AGNR fragments reaches the bulk value, when they extend to over 8 nm, while very short fragments $L < 2$ nm are actually metallic due to the tunneling zigzag states.

We also demonstrate that the transport close to the band gap is resonant-like, with conductance peaks matching localized states on the finite length GNR nanostructure. Furthermore, it is apparent that the general conductance trends are largely independent of the chosen carbon-metal hopping parameters or even the width of the lead. Although, the fine structure of the conductance profile is largely invariant, it is the magnitude of the conductance that shows the largest dependence on either attachment positions or the width of the metallic leads. We reason that the magnitude is closely dependent on the localization patterns of the electron density on the GNR and attachment points coinciding with increased density will lead to larger conductance.

Finally, we designed a basic tight-binding model to gain intuitive understanding of an experimental conductance measurement of a 7-14-7-GNR heterojunction between the STM tip and gold surface. We calculate a typical conductance map vs the STM height (GNR length) and show the emergence of new in-gap states associated with different parts of the heterojunction. Overall, we give an insight into modeling more complex structures closer resembling the experimental setups by a very simple tight-binding model.

9 Concluding Remarks

Since the seminal work of Cai and co-workers [Cai et al., 2010] more than a decade ago, bottom-up synthesized graphene nanoribbons have attracted a large interest as potential building blocks for next-generation nanoelectronics. Part of the appeal arises due to the unprecedented atom-scale control over the GNR structure and hence also the electronic properties. Yet, larger significance can be attributed to the possibility to design GNR junctions, thus providing remarkable opportunity to seamlessly integrate multiple components in complex nanoelectronic devices. Recent efforts in both the synthesis [Wang et al., 2017; Jacobse et al., 2017; Chen et al., 2017b; Rizzo et al., 2018; Sun et al., 2021] and theoretical research [Liwei et al., 2016; Chen et al., 2017a; Saiz-Bretín et al., 2019; Zhou et al., 2020] of GNR junctions has been made, but overarching structure-property relationships in such systems are still eluding and consequently also hampering further progress in this field.

This thesis, therefore, has been devoted to fill this gap by examining electronic transport properties in experimentally produced graphene nanoribbon junctions and by establishing underlying design principles of new junctions. In particular, we focused on three directions – modeling and understanding width-modulated GNR structures, exploring experimentally observable defects in various GNRs and designing potential components for nanoelectronics. Our investigation was based on a combination of DFT, TB and Green's function methods as well as a high-throughtput screening to effectively characterize thousands of GNR junctions.

9.1 Overview of results

In Part I we determined the origin of previously unexplained even-odd phenomena in edge-functionalized GNRs, where guest molecules displayed contrasting behavior depending on their width. Previous assumption that conductance is affected at all energies matching the electronic levels of isolated molecule was disproved by showing that unique electron density localization patterns, based on the number of benzene rings, can lead to non-interacting states. We demonstrated that in cases, where there is zero electron density on linking atoms between the ribbon and the molecule, the conductance is not affected at that energy. This

in turn adds another degree of complexity in order resolve electronic "fingerprint" of guest molecules. We also expanded this research by considering higher theory level models, such as third-nearest-neighbor TB model and DFT calculations, and confirmed that even-odd effect is not an artifact of the simplified 1NN-TB model. However, this phenomenon was found to be less pronounced as a consequence of larger band dispersion.

Next, we investigated the electronic transport in width-modulated heterojunctions that can be seen as extensions of the edge-functionalized systems. Recently synthesized GNR junctions were taken as a basis to explore graphene quantum-dots, embedded in metallic armchair nanoribbon leads. We found that the transport is dominated by the length scale of the quantum dot, where a smooth transition from an antiresonant transport regime to a resonant regime was observed with increasing length of the system. More interestingly, we also noticed that upon exceeding a critical length of the quantum dot a width-dependent transport gap opens, thereby giving rise to built-in one-dimensional metal-semiconductor-metal junctions.

In Part II of the thesis we examined "bite" defects – missing benzene rings at the GNR edges – in a combined experimental and theoretical effort in order to determine the adverse effect on electronic transport properties. "Bite" defects were shown to form by phenyl-ring cleavage from the precursor molecule during the cyclo-dehydrogenation step and were observed in both AGNR and chevron GNRs. First, we showed that "bite" defects can disrupt the electronic transport of 9-AGNRs by reducing the conductance up to 98% in the vicinity of the band edges, depending on the number and configuration of the defects. Second, we expanded our theoretical investigation to wider nanoribbons and discovered that conduction properties become less sensitive to the defects for wider ribbons belonging to the $3p+1$ and $3p+2$ families. Our findings accordingly suggest either utilizing alternative precursor molecules or employing GNRs form the $3p+1$ and $3p+2$ families for electronic devices, in order to mitigate unfavorable effect of the "bite" defects.

Subsequently, we turned our attention to chevron-type GNRs and noticed that particular placements of "bite" defects result in diverse response on the conductance in different bands, thus giving us a degree of control over transport properties. We applied the lessons learned about the impact of defects in single GNRs in order to engineer transport properties in more complex nanostructures. For instance, by strategically placing a pair of "bite" defects in laterally fused triple fluorene-chevron GNR, we constructed a switch to control electron pathways in the nanostructure. Fascinatingly, we also utilized "bite" defects to increase conductance between two leads in a triple chevron GNR junction from 38% to 47%. Overall, in this part of the thesis we outlined how experimentally detected "bite" defects affect transport properties in GNRs and provided guidelines on how to design nanoelectronic components.

Chapter 7 was dedicated to exploring GNR integration in next-generation electronics by screening over 400000 angled GNR junctions for potential interconnects. First, we concluded that irrespective of the lead width and junction angle it was always possible to find junctions with conductance close to the limit defined by the GNR leads. Next, we revealed underlying

structure-property relationships, where either full on or full off conductance of metallic 120° junctions was observed due to the bipartite symmetry of graphene lattice and the presence of resonant states localized at the junction. Whereas for 60°-angled junctions preserving the armchair-type edge structure in the scattering center led to the highest conductance. Finally, we presented our results curated in a library of junctions and also provided an online tool TBETA [Čerņevičs et al., 2020a] that implements user-friendly graphical interface for tight-binding calculations.

Ultimately, we investigated the finite length and contact effects by attaching simple square lattice leads to GNRs. We demonstrated that in contrast to the conventional tight-binding calculations involving semi-infinite GNR leads, drastically different conductance profiles emerged from utilizing fixed-length GNR fragments. For instance, the transport gap of 7-AGNR fragments reached the bulk value, when they were longer than 8 nm, whereas, surprisingly, very short fragments $L < 2$ nm were exhibiting tunneling zigzag states and hence were actually metallic. Besides, we confirmed that these effects are largely robust against different lead configurations, thus validating the inclusion of trivial metallic leads in order to improve the simulations. Overall, we gave an insight into modeling more realistic structures, closer resembling the experimental setups, by a very simple tight-binding model.

9.2   Perspectives

Although apparent progress has been made in both the experimental and theoretical research of GNRs in the past years, new questions and hence potential research directions arise every day. Here, I will briefly provide some of the key problems related to the work done in this thesis that should be tackled in the future.

Despite not mentioned in this thesis, we have also explored spin-polarized transport in ZGNRs with "bite" defects [Pizzochero et al., 2021a], whereas recent work by Sanz and co-workers [Sanz et al., 2022] showed spin-filtering effects in crossed graphene nanoribbon junctions. Both of these works demonstrate the applicability of GNRs as building blocks for exciting spintronic devices, hence further work focusing on integrating such junctions in actual devices is of paramount importance.

Next, to truly unlock the potential of all-carbon based electronics, new solutions need to be found in order to mitigate the effects of Schottky barriers at metal-GNR contacts. One of the possible directions could be eliminating the metal contacts entirely by producing devices consisting entirely out of GNRs, such as side-gate transistors from triple GNR junctions. Recent works [Jiang et al., 2019; Weckbecker et al., 2020; Wu et al., 2020] utilized changes in chemical structure in molecule-graphene(metal) junctions to show transistor-like effects, thus paving way for similar calculations based on functionalized GNR junctions. However, due to the bad screening of semiconducting GNR electrodes, many extra layers are needed, thus drastically limiting the size of accessible systems for finite-bias calculations in DFT [Papior, 2016].

Finally, as a consequence of the work done in Part II and Part III of this thesis, I also envision new experimental challenges arising. First, it is critical to develop more precursors molecules to achieve even wider selection of edge structures, widths and avert formation of defects. Second, there is a need for tighter control over the growth conditions in order to produce GNRs with proper lengths and alignments for more effective device fabrication due to the observed finite length and contact effects. Lastly, another big obstacle to tackle is the on-surface synthesis of precise and well-defined junctions and the subsequent coupling of such junctions in order to produce next-generation components for nanoelectronics.

A Tight-Binding Electronic Transport Application for Graphene Nanoribbon Junctions

Tight-Binding Electronic Transport Application (`TBETA`) [Čerņevičs et al., 2020a] for graphene nanoribbon junctions provides a simple yet powerful graphical interface for building structures of two-terminal junctions of graphene nanoribbons at angles 60°, 120° and 180°. The electronic structure and transport properties of the constructed junctions are calculated using the 1st, 2nd or 3rd nearest-neighbour tight-binding model [Kundu, 2011] in combination with the Landauer formalism and Green's function techniques. All of the numerical calculations are performed using the `Kwant` code [Groth et al., 2014], but instead of the traditional way of writing Python commands, we provide a graphical user interface. We utilize open-source application `Voilà` [Voilà, 2022] to convert Jupyter notebooks [Kluyver et al., 2016] containing our code into standalone web application providing a code-free environment. The interaction with the underlying code is provided through `ipywidgets` library [ipywidgets, 2021] that provides HTML widgets such as sliders, toggle buttons, text boxes, etc.

For instance, the following instructions describe how to design the atomic structure of any junction:

1. Select the desired junction angle, width of GNR leads and four additional parameters called distance, shift, quantum dot width and chirality.

2. Atoms can be removed from the initial scattering region by entering the corresponding atom number(s) and then pressing the 'Remove atoms' button.

3. Initial structure template with no atoms removed can be reset by pressing 'Reset system'.

We display the interface to design the atomic structure in Figure A.1, where we have selected to construct a 120° junction between two 5-AGNR leads and calculated the associated lead band structure with the first-nearest-neighbor tight-binding model. Next, the electronic properties such as conductance and density of states are calculated in a selected energy range, while local density of states, local current map and wavefunctions in the lead channels are displayed for a

selected single energy value defined in terms of the tight-binding nearest-neighbor hopping integral t. Figure A.2 shows the calculated conductance and DOS in a user defined energy range $-1t \leq E \leq 1.5t$, whereas Figure A.3 presents the spatial electronic properties at $E = 0.5t$.
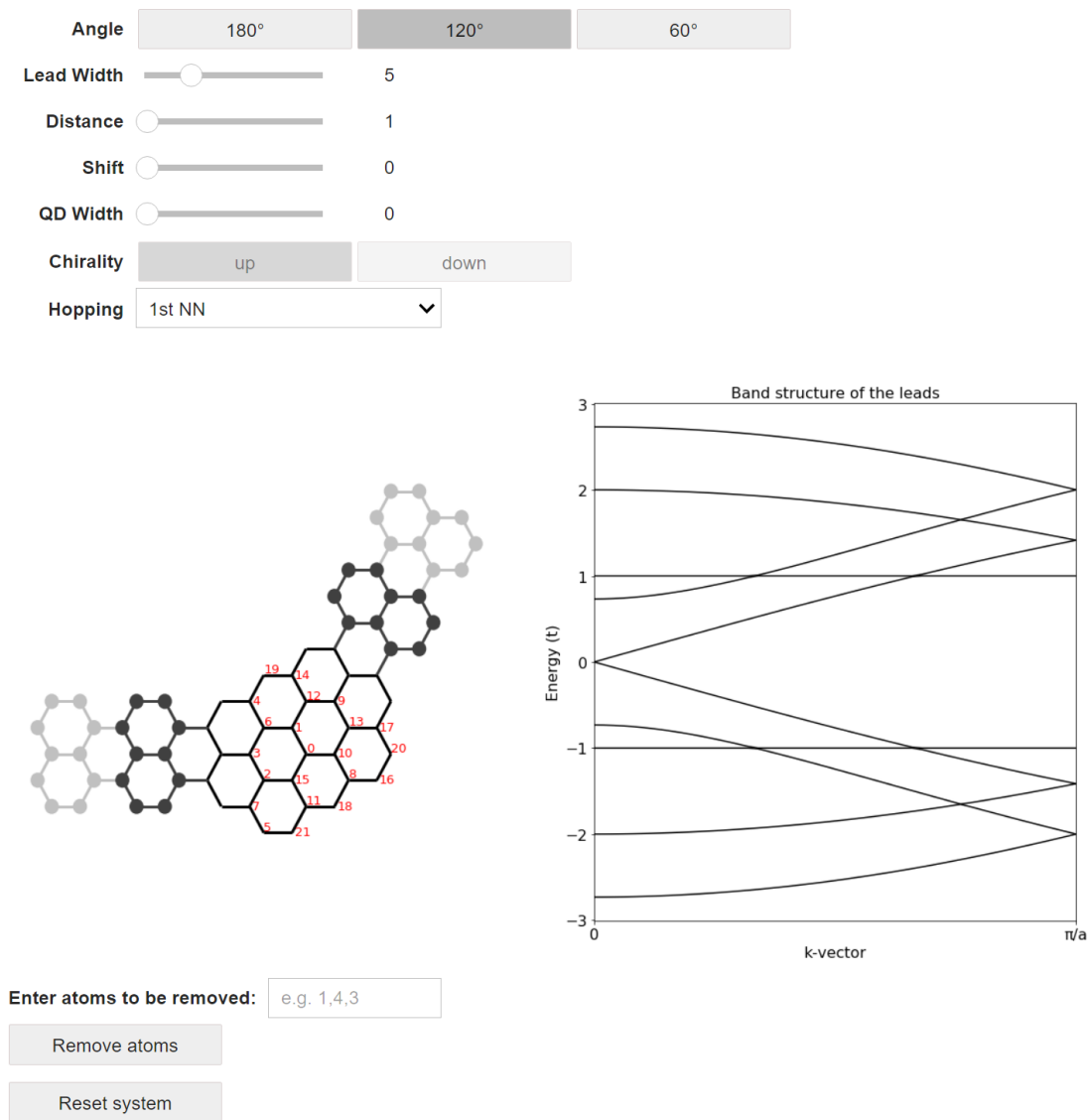
Figure A.1: The graphical interface of TBETA for designing GNR junctions.

Select the energy range ('*Min Energy*' and '*Max Energy*') and press '*Calculate*' for computing the conductance and the density of states of the designed GNR junction. The results are compared to that of the ideal leads. Since this computation may take some time, its progress is indicated by the progress bar. You may copy the datasets to the clipboard.
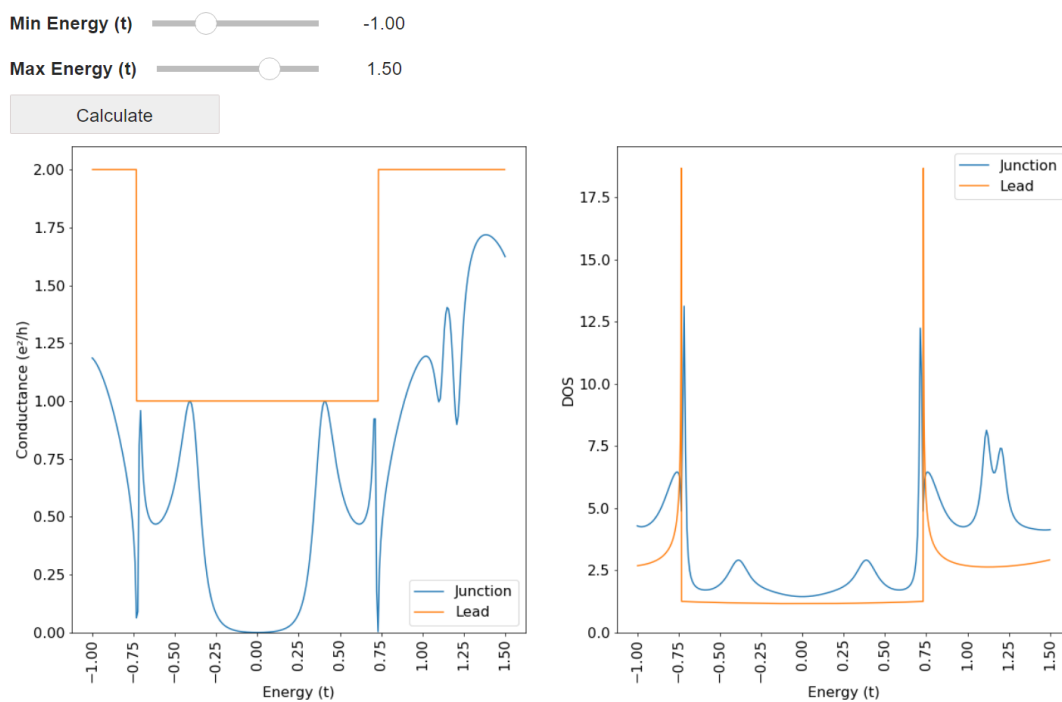
Figure A.2: Calculating electronic transport properties of GNR junctions in TBETA.

Appendix A. Tight-Binding Electronic Transport Application for Graphene Nanoribbon Junctions

Select an energy at which the local density of states, local current map and the wavefunction(s) of the lead channel(s) are displayed. The local current map displays the cumulative current from all channels involved at the selected energy.
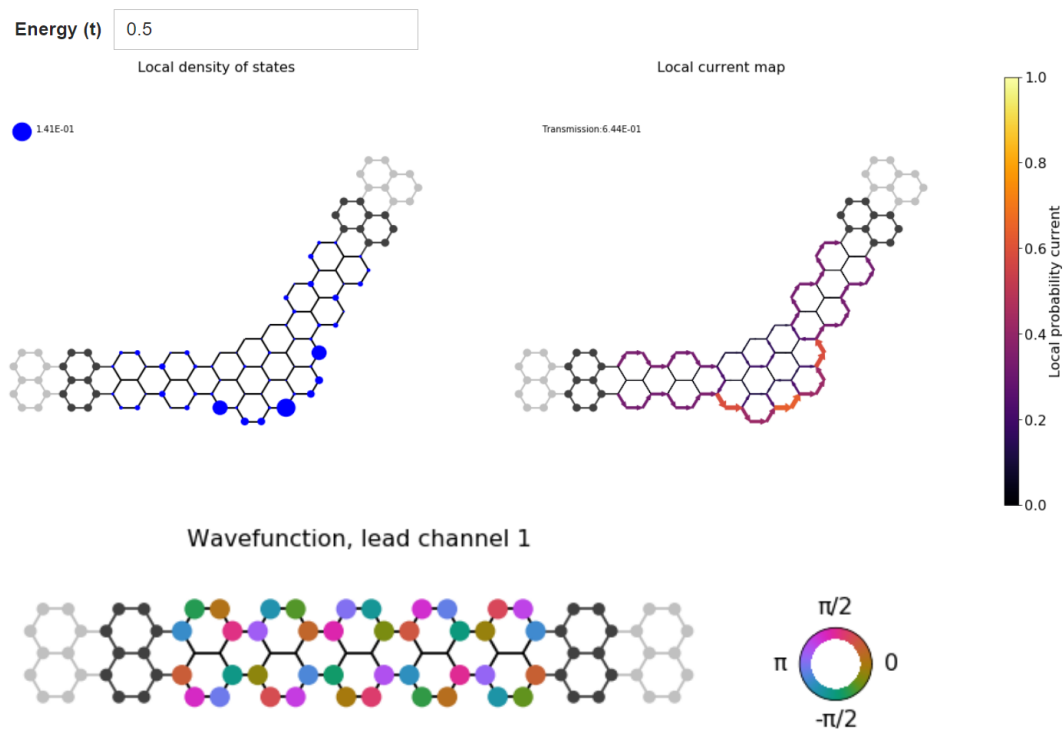
Figure A.3: Spatially-resolved electronic properties of GNR junctions in TBETA.

B Library of Graphene Nanoribbon Angled Junctions

We provide the raw data associated with our high-throughput screening and also curate it in a PDF-based library for easier viewing [Čerņevičs and Yazyev, 2021]. First, we have classified 438187 unique GNR junction configurations hierarchically into 36 distinct classes according to the following descriptors:

1. junction angle (120 or 60 degrees);

2. width (4-AGNR to 9-AGNR);

3. distance between the leads (intersection point class, only for 120 degree);

4. chirality (only even-numbered AGNRs).

For the 27 classes containing less than 4000 configurations each, we sort all of the junctions accordingly to the descriptor τ and present the associated structural and electronic transport characteristics as displayed in Figure B.1. This includes the information about the width, angle, number of atoms, sublattice imbalance and also the atomic structure of a particular AGNR junction. Both the conductance and DOS plots are showcased in the $-3t \leq E \leq 3t$ and $0 \leq E \leq 0.5t$ regions, whereas the probability current and LDOS are plotted at either Fermi level or band edge for metallic and semiconducting junctions, respectively. Whereas for the remaining 9 classes hosting more than 4000 configurations each we only select the structures that display high τ values and compile identical PDFs. For parties interested in uncovering the properties of systems exhibiting low τ values we invite them to access our online tool `TBETA` [Čerņevičs et al., 2020a] that allows reproducing not only all of our results, but also design junctions outside the scope of this thesis.
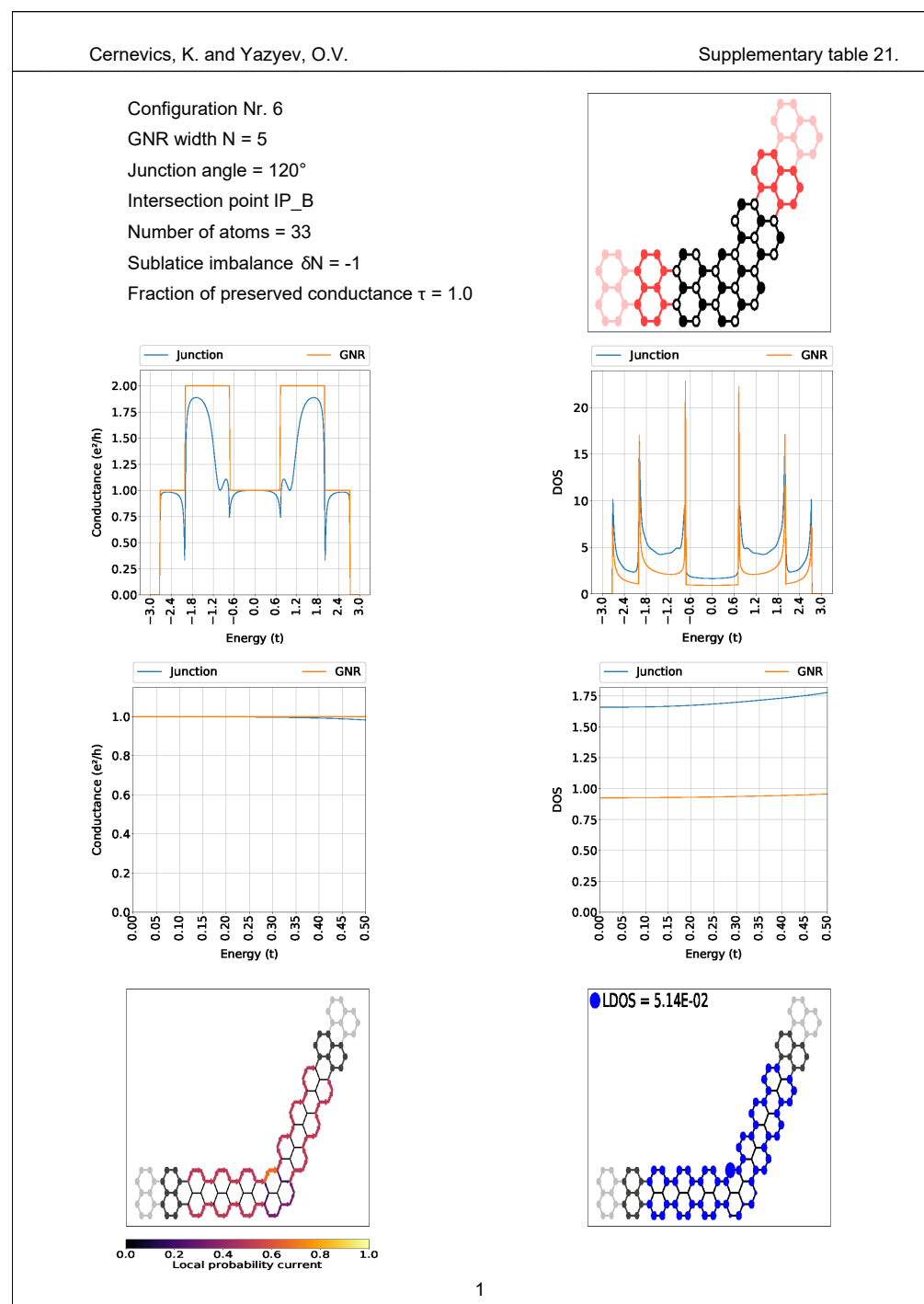
Figure B.1: An example page from Supplementary Tables categorizing a 120° 5-AGNR junction. Starting from the top row: Information regarding the classification of the junction (left), atomic structure of the junction (right). Second row - conductance (left) and DOS (right) plots in the $-3t \leq E \leq 3t$ region. Third row - zoom in of conductance (left) and DOS (right) in the $0 \leq E \leq 0.5t$ region. Last row - probability current (left) and LDOS (right) at $E = 0 + \delta E$.

C Binary Conductance Phenomenon Across Metallic 120° Junctions

Below we discuss the origin of binary conductance in metallic 120° AGNR junctions. We will demonstrate how in the case of no sublattice imbalance the structure of Hamiltonian matrix $\mathbf{H}_D$ results in $\mathbf{T} = 0$, and hence $G = 0$ at $E = 0$. We will be representing our H_D as a block matrix, where zero blocks correspond to the two sublattices and the only hopping terms are between atoms in the complementary sublattices

$$\mathbf{H}_D = \left[\begin{array}{c|c} 0 & \mathbf{t}_{ab} \\ \hline \mathbf{t}_{ab}^{\dagger} & 0 \end{array} \right]. \tag{C.1}$$

Next, as discussed in the Chapter 7, we recall that the self-energy of the leads is acting only on one sublattice for the 120° 2-terminal junctions

$$\mathbf{H}_{eff}(E) = \mathbf{H}_D + \mathbf{\Sigma}_L(E) + \mathbf{\Sigma}_R(E) = \left[\begin{array}{c|c} 0 & \mathbf{t}_{ab} \\ \hline \mathbf{t}_{ab}^{\dagger} & 0 \end{array} \right] + \left[\begin{array}{c|c} \mathbf{\Sigma}_L(E) + \mathbf{\Sigma}_R(E) & 0 \\ \hline 0 & 0 \end{array} \right]. \tag{C.2}$$

We continue by expressing the Green's function as a block matrix

$$\mathbf{G} = ((i\eta)\mathbf{I}_D - \mathbf{H}_{eff})^{-1} = \left[\begin{array}{c|c} i\eta - \mathbf{\Sigma}_{L+R} & -\mathbf{t}_{ab} \\ \hline -\mathbf{t}_{ab}^{\dagger} & i\eta \end{array} \right]^{-1} = \left[\begin{array}{c|c} \mathbf{G}_a & \mathbf{G}_b \\ \hline \mathbf{G}_c & \mathbf{G}_d \end{array} \right], \tag{C.3}$$

where we introduce the subscripts to denote blocks a, b, c and d in the matrix. Remembering that only one sublattice is attached to the leads, the block matrix $\Gamma_{L(R)}$ is similarly expressed as

$$\mathbf{\Gamma}_{L(R)} = \left[\begin{array}{c|c} \mathbf{\Gamma}_{L_a(R_a)} & 0 \\ \hline 0 & 0 \end{array} \right]. \tag{C.4}$$

As the transmission across the junction is obtained by taking the trace of the matrix product in Eq. C.5, we refer to this product as $\mathbf{F}$ for clarity

$$T(E) = Tr[\mathbf{F}] = Tr[\mathbf{F}_1\mathbf{F}_2] = Tr[\mathbf{\Gamma}_L\mathbf{G}\mathbf{\Gamma}_R\mathbf{G}^{\dagger}], \tag{C.5}$$
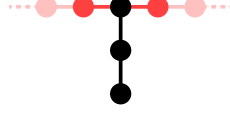
Figure C.1: One-dimensional chain model with 3-site scattering region.

where we also assign $\mathbf{F}_1 = \boldsymbol{\Gamma}_L \mathbf{G}$ and $\mathbf{F}_2 = \boldsymbol{\Gamma}_R \mathbf{G}^\dagger$. Now, we are only interested in block $\mathbf{G}_a$ as the final matrix F can be expressed as block multiplications:

$$\mathbf{F} = \boldsymbol{\Gamma}_L \mathbf{G} \boldsymbol{\Gamma}_R \mathbf{G}^\dagger = \left[\begin{array}{c|c} \boldsymbol{\Gamma}_{L_a} \mathbf{G}_a \boldsymbol{\Gamma}_{R_a} \mathbf{G}_a^\dagger & \boldsymbol{\Gamma}_{L_a} \mathbf{G}_a \boldsymbol{\Gamma}_{R_a} \mathbf{G}_b^\dagger \\ \hline 0 & 0 \end{array} \right] = \left[\begin{array}{c|c} \mathbf{F}_a & \mathbf{F}_b \\ \hline 0 & 0 \end{array} \right], \tag{C.6}$$

where indices a and b once again refer to the corresponding blocks of the matrix. We also note that taking the trace of $\mathbf{F}$ will only involve the block $\mathbf{F}_a$. Therefore, showing that the block $\mathbf{G}_a$ is zero will imply that the block $\mathbf{F}_a$ is also zero, finally leading to $T = 0$. Block matrix inversion is carried out from Eq. C.3 to obtain $\mathbf{G}_a$

$$\mathbf{G}_a = ((i\eta - \boldsymbol{\Sigma}_{L+R}) - (-\mathbf{t}_{ab} \frac{\mathbf{I}}{i\eta} (-\mathbf{t}_{ab}^\dagger)))^{-1}. \tag{C.7}$$

In the limit of $\eta \to 0$ we see that block $\mathbf{G}_a$ approaches 0 as well.

Further, we can show analytically perfect transmission $T = 1$ (and hence $G = G_0$) at $E = 0$ by considering a simplified model system with sublattice imbalance. The model is a one-dimensional chain with the scattering region consisting of 3 sites shown in Fig. C.1. Note that this system inherits the discussed properties of more complex systems such the 120° angled GNR junctions discussed in our work. All energy-dependent variables are calculated for $E = 0$.

We will start by transforming the basis of our matrices as ultimately we are interested in the trace of matrix product F and the trace is invariant under the change of basis. As the new basis we will choose the eigenvectors of $\mathbf{H}_D$; the $\mathbf{H}_D$ is then transformed to diagonal matrix $\tilde{\mathbf{H}}_D$ with the trace of 0 as the eigenvalues are pairwise symmetric around 0.

$$\mathbf{H}_D = \begin{bmatrix} 0 & 0 & t \\ 0 & 0 & t \\ t & t & 0 \end{bmatrix} \tag{C.8}$$

$$\mathbf{P}^{-1} \mathbf{H}_D \mathbf{P} = \tilde{\mathbf{H}}_D \begin{bmatrix} \sqrt{2}t & 0 & 0 \\ 0 & 0 & 0 \\ 0 & 0 & -\sqrt{2}t \end{bmatrix} \tag{C.9}$$

$$\mathbf{P} = \begin{bmatrix} \dfrac{1}{\sqrt{2}} & -1 & \dfrac{-1}{\sqrt{2}} \\ \dfrac{1}{\sqrt{2}} & 1 & \dfrac{-1}{\sqrt{2}} \\ 1 & 0 & 1 \end{bmatrix} \tag{C.10}$$

Similarly, we transform the self-energy energy matrix $\mathbf{\Sigma}_{L(R)}$ in the new basis.

$$\mathbf{\Sigma}_{L(R)} = \begin{bmatrix} it & 0 & 0 \\ 0 & 0 & 0 \\ 0 & 0 & 0 \end{bmatrix} \tag{C.11}$$

$$\tilde{\mathbf{\Sigma}}_{L(R)} = \begin{bmatrix} \frac{ti}{4} & \frac{t\sqrt{2}i}{4} & \frac{-ti}{4} \\ \frac{t\sqrt{2}i}{4} & \frac{ti}{2} & \frac{-t\sqrt{2}i}{4} \\ \frac{-ti}{4} & \frac{-t\sqrt{2}i}{4} & \frac{ti}{4} \end{bmatrix} \tag{C.12}$$

We now obtain the Green's function and we notice that the real part of the trace is zero, hence showing that the symmetry along the diagonal is preserved.

$$\tilde{\mathbf{G}} = \begin{bmatrix} \frac{1}{\sqrt{2}t} & \frac{-1}{2t} & 0 \\ \frac{-1}{2t} & \frac{i}{t} & \frac{-1}{2t} \\ 0 & \frac{-1}{2t} & \frac{-1}{\sqrt{2}t} \end{bmatrix} \tag{C.13}$$

Further, we also show the broadening $\tilde{\mathbf{\Gamma}}_{L(R)}$, where one can notice that the matrix rows and columns have a property similar to the previously mentioned diagonal symmetry, where the elements in the same row (column) have a pair with an opposite sign except for the element associated with the 0 energy state. For example, in the second row (column), this element is $-t$, while in the other cases it is $\frac{(-)t}{\sqrt{2}}$.

$$\tilde{\mathbf{\Sigma}}_{L,R} = \begin{bmatrix} \frac{-t}{2} & \frac{-t}{\sqrt{2}} & \frac{t}{2} \\ \frac{-t}{\sqrt{2}} & -t & \frac{t}{\sqrt{2}} \\ \frac{t}{2} & \frac{t}{\sqrt{2}} & \frac{-t}{2} \end{bmatrix} \tag{C.14}$$

Finally, we show the matrix $\mathbf{F}$ and the corresponding matrices $\mathbf{F}_1$ and $\mathbf{F}_2$ that have the afore-mentioned diagonal pairwise symmetry. Although in our specific case these elements are 0, more complex geometries will yield non-zero values. In the general case, when multiplying $\mathbf{F}_1$ and $\mathbf{F}_2$, only the elements in the row and column associated with the 0 energy state (second row and column) will give non-vanishing values in final matrix $\mathbf{F}$. We notice that the rows of $\mathbf{F}_1$ and $\mathbf{F}_2$ contain pairs of values of the same sign, while columns contain the pairs of values with opposite signs. For example, we show that multiplying row 2 with column 2, to obtain the central element of the matrix $\mathbf{F}$ will result in only one non-vanishing term $-i \times i$, which is exactly 1. We associate this element with the 0 energy state.

$$\mathbf{F} = \mathbf{F}_1 \mathbf{F}_2 = \begin{bmatrix} 0 & \frac{-i}{\sqrt{2}} & 0 \\ 0 & -i & 0 \\ 0 & \frac{i}{\sqrt{2}} & 0 \end{bmatrix} \cdot \begin{bmatrix} 0 & \frac{i}{\sqrt{2}} & 0 \\ 0 & i & 0 \\ 0 & \frac{-i}{\sqrt{2}} & 0 \end{bmatrix} = \begin{bmatrix} 0 & \frac{1}{\sqrt{2}} & 0 \\ 0 & 1 & 0 \\ 0 & \frac{-1}{\sqrt{2}} & 0 \end{bmatrix} \tag{C.15}$$

We note that taking the trace of **F** with more complex system shows that other diagonal terms will cancel out as the final matrix **F** keeps the diagonal pairwise symmetry. Hence, for junctions without sublattice imbalance, the trace of **F** is 0 due to the opposite sign contributions from the energy states. However, for 120° GNR junctions with sublattice imbalance and an eigenvalue of 0, we will see a contribution to transmission in the final matrix **F** from the zero energy state. We have shown this diagonal value to be exactly 1, hence indicating that the zero-energy state is responsible for the resonant transmission.

Bibliography

Abbas, A. N., Liu, G., Narita, A., Orosco, M., Feng, X., Müllen, K., and Zhou, C. (2014). Deposition, characterization, and thin-film-based chemical sensing of ultra-long chemically synthesized graphene nanoribbons. *J. Am. Chem. Soc.*, 136:7555.

Abdurakhmanova, N., Amsharov, N., Stepanow, S., Jansen, M., Kern, K., and Amsharov, K. (2014). Synthesis of wide atomically precise graphene nanoribbons from para-oligophenylene based molecular precursor. *Carbon*, 77:1187.

Abramova, V., Slesarev, A. S., and Tour, J. M. (2013). Meniscus-mask lithography for narrow graphene nanoribbons. *ACS Nano*, 7:6894.

Alcón, I., Calogero, G., Papior, N., and Brandbyge, M. (2021). Electrochemical control of charge current flow in nanoporous graphene. *Adv. Funct. Mater.*, 31:2104031.

Ammon, M., Sander, T., and Maier, S. (2017). On-surface synthesis of porous carbon nanoribbons from polymer chains. *J. Am. Chem. Soc.*, 139:12976.

Aprojanz, J., Power, S. R., Bampoulis, P., Roche, S., Jauho, A.-P., Zandvliet, H. J. W., Zakharov, A. A., and Tegenkamp, C. (2018). Ballistic tracks in graphene nanoribbons. *Nat. Commun.*, 9:4426.

Araújo, F. R. V., da Costa, D. R., Lima, F. N., Nascimento, A. C. S., and Pereira, J. M. (2021). Gate potential-controlled current switching in graphene y-junctions. *J. Phys.: Condens. Matter.*, 33:375501.

Areshkin, D. A. and White, C. T. (2007). Building blocks for integrated graphene circuits. *Nano Lett.*, 7:3253.

Aydin, A., Sisman, A., Fransson, J., Black-Schaffer, A. M., and Dutta, P. (2022). Thermodefect voltage in graphene nanoribbon junctions. *J. Phys.: Condens. Matter*, 34:195304.

Bahamon, D., Pereira, A., and Schulz, P. (2010). Tunable resonances due to vacancies in graphene nanoribbons. *Phys. Rev. B*, 82:165438.

Bai, J., Duan, X., and Huang, Y. (2009). Rational fabrication of graphene nanoribbons using a nanowire etch mask. *Nano Lett.*, 9:2083.

Bibliography

Balandin, A. A., Ghosh, S., Bao, W., Calizo, I., Teweldebrhan, D., Miao, F., and Lau, C. N. (2008). Superior thermal conductivity of single-layer graphene. *Nano Lett.*, 8:902.

Barkan, T. (2019). Graphene: the hype versus commercial reality. *Nat. Nanotechnol.*, 14:904.

Basagni, A., Sedona, F., Pignedoli, C. A., Cattelan, M., Nicolas, L., Casarin, M., and Sambi, M. (2015). Molecules–oligomers–nanowires–graphene nanoribbons: A bottom-up stepwise on-surface covalent synthesis preserving long-range order. *J. Am. Chem. Soc.*, 137:1802.

Bennett, P. B., Pedramrazi, Z., Madani, A., Chen, Y.-C., de Oteyza, D. G., Chen, C., Fischer, F. R., Crommie, M. F., and Bokor, J. (2013). Bottom-up graphene nanoribbon field-effect transistors. *Appl. Phys. Lett.*, 103:253114.

Bergvall, A. and Löfwander, T. (2013). Spectral footprints of impurity scattering in graphene nanoribbons. *Phys. Rev. B*, 87:205431.

Beyer, D., Wang, S., Pignedoli, C. A., Melidonie, J., Yuan, B., Li, C., Wilhelm, J., Ruffieux, P., Berger, R., Müllen, K., Fasel, R., and Feng, X. (2019). Graphene nanoribbons derived from zigzag edge-encased poly(para-2,9-dibenzo[bc,kl]coronenylene) polymer chains. *J. Am. Chem. Soc.*, 141:2843.

Biel, B., Blase, X., Triozon, F., and Roche, S. (2009). Anomalous doping effects on charge transport in graphene nanoribbons. *Phys. Rev. Lett.*, 102:096803.

Björk, J., Hanke, F., and Stafström, S. (2013). Mechanisms of halogen-based covalent self-assembly on metal surfaces. *J. Am. Chem. Soc.*, 135:5768.

Blackwell, R. E., Zhao, F., Brooks, E., Zhu, J., Piskun, I., Wang, S., Delgado, A., Lee, Y.-L., Louie, S. G., and Fischer, F. R. (2021). Spin splitting of dopant edge state in magnetic zigzag graphene nanoribbons. *Nature*, 600:647.

Blankenburg, S., Cai, J., Ruffieux, P., Jaafar, R., Passerone, D., Feng, X., Müllen, K., Fasel, R., and Pignedoli, C. A. (2012). Intraribbon heterojunction formation in ultranarrow graphene nanoribbons. *ACS Nano*, 6:2020.

Blanter, Y. M. and Martin, I. (2007). Transport through normal-metal-graphene contacts. *Phys. Rev. B*, 76:155433.

Bolotin, K. I., Sikes, K. J., Hone, J., Stormer, H. L., and Kim, P. (2008). Temperature-dependent transport in suspended graphene. *Phys. Rev. Lett.*, 101:096802.

Borin Barin, G., Fairbrother, A., Rotach, L., Bayle, M., Paillet, M., Liang, L., Meunier, V., Hauert, R., Dumslaff, T., Narita, A., Müllen, K., Sahabudeen, H., Berger, R., Feng, X., Fasel, R., and Ruffieux, P. (2019). Surface-synthesized graphene nanoribbons for room temperature switching devices: Substrate transfer and ex situ characterization. *ACS Appl. Nano Mater.*, 2:2184.

Borin Barin, G., Sun, Q., Di Giovannantonio, M., Du, C.-Z., Wang, X.-Y., Llinas, J. P., Mutlu, Z., Lin, Y., Wilhelm, J., Overbeck, J., Daniels, C., Lamparski, M., Sahabudeen, H., Perrin, M. L., Urgel, J. I., Mishra, S., Kinikar, A., Widmer, R., Stolz, S., Bommert, M., Pignedoli, C., Feng, X., Calame, M., Müllen, K., Narita, A., Meunier, V., Bokor, J., Fasel, R., and Ruffieux, P. (2022). Growth optimization and device integration of narrow-bandgap graphene nanoribbons. arXiv:2202.01101.

Born, M. and Oppenheimer, R. (1927). Zur quantentheorie der molekeln. *Ann. Phys.*, 389:457.

Brandimarte, P., Engelund, M., Papior, N., Garcia-Lekue, A., Frederiksen, T., and Sánchez-Portal, D. (2017). A tunable electronic beam splitter realized with crossed graphene nanoribbons. *J. Chem. Phys.*, 146:092318.

Braun, O., Overbeck, J., Abbassi, M. E., Käser, S., Furrer, R., Olziersky, A., Flasby, A., Barin, G. B., Darawish, R., Müllen, K., Ruffieux, P., Fasel, R., Shorubalko, I., Perrin, M. L., and Calame, M. (2021). Optimized graphene electrodes for contacting graphene nanoribbons. *Carbon*, 184:331.

Brey, L. and Fertig, A. (2006). Electronic states of graphene nanoribbons studied with the dirac equation. *Phys. Rev. B*, 73:235411.

Bronner, C., Durr, R. A., Rizzo, D. J., Lee, Y.-L., Marangoni, T., Kalayjian, A. M., Rodriguez, H., Zhao, W., Louie, S. G., Fischer, F. R., and Crommie, M. F. (2018). Hierarchical on-surface synthesis of graphene nanoribbon heterojunctions. *ACS Nano*, 12:2193.

Bronner, C., Leyssner, F., Stremlau, S., Utecht, M., Saalfrank, P., Klamroth, T., and Tegeder, P. (2012). Electronic structure of a subnanometer wide bottom-up fabricated graphene nanoribbon: End states, band gap, and dispersion. *Phys. Rev. B*, 86:085444.

Cai, J., Pignedoli, C. A., Talirz, L., Ruffieux, P., Söde, H., Liang, L., Meunier, V., Berger, R., Li, R., Feng, X., Müllen, K., and Fasel, R. (2014). Graphene nanoribbon heterojunctions. *Nat. Nanotechnol.*, 9:896.

Cai, J., Ruffieux, P., Jaafar, R., Bieri, M., Braun, T., Blankenburg, S., Muoth, M., Seitsonen, A. P., Saleh, M., Feng, X., Mullen, K., and Fasel, R. (2010). Atomically precise bottom-up fabrication of graphene nanoribbons. *Nature*, 466:470.

Cai, Z., She, L., Wu, L., and Zhong, D. (2016). On-surface synthesis of linear polyphenyl wires guided by surface steric effect. *J. Phys. Chem. C*, 120(12):6619.

Calogero, G., Alcón, I., Papior, N., Jauho, A.-P., and Brandbyge, M. (2019a). Quantum interference engineering of nanoporous graphene for carbon nanocircuitry. *J. Am. Chem. Soc.*, 141:13081.

Calogero, G., Papior, N. R., Kretz, B., Garcia-Lekue, A., Frederiksen, T., and Brandbyge, M. (2019b). Electron transport in nanoporous graphene: Probing the talbot effect. *Nano Lett.*, 19:576.

Bibliography

Campos, L. C., Manfrinato, V. R., Sanchez-Yamagishi, J. D., Kong, J., and Jarillo-Herrero, P. (2009). Anisotropic etching and nanoribbon formation in single-layer graphene. *Nano Lett.*, 9:2600.

Candini, A., Martini, L., Chen, Z., Mishra, N., Convertino, D., Coletti, C., Narita, A., Feng, X., Müllen, K., and Affronte, M. (2017). High photoresponsivity in graphene nanoribbon field-effect transistor devices contacted with graphene electrodes. *J. Phys. Chem. C*, 121:10620.

Cao, T., Zhao, F., and Louie, S. G. (2017). Topological phases in graphene nanoribbons: Junction states, spin centers, and quantum spin chains. *Phys. Rev. Lett.*, 119:076401.

Carbonell-Sanromà, E., Hieulle, J., Vilas-Varela, M., Brandimarte, P., Iraola, M., Barragán, A., Li, J., Abadia, M., Corso, M., Sánchez-Portal, D., Peña, D., and Pascual, J. I. (2017). Doping of graphene nanoribbons via functional group edge modification. *ACS Nano*, 11:7355.

Ceperley, D. M. and Alder, B. J. (1980). Ground state of the electron gas by a stochastic method. *Phys. Rev. Lett.*, 45:566.

Čerņevičs, K., Granata, V., and Yazyev, O. V. (2020a). Tight-binding electronic transport application (TBETA) for graphene nanoribbon junctions. *Materials Cloud Archive*, 2020.66. https://www.materialscloud.org/work/tools/tbeta.

Čerņevičs, K., Pizzochero, M., and Yazyev, O. V. (2020b). Even–odd conductance effect in graphene nanoribbons induced by edge functionalization with aromatic molecules: basis for novel chemosensors. *Eur. Phys. J. Plus.*, 135:681.

Čerņevičs, K. and Yazyev, O. V. (2021). Design rules for interconnects based on graphene nanoribbon junctions, supplementary tables. *Materials Cloud Archive*, 2021.145.

Čerņevičs, K., Yazyev, O. V., and Pizzochero, M. (2020c). Electronic transport across quantum dots in graphene nanoribbons: Toward built-in gap-tunable metal-semiconductor-metal heterojunctions. *Phys. Rev. B*, 102:201406.

Chau, R., Doyle, B., Datta, S., Kavalieros, J., and Zhang, K. (2007). Integrated nanoelectronics for the future. *Nat. Mater.*, 6:810.

Chen, C., Lin, Y., Zhou, W., Gong, M., He, Z., Shi, F., Li, X., Wu, J. Z., Lam, K. T., Wang, J. N., Yang, F., Zeng, Q., Guo, J., Gao, W., Zuo, J.-M., Liu, J., Hong, G., Antaris, A. L., Lin, M.-C., Mao, W. L., and Dai, H. (2021). Sub-10-nm graphene nanoribbons with atomically smooth edges from squashed carbon nanotubes. *Nat. Electron.*, 4:653.

Chen, P.-A., Chiang, M.-H., and Hsu, W.-C. (2017a). All-zigzag graphene nanoribbons for planar interconnect application. *J. Appl. Phys.*, 122:034301.

Chen, S., Chen, G., and Ratner, M. (2018). Designing principles of molecular quantum interference effect transistors. *J. Phys. Chem. Lett.*, 9:2843.

130

Chen, Y.-C., Cao, T., Chen, C., Pedramrazi, Z., Haberer, D., de Oteyza, D. G., Fischer, F. R., Louie, S. G., and Crommie, M. F. (2015). Molecular bandgap engineering of bottom-up synthesized graphene nanoribbon heterojunctions. *Nat. Nanotechnol.*, 10:156.

Chen, Y.-C., de Oteyza, D. G., Pedramrazi, Z., Chen, C., Fischer, F. R., and Crommie, M. F. (2013). Tuning the band gap of graphene nanoribbons synthesized from molecular precursors. *ACS Nano*, 7:6123.

Chen, Z., Lin, Y.-M., Rooks, M. J., and Avouris, P. (2007). Graphene nano-ribbon electronics. *Phys. E: Low-Dimens. Syst. Nanostruct.*, 40:228.

Chen, Z., Wang, H. I., Bilbao, N., Teyssandier, J., Prechtl, T., Cavani, N., Tries, A., Biagi, R., De Renzi, V., Feng, X., Kläui, M., De Feyter, S., Bonn, M., Narita, A., and Müllen, K. (2017b). Lateral fusion of chemical vapor deposited n = 5 armchair graphene nanoribbons. *J. Am. Chem. Soc.*, 139:9483.

Chen, Z., Zhang, W., Palma, C.-A., Lodi Rizzini, A., Liu, B., Abbas, A., Richter, N., Martini, L., Wang, X.-Y., Cavani, N., Lu, H., Mishra, N., Coletti, C., Berger, R., Klappenberger, F., Kläui, M., Candini, A., Affronte, M., Zhou, C., De Renzi, V., del Pennino, U., Barth, J. V., Räder, H. J., Narita, A., Feng, X., and Müllen, K. (2016). Synthesis of graphene nanoribbons by ambient-pressure chemical vapor deposition and device integration. *J. Am. Chem. Soc.*, 138(47):15488.

Chong, M. C., Afshar-Imani, N., Scheurer, F., Cardoso, C., Ferretti, A., Prezzi, D., and Schull, G. (2018). Bright electroluminescence from single graphene nanoribbon junctions. *Nano Lett.*, 18:175.

Chu, K.-L., Wang, Z.-B., Zhou, J.-J., and Jiang, H. (2017). Transport properties in monolayer–bilayer–monolayer graphene planar junctions. *Chinese Phys. B*, 26:067202.

Ci, L., Xu, Z., Wang, L., Gao, W., Ding, F., Kelly, K. F., Yakobson, B. I., and Ajayan, P. M. (2008). Controlled nanocutting of graphene. *Nano Res.*, 1:116.

Clar, E. and Clar, E. (1972). *The Aromatic Sextet*. A Wiley-Interscience publication. J. Wiley.

Corso, M., Carbonell-Sanromà, E., and de Oteyza, D. G. (2018). Bottom-up fabrication of atomically precise graphene nanoribbons. In *On-Surface Synthesis II*, page 113. Springer International Publishing.

Costa, P. S., Teeter, J. D., Enders, A., and Sinitskii, A. (2018). Chevron-based graphene nanoribbon heterojunctions: Localized effects of lateral extension and structural defects on electronic properties. *Carbon*, 134:310.

Cresti, A., Lopez-Bezanilla, A., Ordejón, P., and Roche, S. (2011). Oxygen surface functionalization of graphene nanoribbons for transport gap engineering. *ACS Nano*, 5:9271.

Bibliography

Cresti, A., Nemec, N., Biel, B., Niebler, G., Triozon, F., Cuniberti, G., and Roche, S. (2008). Charge transport in disordered graphene-based low dimensional materials. *Nano Res.*, 1:361.

Cresti, A. and Roche, S. (2009). Edge-disorder-dependent transport length scales in graphene nanoribbons: From klein defects to the superlattice limit. *Phys. Rev. B*, 79:233404.

Cuong, N. T. (2021). First-principles study on controlling energy gap of graphene using hybrid armchair-zigzag nanostructures. arXiv:2104.00719.

Darancet, P., Olevano, V., and Mayou, D. (2009). Coherent electronic transport through graphene constrictions: Subwavelength regime and optical analogy. *Phys. Rev. Lett.*, 102:136803.

de la Torre, B., Matěj, A., Sánchez-Grande, A., Cirera, B., Mallada, B., Rodríguez-Sánchez, E., Santos, J., Mendieta-Moreno, J. I., Edalatmanesh, S., Lauwaet, K., Otyepka, M., Medveď, M., Buendía, Á., Miranda, R., Martín, N., Jelínek, P., and Écija, D. (2020). Tailoring π-conjugation and vibrational modes to steer on-surface synthesis of pentalene-bridged ladder polymers. *Nat. Commun.*, 11:4567.

de Oteyza, D. G., García-Lekue, A., Vilas-Varela, M., Merino-Díez, N., Carbonell-Sanromà, E., Corso, M., Vasseur, G., Rogero, C., Guitián, E., Pascual, J. I., Ortega, J. E., Wakayama, Y., and Peña, D. (2016). Substrate-independent growth of atomically precise chiral graphene nanoribbons. *ACS Nano*, 10:9000.

Deng, H.-Y., Wakabayashi, K., and Lam, C.-H. (2014). Formation mechanism of bound states in graphene point contacts. *Phys. Rev. B*, 89:045423.

Deng, S., Cai, X., Zhang, Y., and Li, L. (2019a). Enhanced thermoelectric performance of twisted bilayer graphene nanoribbons junction. *Carbon*, 145:622.

Deng, S., Li, L., and Rees, P. (2019b). Bilayer graphene nanoribbons junction with aligned holes exhibiting high ZT values. *Carbon*, 155:438.

Deniz, O., Sánchez-Sánchez, C., Dumslaff, T., Feng, X., Narita, A., Müllen, K., Kharche, N., Meunier, V., Fasel, R., and Ruffieux, P. (2017). Revealing the electronic structure of silicon intercalated armchair graphene nanoribbons by scanning tunneling spectroscopy. *Nano Lett.*, 17:2197.

Denk, R., Hohage, M., Zeppenfeld, P., Cai, J., Pignedoli, C. A., Söde, H., Fasel, R., Feng, X., Müllen, K., Wang, S., Prezzi, D., Ferretti, A., Ruini, A., Molinari, E., and Ruffieux, P. (2014). Exciton-dominated optical response of ultra-narrow graphene nanoribbons. *Nat. Commun.*, 5:4253.

Deretzis, I. and Magna, A. L. (2006). Role of contact bonding on electronic transport in metal-carbon nanotube-metal systems. *Nanotechnology*, 17:5063.

Di Giovannantonio, M., Deniz, O., Urgel, J. I., Widmer, R., Dienel, T., Stolz, S., Sánchez-Sánchez, C., Muntwiler, M., Dumslaff, T., Berger, R., Narita, A., Feng, X., Müllen, K., Ruffieux, P., and Fasel, R. (2018). On-surface growth dynamics of graphene nanoribbons: The role of halogen functionalization. *ACS Nano*, 12:74.

Dienel, T., Kawai, S., Söde, H., Feng, X., Müllen, K., Ruffieux, P., Fasel, R., and Gröning, O. (2015). Resolving atomic connectivity in graphene nanostructure junctions. *Nano Lett.*, 15:5185.

Dong, L., Liu, P. N., and Lin, N. (2015). Surface-activated coupling reactions confined on a surface. *Acc. Chem. Res.*, 48:2765.

Dong, X., Wang, L., Li, K., Zheng, H., Wang, Y., Meng, Y., Shu, H., kwang Mao, H., Feng, S., and Jin, C. (2018). Tailored synthesis of the narrowest zigzag graphene nanoribbon structure by compressing the lithium acetylide under high temperature. *J. Phys. Chem. C*, 122:20506.

Dubey, R. K., Melle-Franco, M., and Mateo-Alonso, A. (2021). Twisted molecular nanoribbons with up to 53 linearly-fused rings. *J. Am. Chem. Soc.*, 143:6593.

Dubois, S. M.-M., Lopez-Bezanilla, A., Cresti, A., Triozon, F., Biel, B., Charlier, J.-C., and Roche, S. (2010). Quantum transport in graphene nanoribbons: Effects of edge reconstruction and chemical reactivity. *ACS Nano*, 4:1971.

Dubois, S. M.-M., Zanolli, Z., Declerck, X., and Charlier, J.-C. (2009). Electronic properties and quantum transport in graphene-based nanostructures. *Eur. Phys. J. B*, 72:1.

El Gemayel, M., Narita, A., Dossel, L., Sundaram, R., Kiersnowski, A., Pisula, W., Hansen, M. R., Ferrari, A., Orgiu, E., Feng, X., Mullen, K., and Samori, P. (2014). Graphene nanoribbon blends with p3ht for organic electronics. *Nanoscale*, 6:6301.

Fu, Y., Yang, H., Gao, Y., Huang, L., Berger, R., Liu, J., Lu, H., Cheng, Z., Du, S., Gao, H.-J., and Feng, X. (2020). On-surface synthesis of NBN-doped zigzag-edged graphene nanoribbons. *Angew. Chem. Int. Ed.*, 59:8873.

Gemayel, M. E., Narita, A., Dössel, L. F., Sundaram, R. S., Kiersnowski, A., Pisula, W., Hansen, M. R., Ferrari, A. C., Orgiu, E., Feng, X., Müllen, K., and Samorì, P. (2014). Graphene nanoribbon blends with p3ht for organic electronics. *Nanoscale*, 6:6301.

Giovannantonio, M. D., Deniz, O., Urgel, J. I., Widmer, R., Dienel, T., Stolz, S., Sánchez-Sánchez, C., Muntwiler, M., Dumslaff, T., Berger, R., Narita, A., Feng, X., Müllen, K., Ruffieux, P., and Fasel, R. (2017). On-surface growth dynamics of graphene nanoribbons: The role of halogen functionalization. *ACS Nano*, 12:74.

González, J. W., Pacheco, M., Rosales, L., and Orellana, P. A. (2011). Transport properties of graphene quantum dots. *Phys. Rev. B*, 83:155450.

Greenwald, J. E., Cameron, J., Findlay, N. J., Fu, T., Gunasekaran, S., Skabara, P. J., and Venkataraman, L. (2021). Highly nonlinear transport across single-molecule junctions via destructive quantum interference. *Nat. Nanotechnol.*, 16:313.

Bibliography

Groth, C. W., Wimmer, M., Akhmerov, A. R., and Waintal, X. (2014). Kwant: a software package for quantum transport. *New J. Phys.*, 16:063065.

Gröning, O., Wang, S., Yao, X., Pignedoli, C. A., Barin, G. B., Daniels, C., Cupo, A., Meunier, V., Feng, X., Narita, A., Mullen, K., Ruffieux, P., and Fasel, R. (2018). Engineering of robust topological quantum phases in graphene nanoribbons. *Nature*, 560:209.

Gunlycke, D. and White, C. T. (2008). Tight-binding energy dispersions of armchair-edge graphene nanostrips. *Phys. Rev. B*, 77:115116.

Habib, K. M. M., Zahid, F., and Lake, R. K. (2011). Negative differential resistance in bilayer graphene nanoribbons. *Appl. Phys. Lett.*, 98:192112.

Haddadi, F., Wu, Q., Kruchkov, A. J., and Yazyev, O. V. (2020). Moiré flat bands in twisted double bilayer graphene. *Nano Lett.*, 20:2410.

Han, D., Fan, Q., Dai, J., Wang, T., Huang, J., Xu, Q., Ding, H., Hu, J., Feng, L., Zhang, W., Zeng, Z., Gottfried, J. M., and Zhu, J. (2020). On-surface synthesis of armchair-edged graphene nanoribbons with zigzag topology. *J. Phys. Chem. C*, 124:5248.

Han, M. Y., Özyilmaz, B., Zhang, Y., and Kim, P. (2007). Energy band-gap engineering of graphene nanoribbons. *Phys. Rev. Lett.*, 98:206805.

Han, P., Akagi, K., Federici Canova, F., Mutoh, H., Shiraki, S., Iwaya, K., Weiss, P. S., Asao, N., and Hitosugi, T. (2014). Bottom-up graphene-nanoribbon fabrication reveals chiral edges and enantioselectivity. *ACS Nano*, 8:9181.

Han, P., Akagi, K., Federici Canova, F., Shimizu, R., Oguchi, H., Shiraki, S., Weiss, P. S., Asao, N., and Hitosugi, T. (2015). Self-assembly strategy for fabricating connected graphene nanoribbons. *ACS Nano*, 9:12035.

Hancock, Y., Uppstu, A., Saloriutta, K., Harju, A., and Puska, M. J. (2010). Generalized tight-binding transport model for graphene nanoribbon-based systems. *Phys. Rev. B*, 81:245402.

Hayashi, H., Yamaguchi, J., Jippo, H., Hayashi, R., Aratani, N., Ohfuchi, M., Sato, S., and Yamada, H. (2017). Experimental and theoretical investigations of surface-assisted graphene nanoribbon synthesis featuring carbon–fluorine bond cleavage. *ACS Nano*, 11:6204.

Hohenberg, P. and Kohn, W. (1964). Inhomogeneous electron gas. *Phys. Rev.*, 136:B864.

ipywidgets (2021). 7.6.3. https://github.com/jupyter-widgets/ipywidgets.

Jacobse, P. H., Kimouche, A., Gebraad, T., Ervasti, M. M., Thijssen, J. M., Liljeroth, P., and Swart, I. (2017). Electronic components embedded in a single graphene nanoribbon. *Nat. Commun.*, 8:119.

Jacobse, P. H., McCurdy, R. D., Jiang, J., Rizzo, D. J., Veber, G., Butler, P., Zuzak, R., Louie, S. G., Fischer, F. R., and Crommie, M. F. (2020). Bottom-up assembly of nanoporous graphene with emergent electronic states. *J. Am. Chem. Soc.*, 142:13507.

Jacobse, P. H., van den Hoogenband, A., Moret, M.-E., Klein Gebbink, R. J. M., and Swart, I. (2016). Aryl radical geometry determines nanographene formation on au(111). *Angew. Chem. Int. Ed.*, 55:13052.

Jiang, F., Trupp, D. I., Algethami, N., Zheng, H., He, W., Alqorashi, A., Zhu, C., Tang, C., Li, R., Liu, J., Sadeghi, H., Shi, J., Davidson, R., Korb, M., Sobolev, A. N., Naher, M., Sangtarash, S., Low, P. J., Hong, W., and Lambert, C. J. (2019). Turning the tap: Conformational control of quantum interference to modulate single-molecule conductance. *Angew. Chem. Int. Ed.*, 58:18987.

Jiao, L., Wang, X., Diankov, G., Wang, H., and Dai, H. (2010). Facile synthesis of high-quality graphene nanoribbons. *Nat. Nanotechnol.*, 5:321.

Jiao, L., Zhang, L., Wang, X., Diankov, G., and Dai, H. (2009). Narrow graphene nanoribbons from carbon nanotubes. *Nature*, 458:877.

Jordan, R. S., Li, Y. L., Lin, C.-W., McCurdy, R. D., Lin, J. B., Brosmer, J. L., Marsh, K. L., Khan, S. I., Houk, K. N., Kaner, R. B., and Rubin, Y. (2017). Synthesis of n = 8 armchair graphene nanoribbons from four distinct polydiacetylenes. *J. Am. Chem. Soc.*, 139:15878.

Jordan, R. S., Wang, Y., McCurdy, R. D., Yeung, M. T., Marsh, K. L., Khan, S. I., Kaner, R. B., and Rubin, Y. (2016). Synthesis of graphene nanoribbons via the topochemical polymerization and subsequent aromatization of a diacetylene precursor. *Chem*, 1:78.

Kane, C. L. and Mele, E. J. (2005). Z2topological order and the quantum spin hall effect. *Phys. Rev. Lett.*, 95:146802.

Kawai, T., Poetschke, M., Miyamoto, Y., Rocha, C. G., Roche, S., and Cuniberti, G. (2011). Mechanically-induced transport switching effect in graphene-based nanojunctions. *Phys. Rev. B*, 83:241405.

Keerthi, A., Sánchez-Sánchez, C., Deniz, O., Ruffieux, P., Schollmeyer, D., Feng, X., Narita, A., Fasel, R., and Müllen, K. (2020). On-surface synthesis of a chiral graphene nanoribbon with mixed edge structure. *Chem. Asian J.*, 15:3807.

Kihira, K. and Aoki, M. (2017). Vacancy-induced shifts of edge states in z-shaped graphene nanoribbon quantum dot. *Mater. Res. Bull.*, 94:208.

Kim, K. T., Jung, J. W., and Jo, W. H. (2013). Synthesis of graphene nanoribbons with various widths and its application to thin-film transistor. *Carbon*, 63:202.

Kimouche, A., Ervasti, M., Drost, R., Halonen, S., Harju, A., Joensuu, P. M., Sainio, J., and Liljeroth, P. (2015). Ultra-narrow metallic armchair graphene nanoribbons. *Nat. Commun.*, 6:10177.

Kluyver, T., Ragan-Kelley, B., Pérez, F., Granger, B., Bussonnier, M., Frederic, J., Kelley, K., Hamrick, J., Grout, J., Corlay, S., Ivanov, P., Avila, D., Abdalla, S., Willing, C., and development

Bibliography

team, J. (2016). Jupyter notebooks - a publishing format for reproducible computational workflows. In Loizides, F. and Scmidt, B., editors, *Positioning and Power in Academic Publishing: Players, Agents and Agendas*, pages 87–90, Netherlands. IOS Press.

Koch, M., Ample, F., Joachim, C., and Grill, L. (2012). Voltage-dependent conductance of a single graphene nanoribbon. *Nat. Nanotechnol.*, 7:713.

Kohn, W. and Sham, L. J. (1965). Self-consistent equations including exchange and correlation effects. *Phys. Rev.*, 140:A1133.

Kong, X.-L. and Xiong, Y.-J. (2010). Resonance transport of graphene nanoribbon t-shaped junctions. *Chinese Phys. Lett.*, 27:047202.

Kosynkin, D. V., Higginbotham, A. L., Sinitskii, A., Lomeda, J. R., Dimiev, A., Price, B. K., and Tour, J. M. (2009). Longitudinal unzipping of carbon nanotubes to form graphene nanoribbons. *Nature*, 458:872.

Krompiewski, S. (2004). Non-equilibrium transport in ferromagnetically contacted metallic carbon nanotubes. *J. Magn. Magn. Mater.*, 272-276:1645.

Krukau, A. V., Vydrov, O. A., Izmaylov, A. F., and Scuseria, G. E. (2006). Influence of the exchange screening parameter on the performance of screened hybrid functionals. *J. Chem. Phys.*, 125:224106.

Kundu, R. (2011). Tight-binding parameters for graphene. *Mod. Phys. Lett. B*, 25:163.

Landauer, R. (1957). Spatial variation of currents and fields due to localized scatterers in metallic conduction. *IBM J. Res. Dev.*, 1:223.

Lee, C., Wei, X., Kysar, J. W., and Hone, J. (2008). Measurement of the elastic properties and intrinsic strength of monolayer graphene. *Science*, 321:385.

Li, H., Li, H., Zheng, Y., and Niu, J. (2011). Electron transport of step-shaped graphene nanoribbon. *Phys. B Condens. Matter*, 406:1385.

Li, J., Li, S., Ouyang, T., Zhang, C., Tang, C., He, C., and Zhong, J. (2021a). Two-dimensional carbon allotropes and nanoribbons based on 2,6-polyazulene chains: Stacking stabilities and electronic properties. *J. Phys. Chem. Lett.*, 12:732.

Li, J., Sanz, S., Corso, M., Choi, D. J., Peña, D., Frederiksen, T., and Pascual, J. I. (2019a). Single spin localization and manipulation in graphene open-shell nanostructures. *Nat. Commun.*, 10:200.

Li, J., Sanz, S., Merino-Díez, N., Vilas-Varela, M., Garcia-Lekue, A., Corso, M., de Oteyza, D. G., Frederiksen, T., Peña, D., and Pascual, J. I. (2021b). Topological phase transition in chiral graphene nanoribbons: from edge bands to end states. *Nat. Commun.*, 12:5538.

Li, Y., Buerkle, M., Li, G., Rostamian, A., Wang, H., Wang, Z., Bowler, D. R., Miyazaki, T., Xiang, L., Asai, Y., Zhou, G., and Tao, N. (2019b). Gate controlling of quantum interference and direct observation of anti-resonances in single molecule charge transport. *Nat. Mater.*, 18:357.

Linden, S., Zhong, D., Timmer, A., Aghdassi, N., Franke, J. H., Zhang, H., Feng, X., Müllen, K., Fuchs, H., Chi, L., and Zacharias, H. (2012). Electronic structure of spatially aligned graphene nanoribbons on au(788). *Phys. Rev. Lett.*, 108:216801.

Liu, J., Li, B.-W., Tan, Y.-Z., Giannakopoulos, A., Sanchez-Sanchez, C., Beljonne, D., Ruffieux, P., Fasel, R., Feng, X., and Müllen, K. (2015). Toward cove-edged low band gap graphene nanoribbons. *J. Am. Chem. Soc.*, 137:6097.

Liu, M., Liu, M., She, L., Zha, Z., Pan, J., Li, S., Li, T., He, Y., Cai, Z., Wang, J., Zheng, Y., Qiu, X., and Zhong, D. (2017). Graphene-like nanoribbons periodically embedded with four- and eight-membered rings. *Nat. Commun.*, 8:14924.

Liu, W., Meng, F., Zhao, J., and Jiang, X. (2019). Electronic transport through hybrid armchair graphane/graphene nanoribbons. *Phys. B Condens. Matter*, 554:144.

Liwei, J., Zhe, L., Xudong, Z., and Yisong, Z. (2016). Armchair-edged nanoribbon as a bottleneck to electronic total transmission through a topologically nontrivial graphene nanojunction. *J. Phys.: Condens. Matter*, 28:085501.

Llinas, J. P., Fairbrother, A., Borin Barin, G., Shi, W., Lee, K., Wu, S., Yong Choi, B., Braganza, R., Lear, J., Kau, N., Choi, W., Chen, C., Pedramrazi, Z., Dumslaff, T., Narita, A., Feng, X., Müllen, K., Fischer, F., Zettl, A., Ruffieux, P., Yablonovitch, E., Crommie, M., Fasel, R., and Bokor, J. (2017). Short-channel field-effect transistors with 9-atom and 13-atom wide graphene nanoribbons. *Nat. Commun.*, 8:633.

Lopez-Bezanilla, A. and Roche, S. (2012). Embedded boron nitride domains in graphene nanoribbons for transport gap engineering. *Phys. Rev. B*, 86:165420.

López-Bezanilla, A., Triozon, F., and Roche, S. (2009). Chemical functionalization effects on armchair graphene nanoribbon transport. *Nano Lett.*, 9:2537.

Ma, C., Liang, L., Xiao, Z., Puretzky, A. A., Hong, K., Lu, W., Meunier, V., Bernholc, J., and Li, A.-P. (2017a). Seamless staircase electrical contact to semiconducting graphene nanoribbons. *Nano Lett.*, 17:6241.

Ma, C., Xiao, Z., Huang, J., Liang, L., Lu, W., Hong, K., Sumpter, B. G., Bernholc, J., and Li, A.-P. (2019). Direct writing of heterostructures in single atomically precise graphene nanoribbons. *Phys. Rev. Materials*, 3:016001.

Ma, C., Xiao, Z., Zhang, H., Liang, L., Huang, J., Lu, W., Sumpter, B. G., Hong, K., Bernholc, J., and Li, A.-P. (2017b). Controllable conversion of quasi-freestanding polymer chains to graphene nanoribbons. *Nat. Commun.*, 8:14815.

Majhi, J., Maiti, S. K., and Ganguly, S. (2022). Enhanced current rectification in graphene nanoribbons: effects of geometries and orientations of nanopores. *Nanotechnology*, 33:255704.

Marangoni, T., Haberer, D., Rizzo, D. J., Cloke, R. R., and Fischer, F. R. (2016). Heterostructures through divergent edge reconstruction in nitrogen-doped segmented graphene nanoribbons. *Chem. Eur. J.*, 22:13037.

Marconcini, P., Cresti, A., Triozon, F., Fiori, G., Biel, B., Niquet, Y.-M., Macucci, M., and Roche, S. (2012). Atomistic boron-doped graphene field-effect transistors: A route toward unipolar characteristics. *ACS Nano*, 6:7942.

Martín-Martínez, F. J., Fias, S., Van Lier, G., De Proft, F., and Geerlings, P. (2012). Electronic structure and aromaticity of graphene nanoribbons. *Chem. Eur. J.*, 18:6183.

Martini, L., Chen, Z., Mishra, N., Barin, G. B., Fantuzzi, P., Ruffieux, P., Fasel, R., Feng, X., Narita, A., Coletti, C., Müllen, K., and Candini, A. (2019). Structure-dependent electrical properties of graphene nanoribbon devices with graphene electrodes. *Carbon*, 146:36.

McCurdy, R. D., Jacobse, P. H., Piskun, I., Veber, G. C., Rizzo, D. J., Zuzak, R., Mutlu, Z., Bokor, J., Crommie, M. F., and Fischer, F. R. (2021). Synergetic bottom-up synthesis of graphene nanoribbons by matrix-assisted direct transfer. *J. Am. Chem. Soc.*, 143:4174.

Mehdi Pour, M., Lashkov, A., Radocea, A., Liu, X., Sun, T., Lipatov, A., Korlacki, R. A., Shekhirev, M., Aluru, N. R., Lyding, J. W., Sysoev, V., and Sinitskii, A. (2017). Laterally extended atomically precise graphene nanoribbons with improved electrical conductivity for efficient gas sensing. *Nat. Commun.*, 8:820.

Mendoza, M., Schulz, P. A., Vallejos, R. O., and Lewenkopf, C. H. (2008). Fano resonances in the conductance of quantum dots with mixed dynamics. *Phys. Rev. B*, 77:155307.

Meunier, V., Souza Filho, A., Barros, E., and Dresselhaus, M. (2016). Physical properties of low-dimensional sp2-based carbon nanostructures. *Rev. Mod. Phys.*, 88:025005.

Miroshnichenko, A. E., Flach, S., and Kivshar, Y. S. (2010). Fano resonances in nanoscale structures. *Rev. Mod. Phys.*, 82:2257.

Mohammadi, A. and Haji-Nasiri, S. (2018). The electronic transport properties of defected bilayer sliding armchair graphene nanoribbons. *Phys. Lett. A*, 382:1040.

Mohanty, N., Moore, D., Xu, Z., Sreeprasad, T., Nagaraja, A., Rodriguez, A. A., and Berry, V. (2012). Nanotomy-based production of transferable and dispersible graphene nanostructures of controlled shape and size. *Nat. Commun.*, 3:844.

Moore, G. (1998). Cramming more components onto integrated circuits. *Proc. IEEE*, 86:82.

Moreno, C., Vilas-Varela, M., Kretz, B., Garcia-Lekue, A., Costache, M. V., Paradinas, M., Panighel, M., Ceballos, G., Valenzuela, S. O., Pena, D., and Mugarza, A. (2018). Bottom-up synthesis of multifunctional nanoporous graphene. *Science*, 360:199.

Morozov, S. V., Novoselov, K. S., Katsnelson, M. I., Schedin, F., Elias, D. C., Jaszczak, J. A., and Geim, A. K. (2008). Giant intrinsic carrier mobilities in graphene and its bilayer. *Phys. Rev. Lett.*, 100:016602.

Motta, C., Sanchez-Portal, D., and Trioni, M. (2012). Transport properties of armchair graphene nanoribbon junction between graphene electrodes. *Phys. Chem. Chem. Phys.*, 14:10683.

Mutlu, Z., Jacobse, P. H., McCurdy, R. D., Llinas, J. P., Lin, Y., Veber, G. C., Fischer, F. R., Crommie, M. F., and Bokor, J. (2021). Bottom-up synthesized nanoporous graphene transistors (adv. funct. mater. 47/2021). *Adv. Funct. Mater.*, 31:2170348.

Muñoz-Rojas, F., Jacob, D., Fernández-Rossier, J., and Palacios, J. (2006). Coherent transport in graphene nanoconstrictions. *Phys. Rev. B*, 74:195417.

Nakada, K., Fujita, M., Dresselhaus, G., and Dresselhaus, M. S. (1996). Edge state in graphene ribbons: Nanometer size effect and edge shape dependence. *Phys. Rev. B*, 54:17954.

Nemec, N., Tománek, D., and Cuniberti, G. (2006). Contact dependence of carrier injection in carbon nanotubes: An ab initio study. *Phys. Rev. Lett.*, 96:076802.

Nguyen, G. D., Tsai, H.-Z., Omrani, A. A., Marangoni, T., Wu, M., Rizzo, D. J., Rodgers, G. F., Cloke, R. R., Durr, R. A., Sakai, Y., Liou, F., Aikawa, A. S., Chelikowsky, J. R., Louie, S. G., Fischer, F. R., and Crommie, M. F. (2017). Atomically precise graphene nanoribbon heterojunctions from a single molecular precursor. *Nat. Nanotechnol.*, 12:1077.

Niu, L.-L., Fu, H.-Y., Suo, Y.-Q., Liu, R., Sun, F., Wang, S.-S., Zhang, G.-P., Wang, C.-K., and Li, Z.-L. (2021). Doping-induced large spin-filter behavior and rectification behavior in zigzag graphene nano-ribbon junction. *Phys. E: Low-Dimens. Syst. Nanostruct.*, 128:114542.

Novoselov, K. S., Geim, A. K., Morozov, S. V., Jiang, D., Katsnelson, M. I., Grigorieva, I. V., Dubonos, S. V., and Firsov, A. A. (2005). Two-dimensional gas of massless dirac fermions in graphene. *Nature*, 438:197.

Novoselov, K. S., Geim, A. K., Morozov, S. V., Jiang, D., Zhang, Y., Dubonos, S. V., Grigorieva, I. V., and Firsov, A. A. (2004). Electric field effect in atomically thin carbon films. *Science*, 306:666.

Orellana, P., Dominguez-Adame, F., Gomez, I., and Ladron De Guevara, M. (2003). Transport through a quantum wire with a side quantum-dot array. *Phys. Rev. B*, 67:085321.

OuYang, F., Xiao, J., Guo, R., Zhang, H., and Xu, H. (2009). Transport properties of t-shaped and crossed junctions based on graphene nanoribbons. *Nanotechnology*, 20:055202.

Papior, N. (2016). *Computational Tools and Studies of Graphene Nanostructures.* PhD thesis, Technical University of Denmark.

Bibliography

Papior, N., Lorente, N., Frederiksen, T., Garcia, A., and Brandbyge, M. (2017). Improvements on non-equilibrium and transport Green function techniques: The next-generation TRAN-SIESTA. *Comput. Phys. Commun.*, 212:8.

Pawlak, R., Liu, X., Ninova, S., d'Astolfo, P., Drechsel, C., Sangtarash, S., Häner, R., Decurtins, S., Sadeghi, H., Lambert, C. J., Aschauer, U., Liu, S.-X., and Meyer, E. (2020). Bottom-up synthesis of nitrogen-doped porous graphene nanoribbons. *J. Am. Chem. Soc.*, 142:12568.

Peierls, R. (1935). Quelques propriétés typiques des corps solides. In *Ann. Henri Poincaré*, volume 5, page 177.

Perdew, J. P., Burke, K., and Ernzerhof, M. (1996a). Generalized gradient approximation made simple. *Phys. Rev. Lett.*, 77:3865.

Perdew, J. P., Ernzerhof, M., and Burke, K. (1996b). Rationale for mixing exact exchange with density functional approximations. *J. Chem. Phys.*, 105:9982.

Perdew, J. P. and Wang, Y. (1992). Accurate and simple analytic representation of the electron-gas correlation energy. *Phys. Rev. B*, 45:13244.

Pizzochero, M., Barin, G. B., Černevičs, K., Wang, S., Ruffieux, P., Fasel, R., and Yazyev, O. V. (2021a). Edge disorder in bottom-up zigzag graphene nanoribbons: Implications for magnetism and quantum electronic transport. *J. Phys. Chem. Lett.*, 12:4692.

Pizzochero, M., Černevičs, K., Barin, G. B., Wang, S., Ruffieux, P., Fasel, R., and Yazyev, O. V. (2021b). Quantum electronic transport across 'bite' defects in graphene nanoribbons. *2D Mater.*, 8:035025.

Pizzochero, M. and Kaxiras, E. (2021). Imprinting tunable π-magnetism in graphene nanoribbons via edge extensions. *J. Phys. Chem. Lett.*, 12:1214.

Pizzochero, M. and Kaxiras, E. (2022). Hydrogen atoms on zigzag graphene nanoribbons: Chemistry and magnetism meet at the edge. arXiv:2201.10482.

Qi, C., Peng, W., Zhou, J., Yi, L., Wang, J., and Zhang, Y. (2020). From graphene to graphene ribbons: atomically precise cutting via hydrogenation pseudo-crack. *Nanotechnology*, 31:415705.

Reich, S., Maultzsch, J., Thomsen, C., and Ordejón, P. (2002). Tight-binding description of graphene. *Phys. Rev. B*, 66:035412.

Reiss, T., Hjelt, K., and Ferrari, A. C. (2019). Graphene is on track to deliver on its promises. *Nat. Nanotechnol.*, 14:907.

Ribeiro, R., Poumirol, J.-M., Cresti, A., Escoffier, W., Goiran, M., Broto, J.-M., Roche, S., and Raquet, B. (2011). Unveiling the magnetic structure of graphene nanoribbons. *Phys. Rev. Lett.*, 107:086601.

Richter, N., Chen, Z., Tries, A., Prechtl, T., Narita, A., Müllen, K., Asadi, K., Bonn, M., and Kläui, M. (2020). Charge transport mechanism in networks of armchair graphene nanoribbons. *Sci. Rep.*, 10:1988.

Rizzo, D. J., Jiang, J., Joshi, D., Veber, G., Bronner, C., Durr, R. A., Jacobse, P. H., Cao, T., Kalayjian, A., Rodriguez, H., Butler, P., Chen, T., Louie, S. G., Fischer, F. R., and Crommie, M. F. (2021). Rationally designed topological quantum dots in bottom-up graphene nanoribbons. *ACS Nano*, 15:20633.

Rizzo, D. J., Veber, G., Cao, T., Bronner, C., Chen, T., Zhao, F., Rodriguez, H., Louie, S. G., Crommie, M. F., and Fischer, F. R. (2018). Topological band engineering of graphene nanoribbons. *Nature*, 560:204.

Rizzo, D. J., Veber, G., Jiang, J., McCurdy, R., Cao, T., Bronner, C., Chen, T., Louie, S. G., Fischer, F. R., and Crommie, M. F. (2020). Inducing metallicity in graphene nanoribbons via zero-mode superlattices. *Science*, 369:1597.

Rosales, L., Pacheco, M., Barticevic, Z., Latge, A., and Orellana, P. (2008a). Transport properties of graphene nanoribbons with side-attached organic molecules. *Nanotechnology*, 19:065402.

Rosales, L., Pacheco, M., Barticevic, Z., and Orellana, P. (2008b). Conductance of armchair gnrs with side-attached organic molecules. *Microelectron. J.*, 39:1233.

Rozhkov, A., Savel'ev, S., and Nori, F. (2009). Electronic properties of armchair graphene nanoribbons. *Phys. Rev. B*, 79:125420.

Ruffieux, P., Cai, J., Plumb, N. C., Patthey, L., Prezzi, D., Ferretti, A., Molinari, E., Feng, X., Müllen, K., Pignedoli, C. A., and Fasel, R. (2012). Electronic structure of atomically precise graphene nanoribbons. *ACS Nano*, 6:6930.

Ruffieux, P., Wang, S., Yang, B., Sánchez-Sánchez, C., Liu, J., Dienel, T., Talirz, L., Shinde, P., Pignedoli, C. A., Passerone, D., Dumslaff, T., Feng, X., Müllen, K., and Fasel, R. (2016). On-surface synthesis of graphene nanoribbons with zigzag edge topology. *Nature*, 531:489.

Saiz-Bretín, M., Sandonas, L. M., Gutierrez, R., Cuniberti, G., and Domínguez-Adame, F. (2019). Impact of device geometry on electron and phonon transport in graphene nanorings. *Phys. Rev. B*, 99:165428.

Sanz, S., Papior, N., Giedke, G., Sánchez-Portal, D., Brandbyge, M., and Frederiksen, T. (2022). A spin-polarizing electron beam splitter from crossed graphene nanoribbons. arXiv:2201. 07147.

Sautet, P. and Joachim, C. (1988). Electronic interference produced by an benzene embedded in a polyacetylene chain. *Chem. Phys. Lett.*, 153:511.

Bibliography

Schulz, F., Jacobse, P. H., Canova, F. F., van der Lit, J., Gao, D. Z., van den Hoogenband, A., Han, P., Klein Gebbink, R. J. M., Moret, M.-E., Joensuu, P. M., Swart, I., and Liljeroth, P. (2017). Precursor geometry determines the growth mechanism in graphene nanoribbons. *J. Phys. Chem. C*, 121:2896.

Schwierz, F. (2010). Graphene transistors. *Nat. Nanotechnol.*, 5:487.

Senkovskiy, B. V., Nenashev, A. V., Alavi, S. K., Falke, Y., Hell, M., Bampoulis, P., Rybkovskiy, D. V., Usachov, D. Y., Fedorov, A. V., Chernov, A. I., Gebhard, F., Meerholz, K., Hertel, D., Arita, M., Okuda, T., Miyamoto, K., Shimada, K., Fischer, F. R., Michely, T., Baranovskii, S. D., Lindfors, K., Szkopek, T., and Grüneis, A. (2021). Tunneling current modulation in atomically precise graphene nanoribbon heterojunctions. *Nat. Commun.*, 12:2542.

Silva, P. V. and Girão, E. C. (2021). Electronic and transport properties of graphene nanoribbons based on super-heptazethrene molecular blocks. *J. Phys. Chem. C*, 125:11235.

Simmons, J. G. (1963a). Electric tunnel effect between dissimilar electrodes separated by a thin insulating film. *J. Appl. Phys.*, 34:2581.

Simmons, J. G. (1963b). Generalized formula for the electric tunnel effect between similar electrodes separated by a thin insulating film. *J. Appl. Phys.*, 34:1793.

Soler, J. M., Artacho, E., Gale, J. D., García, A., Junquera, J., Ordejón, P., and Sánchez-Portal, D. (2002). The SIESTA method for ab initio order-N materials simulation. *J. Phys.: Condens. Matter*, 14:2745.

Son, Y.-W., Cohen, M. L., and Louie, S. G. (2006). Energy gaps in graphene nanoribbons. *Phys. Rev. Lett.*, 97:216803.

Sun, J., Marsman, M., Csonka, G. I., Ruzsinszky, A., Hao, P., Kim, Y.-S., Kresse, G., and Perdew, J. P. (2011). Self-consistent meta-generalized gradient approximation within the projector-augmented-wave method. *Phys. Rev. B*, 84:035117.

Sun, J., Ruzsinszky, A., and Perdew, J. (2015). Strongly constrained and appropriately normed semilocal density functional. *Phys. Rev. Lett.*, 115:036402.

Sun, K., Ji, P., Zhang, J., Wang, J., Li, X., Xu, X., Zhang, H., and Chi, L. (2019a). On-surface synthesis of 8- and 10-armchair graphene nanoribbons. *Small*, 15:1804526.

Sun, K., Krejči, O., Foster, A. S., Okuda, Y., Orita, A., and Kawai, S. (2019b). Synthesis of regioisomeric graphene nanoribbon junctions via heteroprecursors. *J. Phys. Chem. C*, 123:17632.

Sun, Q., Yan, Y., Yao, X., Müllen, K., Narita, A., Fasel, R., and Ruffieux, P. (2021). Evolution of the topological energy band in graphene nanoribbons. *J. Phys. Chem. Lett.*, 12:8679.

Sun, Q., Yao, X., Groning, O., Eimre, K., Pignedoli, C. A., Müllen, K., Narita, A., Fasel, R., and Ruffieux, P. (2020). Coupled spin states in armchair graphene nanoribbons with asymmetric zigzag edge extensions. *Nano Lett.*, 20:6429.

Sánchez-Sánchez, C., Dienel, T., Deniz, O., Ruffieux, P., Berger, R., Feng, X., Müllen, K., and Fasel, R. (2016). Purely armchair or partially chiral: Noncontact atomic force microscopy characterization of dibromo-bianthryl-based graphene nanoribbons grown on cu(111). *ACS Nano*, 10:8006.

Sánchez-Sánchez, C., Nicolaï, A., Rossel, F., Cai, J., Liu, J., Feng, X., Müllen, K., Ruffieux, P., Fasel, R., and Meunier, V. (2017). On-surface cyclization of ortho-dihalotetracenes to four- and six-membered rings. *J. Am. Chem. Soc.*, 139:17617.

Söde, H., Talirz, L., Gröning, O., Pignedoli, C. A., Berger, R., Feng, X., Müllen, K., Fasel, R., and Ruffieux, P. (2015). Electronic band dispersion of graphene nanoribbons via fourier-transformed scanning tunneling spectroscopy. *Phys. Rev. B*, 91:045429.

Talirz, L., Kumbhar, S., Passaro, E., Yakutovich, A. V., Granata, V., Gargiulo, F., Borelli, M., Uhrin, M., Huber, S. P., Zoupanos, S., Adorf, C. S., Andersen, C. W., Schütt, O., Pignedoli, C. A., Passerone, D., VandeVondele, J., Schulthess, T. C., Smit, B., Pizzi, G., and Marzari, N. (2020). Materials cloud, a platform for open computational science. *Sci. Data*, 7:299.

Talirz, L., Söde, H., Kawai, S., Ruffieux, P., Meyer, E., Feng, X., Müllen, K., Fasel, R., Pignedoli, C. A., and Passerone, D. (2019). Band gap of atomically precise graphene nanoribbons as a function of ribbon length and termination. *ChemPhysChem*, 20:2348.

Talirz, L., Söde, H., Dumslaff, T., Wang, S., Sanchez-Valencia, J. R., Liu, J., Shinde, P., Pignedoli, C. A., Liang, L., Meunier, V., Plumb, N. C., Shi, M., Feng, X., Narita, A., Müllen, K., Fasel, R., and Ruffieux, P. (2017). On-surface synthesis and characterization of 9-atom wide armchair graphene nanoribbons. *ACS Nano*, 11:1380.

Tapasztó, L., Dobrik, G., Lambin, P., and Biró, L. P. (2008). Tailoring the atomic structure of graphene nanoribbons by scanning tunnelling microscope lithography. *Nat. Nanotechnol.*, 3:397.

Teeter, J. D., Costa, P. S., Dobner, C., Sarker, M., Sinitskii, A., and Enders, A. (2021). Structure formation and coupling reactions of hexaphenylbenzene and its brominated analog. *ChemPhysChem*, 22:1769.

Teeter, J. D., Zahl, P., Pour, M. M., Costa, P. S., Enders, A., and Sinitskii, A. (2019). On-surface synthesis and spectroscopic characterization of laterally extended chevron graphene nanoribbons. *ChemPhysChem*, 20:2281.

Tepliakov, N. V., Lischner, J., Kaxiras, E., Mostofi, A. A., and Pizzochero, M. (2022). Unveiling and manipulating hidden symmetries in graphene nanoribbons. arXiv:2203.02808.

Bibliography

Tersoff, J. and Hamann, D. R. (1985). Theory of the scanning tunneling microscope. *Phys. Rev. B*, 31:805.

Tien, N. T., Ut, N. V., Hoc, B. T., Thao, T. T. N., and Khanh, N. D. (2019). Electronic transport in the v-shaped edge distorted zigzag graphene nanoribbons with substitutional doping. *Adv. Condens. Matter Phys.*, 2019:1.

Torres, L. E. F. F., Roche, S., and Charlier, J.-C. (2020). *Introduction to Graphene-Based Nano-materials*. Cambridge University Press.

Tran, V.-T. and Cresti, A. (2021). Thermoelectric properties of in-plane 90^0-bent graphene nanoribbons with nanopores. arXiv:2103.15427.

Tries, A., Richter, N., Chen, Z., Narita, A., Müllen, K., Wang, H. I., Bonn, M., and Kläui, M. (2020). Hysteresis in graphene nanoribbon field-effect devices. *Phys. Chem. Chem. Phys.*, 22:5667.

Troullier, N. and Martins, J. L. (1991). Efficient pseudopotentials for plane-wave calculations. *Phys. Rev. B*, 43:1993.

Valdiviezo, J., Rocha, P., Polakovsky, A., and Palma, J. L. (2021). Nonexponential length dependence of molecular conductance in acene-based molecular wires. *ACS Sens.*, 6:477.

van der Lit, J., Boneschanscher, M. P., Vanmaekelbergh, D., Ijäs, M., Uppstu, A., Ervasti, M., Harju, A., Liljeroth, P., and Swart, I. (2013). Suppression of electron–vibron coupling in graphene nanoribbons contacted via a single atom. *Nat. Commun.*, 4:3023.

Vergés, J. A., Chiappe, G., San-Fabián, E., and Louis, E. (2018). Conductance through the armchair graphene nanoribbons 9-agnr: Strong dependence on contact to leads. *Phys. Rev. B*, 98:155415.

Vo, T. H., Shekhirev, M., Kunkel, D. A., Morton, M. D., Berglund, E., Kong, L., Wilson, P. M., Dowben, P. A., Enders, A., and Sinitskii, A. (2014). Large-scale solution synthesis of narrow graphene nanoribbons. *Nat. Commun.*, 5:3189.

Voilà (2022). v0.3.5. https://github.com/voila-dashboards/voila.

Wakabayashi, K. (2001). Electronic transport properties of nanographite ribbon junctions. *Phys. Rev. B*, 64:125428.

Wakabayashi, K., Fujita, M., Ajiki, H., and Sigrist, M. (1999). Electronic and magnetic properties of nanographite ribbons. *Phys. Rev. B*, 59:8271.

Wakabayashi, K., Sasaki, K., Nakanishi, T., and Enoki, T. (2010). Electronic states of graphene nanoribbons and analytical solutions. *Sci. Technol. Adv. Mater.*, 11:05450411.

Wakabayashi, K. and Sigrist, M. (2000). Zero-conductance resonances due to flux states in nanographite ribbon junctions. *Phys. Rev. Lett.*, 84:3390.

Wallace, P. R. (1947). The band theory of graphite. *Phys. Rev.*, 71:622.

Wang, H., Wang, H. S., Ma, C., Chen, L., Jiang, C., Chen, C., Xie, X., Li, A.-P., and Wang, X. (2021a). Graphene nanoribbons for quantum electronics. *Nat. Rev. Phys.*, 3:791.

Wang, S., Hung, N. T., Tian, H., Islam, M. S., and Saito, R. (2021b). Switching behavior of a heterostructure based on periodically doped graphene nanoribbon. *Phys. Rev. Appl.*, 16:024030.

Wang, S., Kharche, N., Costa Girão, E., Feng, X., Müllen, K., Meunier, V., Fasel, R., and Ruffieux, P. (2017). Quantum dots in graphene nanoribbons. *Nano Lett.*, 17:4277.

Wang, T., Sanz, S., Castro-Esteban, J., Lawrence, J., Berdonces-Layunta, A., Mohammed, M. S. G., Vilas-Varela, M., Corso, M., Peña, D., Frederiksen, T., and de Oteyza, D. G. (2021c). Magnetic interactions between radical pairs in chiral graphene nanoribbons. *Nano Lett.*, 22:164.

Wang, W. L., Yazyev, O. V., Meng, S., and Kaxiras, E. (2009). Topological frustration in graphene nanoflakes: Magnetic order and spin logic devices. *Phys. Rev. Lett.*, 102:157201.

Wang, X. and Dai, H. (2010). Etching and narrowing of graphene from the edges. *Nat. Chem.*, 2:661.

Wang, X., Ma, J., Zheng, W., Osella, S., Arisnabarreta, N., Droste, J., Serra, G., Ivasenko, O., Lucotti, A., Beljonne, D., Bonn, M., Liu, X., Hansen, M. R., Tommasini, M., Feyter, S. D., Liu, J., Wang, H. I., and Feng, X. (2021d). Cove-edged graphene nanoribbons with incorporation of periodic zigzag-edge segments. *J. Am. Chem. Soc.*, 144:228.

Wassmann, T., Seitsonen, A. P., Saitta, A. M., Lazzeri, M., and Mauri, F. (2010). Clar's theory, pi-electron distribution, and geometry of graphene nanoribbons. *J. Am. Chem. Soc.*, 132:3440.

Weckbecker, D., Coto, P. B., and Thoss, M. (2020). Molecular transistor controlled through proton transfer. *J. Phys. Chem. Lett.*, 12:413.

White, C. T., Li, J., Gunlycke, D., and Mintmire, J. W. (2007). Hidden one-electron interactions in carbon nanotubes revealed in graphene nanostrips. *Nano Lett.*, 7:825.

Wu, C., Bates, D., Sangtarash, S., Ferri, N., Thomas, A., Higgins, S. J., Robertson, C. M., Nichols, R. J., Sadeghi, H., and Vezzoli, A. (2020). Folding a single-molecule junction. *Nano Lett.*, 20:7980.

Wurm, J., Wimmer, M., Adagideli, I., Richter, K., and Baranger, H. U. (2009). Interfaces within graphene nanoribbons. *New J. Phys.*, 11:095022.

Xia, Y., Li, T., Yuan, C., Fletcher, C., Dai, X., Zhang, X., Zhang, L., Jiang, Y., and Li, H. (2020). Odd-even effects on transport properties of polycyclic arene molecular devices with decreasing numbers of benzene rings. *ChemPhysChem*, 21:568.

Xiong, Y.-J. and Xiong, B.-K. (2011). Resonant transport through graphene nanoribbon quantum dots. *J. Appl. Phys.*, 109:103707.

Bibliography

Xu, J. G., Wang, L., and Weng, M. Q. (2013). Quasi-bound states and fano effect in t-shaped graphene nanoribbons. *J. Appl. Phys.*, 114:153701.

Xu, Y. and Wu, W. (2020). High-efficiency switching effect and negative differential conductance in cyclo[18]carbon–graphene nanoribbon junction. *J. Appl. Phys.*, 128:194303.

Yamaguchi, J., Hayashi, H., Jippo, H., Shiotari, A., Ohtomo, M., Sakakura, M., Hieda, N., Aratani, N., Ohfuchi, M., Sugimoto, Y., Yamada, H., and Sato, S. (2020). Small bandgap in atomically precise 17-atom-wide armchair-edged graphene nanoribbons. *Commun. Mater.*, 1:36.

Yang, R., Zhang, L., Wang, Y., Shi, Z., Shi, D., Gao, H., Wang, E., and Zhang, G. (2010). An anisotropic etching effect in the graphene basal plane. *Adv. Mater.*, 22:4014.

Yang, S., Olishevski, P., and Kertesz, M. (2004). Bandgap calculations for conjugated polymers. *Synth. Met.*, 141:171.

Yang, Z., Pan, J., Cheng, X., Xiong, X., and Ouyang, F. (2019). A first-principles study on transport properties of polyacene in zigzag graphene nanoribbon: Configuration, length and doping effects. *J. Appl. Phys.*, 126:104501.

Yano, Y., Wang, F., Mitoma, N., Miyauchi, Y., Ito, H., and Itami, K. (2020). Step-growth annulative π-extension polymerization for synthesis of cove-type graphene nanoribbons. *J. Am. Chem. Soc.*, 142:1686.

Yao, X., Zheng, W., Osella, S., Qiu, Z., Fu, S., Schollmeyer, D., Müller, B., Beljonne, D., Bonn, M., Wang, H. I., Müllen, K., and Narita, A. (2021). Synthesis of nonplanar graphene nanoribbon with fjord edges. *J. Am. Chem. Soc.*, 143:5654.

Yazyev, O. (2013). A guide to the design of electronic properties of graphene nanoribbons. *Acc. Chem. Res*, 46:2319.

Yin, D., Liu, W., Li, X., Geng, L., Wang, X., and Huai, P. (2013). Mono-bi-monolayer graphene junction introduced quantum transport channels. *Appl. Phys. Lett.*, 103:173519.

Zaminpayma, E., Nayebi, P., and Emami-Razavi, M. (2021). Rectification, transport properties of doped defective graphene nanoribbon junctions. *Nanotechnology*, 32:205204.

Zang, Y., Fu, T., Zou, Q., Ng, F., Li, H., Steigerwald, M. L., Nuckolls, C., and Venkataraman, L. (2020). Cumulene wires display increasing conductance with increasing length. *Nano Lett.*, 20:8415.

Zarea, M. and Sandler, N. (2007). Electron-electron and spin-orbit interactions in armchair graphene ribbons. *Phys. Rev. Lett.*, 99:256804.

Zdetsis, A. and Economou, E. (2021). Topological metal-insulator transition in narrow graphene nanoribbons? *Carbon*, 176:548.

Zhang, H., Lin, H., Sun, K., Chen, L., Zagranyarski, Y., Aghdassi, N., Duhm, S., Li, Q., Zhong, D., Li, Y., Müllen, K., Fuchs, H., and Chi, L. (2015). On-surface synthesis of rylene-type graphene nanoribbons. *J. Am. Chem. Soc.*, 137:4022.

Zhang, P., Tang, X., Wang, Y., Wang, X., Gao, D., Li, Y., Zheng, H., Wang, Y., Wang, X., Fu, R., Tang, M., Ikeda, K., Miao, P., Hattori, T., Sano-Furukawa, A., Tulk, C. A., Molaison, J. J., Dong, X., Li, K., Ju, J., and kwang Mao, H. (2020). Distance-selected topochemical dehydro-diels–alder reaction of 1,4-diphenylbutadiyne toward crystalline graphitic nanoribbons. *J. Am. Chem. Soc.*, 142:17662.

Zhang, S., Chen, H., Hu, J., Zhao, X., and Niu, X. (2022). First-principles calculations on lateral heterostructures of armchair graphene antidot nanoribbons for band alignment. *ACS Appl. Nano Mater.*, In press.

Zhang, X. and Liu, Y. (2022). Effects of antidot lattices density on transport features in zigzag graphene nanoribbons. *Electron. Struct.*, 4:025002.

Zhao, X., Geskin, V., and Stadler, R. (2017). Destructive quantum interference in electron transport: A reconciliation of the molecular orbital and the atomic orbital perspective. *J. Chem. Phys.*, 146:092308.

Zheng, J., Guo, P., Ren, Z., Jiang, Z., Bai, J., and Zhang, Z. (2012). Conductance fluctuations as a function of sliding motion in bilayer graphene nanoribbon junction: A first-principles investigation. *Appl. Phys. Lett.*, 101:083101.

Zhou, M., Jin, H., and Xing, Y. (2020). In-plane dual-gated spin-valve device based on the zigzag graphene nanoribbon. *Phys. Rev. Appl.*, 13:044006.

Zhou, Y.-H., Li, Y., Zheng, X., and Chen, K. (2021). The effects of covalent coupling strength on the electron transport properties and rectification in graphene/porphine/graphene molecular junctions. *Phys. E: Low-Dimens. Syst. Nanostruct.*, 134:114867.

Zschieschang, U., Klauk, H., Müeller, I. B., Strudwick, A. J., Hintermann, T., Schwab, M. G., Narita, A., Feng, X., Müellen, K., and Weitz, R. T. (2015). Electrical characteristics of field-effect transistors based on chemically synthesized graphene nanoribbons. *Adv. Electron. Mater.*, 1:1400010.

Zuzak, R., Stoica, O., Blieck, R., Echavarren, A. M., and Godlewski, S. (2020). On-surface synthesis and intermolecular cycloadditions of indacenoditetracenes, antiaromatic analogues of undecacene. *ACS Nano*, 15:1548.

Kristiāns Čerņevičs

Curriculum Vitae

EPFL
Institute of Physics
CH-1015
Lausanne, Switzerland
Office: PH H2 454

📱 +41 76 709 61 36
☎ +41 21 693 34 25
✉ kristians.cernevics@epfl.ch
Ⓢ Kristians Cernevics

Personal information

Born: September 15, 1993 in Riga, Latvia
Citizenship: Latvian (EU), Swiss permit B
Martial status: Not married

Education

Swiss Federal Institute of Technology (EPFL), Lausanne   2018-Present
PhD candidate in Doctoral school of Chemistry and Chemical engineering
University of Glasgow, Scotland   2012-2017
Msci in Chemical Physics with work placement, 1st class honors

Research experience

EPFL, Chair of Computational Condensed Matter Physics, Lausanne 04.2018-Present
"Electronic transport across graphene nanoribbon junctions" doctoral thesis
- Computational investigation of electronic structure of low dimensional materials, such as graphene, graphene nanoribbons, graphene nano-onions and transition metal dichalcogenides. Focus on electronic transport properties in graphene nanoribbon junctions for applications in nanoelectronics.

Jacobs University Bremen, Germany   09.2017-04.2018
Research assistant, Computational Physics and Biophysics group
- QM/MM hybrid approach of modeling the charge transport in metal-organic frameworks for applications in solar cells.

University of Glasgow, Scotland   09.2016-06.2017
Research intern, Computational chemistry and simulations group
- Density-functional theory based simulation of ion-pair transport through membranes in human mitochondria.

King Abdullah University of Science and Technology, Saudi Arabia 09.2015-06.2016
Visiting student researcher, Clean Combustion Center
- Interdisciplinary research of plasma physics in liquids. Experimental work with high-voltage plasma discharges, supplemented with theoretical modeling in COMSOL software.

Professional Service

Polyphys, EPFL, Switzerland   02.2021-02.2022
Vice President
- The association works as a representative body for PhD students from all physics sections. I'm in charge of organizing both formal and informal events for PhD candidates in order to socialize and explore potential collaboration opportunities in EPFL.

Marvel junior seminars, EPFL, Switzerland   09.2019-present
Organizing committee
- Organization and session chairing of monthly scientific seminars by members of the center on Computational Design and Discovery of Novel Materials (MARVEL).

Teaching and supervision activity

Computational physics III, TA, with Prof. O. V. Yazyev, EPFL   2018, 2019, 2020
General physics: electromagnetism, TA, with Prof. O.Boyarkine, EPFL   2018, 2019
Comp. simulations of phys. sys., Exam obs., with Prof. A.Pasquarello, EPFL   2019, 2021
Quantum physics III, TA, with Prof. O. V. Yazyev, EPFL   2020
Practical works 4, project supervisor, with Prof. O. V. Yazyev, EPFL 2020
Summer intern supervisor, with Prof. O. V. Yazyev, EPFL   2021

Technical skills

•**Programming**: Python, Shell/Bash, MATLAB   •Modeling: COMSOL
•**Machine learning**: PyTorch   •**Cloud computing**: Dokku   •**High-performance computing**
•Source code management: Git   •Productivity: MS Office, Latex   •OS: Windows, Linux, macOS
•**Graphics**: Adobe Illustrator   •Visualization: Xmgrace, gnuplot, Vesta, XCrySDen
•Electronic structure software: VASP, Quantum ESPRESSO, SIESTA   •Data analysis

Languages

• English - C2   •Russian - B2   •French - A2/B1   • Latvian - Native

Publications
* - contributed equally, ‡ - web application

[14]   Jacobse, P.H.*; McCurdy, R.D.*; Čerņevičs, K.*; Daugherty, M.; Wang, Z.; Dorit, R.; Liu K.; Lu, J.; Yazyev, O.V.; Fischer, F.R. and Crommie, M.F.
       Exploring topological magnetism in graphene nanoribbons through five-membered rings.
       In preparation

[13]   Čerņevičs, K. & Yazyev, O.V.
       Finite length and contact effects on electronic transport in graphene nanoribbon heterostructures
       In preperation

[12]   Čerņevičs, K. & Yazyev, O.V.
       From defect to effect: controlling electronic transport in chevron-type graphene nanoribbon nanostructures
       In preperation

[11] Pasquale, G.; Lopriore, E.; Sun, Z., Čerņevičs, K.; Tagarelli, F.; Watanabe, K.; Taniguchi, T.; Yazyev, O.V. & Kis, A.
Flat-band detection by out-of-plane tunneling photocurrent in a layered semiconductor
In preparation

[10] Pasquale, G.; Sun, Z., Čerņevičs, K.; Perea-Causin, R.; Tagarelli, F.; Watanabe, K.; Taniguchi, T.; Malic, E.; Yazyev, O.V. & Kis, A.
Exciton complexes in a charge-tunable metal monochalcogenide semiconductor
Submitted

[9]   Zhao, Y.; Tripathi, M.; Čerņevičs, K.; Avsar, A.; Ji, H.G.; Gonzalez Marin, H.F.; Cheon, C.Y.; Wang, Z.; Yazyev, O.V. & Kis, A.
Electrical spectroscopy of defect states and their hybridization in monolayer MoS$_2$
Submitted

[8]   Čerņevičs, K. & Yazyev, O.V.
Design Rules for Interconnects Based on Graphene Nanoribbon Junctions
Submitted

[7]   Pizzochero, M.*; Čerņevičs, K.*; Borin Barin, G.; Wang, S.; Ruffieux, P.; Fasel, R. & Yazyev, O.V.
Quantum Electronic Transport Across "Bite" Defects in Graphene Nanoribbons
2D Materials, 8, 035025. (2021)

[6]   Pizzochero, M.; Borin Barin, G.; Čerņevičs, K.; Wang, S.; Ruffieux, P.; Fasel, R. & Yazyev, O. V.
Edge Disorder in Bottom-Up Zigzag Graphene Nanoribbons: Implications for Magnetism and Quantum Electronic Transport
The Journal of Physical Chemistry Letters, 12, 4692. (2021)

[5]   Čerņevičs, K.; Granata, V. & Yazyev, O. V.
‡*Tight-binding electronic transport application (TBETA) for graphene nanoribbon junctions*
Materials Cloud Archive, 2020.66. (2020), doi: 10.24435/materialscloud:av-24, url: http:/www.materialscloud.org/work/tools/tbeta

[4]   Čerņevičs, K.; Yazyev, O. V. & Pizzochero, M.
M. Electronic transport across quantum dots in graphene nanoribbons: Toward built-in gap-tunable metal-semiconductor-metal heterojunctions
Physical Review B, 102, 201406(R). (2020)

[3]   Čerņevičs, K.; Pizzochero, M. & Yazyev, O. V.
Even–odd conductance effect in graphene nanoribbons induced by edge functionalization with aromatic molecules: basis for novel chemosensors
The European Physical Journal Plus, 135, 681. (2020)

[2]   Martino, E.; Santos-Cottin, D.; Mardelé, F. L.; Semeniuk, K.; Pizzochero, M.; Čerņevičs, K.; Baptiste, B.; Delbes, L.; Klotz, S.; Capitani, F.; Berger, H.; Yazyev, O. V. & Akrap, A.
Structural Phase Transition and Bandgap Control through Mechanical Deformation in Layered Semiconductors 1T–ZrX2 (X = S, Se)
ACS Materials Letters, 2, 1115. (2020)

[1]   Hamdan, A.; Čerņevičs, K. & Cha, M. S.
The effect of electrical conductivity on nanosecond discharges in distilled water and in methanol with argon bubbles
Journal of Physics D: Applied Physics, 50, 185207. (2017)